UNIVERSITY OF OKLAHOMA

GRADUATE COLLEGE

EHD-INDUCED FLOW AND HEAT TRANSFER ENHANCEMENT IN A SQUARE CHANNEL WITH TWO-STAGE ELECTRODES

A DISSERTATION

SUBMITTED TO THE GRADUATE FACULTY

in partial fulfillment of the requirements for the

Degree of

DOCTOR OF PHILOSOPHY

By

A. K. M. MONAYEM HOSSAIN MAZUMDER
Norman, Oklahoma
2012

EHD-INDUCED FLOW AND HEAT TRANSFER ENHANCEMENT
IN A SQUARE CHANNEL WITH TWO-STAGE ELECTODES

A DISSERTATION APPROVED FOR THE
SCHOOL OF AEROSPACE AND MECHANICAL ENGINEERING

BY

Dr. Feng C. Lai, Chair

Dr. Wilson E. Merchan-Merchan

Dr. Prakash Vedula

Dr. Li Song

Dr. Shihshu Walter Wei

To my parents and friends
for their love and support

ACKNOWLEDGMENTS

I would like to take this opportunity to thank my advisor, Dr. Feng C. Lai, for his guidance, suggestions, and patience while I am working under him as a graduate student. None of this would be possible without Dr. Lai's hard work and dedication to his students. Significant knowledge I have gained over the last two years from Dr. Lai and his heat transfer group. I am greatly thankful for all the opportunities that he created for me to attend various conferences, which have enhanced my presentation skills considerably. Most significantly, my PhD study was made possible because of Dr. Lai's continuous financial support over my entire period in the University of Oklahoma.

I would also like to thank Drs. Wilson E. Merchan-Merchan, Prakash Vedula, Li Song, and Shihshu Walter Wei for being a part of my dissertation committee and their time, and valuable suggestions.

Special thanks go to the School of Aerospace and Mechanical Engineering for the opportunities of being a teaching assistant for the past two years.

I would also like to thank Mr. Billy Mays and Greg Williams, staff of the School of Aerospace and Mechanical Engineering, for their assistance in constructing the apparatus utilized in this experiment.

Finally, I would like to thank all my family and friends for their support throughout the years while I pursed my PhD in Mechanical Engineering. They have always been there for me with constant support in difficult times and made the good times even more enjoyable, and for that I am very grateful.

TABLE OF CONTENTS

LIST OF TABLES

LIST OF FIGURES

ABSTRACT

The generation of a fluid flow and consequent effects on heat transfer enhancement within a square channel by electrohydrodynamic (EHD) gas pump are examined using both experimental and numerical methods. Experiments are conducted first to provide important information for the computing of electric field in the numerical study.

In this study, flow field inside a square channel with a two-stage EHD gas pump is first investigated via experimentation. Electrode pins are flush mounted on the channel walls and charged with a high voltage. The study has been performed for the EHD gas pump with three grounded electrode configurations: 0.5-inch, 1-inch, and 2-inch wide at top with 0.5-inch wide at bottom of two-stage unit. The EHD gas pump with 28 emitting electrodes in each stage is tested for a wide range of operating voltages starting from the corona onset up to 28 kV for further improvement in its performance over a single-stage one. Both corona current and corona wind velocity inside the channel are measured for operations using positive corona discharges. The performance of the EHD gas pump is then evaluated against that of conventional cooling fans used in personal computers. The experimental results provide important insights for the optimal design of an EHD gas pump.

Based on the experimental study, a numerical model is developed. The three-dimensional governing equations for the electric, flow, and temperature fields are solved using the finite volume method. Corona-driven (i.e. EHD-Induced) flow is calculated first, and its results are compared with the experimental data to validate the

computational code. The numerical results enable vivid flow visualizations inside the channel, providing a great understanding of the development of the induced flow.

The influence of electric field on the flow and temperature fields is also investigated with forced convection. Numerical simulations are performed for the EHD gas pump with all three electrode configurations at various applied voltages and a wide range of Reynolds numbers. The heat transfer enhancement and thermal hydraulic performance are then evaluated. To achieve the maximum enhancement in heat transfer, the emitting electrodes of the corona wind generator are flush mounted on the channel walls so that the corona wind produced can directly perturb the boundary layer. The results of the numerical study show that EHD technique has a great potential for many engineering applications, particularly for thermal management.

CHAPTER ONE

INTRODUCTION AND LITERATURE REVIEW

1.1 Introduction

A subject of great interest for many years is the use of electrical field to enhance the heat and mass transfer processes. This mechanism is based on using an electrical body force to induce a secondary flow (or simply create a flow) where none would otherwise exist.

Corona discharge usually involves two asymmetric electrodes; one highly curved (such as the tip of a needle, or a small diameter wire) and one of low curvature (such as a plate, or the ground). The high curvature ensures a high potential gradient around one electrode, for the generation of a plasma. Coronas may be positive or negative. This is determined by the polarity of the voltage applied to the highly-curved electrode. If the voltage applied to the curved electrode is positive with respect to the grounded electrode, then it is known as positive corona. Otherwise, it is a negative corona.

A corona discharge occurs in the narrow region close to the highly curved electrode (a needle or a fine wire) and gas molecules are ionized by a high electrical field. Controlled by the Coulomb force, these ions migrate to the grounded electrode. These ions transfer their momentum to neutral molecules via collision during the migration to the grounded electrode (Fig. 1.1). This creates a bulk flow, which is usually called ionic wind, or corona wind.

Corona discharge has the following commercial and industrial applications.

- EHD thrusters, Lifters, and other ionic wind devices
- Drag reduction over a flat surface
- Removal of unwanted electric charges from the surface of aircraft
- Sanitization of pool water
- Scrubbing particles from air in air-conditioning systems
- Removal of unwanted volatile organics, such as chemical pesticides, solvents, or chemical weapons agents, from the atmosphere
- Photocopying
- Surface treatment for tissue culture (polystyrene)
- Ionization of a gaseous sample for subsequent analysis in a mass spectrometer or an ion mobility spectrometer
- Generation of ozone

There are a few problems caused by corona discharges. Coronas can generate audible and radio-frequency noise. They also represent a power loss, and their action on atmospheric particulates, along with associated ozone and Nitric Oxide (NO_x) production, which can also be disadvantageous to human health. Corona discharge is undesirable in the following situations.

- Electric power transmission where it causes power loss, audible noise, electromagnetic interference and ozone production.
- Inside electrical components such as transformers, capacitors, electric motors and generators. Corona progressively damages the insulation of these devices leading to premature equipment failure.
- Static electricity discharge and lightning.

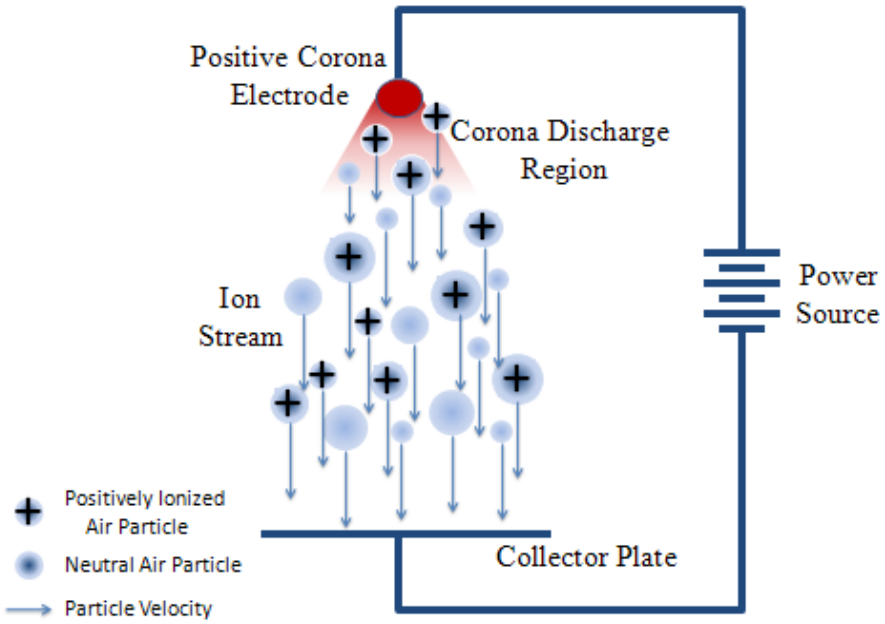

Figure 1.1 Schematic Diagram of the Mechanism of Corona Wind Migration.

Electrohydrodynamic (EHD) flows have been applied to wide industrial and engineering fields. For example, in the food industry, corona wind has become a novel drying method to enhance the dehydration process. EHD actuators are used in the aerospace industry to reduce the drag of an aircraft or to stabilize the air flow. In the thermal management of electronic systems, corona wind can produce a substantial increase in the heat transfer coefficient, which is also referred to as the electrohydrodynamic (EHD) enhancement technique. In addition, EHD technique has been widely used in manufacturing and power industries (i.e., electrostatic precipitators) to control particle emission and increase the efficiency of particle collection. Recently, as microelectronics has become an emerging technology, EHD techniques have played an important role in the development of microelectromechanical system (MEMS).

Electrohydrodynamic (EHD) technique has many advantages. Firstly, this technique directly converts electric energy into kinetic energy without involving moving mechanical parts, and therefore the maintenance cost can be greatly reduced. Secondly, this technique is operated electronically and it may be incorporated into the existing systems to be conveniently controlled by a computer. Thirdly, it is highly compatible with chips and chip-level structures. Thus, miniaturization can be easily implemented. Lastly and most importantly, the power consumption is usually very small, which makes this technique particularly attractive from the energy point of view. Its only disadvantage is the generation of extraneous gases such as ozone that might be harmful to human beings. However, ozone generation can be effectively monitored and minimized.

The characteristics of corona discharge vary significantly, depending on the working medium, device configuration, and ambient conditions. Corona discharges can occur either in liquids or gases. However, the liquid state is usually more chemically reactive compared to that of gases, which makes the electrohydrodynamic study more complicated. Device configurations are mostly determined by the purpose of their applications and directly affect the energy efficiency. The performance of corona wind is very sensitive to ambient conditions, such as temperature, pressure, and relative humidity, etc. For example, it has been shown that humidity affects the corona onset voltage. The discharge current decreases when air humidity increases in the range between +20 °C and +65 °C, but the wall temperature has no influence over the discharge. In addition, the efficiency of the corona wind device depends on the polarity

that it operates. For the case of flow separation control, it has been found that negative coronas are generally less efficient than positive coronas.

1.2 Literature Review

Numerous studies have been conducted in various fields that utilize corona discharge. This study has been focused on the effect of corona discharge on a flow field, specifically air flow, and the resulting heat transfer enhancement.

1.2.1 EHD-Induced Flow

Goldman et al. (1985) reviewed the main properties of corona discharges, with emphasis on the features which make them unique for use as non-equilibrium chemical reactors : their stability and ease of operation over a wide range of gases and pressures, including atmospheric ; their sharply confined ionization regions where hot electrons interact with cold gas, inducing reactions without back reactions ; and their extended low field drift regions which act as gaseous electrolytes, inducing electrochemical reactions on surfaces. They also discussed the present and future applications: synthesis of ozone and ammonia, promotion of flames and combustion, surface treatment, and electrical insulation improvement.

Bondar and Bastien (1986) examined the conversion efficiency from electrical energy to fluid kinetic energy. They showed that an increase of fluid velocity leads to a higher conversion efficiency. They investigated experimentally the case of a corona discharge from a moving point in ambient air. The experimental results obtained by

them on a moving corona point show that at least up to 50 m/s the conversion efficiency of electrical energy into fluid kinetic energy increases with neutral fluid velocity.

Mendes and Dente (1998) focused their study on controlling the profile of boundary layer. The profile has a direct effect on the laminar or turbulent nature of the flow which, in a simplified manner, they estimated by a local Reynolds number ($Re = uy^*/v$) defined as a function of the effective thickness y^*. Another relevant aspect, of course, is the active control of the transition instabilities that can be achieved by electromagnetic body forces on the charged fluid. A simplified treatment of the Tollmien-Schlichting fluctuations leads to the conclusion that a space-time modulation of the electric field, with the appropriate phase, is equivalent to an effective viscous damping effect which delays the growth of the transition instability. For this to be effective one needs to detect the phase of the wave instabilities by electromagnetic probes. Absolute synchronization of the feedback electric modulation is, however, not as critical as in acoustic noise cancelation because here the objective is only to obtain an effective damping effect. The effective damping gives an intuitive understanding of why a feedback electric modulation might work. A more rigorous treatment requires the solution of an integro-differential eigenvalue problem. Because of the perturbation induced by the injection method, it seems advisable to use this method in conjunction with suction and passive control in the rear part of the airfoil. Even if a fully laminar boundary layer may never be completely achieved, any small improvement will become, in the long run, quite significant in terms of fuel consumption.

Hyun and Chun (2003) observed that active and passive flow control methods have been studied for decades, but there have been only a few studies of flow control methods using ion wind, which is the bulk motion of neutral molecules driven by locally ionized air from a corona discharge. They described in this paper an experimental study of ion wind wake control behind a circular cylinder. Their experimental conditions consisted of a range of electro-hydrodynamic numbers which means the ratio of an electrical body force to a fluid inertial force from 0 to 2 and a range of Reynolds numbers from 4,000 to 8,000. They measured the pressure distributions over the cylinder surface and flow visualizations were carried out using a smoke-wire method. The flow visualizations confirmed that ion wind significantly affects the wake structure behind a circular cylinder, and that the pressure drag can be dramatically reduced by superimposing ion wind.

Roth (2003) studied the development of the One Atmosphere Uniform Glow Discharge Plasma which made it possible to cover the wings and fuselage of aircraft with a thin layer of glow discharge plasma at low energy cost. This plasma layer provides, through Lorentzian collisions, a purely electrohydrodynamic coupling between an electric field and the neutral gas in the boundary layer. This coupling is strong enough to cause aerodynamically significant acceleration and manipulation of the boundary layer and free stream flow, including re-attachment of flow to an airfoil at high angles of attack, and the peristaltic induction of neutral gas flow by a traveling electrostatic wave on the surface of a flat plate.

Forte et al. (2005) investigated the measurement of the instantaneous flow velocity induced by surface plasma actuators in air at atmospheric pressure. They conducted experiments with Laser Doppler Velocimetry (LDV) with two different types of plasma actuators in order to determine the establishment time of the induced airflow. They also investigated the DC corona discharges and AC dielectric barrier discharges in their non-stationary running (ignition and stop of the discharge) using a synchronization between power supplies and the LDV system. Their results showed: (a) the discharge-induced velocity is some m/s, (b) there is a strong correlation between the transient regime of the discharge current and the ionic wind velocity, (c) the AC discharge seems to induce a pulsed airflow at a frequency corresponding to the high voltage waveform frequency, (d) the DC discharge generates airflow with important fluctuations which cannot be correlated with current fluctuations.

Kawamoto and Umezu (2005) investigated the electro-hydrodynamic deformation of water surface in a pin-to-plate gas discharge system that consisted of a pin electrode made of metal and an ion-conductive water electrode. In the condition of a lower applied voltage than the corona threshold, because an extremely small electrostatic attractive force, a Coulomb force in the order of 10 μN, was induced, water lifted up in the order of several tens of micrometers at the centre. Over the threshold voltage corona discharge took place and a relatively large repulsive force, in the order of 100 μN, was induced due to the ionic wind. It depressed water in the order of several hundred micrometers at the centre. Deformation of the water level coincided with the pressure distribution on the metal plate electrode, if the surface tension of water and the Coulomb force was included in the estimation to derive the pressure distribution from

the measured deformation of the water level. If the applied voltage was lower than the corona threshold, total force to the water electrode coincided with that to the pin electrode. However, it was larger than that to the pin electrode at the corona discharge because the reaction force due to the ionic wind was applied not only to the pin electrode but also to other parts of the electrode at the corona discharge.

Rickard et al. (2005) observed when a strong electric field is generated between a sharp object at high voltage and a grounded electrode in a gas medium, a corona is formed near the tip of the sharp object and, as a result, the gas medium is set in motion. They reported on the flow behavior of a single-stage ion wind generator with and without a nozzle attached. Ion winds have rarely been measured quantitatively because traditional velocimeters (e.g., pitot tubes) have difficulty detecting their low flow speeds. In addition, seed-based measurement techniques (e.g., particle image velocimetry) are complicated by the possibility of electrical charging of the flow seed. Therefore, in the present study, they obtained the velocity profile at the exit plane of an enclosed pin-to-ring ion wind generator using two techniques to help validate their results: (1) particle image velocimetry downstream of the charge containing region and (2) hot wire anemometry. The velocity profiles indicated consistently that a pin-to-ring ion wind generator produces a velocity field with a deficit at its core. The velocities are sensitive to electrode alignment and consequently, producing symmetric profiles is difficult. The results also showed that by placing a converging nozzle downstream of the electrodes, only a slight increase in velocity can be achieved.

Chang et al. (2006) conducted experimental and theoretical investigations for the onset of electrohydrodynamically induced turbulence for cylinder in cross-flow. They conducted the experiments for Reynolds numbers from 0.2 to 80 based on cylinder diameters, and Reynolds numbers from 10^3 to 4 x 10^3 based on the flow channel width. This flow conditions represent laminar to transitional-flow before the on-set of the EHD-turbulent flow. Their theoretical analysis was based on the mass, momentum, and charged particle conversion equations coupled with the Poisson's equation for the electric field evaluation. Their results showed that: (a) onset of EHD turbulence is initiated near the real-stagnation point; (b) EHD turbulence can be generated even for Reynolds numbers (Re) less than 0.2, if the EHD number (Ehd) is larger than the critical Reynolds number square ($Ehd > Re^2$); and (c) The electrical origin of instability, which is leading into the on-set of turbulence can be estimated from $Ehd/Db^2 > Re^2$relation, where Db is the Debye number.

Jewell-Larsen et al. (2006) studied that electrostatic air propulsion is a promising technology with such potential applications as energy-efficient ventilation, air sterilization, cooling of electronics, and dehumidification. They found that the challenges of existing designs include the need to increase airspeed, backpressure, energy efficiency, and heat exchange capability. Their ultimate goal of this direction of research is to create multi-channel energy efficient ionic pumps. In the described project, they conducted a single cell analysis in their study as a building block of future designs. They presented in this paper the numerical simulation and experimental results of electrostatic fluid accelerators. They conducted this study for the purpose of optimizing device characteristics through the control of the electric field distribution.

They performed the simulations for multiple collector electrode voltage distributions. They presented a method to quantify the change in pump performance between different voltage distributions. They also discussed the influence of space charge on pump performance. They achieved using the proposed approach, a significant improvement of air velocity generated by optimized electrostatic fluid accelerators.

Li (2006) investigated the effect of the pulsed voltage on the meniscus deformation by using C_2H_5OH as the sprayed liquid. His results showed that pulsed voltage and its width as well as the bias voltage affected the behavior of spraying. Three spraying modes were appeared, e. g. dripping, pulsating jet and cone-jet. He created a cone-jet by applying a pulsed voltage of 1.5 kV to a bias voltage of 5.0 kV for 300 ms. He found the pulsed voltage provides a tangential electric stress on the meniscus that is helpful in jet formation. With increasing width of the pulsed voltage, the spraying is mainly dominated by the total voltage. He also found that the formation of the pulsating jet or cone-jet requires time to fully develop. The time required is related to both the pulsed and bias voltages.

Komeili et al. (2006) experimentally investigated the electrohydrodynamic (EHD) flow characteristics for a wire to rod type EHD gas pump. They conducted the experiments for DC negative and positive applied high voltage to a corona wire of diameter 0.24 mm from 0-24kV, grounding rod electrode diameter from 1.5 mm to 3.1 mm and wire/rod electrode distance to pipe diameter ratio from 0.63 to 1.16. They observed that applied voltage and polarity plays an important role, where a negative high voltage generates a higher gas flow than that of a positive polarity. They also observed pressure generated by the EHD pump increases with increasing EHD

generated flow velocity and no significant electrode gap distance to pipe diameter effect for negative polarity; however a larger effect was obtained for positive polarity. Their results showed that a maximum of 40 L/min of gas flow rate is generated at 0.37 W energy input when the pipe diameter is 20 mm with the corona wire electrode and grounding rod electrode gap distant set to 12.6 mm under negative applied voltage compared to 25 L/min at 0.23 W energy input for the positive case at the same specific energy density (power input/flow rate).

Moreau et al. (2006) experimentally analyzed the ability to actively modify low-velocity airflow along a flat plate by a DC surface-corona discharge. In order to create a tangential corona discharge at close vicinity to the wall usually in the direction of the airflow, this electro-fluid-dynamic (EFD) actuator consists of two electrodes flush mounted on the insulating surface of the plate. In this paper, they presented the velocity profiles within the boundary layer of the flat plate for a free air stream velocity U_o of up to 25 m/s (Re = 375,000). On one hand, the velocity profiles show that the ionic wind induced by the corona discharge results in a velocity increase inside the boundary layer when the ionic wind and the free air stream are in the same direction. On the other hand, the velocity at the wall decreases when they are in opposite directions. In summary, the main results are in as follows: (1) a stable corona discharge may be obtained between two wire electrodes flush mounted on the wall of an insulating flat plate. However, the discharge properties depend highly on the properties of the gas, the substrate and the electrodes. (2) The velocity of the ionic wind at the wall increases with the discharge current and reaches about 3 m/s. When the discharge current increases, the increase in airflow is closer to the wall. (3) At a given voltage/gap ratio value, the

discharge current lightly increases with the free air stream velocity. (4) The discharge-induced kinetic power increases linearly with the discharge current. (5) The use of the EFD actuator induces a drag reduction of 30% at U_o = 10 m/s. (6) The efficiency of the EFD actuator (rate of electrical power converted into kinetic power) is rather low (a few percent) in this aerodynamic configuration and decreases with the discharge current. (7) The plasma layer must be as thin as possible to have an electro-hydrodynamic (EHD) number greater than one and good efficiency.

Goodenough et al. (2007) studied the work which pertains to a novel drying method, the "corona wind," and looks at the potential to optimize a corona wind blower for application to the food industry. The corona wind is a method of including forced convection by ionic injection and subsequent acceleration between two electrodes. They found the wind velocity of a blower to be proportional to the voltage applied for specific electrode spacing and with cube root proportionality to the electrical power used. They showed the power consumption to be independent of the electrode spacing, allowing a generic calculation for a corona wind blower in air of 1.5% conversion of electric energy into kinetic energy. This low energetic efficiency is offset by the unique properties of the corona wind, which allows the wind to be directed. Compare to conventional drying methods, experiments using the corona wind to evaporate water from paper towels and biscuits showed significant drying enhancement at an overall efficiency. The caveat is that the arrangement of electrodes is crucial for effective operation.

Magnier et al. (2007) described a DC surface corona discharge designed to modify the airflow around a flat plate. The electrode configuration consisted of two thin copper layers placed on each side of the plate's attack edge. Discharge optical measurements with a photomultiplier tube indicated that the light emitted by the plasma is pulsating at a frequency that increases with applied voltage. Moreover, with voltage higher than a threshold value, the electric discharge changes regime with brighter pulses. This discharge also induced an "ionic wind" whose velocity was measured with a pressure sensing probe up to 1 m/s. Experiments with the particle image system in a subsonic wind tunnel showed that this discharge can reduce the separated airflow on the flat plate for a flow of 14 m/s (Reynolds number of 187,000). This result encourages further studies on a wing airfoil in a subsonic wind tunnel.

Kim et al. (2008) presented a design and fabrication of optimized geometry structure of electrostatic inkjet head. They simulated electric field intensity according to the head structure in order to verify effect of geometry shape. The electric field strength increases linearly with increasing height of the micro nozzle. The electric field along the periphery of the meniscus can be more concentrated as the nozzle diameter decreases. They design and fabricated the electrostatic inkjet heads, hole type and pole type, with optimized structure. They fabricated using thick-thermal oxidation and silicon micromachining technique such as the deep reactive ion etching (DRIE) and chemical wet etching process. They verified experimentally that the use of the MEMS inkjet head allows a stable and sustainable micro-dripping mode of droplet ejection. They observed a stable micro dripping mode of ejection under the voltages 2.5 kV and droplet diameter is 10 μm.

Komeili et al. (2008) experimentally investigated the electro-hydrodynamic (EHD) flow characteristics for a wire to rod type EHD gas pump for pipe diameter sizes of 6.5, 10, and 20 mm. They conducted the experiments for dc negative applied voltage ranging from 0 to 24 kV applied between a corona wire with a diameter of 0.24 mm and a grounded rod electrode. The grounded rod electrode diameter is varied from 1.5 to 3.1 mm. The wire/rod electrode distance to pipe diameter ratio is varied from 0.63 to 1.16. The results showed that gas flow rate increases with increasing EHD number or discharge current. A maximum of 40.1 L/min of gas flow rate is generated for a pipe diameter of 20 mm, with a grounding rod diameter electrode of 3.1 mm and corona wire to grounding rod electrode gap distant of 12.6 mm.

Lee et al. (2008) presented a novel mechanism for an electrostatic field induced drop-on-demand ink-jetting device that features a nozzle with a conductive pole located inside the nozzle, referred to here as a pole-type nozzle. They investigated the effects of the pole-type nozzle on the efficiency of the jetting both numerically and experimentally. Micro-dripping ejection of droplet takes place when the electric voltage signal applied allows for a strong electric field to be concentrated in the vicinity of the apex of the apex of the liquid meniscus. That is, a tiny droplet is removed from the peak of the dome-shaped liquid meniscus. Electrostatic jetting of liquids is a physical process caused by an electric force applied to the surface of a liquid. The electrical shear stress elongates the liquid meniscus formed at the opening of the nozzle and generates a tiny droplet as a result of the balance between electrical and surface tension forces. They presented in this paper the optimal conditions for applied voltage, electric conductivity, and flow rate for generating a stable drop-on-demand droplet

using the micro-dripping mode. They also verified experimentally that the use of the pole-type nozzle allows a stable and sustainable micro-dripping mode of droplet ejection for a wide range of applied voltages, demonstrating the feasibility of an electrostatic field induced drop-on-demand ink-jetting device as an alternative to conventional inkjet print heads.

Meng et al. (2008) experimentally investigated with coarse polyurethane powder, the characteristics of particle charging and deposition during corona charging processes of powder coating by measuring the charge-to-mass ratio (Q/M) and mass-to-surface ratio (M/S) of deposited particles. They disclosed that the deposited particles present a cone-shaped distribution on the substrate, which is mainly a direct result of the inhomogeneous concentrations of in-flight charged particles, but the edge effect leads to a rise in particle accumulation in the fringe region. They further disclosed that the particle deposition efficiency not only has a strong dependence on the particle primary charging efficiency but suffers a strong influence from back corona as well. The highest deposition efficiency is a compromise between the primary charging efficiency and the intensity of back corona. In addition, the number of overall deposited particles increases but the deposition rate decreases with spraying duration. On the other hand, they demonstrated that the secondary charging mechanism dominates the characteristics of the charge-to-mass ratio of local deposited particles, but may suffer some influence from their particle sizes. For this coarse powder, the charge-to-mass ratio distribution presents a concave characteristic. Furthermore, the average charge-to-mass ratio of the overall deposited particles increases with charging voltage, due to the improvement in their charging efficiency, but decreases with spraying duration, due to the intensifying

effect of back corona with the growing deposited layer. Significantly, their study in this paper provides a deeper insight into the charging and deposition mechanisms during powder coating processes and will be of great help for the improvement in related technologies of corona charging as well.

Meng et al. (2008) investigated the current densities during corona charging of particulates with a negative point-to-plane geometry and two (coarse and fine) particulate systems. Their results disclosed that, due to the addition of powder particles, both particulate systems incur strong corona quenching in currents. At low charging voltage the coarse and the fine systems present similar behaviors in current density with a slight deformation of the distribution, mainly attributed to inefficient particle charging and weak shielding effect of charged particles. At high charging voltage, however, in comparison with the fine system, the coarse system produces weaker quenching effect on its current density but more severe deformation on its current density distribution, due to its inferiority in particle amount and more concentrated charged particles in the internal space of the powder cloud. They demonstrated that the characteristics of the current density during corona charging are closely related to particulate properties, but charging voltage also produces some influence.

Meng et al. (2008) demonstrated that with a point-to-plane geometry, the experimental investigation of the current-voltage characteristics in corona discharges, the existing empirical formulae met with some physical difficulties in explaining the results. By mathematically processing the experimental data and applying the updated knowledge of corona inception, they derived and expressed a new general formula in characterizing the relationship of corona current-voltage as $I = K(V-V_0)^n$. They

demonstrated that the exponent *n* falls into a limited scope of 1.5-2.0, and there always exists an optimal exponent *n* in the scope, which can be determined by maximizing the R-square of regression. Of all the potentially influential factors, they disclosed that the point radius has the strongest influence on the optimal exponent *n*, and the effects of ambient conditions and corona polarities are not noticeable. The optimal exponent *n* holds a fixed value of 2.0 for microscopic points and of 1.5 for large points with a radius in millimeters, but changes decreasingly with the radius for the points of microns. For given experimental conditions, the optimal exponent *n* almost does not change with the inter-electrode distance. Furthermore, they demonstrated that the formula is applicable not only for both negative and positive coronas in point-to-plane geometries but also for both polarities in point-to-ring geometries. With the optimal exponent *n*, the formula can well explain the inconsistencies met by other existing formulae and best represent the characteristics of corona current-voltage with an accuracy of 1 μm.

Moreau and Touchard (2008) deal with experimental measurements of the electric wind velocity induced by corona discharges in air at atmospheric pressure. They established the DC coronas inside a tube of a few cm in diameter, between a HV needle and a grounded electrode (grid and ring), in order to produce an electric wind for airflow applications or EHD gas pumps. Their goal in this paper is to optimize the corona properties to increase its mechanical efficiency, such as electric wind velocity. They investigated the following parameters: electrode polarity, collecting electrode geometry, electrode gap and tube diameter. Measurements of time-averaged velocity profiles at the tube outlet have allowed them to compute flow rate, induced mechanical

power and efficiency of each configuration. This has shown that: (1) the maximum velocity is higher in the case of positive coronas than in the case of negative ones, (2) this is certainly due to the presence of streamers in the case of positive coronas, (3) mesh size plays a fundamental role and using a grid as a collecting electrode is more efficient than a ring, and (4) the most efficient configuration allowed them to produce a 10 m/s electrical wind, a flow rate of about one l/s, a mechanical power of a few mW with an efficiency of about one percent.

Tsubone et al. (2008) conducted an experimental investigation to study the effect of grounded electrode location and polarity on time averaged discharge current, velocity profile, volumetric flow rate and pressure generation for a wire-non-parallel plate type EHD gas pump. They conducted the experiments with two different electrode configurations for the negative and positive applied voltage from 0 to 14 kV at atmospheric pressure and room temperature, where air was used as the working fluid. The experimental results showed that: (1) maximum average gas velocity of 1.9 m/s corresponding to a volumetric flow rate of 44 L/min was achieved; (2) the volumetric flow rate, gas velocity and pressure generation basically increase with increasing applied dc voltage or EHD number until the maximum value; (3) a non-linear relationship between the pressure generation and the gas velocity was observed and the flow generated was always turbulent or limited re-circulating laminar flow; (4) the effects of GND electrode location and polarity on the velocity, volumetric flow rate and pressure generation are experimentally obtained; and (5) experimental correlations between the Reynolds number and EHD numbers shows a power law dependence of Re on Ehd^{α}, where $\alpha = 0.142$ for type A and 0.176 for type B under a negative applied

voltage and $\alpha = 0.358$ for type A and 0.573 for type B under a positive applied voltage regardless of type of EHD number. They discussed in detail the mechanism of unidirectional EHD generation.

Chang et al. (2009) conducted an experimental investigation and one-dimensional modeling to study the mechanism of net flow direction induced by electro-hydrodynamic (EHD) forces in a wire-non-parallel plate electrode type EHD gas pump. They conducted the experiments with various different locations of corona wire electrode for negative and positive applied voltage from 0 to 14 kV at atmospheric pressure and room temperature, where air was used as the working fluid. They also developed a one-dimensional cross-sectional averaged model based on mass and momentum conservation as well as Poisson electric field and ion transport equations. The results showed that the net flow direction of electrohydrodynamically induced gas flow in a wire-non-parallel plate electrode system significantly depends on the location of the corona wire electrode relative to the grounded electrode position. They also investigated and discussed in detail the effect of conversion angle of non-parallel plate electrode on the net flow direction and pressure drop.

Takeuchi et al. (2009) conducted an experimental investigation to study the effects of corona wire diameter, pipe length, and corona polarity on outlet flow velocity distribution profile of a wire-rod type electrohydrodynamic (EHD) gas pump. They found corona discharge occurs by applying negative or positive direct current (dc) high voltage between a wire electrode (outer diameter (o.d.) 60 μm, 200 μm, or 300 μm) and a rod electrode (o.d. 3 mm) in atmospheric air. EHD gas flow is generated in the direction from the wire electrode to the rod electrode through a cylindrical pipe (inner

diameter (i.d.) 20 mm). They also found the discharge current and average flow velocity increase monotonically on increasing the applied voltage for both polarities before the onset of spark discharge. Stable corona discharge between corona onset and spark onset is generated in a wider voltage range by using wire electrodes with a smaller diameter and the discharge current becomes larger, resulting in a higher flow velocity. They achieved the maximum average flow velocity of 2.0 m/s, corresponding to flow rate of 38 L/min with a wire of diameter 60 μm by applying a voltage of -16 kV.

Zeng et al. (2009) studied that the electric force is exploit one of the leading mechanism for driving and controlling the movement of the operating fluid (electrohydrodynamics) and the charge suspensions (electrokinetics), since the inception of microfluidics. In miniaturized devices, electric force has an intrinsic advantage. They observed a very high electric field is easy to obtain as the electrodes are placed cross a small distance, from sub-millimeter to a few microns. The electric force can be highly localized with its strength rapidly decaying away from the peak which makes it an ideal candidate for spatial precision control. The geometry and placement of the electrodes can be used to design electric fields of varying distributions. In this paper they examined several electrically driven liquid handling operations. They discussed the theoretical treatment and numerical methods. They used modeling and simulations to unveil the associated electrohydrodynamic phenomena. To illustrate the applications this modeling based investigation is interwoven with examples of microfluidic devices. In this paper they also focused on detailed physical simulations of component-level operations. Since the components must be integrated to form a

functional system in order to provide desired services, system-level complexities in both architecture and execution also need to be addressed.

Choi et al. (2010) presented a growing interest in direct patterning of metallic contents on the surface of the substrate without including complex steps of the micro-fabrication lithography process. They expected the direct fabrication process using electrostatic ink-jet printing to be a powerful tool for both nanotechnology research and applications such as microelectronics. The droplet ejection voltage, meniscus, cone-jet behavior, and counter electrode distance depends on the ink properties such as surface tension, viscosity, and percentage of metallic pigments. In this paper they studied and analyzed 2-µm level needle-type electrostatic head designs for contact-less fabrication of printed electronics, composed of differently treated surface materials. They tested the electrostatically actuated ink-jet heads and compared for low power and high resolution on ink containing metallic nano-particle as pigments. They compared the two laboratory-fabricated discrete and electrostatically actuated ink-jet heads, one made by poly di-methyl siloxane modeling process and other through micro-electrical discharge machine techniques, and they discussed their orifice outlet surface (hydrophobic and hydrophilic) condition influence. They also investigated different dripping behaviors of metallic ink under the influence of counter electrode distance, voltages, and materials. The observation of droplet ejection with high-speed camera revealed that in the case of hydrophobic head, they achieved better meniscus shape and ejection even at low voltage compared to the hydrophilic head. They also found that the less flow rate is required in hydrophobic head. They also compared the printing

characteristic of the hydrophilic nozzle head with the hydrophobic head on PET substrate.

Foroughi et al. (2010) presented an experimental study on the characterization of a planar, multistage, electrohydrodynamic (EHD) ion-drag micropump for pumping liquid nitrogen, which can have a wide range of applications in cryogenic liquid cooling devices, as well as in bioengineering applications where a small dose of liquid nitrogen needs to be delivered to a particular spot. They tested two designs of the pump, consisting of different emitter configurations (flat and saw-tooth), similar emitter-collector spacing (50 microns), and similar gaps between successive electrode pairs (100 microns) at DC voltage ranging from 0 to 2.5 kV. They measured the generated electric currents and the corresponding static pressure heads to characterize the pumping performance. They investigated experimentally the pressure and current onset voltages as well as the relationships between pressure-voltage (P-V) and pressure-current (P-I). They generated the highest pressure head (30 Pa at 1700 V) with the saw-tooth design. After collecting and processing the data for various prototypes, they found that incorporating saw-tooth electrodes can significantly improve the performance of the micropump compared to flat electrodes.

Pekker and Young (2010) theoretically examined the idea of using the Electrohydrodynamic (EHD) ionic wind pump effect in thruster applications. This idea has been under discussion for many decades. However, there is still no commonly accepted view on EHD-thrusters, e.g., whether EHD thruster is worthwhile or not, what level of thrust and thrust efficiency can be obtained from EHD-thrusters, etc. They presented in this paper a simple one-dimensional model of an ideal EHD-thruster for

calculating thrust efficiency and thrust of EHD-thrusters. They also calculate the maximum current that can be achieved for an ideal EHD-thruster at a given voltage. This allowed them to calculate the maximum thrust that can be obtained from the thruster and the corresponding thrust efficiency. They also showed that with an increase in the voltage, the maximum thrust and the corresponding thrust efficiency move in opposite directions: the thrust efficiency decreases, while the thrust increases. Their model illuminates the physical limitations of EHD-thrusters and provides reasonable estimates of the performance of real EHD-thrusters.

1.2.2 EHD-Enhanced Heat Transfer

Molki et al. (2000) performed a numerical and experimental investigation to study the effect of corona discharge on the flow field and heat transfer enhancement of airflow in a square channel. The computations indicated that, in the range of test parameters, the flow did not fluctuate, and the flow field was 2D, with no axial variation. They applied the electric filed via a charged electrode situated at the centerline along the channel axis. The numerical approach they used was based on the Large-Eddy Simulation turbulence model to investigate the potential turbulence generated by the electric field and was applied to the fully-developed region. They performed the experiments in an earlier study and represent the data available to compare with the present computations. Thermal boundary condition was the uniform wall heat flux. In both numerical and experimental approaches, Reynolds number ranged from 500 to 2000, corona current 0.059 to 2.420 mA/m, and applied voltage -5.655 to -6.900 kV. The numerical results revealed the secondary flows in the cross-

section of the channel. This corona-induced secondary flow was the main mechanism behind the enhanced heat transfer coefficients in both fully-developed and developing regions of the channel. From the computational results, the maximum heat transfer enhancement in the fully-developed flow was $Nu/Nu_o = 3.4$ for Re = 500, 1000, and 2000. The experimental results, however, indicated a much smaller enhancement of $Nu/Nu_o = 1.99$, 2.01 and 1.56 in the developing flow zone, corresponding to Re=500, 1000, and 2000 respectively.

Kalmanand Sher (2001) studied an electrostatic blower, which is utilized to cool heat-generating bodies, such as typical power-unit chips. The device, employs a long stretched thin wire electrode, which is confined by two inclined wings. The letter provides a longitudinal nozzle for the air stream and at the same time an electric shield. They concluded that the heat transfer coefficient can easily be increased by a factor of more than two, as compared with a natural convection mechanism. They found a linear relationship between the Nusselt and the Reynolds number. This is explained by the complex structure of the boundary layer due to the air stream impingement effect.

Rashkovan et al. (2002) experimentally investigated the effect of corona wind produced by stretched steel wire and two copper wings on the heat transfer from a heated horizontal plate. They postulated some advantages, although in such an arrangement the heat transfer augmentation is expected to be lower. They can be used electric blower by corona wind for cooling of electronic components instead of fans. It has the advantages of noise and vibrations-free system, higher reliability since there are not moving parts and easiness of directing the wind to components that can hardly approach. In such a construction, they presented in this paper have further advantages

over conventional corona wind blowers that the plate to be cooled is not a part of the wind generation system, it is not charged, the electrical field next to it is negligible, and it may be constructed from non-metallic materials. In the course of the study, they established the optimal geometric parameters of the electric blower together with optimal value of high voltage supply. Under these optimal conditions, they achieved augmentation by three times of the heat transfer coefficient over that for the natural convection. They also found that the augmentation of the heat transfer rate dependent on the heat flux used for heating the plate.

Molki et al. (2004) conducted an experimental research to investigate the level of heat transfer enhancement that can be achieved by corona wind in the developing region of circular tubes. Their study focused on transitional and lower range of turbulent flows with Reynolds number and voltage ranging from 2500 to 13000 and 0 to 10.5 kV, respectively. They obtained the maximum enhancement of the local heat transfer coefficient at the downstream end of the tube where the 0-kV heat transfer coefficient was the lowest. The level of enhancement decreased with Reynolds number. The maximum enhancement ranged from14% at Re = 13000 to 23% at Re = 2500, both corresponding to the applied voltage of 10.5 kV. The corona wind also increased the average heat transfer coefficient. The highest enhancement occurred at 10.5 kV, ranging from 6% to 8%, corresponding to Re = 2500 and 13000, respectively. These values indicate the level of enhancement beyond the conventional (0-kV base) values in the developing region of the circular tubes.

Yamada (2004) carried out a series of measurements with a point-grid electrode system has clarified that the current-voltage characteristics of the negative corona discharge in the atmospheric air obey the Townsend relation. Further, they experimentally confirmed that the coefficient in the Townsend relation was proportional to temperature and the power of the electrode gap independently, and the corona onset voltage was proportional to the product of the reciprocal of temperature and the power of the electrode gap. The empirical formula derived from these results could estimate the corona currents with an accuracy of 1 μA for a given parameter set. The significance of the empirical formula is that it provides a useful design tool to give the negative ion generator, which is most suitable regarding miniaturization and reduction of production cost.

Hsu et al. (2007) studied the concept of Electrostatic Fluid Accelerators (EFA) enhanced forced convection cooling using a micro fabricated cantilever. They found existing thermalmanagement methods for electronics do not meet the technology needs and remain a major bottleneck in the evolution of computing, sensing, and information technology. The decreasing size of microelectronic components and the resulting increasing thermal output density require novel cooling solutions. Electrostatic fluid accelerators (EFAs), also known as electrohydrodynamic ionic wind pumps, have the potential of becoming a critical element of electronic thermal management solutions. In order to take full advantage of EFA-based thermal management, it is essential to miniaturize EFA technology. They demonstrated the successful operation of mesoscale micro fabricated silicon EFA. They fabricated several cantilever structures in bulk silicon with radii of tip curvature ranging from 0.5 to 25 μm, which were used as the

corona electrode. They fabricated the device using the combination of deep reactive ion etching (DRIE) and reactive ions etch (RIE) micro fabrication processes. They also demonstrated forced convection cooling using infrared imaging, showing a 25 ^{o}C surface temperature reduction over an actively heated substrate at an applied voltage of 8.5 kV, with an operating current and power of 70 μA and 0.6 W, respectively.

Atalik and Sonmezler (2010) investigated the effect of an electric field for heat transfer properties in a laminar, incompressible, non-isothermal boundary layer gas flow over a wedge. Using similarity transformations, they reduced the governing boundary layer equations to an ordinary differential equation system. They solved the reduced ordinary differential equations numerically for different values of electric and flow field parameters characterizing the ratio of electric force to fluid inertia force, Joule heating and ion kinetic work. They revealed differences in heat transfer properties near the wall as well as thermal profiles in the layer for constant wall temperature flat plate and constant wall heat flux wedge flow with wedge angle $\pi/6$. They observed the thinning of the velocity boundary layer due to the additional acceleration of fluid particles near the wall under the presence of an electric field being most effective with faster decaying electric function forms and higher values of the electrohydrodynamic number. Velocity boundary layer thinning is a necessary condition for improving the local heat transfer properties. The level of enhancement is controlled by the electric body force with additional effects of Joule heating and ionic kinetic work on the bulk flow. The increase in the value of the ratio of ion kinetic work parameter to Joule heating parameter increases the heat transfer enhancement. They also demonstrated the effects

of low and high Prandtl numbers. They observed heat transfer enhancement is increase with increasing Prandtl number.

Kamkari and Alemrajabi (2010) experimentally evaluated the enhancement of forced flow evaporation rate by applying electric field (corona wind). Corona wind produced by a fine wire electrode which was charged with positive high DC voltage impinges to water surface and leads to evaporation enhancement by disturbing the saturated air layer over the water surface. They focused in this study on the effects of corona wind velocity, electrode spacing and air flow velocity on the level of evaporation enhancement. They conducted two sets of experiments, i. e. with or without electric field. They used the data obtained from the first experiment as the reference for evaluation of evaporation enhancement at the presence of electric field. Their applied voltages ranged from corona threshold voltage to spark over voltage at 1 kV increments. Their results showed that corona wind has great enhancement effect on the water evaporation rate, but its effectiveness gradually diminishes by increasing air flow velocity. They found the maximum enhancement ratios were 7.3 and 3.6 for air velocities of 0.125 and 1.75 m/s respectively. The evaporation enhancement increases with increasing voltage and decreases with increasing the electrode spacing at a fixed applied voltage. They deduced that evaporation enhancement is nearly independent of electrode spacing at a fixed corona wind velocity. This result strengthens the postulate that corona wind velocity is the main mechanism in evaporation enhancement. They found that except for very low air flow velocities, evaporation enhancement is a linear function of EHD number.

Kasayapanand (2010) investigated the electrohydrodynamic heat transfer enhancement of natural convection inside the finned channels via a computational fluid dynamics (CFD) technique. He numerically determined the interactions between electric field, flow field, and temperature field. He found at low Rayleigh number flow and heat transfer enhancements are significantly influenced. In relation with the supplied voltage, the flow and heat transfer with the presence of electric field increase. He expressed the effect of electrode arrangement and number of electrodes to the average velocity and Nusselt number. He recommended an optimum inclined angle of the channel. The inclined angle for facing up geometry of a hot wall performs more volume flow rate and heat transfer. He also analyzed the relation between the number of fins and fin length to the augmented flow and heat transfer.

Lai and Tay (2010) revealed the existence of oscillatory flows from the prior studies on electrohydrodynamically enhanced forced convection in a horizontal channel. These oscillatory flows are the product of interactions between the electric body force and flow inertia of the primary flow. When operating in this oscillatory flow mode, they had shown that heat transfer can be significantly enhanced. They speculated that heat transfer may be further enhanced by exciting the primary flow in a frequency similar to those observed for the oscillatory flows (i.e., the so-called resonant effect). They performed computations to verify this speculation for primary flows excited with a frequency that is either a fraction or multiple of the natural frequency observed in the original oscillatory flows. The results showed that an inlet flow excited at the natural frequencies produces the best heat transfer enhancement in the single-cell regime, and

the enhancement increases with the Reynolds number. But the results showed an opposite trend in the single-cells regime.

1.3 Objective of the Present Study

Earlier studies reveal that an electrohydrodynamically induced secondary flow has significant influence on the primary flow as well as the resulting heat transfer coefficient. These influences directly depend on the electrode arrangement and its system configuration. The majority of studies on EHD applications so far have the emitting electrode (either single or multiple) placed at the center of the channel. To enhance heat and mass tranfer, the boundary layer near the channel wall needs to be perturbed. Placing the emitting electrode and thus the corona-driven flow close to the wall can produce this disturbance more efficiently. Research to date on the surface corona which refers to the electrodes being flush mounted on the surface of the plate or the wall is focused on flow control and drag reduction. Clearly, it also has great potential on the heat transfer enhancement.

Because of the complications involved, most studies on EHD are based on experiments. With the advancement of computer technology, numerical simulations are becoming more popular as they are cost effective and less affected by the ambient conditions. However, most numerical models for EHD applications are two-dimensional (2D), and only very few are three-dimensional (3D). Solving EHD problems in 3D is quite complicated and challenging, due to the interactions between the electric, flow, and temperature fields, particularly the present EHD gas pump design which consists of electrodes flush mounted on the inner wall of a square channel. For

forced convection numerical simulations, the EHD-induced secondary flow directly interferes with the boundary layer, causing the additional mixing and increase the convective heat transfer coefficient.

The purpose of the present study is to evaluate the performance of an EHD gas pump as well as its application in heat transfer field. Experiments are conducted first to study the EHD-induced gas flow alone in a square channel with electrodes flush mounted on the wall. Several important parameters such as the size of grounded plate, their corresponding arrangement, applied voltage and polarity, are investigated in search of the optimal operating conditions for its performance. Experimental results not only provide important insights to the design of an EHD gas pump, but also contribute important information for the subsequent numerical study. The second part of this study is to solve the electric potential and space charge density first. Once the electric field becomes available, the electric body force is calculated and added to the momentum equations for solving the flow and temperature fields using numerical simulations.

CHAPTER TWO

EXPERIMENTAL APPARATUS AND PROCEDURE

An experimental study was conducted in the Heat Transfer Laboratory at the main campus of the university. This chapter presents the experimental setup, procedure, and analysis of the electrohydrodynamic (EHD) gas pump in a square channel. Corona current and corona wind velocity measured from the experiments will provide important information for the subsequent numerical simulations.

2.1 Experimental Setup and Apparatus

The schematic diagram of experimental setup used in this study is shown in Figs. 2.1 and 2.2 for single-stage and two-stage corona wind generators, respectively. The main components of the setup are: EHD pump test unit, high voltage power supply, air velocity transducer, and data acquisition system (DAQ). The detailed descriptions about each unit are given below.

2.1.1 EHD Pump Test Unit

The test channel is constructed from Plexiglas with 1/4 inch thickness. The inner dimensions of the channel for both single-stage and two-stage units are 4 inches by 4 inches with a length of 24 inches for the single-stage unit and 30 inches for the two-stage unit. The dimensions of the wire-electrode and system configuration are shown in Figs. 2.3 and 2.4, respectively. A copper wire of 20 GA (0.03196-inch diameter) is first bent and welded to form the electrode loop flush mounted on the inner

wall of the channel. Additional one-inch-long copper wires of the same size are welded to the base loop to serve as the emitting electrodes. A 0.5-, 1-, and 2-inch wide copper strip with a thickness of 0.025 inch is also flush mounted on all four sides of the inner wall of the single-stage unit as well as the bottom stage of the two-stage unit to serve as the grounded electrode. A 0.5-inch wide of same thickness copper strip is flush mounted of the inner wall at second stage of two stages unit. The gap between the tips of the emitting electrodes and the grounded plate is fixed at 1.5 inches for each stage of the two-stage unit as well as the single-stage unit. The gap between the electrode wire loops of the top stage to that of the bottom stage is maintained at 6 inches for the two-stage unit. The pins of the emitting electrode are evenly distributed over the channel walls. The electrode assembly and the grounded plate are press-fitted to pre-cut grooves on the inner wall of the channel so that their surfaces are flushed with the channel wall. In this arrangement, the corona wind produced by the electrode will resemble that of a wall jet. Also, the emitting electrodes are intended to align with the direction of primary flow to maximize its effect.

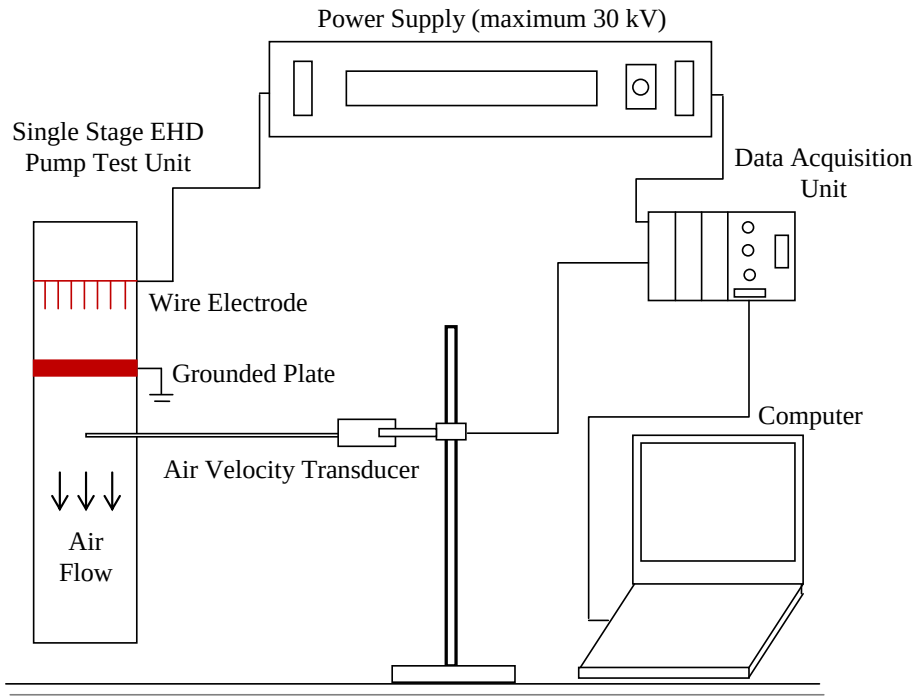

Figure 2.1 Schematic of Experimental Setup (single-stage).

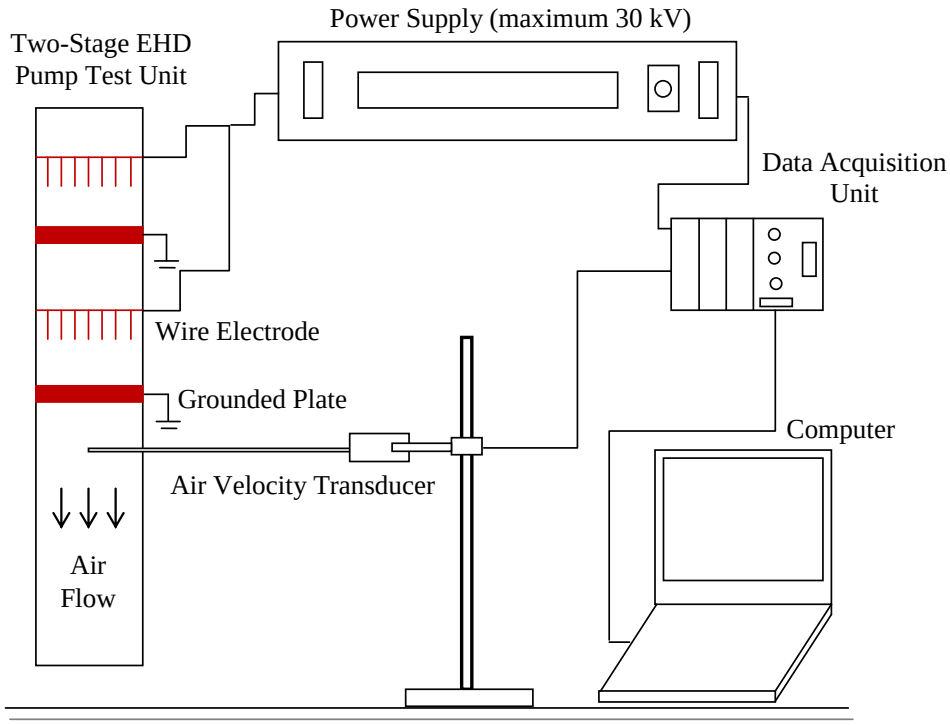

Figure 2.2 Schematic of Experimental Setup (two-stage).

For all configurations, pins are distributed evenly over the channel walls. For the present study, there are 7 pins on each wall and the spacing between two neighboring pins is 0.5 inch. Figure 2.3 shows only 28 electrode pins, 7 pins on each wall and space between the pins is 0.5 inch. Therefore, for the single-stage unit, there are 28 pins altogether while there are a total of 56 pins for the two-stage unit.

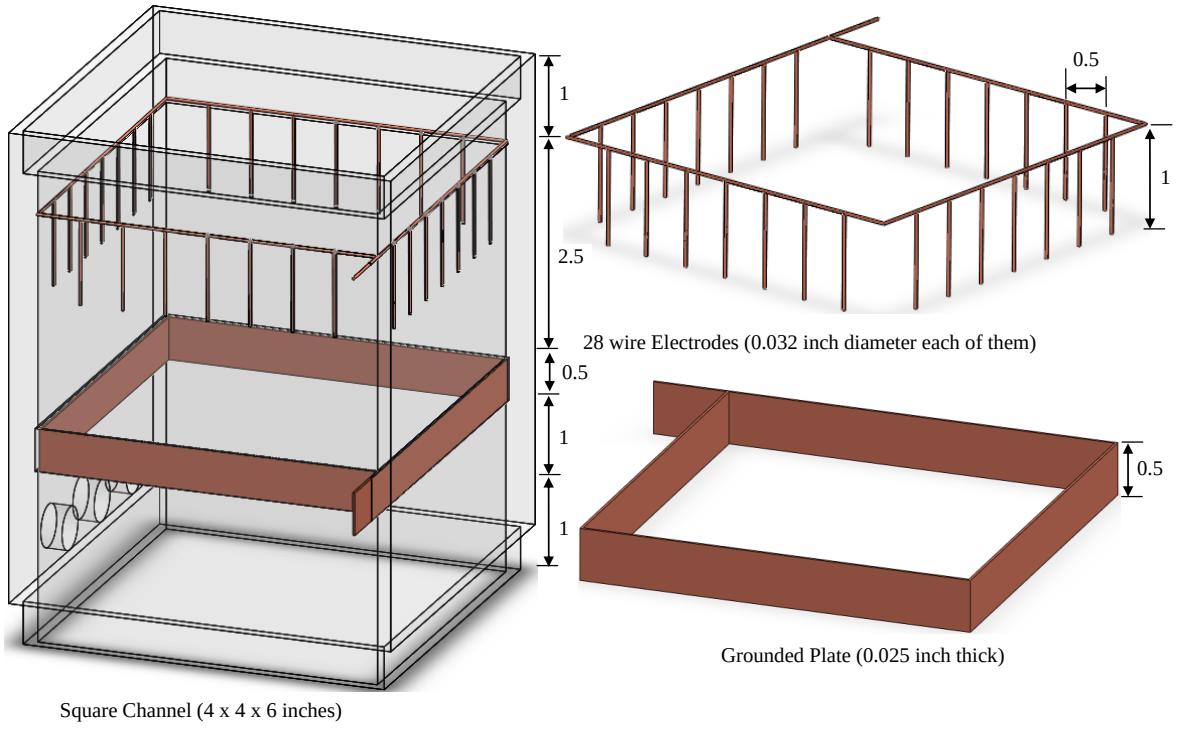

Figure 2.3 EHD Pump Test Unit with a Single-Stage Corona Wind Generator.

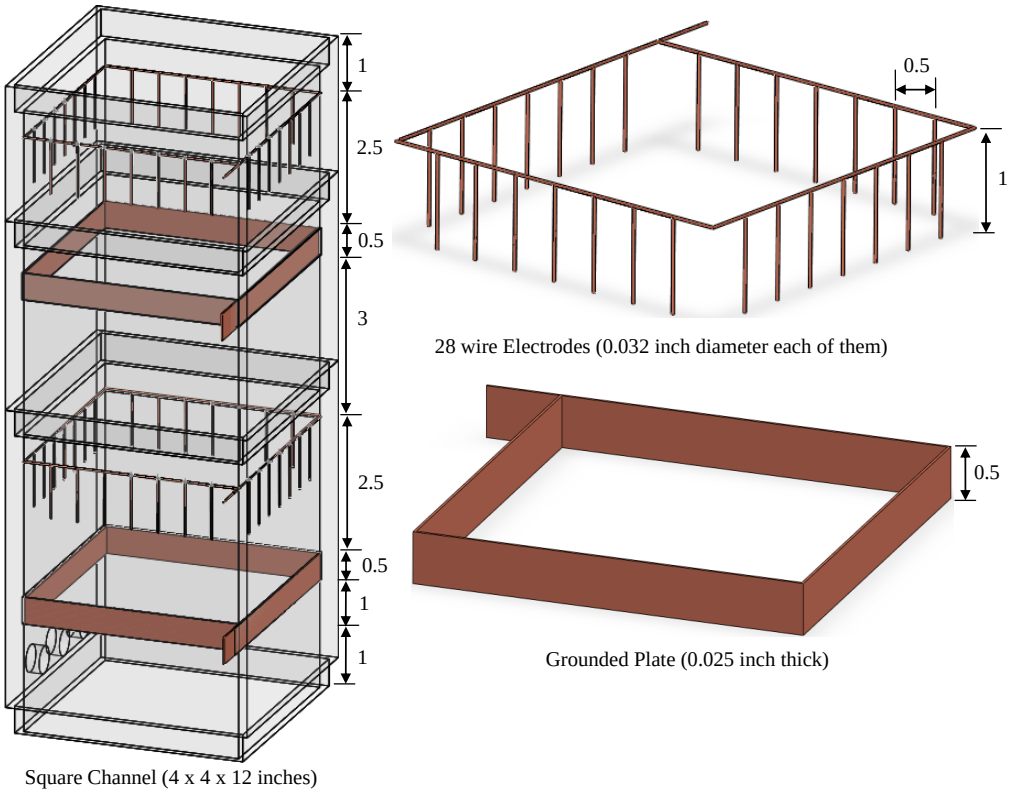

Figure 2.4 EHD Pump Test Unit with a Two-Stage Corona Wind Generator.

2.1.2 High-Voltage Power Supply

The voltage applied to the wire electrode is supplied from a direct current (DC) power supply manufactured by Bertan Associates, Inc. (Series 205 B-30R) as shown in Fig. 2.5. A maximum voltage of 30 kV can be provided by the power supply with either positive or negative polarity. The accuracy of this power supplys is $\pm 0.1\%$ of reading and + 0.1% of maximum for voltage. It is $\pm 0.25\%$ of reading and + 0.25% of maximum for current.

Figure 2.5 High Voltage Power Supply.

2.1.3 Velocity Transducer

The hot-wire anemometer (Omega FMA 902-I) used for the present study, which is shown in Fig. 2.6, can accurately measure air velocity from 0 to 500 fpm (2.54 m/s) with an accuracy of 2.7% of full scale at room temperature. To facilitate air flow measurement, the anemometer is securely mounted in the channel with the use of 1/4-inch NPT compression fittings. The velocity probe extended horizontally from channel wall allowing measurements be taken on three levels; 1, 2.5 and 4 inches downstream of the grounded plate for the single-stage unit and that of the bottom stage for the two-stage unit. A total of twenty-one sampling points are evenly distributed over the channel cross-section of each level. Figure 2.7 illustrates the locations of these velocity measurement points.

Figure 2.6 Velocity Transducer.

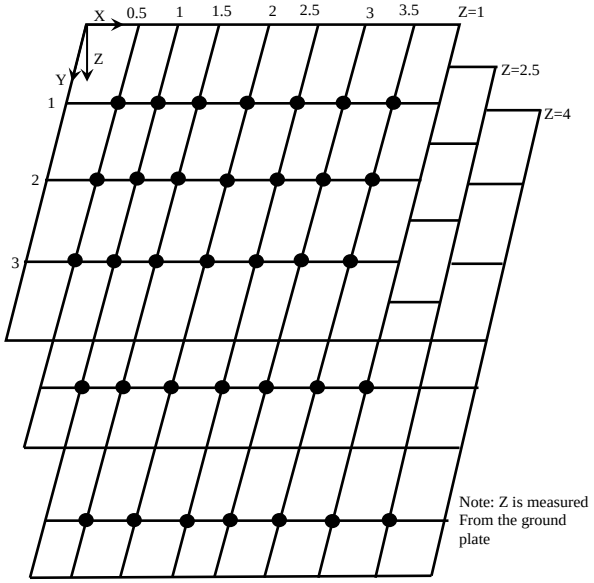

Figure 2.7 Locations of Velocity Measurement Points (in inch).

2.1.4 Data Acquisition System

The data acquisition system used is manufactured by National Instruments as shown in Fig. 2.8. The data sampling and collection are aided by the LabView program. The current signal received from the power supply and the velocity transducer are first calibrated and scaled to the correct current and air velocities. A sampling rate of 1 Hz (1 cycle per second) is used for all experiments. It has been determined by systematic trials that 1 Hz is sufficient to capture the variations of electric and flow fields.

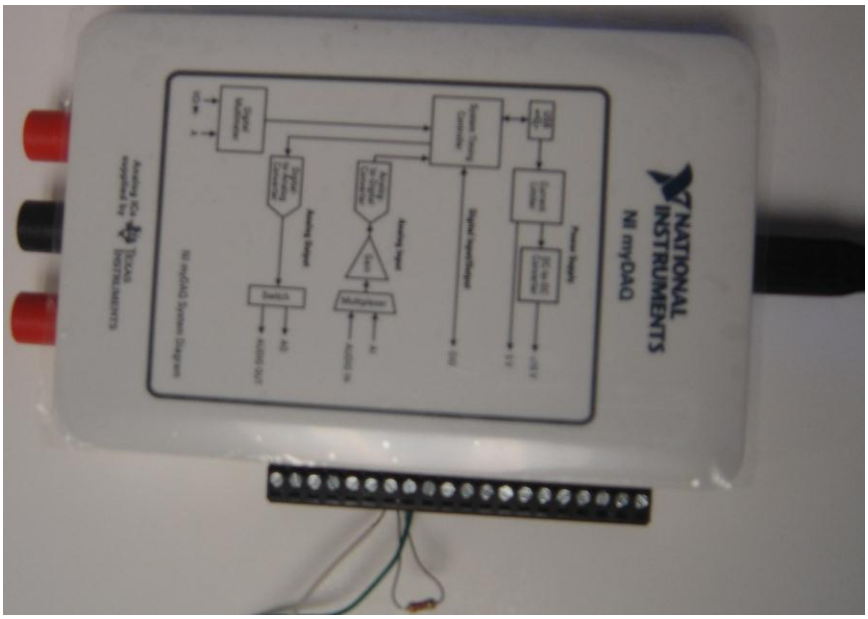

Figure 2.8 Data Acquisition System (DAQ).

2.2 Experimental Procedures

For the present study, only positive polarity is considered. Negative polarity will be considered in the future for comparison. The steps in each test are outlined as follows.

1. The air velocity transducer is connected to the Data acquisition system (DAQ) and personal computer (PC). A virtual instrument (VI) is built in LabView to collect and record the signals.
2. The high-voltage power supply is set to the desired polarity (positive).
3. The wire electrodes are connected to the high voltage power supply and the copper strip is grounded.

4. The air velocity transducer is properly aligned with the channel wall and the sensor is positioned at the testing point.
5. The power supply is then turned on and the applied voltage is gradually increased until it reaches the threshold voltage, at which point a hissing sound can be heard. This threshold voltage marks the onset of corona discharge.
6. The data collection starts from the threshold voltage up to 28 kV with an increment of 2 kV. For the present setup, corona wind is too weak to be detected for an applied voltage which is less than 20 kV (which is thus considered as the threshold voltage in this study).
7. Steps 2 through 6 are repeated at each velocity measurement point for all configurations.

It is important to know the onset voltage and sparkover voltage for EHD gas pumps before starting the experiment. Operating at or beyond the sparkover voltage should be avoided because it may damage the power supply or the data acquisition system. In the current study, the onset voltage is found to be 20 kV for most cases. For all configurations, the sparkover voltage goes beyond 30 kV, which is the maximum output voltage of the power supply.

Sparkover can be easily observed by a visible bright light and cracking sound that it produces. Figure 2.9 shows the sparkover phenomenon in a dark room. When it occurs, electric field becomes unstable and fluctuates violently. As such, it should be avoided to operate beyond the sparkover voltage.

This experiment is used to measure the corona current without forced air flow and heat transfer. Previous work by Molki, et al. (2000) shows that the voltage-current relation (V-I curve) for flow through square ducts is independent of Reynolds number. Therefore, current measured from experiments without air flow can be used for future numerical simulation of forced flow and heat transfer. A picture of the complete experimental setup is shown in Fig. 2.10.

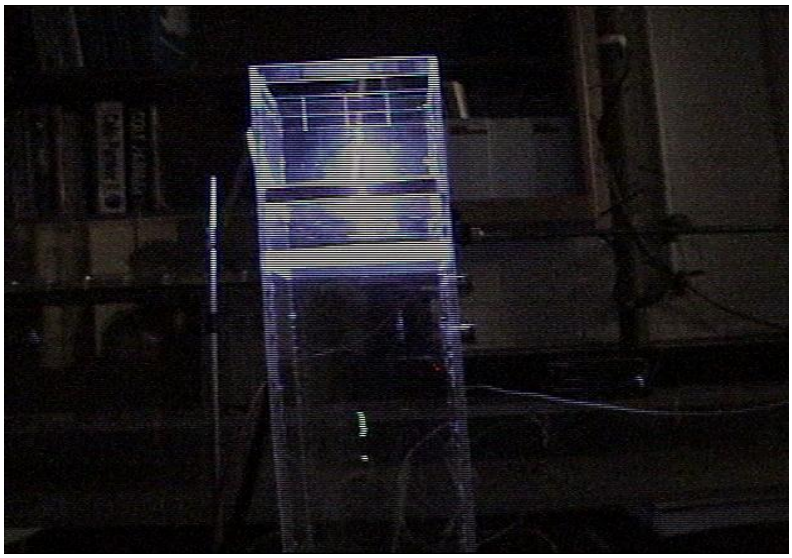

Figure 2.9 Sparkover Observed in the Experiment.

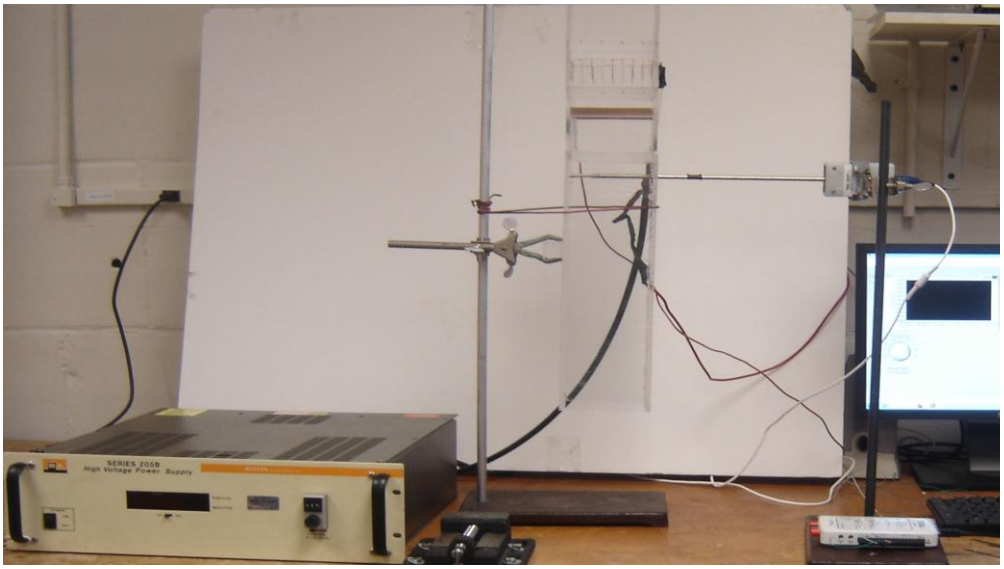

Figure 2.10 Complete Experimental Setup.

CHAPTER THREE

THEORETICAL BACKGROUND AND NUMERICAL FORMULATIONS

This chapter presents a theoretical foundation for the corona wind phenomenon. First, the interactions among electric fields, flow fields, and temperature fields will be discussed. Then in the following section governing equations for each field will be presented, upon which numerical calculations are based.

3.1 Interactions among Electric, Flow and Temperature Fields

The electric body force, the main driving force behind corona-induced flow and resulting heat transfer enhancement, is expressed as

$$f_e = \rho_c E - \frac{1}{2} E^2 \nabla \varepsilon + \frac{1}{2} \nabla \left[E^2 \rho \left(\frac{\partial \varepsilon}{\partial \rho} \right) \right]. \tag{3.1}$$

The first term, $\rho_c E$, represents the Coulomb force acting on the charged particles. This is the force applied by the electric field on the electrons and ions that may exist in the fluid. The second term, $-\frac{1}{2} E^2 \nabla \varepsilon$, represents the force produced by the spatial change of electrical permittivity. The third term, $\frac{1}{2} \nabla \left[E^2 \rho \left(\frac{\partial \varepsilon}{\partial \rho} \right) \right]$, represents the force caused by the inhomogeneity of the electric field strength and is called electrostrictive force.

Many EHD applications use air as the working fluid. Electric permittivity can be assumed to be constant for corona discharge in air under atmospheric pressure and at room temperature. The second and third terms on the right-hand side of equation (3.1)

can thus be neglected. In such cases, the electric body force is simply the Coulomb force.

No corona discharge occurs at low voltages, but when the applied voltage increases to a certain threshold value, ionization occurs at the nearby wire electrode or region of a needle. Controlled by the Coulomb force, ions accelerate and migrate to the grounded plate. This migration causes collisions between charged particles and neutral molecules to produce a bulk of airflow, which is corona wind, but also creates an electric current, which is also called corona current or convective current.

Electric current is defined by

$$J = \rho_c bE + \rho_c u, \tag{3.2}$$

where "u" is the bulk fluid velocity. The second term provides the coupling relation between flow field and electric field.

Typical interactions among the electric, flow, and temperature fields for corona discharge in air are shown in Fig. 3.1. In theory, electric field and flow field can interfere with each other. Corona wind produced by the electric field changes the flow pattern and the fluid velocity in turn affects the electric field by changing the corona current. However, the ions travel at a speed which is generally several orders of magnitude larger than the speed of the bulk fluid. Therefore, the effect of the bulk flow on the electric field is negligible, which leads to the so-called one-way coupling assumption in the literature. One-way coupling states that the electric field can have influences on the flow field, but not vice versa. This assumption has been verified by Huang and Lai (2003).

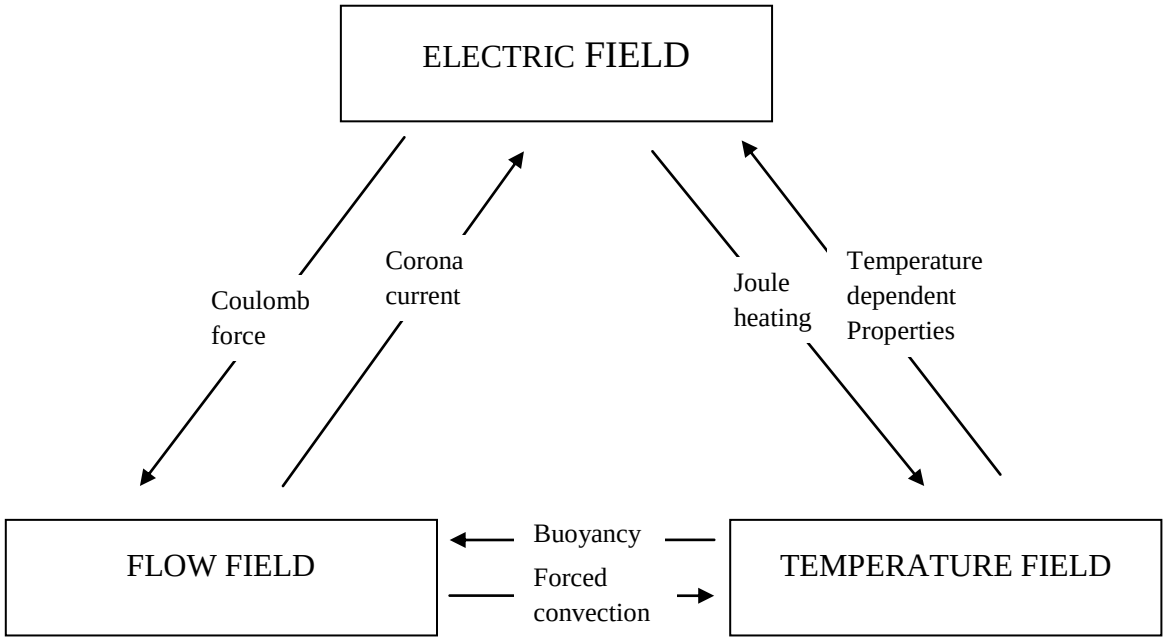

Figure 3.1 Interactions among Electric, Flow, and Temperature Fields.

Both thermal buoyancy and Coulomb force affect the flow field. It has been shown that the flow field may become steady, periodic, or non-periodic depending on the flow Reynolds number due to the interaction between electric forces and flow inertia forces (Lai et al., 1995). When the flow inertia is weak and the electric force is strong, the flow and temperature field become oscillatory (Lai and Mathew, 2006; Lai and Tay, 2010). The addition of thermal buoyancy augments this instability (Lai, 1998; Lai and Kulkarni, 2007).

Joule heating is released when current flows through wires and charged particles collide with ions or neutral molecules. For forced convection, the contribution to the heat transfer enhancement by Joule heating is negligible when compared to that by EHD flow convection alone. However, this is not the case for natural convection (Huang and Lai, 2006).

3.2 Governing Equations

In spite of complicated interactions between various fields, the electrohydrodynamic phenomenon is governed by the fundamental equations of electrostatics, fluid flow and heat transfer. For incompressible fluid with constant thermophysical properties, the EHD governing equations for EHD-induced flows and heat transfer can be summarized as follows.

Maxwell equation:

$$\nabla \cdot \varepsilon E = \rho_c \cdot \tag{3.3}$$

Conservation of electric current:

$$\frac{\partial \rho_c}{\partial t} + \nabla \cdot J = 0 \cdot \tag{3.4}$$

Continuity:

$$\nabla \cdot u = 0 \cdot \tag{3.5}$$

Navier-Stokes equation:

$$\rho \frac{\partial u}{\partial t} + \rho(u \cdot \nabla)u = -\nabla p + \mu \nabla^2 u + \rho g + f_e \cdot \tag{3.6}$$

Energy equation:

$$\frac{\partial T}{\partial t} + (u \cdot \nabla)T = \alpha \nabla^2 T \cdot \tag{3.7}$$

As seen from the above equations, the complexity of the EHD phenomena is partly caused by the coupling of equations. One typical example of this is that the electric body force, f_e, is included as the external force in the Navier-Stokes equation of the flow field (Eq. 3.6), and at the same time, the fluid velocity, "u", is involved in

the electric current (Eq. 3.2). However, for any particular application appropriate assumptions can be made to simplify the equations.

3.3 Numerical Formulations and Procedures

The working fluid in this study is air, under atmospheric pressure and room temperature. The following assumptions have been made in the development of numerical model.

1. The thermophysical properties of air, which include density, viscosity, thermal conductivity, mobility, and permittivity are assumed constant.
2. The polarity of the generated ions is the same as the emitting electrode (unipolar charge condition).
3. The dominant electrical body force is Coulomb force while the force due to the gradient of the dielectric constant and the electrostrictive force are negligible.
4. The effect of a magnetic field is negligible which is generated by the corona current.
5. The coupling between the electric field and flow field is assumed one-way. In other words, the electric field affects the flow field, but not vice versa.
6. Joule heating is negligible.

With the above assumptions, the governing equations from the previous section can be simplified.

Introducing the electric field strength $\left(E = -\nabla V\right)$, the Maxwell equation (Eq. 3.3) can be rearranged to give

$$\nabla^2 V = -\frac{\rho_c}{\varepsilon}. \tag{3.8}$$

The one-way coupling assumption gives $J = \rho_c bE$. Thus, for a steady DC power source, the conservation of electric current now becomes

$$\frac{\rho_c^2}{\varepsilon} + \nabla\rho_c \cdot E = 0 \cdot \tag{3.9}$$

For the flow fields, with the electrical body force, $f_e = \rho_c E$, the Navier-Stokes equations become

$$\rho\frac{\partial u}{\partial t} + \rho(u \cdot \nabla)u = -\nabla p + \mu\nabla^2 u + \rho_c E \cdot \tag{3.10}$$

For the temperature field, the energy equation remains the same,

$$\frac{\partial T}{\partial t} + (u \cdot \nabla)T = \alpha\nabla^2 T \cdot \tag{3.11}$$

A review of the above equations reveals that the electric field equations (3.8-3.9) are decoupled from the flow and temperature field equations (3.10-3.11) due to the one-way coupling assumption. However, the electric field needs to be solved first so that the electric body force can be included as the external body force in the momentum equation. Since energy equation is decoupled from the electric and flow fields, it can be solved separately once the flow filed is known.

3.3.1 Electric Field

In Cartesian coordinates, equations (3.8) and (3.9) can be rewritten to give

$$\frac{\partial^2 V}{\partial x^2} + \frac{\partial^2 V}{\partial y^2} + \frac{\partial^2 V}{\partial z^2} = -\frac{\rho_c}{\varepsilon} \cdot \tag{3.12}$$

$$\frac{\rho_c^2}{\varepsilon} + \frac{\partial\rho_c}{\partial x}E_x + \frac{\partial\rho_c}{\partial y}E_y + \frac{\partial\rho_c}{\partial z}E_z = 0 \cdot \tag{3.13}$$

The finite difference method is used to solve the above differential equations. A uniform mesh is employed for numerical calculations. A control volume of nodal P in a three-dimensional (3D) computational domain is shown in Fig. 3.2. Integrating equation (3.12) over the control volume yields

$$\int_{z,b}^{z,t}\int_{y,s}^{y,n}\int_{x,w}^{x,e}\left(\frac{\partial^2 V}{\partial x^2}+\frac{\partial^2 V}{\partial y^2}+\frac{\partial^2 V}{\partial z^2}\right)dx\,dy\,dz=-\int_{z,b}^{z,t}\int_{y,s}^{y,n}\int_{x,w}^{x,e}\frac{\rho_c}{\varepsilon}\,dx\,dy\,dz\cdot \tag{3.14}$$

Integrate once, one obtains

$$\begin{aligned}&\int_{z,b}^{z,t}\int_{y,s}^{y,n}\left[\left(\frac{\partial V}{\partial x}\right)_e-\left(\frac{\partial V}{\partial x}\right)_w\right]dy\,dz+\int_{z,b}^{z,t}\int_{x,w}^{x,e}\left[\left(\frac{\partial V}{\partial y}\right)_n-\left(\frac{\partial V}{\partial y}\right)_s\right]dx\,dz\\&+\int_{y,s}^{y,n}\int_{x,w}^{x,e}\left[\left(\frac{\partial V}{\partial z}\right)_t-\left(\frac{\partial V}{\partial x}\right)_b\right]dx\,dy=-\int_{z,b}^{z,t}\int_{y,s}^{y,n}\int_{x,w}^{x,e}\frac{\rho_c}{\varepsilon}\,dx\,dy\,dz\cdot\end{aligned} \tag{3.15}$$

A central difference scheme is employed for the approximations of derivative terms. Then, equation (3.15) can be rewritten as

$$\begin{aligned}&\left(\frac{V_E-V_P}{x_E-x_P}-\frac{V_P-V_W}{x_P-x_W}\right)(y_n-y_s)(z_t-z_b)+\left(\frac{V_N-V_P}{y_N-y_P}-\frac{V_P-V_S}{y_P-y_S}\right)(x_e-x_w)(z_t-z_b)\\&+\left(\frac{V_T-V_P}{z_T-z_P}-\frac{V_P-V_B}{z_P-z_B}\right)(y_n-y_s)(x_e-x_w)=-\frac{\rho_c}{\varepsilon}(x_e-x_w)(y_n-y_s)(z_t-z_b)\cdot\end{aligned} \tag{3.16}$$

For a uniform mesh, $\Delta x=\Delta y=\Delta z=\Delta$, equation (3.16) can be further simplified to give

$$\left(\frac{V_E-V_P}{\Delta}-\frac{V_P-V_W}{\Delta}\right)+\left(\frac{V_N-V_P}{\Delta}-\frac{V_P-V_S}{\Delta}\right)+\left(\frac{V_T-V_P}{\Delta}-\frac{V_P-V_B}{\Delta}\right)=-\frac{\rho_c}{\varepsilon}\Delta\cdot \tag{3.17}$$

Multiplying equation (3.17) by Δ and combining like terms yields

$$-6V_P+V_E+V_W+V_N+V_S+V_T+V_B=-\frac{\rho_c}{\varepsilon}\Delta^2\cdot \tag{3.18}$$

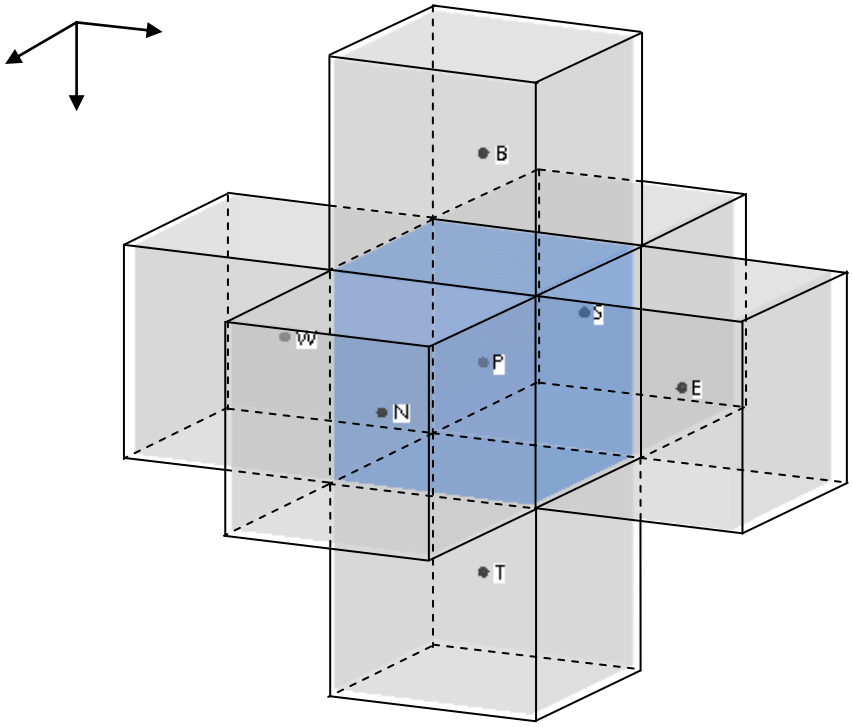

Figure 3.2 A Control Volume in a Three-Dimensional Computational Domain.

The final finite difference form for equation (3.12) becomes

$$V_P = \frac{1}{6}\left(V_E + V_W + V_N + V_S + V_T + V_B + \frac{\rho_c}{\varepsilon}\Delta^2 \right). \tag{3.19}$$

Similarly, the finite difference form of the current continuity equation can be derived by integrating the partial differential equation over a control volume, which gives

$$\int_{z,b}^{z,t}\int_{y,s}^{y,n}\int_{x,w}^{x,e}\frac{\rho_c^2}{\varepsilon}\,dxdy\,dz + \int_{z,b}^{z,t}\int_{y,s}^{y,n}\int_{x,w}^{x,e}\frac{\partial\rho_c}{\partial x}E_x\,dxdy\,dz + \int_{z,b}^{z,t}\int_{y,s}^{y,n}\int_{x,w}^{x,e}\frac{\partial\rho_c}{\partial y}E_y\,dxdy\,dz + \int_{z,b}^{z,t}\int_{y,s}^{y,n}\int_{x,w}^{x,e}\frac{\partial\rho_c}{\partial z}E_z\,dxdy\,dz = 0. \tag{3.20}$$

Carrying out the integrations, one obtains

$$\frac{\rho_c^2}{\varepsilon}\Delta x\Delta y\Delta z+(\rho_{ce}-\rho_{cw})E_x\Delta y\Delta z+(\rho_{cn}-\rho_{cs})E_y\Delta x\Delta z+(\rho_{ct}-\rho_{cb})E_z\Delta x\Delta y=0\cdot \quad (3.21)$$

With a uniform mesh, $\Delta x=\Delta y=\Delta z=\Delta$, the above equation can be simplified to give

$$\frac{\rho_c^2}{\varepsilon}\Delta+(\rho_{ce}-\rho_{cw})E_x+(\rho_{cn}-\rho_{cs})E_y+(\rho_{ct}-\rho_{cb})E_z=0\cdot \quad (3.22)$$

A backward difference scheme is applied for the charge density terms to eliminate the numerical instability which may occur. Thus, equation (3.22) can be reformulated by taking into account eight possible scenarios.

(1) $E_x\ge 0,\ E_y\ge 0,\ E_z\ge 0$

$$\frac{\Delta}{\varepsilon}\rho_{cP}^2+(\rho_{cP}-\rho_{cW})E_x+(\rho_{cP}-\rho_{cS})E_y+(\rho_{cP}-\rho_{cB})E_z=0,$$

which can be rearranged to give

$$\frac{\Delta}{\varepsilon}\rho_{cP}^2+(E_x+E_y+E_z)\rho_{cP}+(-E_x\rho_{cW}-E_y\rho_{cS}-E_z\rho_{cB})=0. \quad (3.23a)$$

(2) $E_x\le 0,\ E_y\ge 0,\ E_z\ge 0$

$$\frac{\Delta}{\varepsilon}\rho_{cP}^2+(\rho_{cE}-\rho_{cP})E_x+(\rho_{cP}-\rho_{cS})E_y+(\rho_{cP}-\rho_{cB})E_z=0,$$

which can be rearranged to give

$$\frac{\Delta}{\varepsilon}\rho_{cP}^2+(-E_x+E_y+E_z)\rho_{cP}+(E_x\rho_{cE}-E_y\rho_{cS}-E_z\rho_{cB})=0. \quad (3.23b)$$

(3) $E_x\ge 0,\ E_y\le 0,\ E_z\ge 0$

$$\frac{\Delta}{\varepsilon}\rho_{cP}^2+(\rho_{cP}-\rho_{cW})E_x+(\rho_{cN}-\rho_{cP})E_y+(\rho_{cP}-\rho_{cB})E_z=0,$$

which can be rearranged to give

$$\frac{\Delta}{\varepsilon}\rho_{cP}^2+(E_x-E_y+E_z)\rho_{cP}+(-E_x\rho_{cW}+E_y\rho_{cN}-E_z\rho_{cB})=0. \quad (3.23c)$$

(4) $E_x \geq 0,\ E_y \geq 0,\ E_z \leq 0$

$$\frac{\Delta}{\varepsilon}\rho_{cP}^2 + (\rho_{cP} - \rho_{cW})E_x + (\rho_{cP} - \rho_{cS})E_y + (\rho_{cT} - \rho_{cP})E_z = 0,$$

which can be rearranged to give

$$\frac{\Delta}{\varepsilon}\rho_{cP}^2 + (E_x + E_y - E_z)\rho_{cP} + (-E_x\rho_{cW} - E_y\rho_{cS} + E_z\rho_{cT}) = 0. \qquad (3.23d)$$

(5) $E_x \leq 0,\ E_y \leq 0,\ E_z \geq 0$

$$\frac{\Delta}{\varepsilon}\rho_{cP}^2 + (\rho_{cE} - \rho_{cP})E_x + (\rho_{cN} - \rho_{cP})E_y + (\rho_{cP} - \rho_{cB})E_z = 0,$$

which can be rearranged to give

$$\frac{\Delta}{\varepsilon}\rho_{cP}^2 + (-E_x - E_y + E_z)\rho_{cP} + (E_x\rho_{cE} - E_y\rho_{cN} - E_z\rho_{cB}) = 0. \qquad (3.23e)$$

(6) $E_x \geq 0,\ E_y \leq 0,\ E_z \leq 0$

$$\frac{\Delta}{\varepsilon}\rho_{cP}^2 + (\rho_{cP} - \rho_{cW})E_x + (\rho_{cN} - \rho_{cP})E_y + (\rho_{cT} - \rho_{cP})E_z = 0,$$

which can be rearranged to give

$$\frac{\Delta}{\varepsilon}\rho_{cP}^2 + (E_x - E_y - E_z)\rho_{cP} + (-E_x\rho_{cW} + E_y\rho_{cN} + E_z\rho_{cT}) = 0. \qquad (3.23f)$$

(7) $E_x \leq 0,\ E_y \geq 0,\ E_z \leq 0$

$$\frac{\Delta}{\varepsilon}\rho_{cP}^2 + (\rho_{cE} - \rho_{cP})E_x + (\rho_{cP} - \rho_{cS})E_y + (\rho_{cT} - \rho_{cP})E_z = 0,$$

which can be rearranged to give

$$\frac{\Delta}{\varepsilon}\rho_{cP}^2 + (-E_x + E_y - E_z)\rho_{cP} + (E_x\rho_{cE} - E_y\rho_{cS} + E_z\rho_{cT}) = 0. \qquad (3.23g)$$

(8) $E_x \le 0,\ E_y \le 0,\ E_z \le 0$

$$\frac{\Delta}{\varepsilon}\rho_{cP}^2 + (\rho_{cE} - \rho_{cP})E_x + (\rho_{cN} - \rho_{cP})E_y + (\rho_{cT} - \rho_{cP})E_z = 0,$$

which can be rearranged to give

$$\frac{\Delta}{\varepsilon}\rho_{cP}^2 + (-E_x - E_y - E_z)\rho_{cP} + (E_x\rho_{cE} + E_y\rho_{cN} + E_z\rho_{cT}) = 0. \qquad (3.23h)$$

Finally, the quadratic formula is used to solve the charge density "ρ_{cP}" in the above equations, $\rho_{cP} = \dfrac{-b \pm \sqrt{b^2 - 4ac}}{2a}$.

Equations (3.12) and (3.13) must be solved simultaneously to determine the electric potential and space charge density distribution. A numerical procedure proposed by Yamamoto and Velkoff (1981) is employed for the present calculations. In this procedure, the electric potential is first estimated by solving equation (3.12) without space charge density (i.e., in the form of Laplace equation). Since the space charge density distribution is not known a priori, an assumed value of space charge density at the wire tip is needed to solve the equation (3.13). After the calculation of the space charge density distribution, equation (3.12) is re-calculated with the space charge density obtained (i.e., in the form of Poisson equation). Then, the total current is calculated using the following equation (3.24). The validity of the solution is checked by comparing the predicted total current with the measured experimental current at the corresponding voltage. If the currents do not match, a new value of space charge density at the wire tip is assumed and the calculation is repeated until the calculated total current agrees well with the measured value for that given applied voltage. The

flow chart of this numerical procedure is illustrated in Fig. 3.3. The corona current is related to the space charge density via

$$I = \int_A \rho_c b \nabla V \cdot dA. \tag{3.24}$$

where A represents the surface area of the grounded plate and b is the ion mobility.

The convergence criterion for electric field calculations is. $\left| \frac{I_{cal} - I_{exp}}{I_{exp}} \right| \leq 10^{-3}$

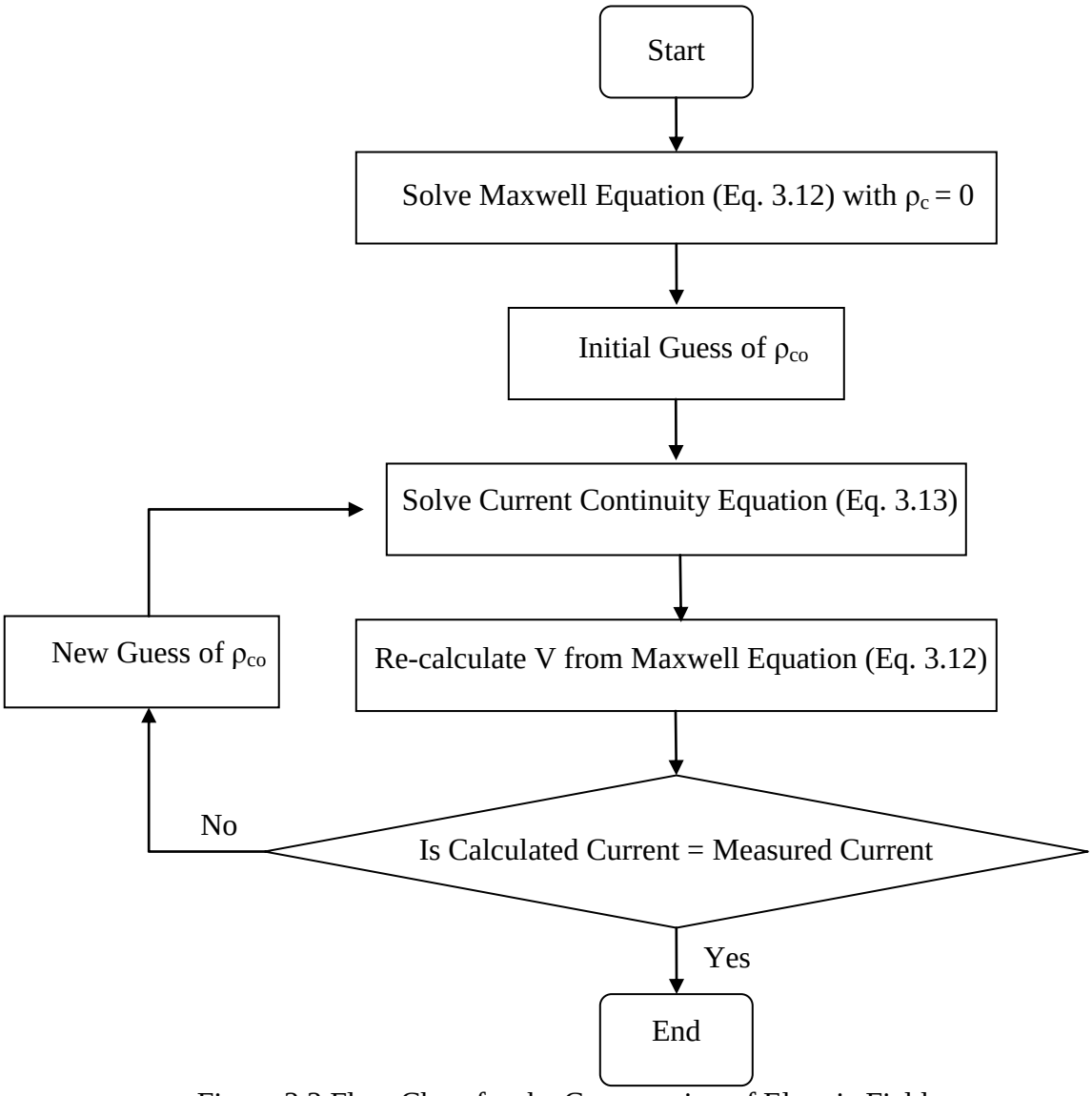

Figure 3.3 Flow Chart for the Computation of Electric Field.

3.3.2 Flow and Temperature Fields

The continuity, momentum, and energy equations in Cartesian coordinates for steady, three-dimensional, incompressible, laminar flows in a channel with constant properties are shown below in equations (3.25), (3.26-28), and (3.29), respectively.

$$\frac{\partial u}{\partial x}+\frac{\partial v}{\partial y}+\frac{\partial w}{\partial z}=0, \tag{3.25}$$

$$u\frac{\partial u}{\partial x}+v\frac{\partial u}{\partial y}+w\frac{\partial u}{\partial z}=-\frac{1}{\rho}\frac{\partial p}{\partial x}+\nu\left(\frac{\partial^2 u}{\partial x^2}+\frac{\partial^2 u}{\partial y^2}+\frac{\partial^2 u}{\partial z^2}\right)+\frac{\rho_c}{\rho}E_x, \tag{3.26}$$

$$u\frac{\partial v}{\partial x}+v\frac{\partial v}{\partial y}+w\frac{\partial v}{\partial z}=-\frac{1}{\rho}\frac{\partial p}{\partial y}+\nu\left(\frac{\partial^2 v}{\partial x^2}+\frac{\partial^2 v}{\partial y^2}+\frac{\partial^2 v}{\partial z^2}\right)+\frac{\rho_c}{\rho}E_y, \tag{3.27}$$

$$u\frac{\partial w}{\partial x}+v\frac{\partial w}{\partial y}+w\frac{\partial w}{\partial z}=-\frac{1}{\rho}\frac{\partial p}{\partial z}+\nu\left(\frac{\partial^2 w}{\partial x^2}+\frac{\partial^2 w}{\partial y^2}+\frac{\partial^2 w}{\partial z^2}\right)+\frac{\rho_c}{\rho}E_z, \tag{3.28}$$

$$u\frac{\partial T}{\partial x}+v\frac{\partial T}{\partial y}+w\frac{\partial T}{\partial z}=\alpha\left(\frac{\partial^2 T}{\partial x^2}+\frac{\partial^2 T}{\partial y^2}+\frac{\partial^2 T}{\partial z^2}\right)\cdot \tag{3.29}$$

In momentum equations (3.26-3.28), the last terms are the electric body forces which will calculate once the electric potential and charge density distribution are known. By introducing the following parameters, the above equations can be non-dimensionalized for EHD-Induced flow,

$$\bar{x}=\frac{x}{D},\ \bar{y}=\frac{y}{D},\ \bar{z}=\frac{z}{D},\ \bar{u}=\frac{u}{u_e},\ \bar{v}=\frac{v}{u_e},\ \bar{w}=\frac{w}{u_e},\ \bar{p}=\frac{p-p_i}{\rho u_e^2},\ Re_{EHD}=\frac{u_e D}{\nu},$$

$$u_e=\sqrt{\frac{\rho_{c0}V_0}{\rho}},\ \bar{\rho_c}=\frac{\rho_c}{\rho_{c0}},\ \bar{V}=\frac{V}{V_0},\ \theta=\frac{T-T_w}{T_i-T_w},\ Pr=\frac{\nu}{\alpha}, \tag{3.30a}$$

By introducing the following parameters, the above equations can be non-dimensionalized for forced flow,

$$\bar{x}=\frac{x}{D},\ \bar{y}=\frac{y}{D},\ \bar{z}=\frac{z}{D},\ \bar{u}=\frac{u}{u_i},\ \bar{v}=\frac{v}{u_i},\ \bar{w}=\frac{w}{u_i},\ \bar{p}=\frac{p-p_i}{\rho u_i^2},\ \mathrm{Re}=\frac{u_i D}{\nu},$$

$$u_e=\sqrt{\frac{\rho_{c0}V_0}{\rho}},\ \bar{\rho}_c=\frac{\rho_c}{\rho_{c0}},\ \bar{V}=\frac{V}{V_0},\ \theta=\frac{T-T_w}{T_i-T_w},\ \mathrm{Pr}=\frac{\nu}{\alpha}, \tag{3.30b}$$

Where "D" is the hydraulic diameter (which is the width of the square channel in the present study). Also, u_i is the flow velocity at the inlet, and u_e is the characteristic corona wind velocity. With the above dimensionless parameters, the momentum and energy equations can be writing as following for EHD-Induced flow (3.31a-3.35a) and forced flow (3.31b-3.35b).

Continuity:

$$\frac{\partial\bar{u}}{\partial\bar{x}}+\frac{\partial\bar{v}}{\partial\bar{y}}+\frac{\partial\bar{w}}{\partial\bar{z}}=0, \tag{3.31a}$$

Momentum:

$$\bar{u}\frac{\partial\bar{u}}{\partial\bar{x}}+\bar{v}\frac{\partial\bar{u}}{\partial\bar{y}}+\bar{w}\frac{\partial\bar{u}}{\partial\bar{z}}=-\frac{\partial\bar{p}}{\partial\bar{x}}+\frac{1}{\mathrm{Re}_{EHD}}\left(\frac{\partial^2\bar{u}}{\partial\bar{x}^2}+\frac{\partial^2\bar{u}}{\partial\bar{y}^2}+\frac{\partial^2\bar{u}}{\partial\bar{z}^2}\right)+\bar{\rho}_c\left(\frac{\partial\bar{V}}{\partial\bar{x}}\right), \tag{3.32a}$$

$$\bar{u}\frac{\partial\bar{v}}{\partial\bar{x}}+\bar{v}\frac{\partial\bar{v}}{\partial\bar{y}}+\bar{w}\frac{\partial\bar{v}}{\partial\bar{z}}=-\frac{\partial\bar{p}}{\partial\bar{y}}+\frac{1}{\mathrm{Re}_{EHD}}\left(\frac{\partial^2\bar{v}}{\partial\bar{x}^2}+\frac{\partial^2\bar{v}}{\partial\bar{y}^2}+\frac{\partial^2\bar{v}}{\partial\bar{z}^2}\right)+\bar{\rho}_c\left(\frac{\partial\bar{V}}{\partial\bar{y}}\right), \tag{3.33a}$$

$$\bar{u}\frac{\partial\bar{w}}{\partial\bar{x}}+\bar{v}\frac{\partial\bar{w}}{\partial\bar{y}}+\bar{w}\frac{\partial\bar{w}}{\partial\bar{z}}=-\frac{\partial\bar{p}}{\partial\bar{z}}+\frac{1}{\mathrm{Re}_{EHD}}\left(\frac{\partial^2\bar{w}}{\partial\bar{x}^2}+\frac{\partial^2\bar{w}}{\partial\bar{y}^2}+\frac{\partial^2\bar{w}}{\partial\bar{z}^2}\right)+\bar{\rho}_c\left(\frac{\partial\bar{V}}{\partial\bar{z}}\right), \tag{3.34a}$$

Energy:

$$\bar{u}\frac{\partial\theta}{\partial\bar{x}}+\bar{v}\frac{\partial\theta}{\partial\bar{y}}+\bar{w}\frac{\partial\theta}{\partial\bar{z}}=\frac{1}{\mathrm{Pr}\,\mathrm{Re}_{EHD}}\left(\frac{\partial^2\theta}{\partial\bar{x}^2}+\frac{\partial^2\theta}{\partial\bar{y}^2}+\frac{\partial^2\theta}{\partial\bar{z}^2}\right). \tag{3.35a}$$

Continuity:

$$\frac{\partial \bar{u}}{\partial \bar{x}} + \frac{\partial \bar{v}}{\partial \bar{y}} + \frac{\partial \bar{w}}{\partial \bar{z}} = 0, \tag{3.31b}$$

Momentum:

$$\bar{u}\frac{\partial \bar{u}}{\partial \bar{x}} + \bar{v}\frac{\partial \bar{u}}{\partial \bar{y}} + \bar{w}\frac{\partial \bar{u}}{\partial \bar{z}} = -\frac{\partial \bar{p}}{\partial \bar{x}} + \frac{1}{\mathrm{Re}}\left(\frac{\partial^2 \bar{u}}{\partial \bar{x}^2} + \frac{\partial^2 \bar{u}}{\partial \bar{y}^2} + \frac{\partial^2 \bar{u}}{\partial \bar{z}^2}\right) + \frac{u_e^2}{u_i^2}\bar{\rho}_c\left(\frac{\partial \bar{V}}{\partial \bar{x}}\right), \tag{3.32b}$$

$$\bar{u}\frac{\partial \bar{v}}{\partial \bar{x}} + \bar{v}\frac{\partial \bar{v}}{\partial \bar{y}} + \bar{w}\frac{\partial \bar{v}}{\partial \bar{z}} = -\frac{\partial \bar{p}}{\partial \bar{y}} + \frac{1}{\mathrm{Re}}\left(\frac{\partial^2 \bar{v}}{\partial \bar{x}^2} + \frac{\partial^2 \bar{v}}{\partial \bar{y}^2} + \frac{\partial^2 \bar{v}}{\partial \bar{z}^2}\right) + \frac{u_e^2}{u_i^2}\bar{\rho}_c\left(\frac{\partial \bar{V}}{\partial \bar{y}}\right), \tag{3.33b)0}$$

$$\bar{u}\frac{\partial \bar{w}}{\partial \bar{x}} + \bar{v}\frac{\partial \bar{w}}{\partial \bar{y}} + \bar{w}\frac{\partial \bar{w}}{\partial \bar{z}} = -\frac{\partial \bar{p}}{\partial \bar{z}} + \frac{1}{\mathrm{Re}}\left(\frac{\partial^2 \bar{w}}{\partial \bar{x}^2} + \frac{\partial^2 \bar{w}}{\partial \bar{y}^2} + \frac{\partial^2 \bar{w}}{\partial \bar{z}^2}\right) + \frac{u_e^2}{u_i^2}\bar{\rho}_c\left(\frac{\partial \bar{V}}{\partial \bar{z}}\right), \tag{3.34b}$$

Energy:

$$\bar{u}\frac{\partial \theta}{\partial \bar{x}} + \bar{v}\frac{\partial \theta}{\partial \bar{y}} + \bar{w}\frac{\partial \theta}{\partial \bar{z}} = \frac{1}{\mathrm{Pr}\,\mathrm{Re}}\left(\frac{\partial^2 \theta}{\partial \bar{x}^2} + \frac{\partial^2 \theta}{\partial \bar{y}^2} + \frac{\partial^2 \theta}{\partial \bar{z}^2}\right). \tag{3.35b}$$

To solve the above equations finite volume method is used. The computational domain is divided into discrete control volumes, and the discretized equations are derived by integrating the differential equations over a control volume. Each control volume is associated with a nodal point at the center where the dependent variables such as velocity, pressure and temperature are to be calculated. However, there are unknown values on the surfaces of the control volume which are required for the calculation of convective terms in the discrete equations. These face-values can be either assigned according to some special numerical scheme or be interpolated from the values at the centers of the neighboring control volumes. Many studies reported in the literature, an upwind scheme has been frequently used to ensure the stability of numerical calculations. In this scheme, the unknown face-values of a control volume take the

values of the cell upstream or upwind, relative to the direction of normal velocity (Patankar, 1980). For the present study, to discretize the convective terms in the momentum and energy equations this upwind scheme is also employed.

In solving momentum equations, one of the challenges is to dealing with the pressure gradient terms. As observed from the above set of momentum equations (3.32-3.34), the velocities cannot be solved until the pressure field is specified. If the pressure fields are specified differently, it will lead to different solutions of the velocity fields for the momentum equations. The constraint that uniquely determines the pressure field is the continuity equation. While solving the momentum equations, one must have the correct pressure field so that the resulting velocity field will satisfy the continuity equation. However, the pressure gradient terms cannot be explicitly expressed in terms of velocities. Therefore, an algorithm is needed for solving the flow field.

Pressure-velocity coupling is achieved by applying the SIMPLE algorithm (Moss et al., 1966), which stands for Semi-Implicit Method for Pressure-Linked Equations. In this algorithm, the momentum equations are initially solved using an estimated pressure field, p^*. In general, the resulting velocity field will not satisfy the continuity equation. Consequently, a pressure correction p' needs to be obtained by solving the so-called pressure-correction equation so that the resulting pressure $\left(p = p^* + p'\right)$ can be used to solve for velocities. This process is repeated until the velocity components satisfy the continuity equation. This SIMPLE algorithm is proposed by Patankar and a more detailed description can be found in reference (Patankar, 1980).

A second-order central difference scheme is used to discretized the diffusion terms in the momentum and energy equations. The convergence criteria for the continuity, momentum and energy equations are that the residuals are reduced to 10^{-3}, 10^{-3}, and 10^{-6} respectively.

The commercial code Fluent 6.3.26 (Huang et al., 2006) is used for the calculations of flow and temperature fields. The Pressure-based segregated algorithm is used to solve equations (3.32-3.35). In this algorithm, the governing equations solved sequentially (i.e., segregated from each other), in other words, the individual governing equations for the variables (e.g. $\bar{u}$, $\bar{v}$, $\bar{w}$, $\bar{p}$, and $\bar{T}$) are solved one after another. While being solved, each governing equation is "segregated" or "decoupled" from other equations, hence its name (FLUENT 6.3 user's guide, 2006). In Fig. 3.4, the procedure of Pressure-based segregated algorithm is outlined. As the discretized equations need only be stored in the memory one at a time, therefore the segregated algorithm is memory-efficient. But the solution convergence is relatively slow, because the equations are solved in a decoupled manner.

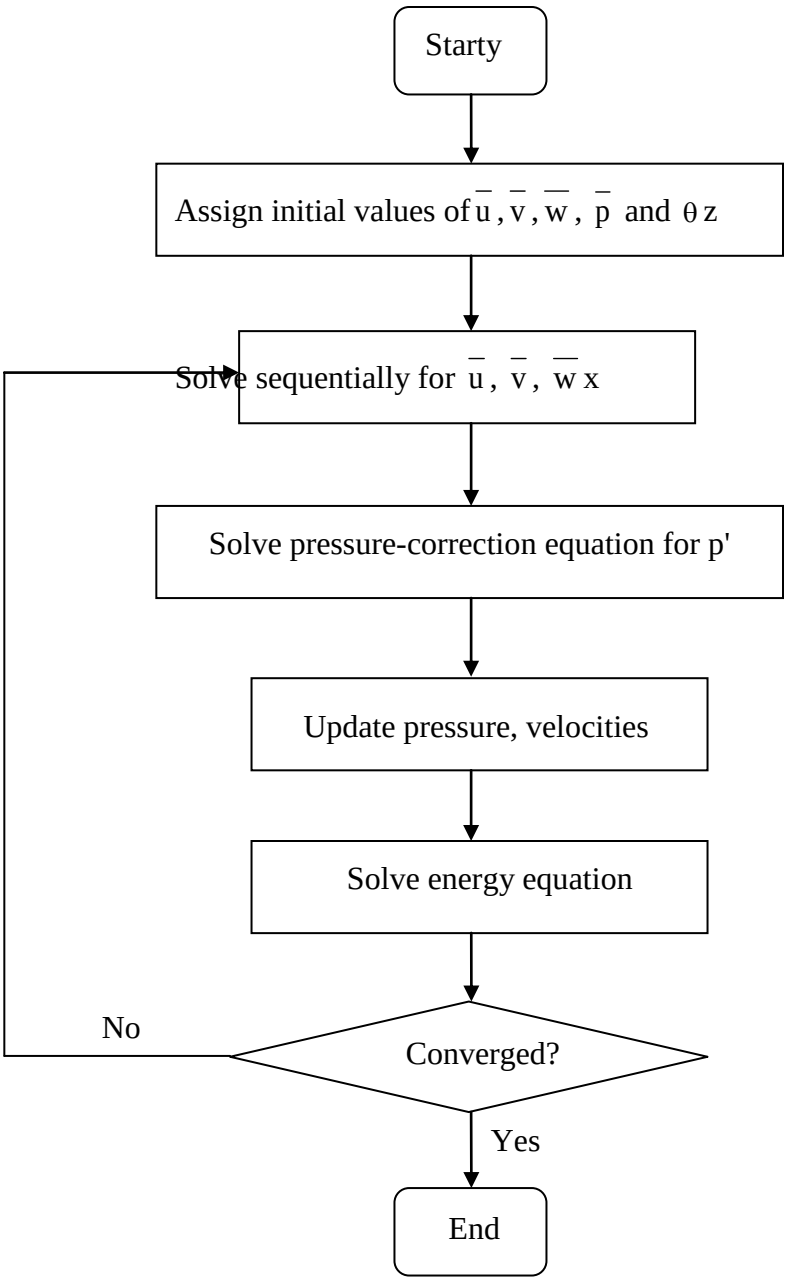

Figure 3.4 Flow Chart for the Computation of Flow and Temperature Fields.

3.4 Boundary Conditions

Solutions to the governing equations for the electric, flow, and temperature fields must be obtained subject to the existing boundary or initial conditions. A numerical model of a two-stage EHD gas pump with 28 electrode pins in each stage

(total 56 electrode pins) is shown in Fig. 3.5. To save the computational time, only a quarter of the model is considered as the computational domain, which is shown as the shaded region.

The corresponding boundary conditions for solving the electric field are given below,

At the wire electrodes, $V = V_o$. (3.36a)

At the grounded plates, $V = 0$. (3.36b)

On the channel walls, $x = 0$, $\frac{\partial V}{\partial x} = 0$. (3.36c)

$y = 0$, $\frac{\partial V}{\partial y} = 0$. (3.36d)

On the symmetric planes, $x = D/2$, $\frac{\partial V}{\partial x} = 0$. (3.36e)

$y = D/2$, $\frac{\partial V}{\partial y} = 0$. (3.36f)

At the inlet of the channel, $z = 0$, $\frac{\partial V}{\partial z} = 0$. (3.36g)

At the outlet of the channel, $z = H$, $\frac{\partial V}{\partial z} = 0$. (3.36h)

The corresponding boundary conditions for solving the momentum equations of EHD-induced flow are given below in dimensionless form,

On the channel walls, $\bar{x} = 0$, $\bar{u} = 0$, $\bar{v} = 0$, $\bar{w} = 0$, (3.37a)

$\bar{y} = 0$, $\bar{u} = 0$, $\bar{v} = 0$, $\bar{w} = 0$, (3.37b)

On the symmetric planes, $\bar{x} = D/2$, $\bar{u} = 0$, $\frac{\partial \bar{v}}{\partial \bar{x}} = 0$, $\frac{\partial \bar{w}}{\partial \bar{x}} = 0$, (3.37c)

$$\bar{y} = D/2,\ \frac{\partial \bar{u}}{\partial \bar{y}} = 0,\ \bar{v} = 0,\ \frac{\partial \bar{w}}{\partial \bar{y}} = 0, \tag{3.37d}$$

At the inlet of the channel, $\bar{z} = 0,\ \overline{p_{total}} = 0,\ \overline{p_{initial}} = 0.$ (3.37e)

At the outlet of the channel, $\bar{z} = H/D,\ \frac{\partial \bar{u}}{\partial \bar{z}} = 0,\ \frac{\partial \bar{v}}{\partial \bar{z}} = 0,\ \frac{\partial \bar{w}}{\partial \bar{z}} = 0,\ \bar{p} = \frac{p - p_i}{\rho u_e^2}.$ (3.37f)

The corresponding boundary conditions for solving the momentum equations of forced flow are given below in dimensionless form,

On the channel walls, $\bar{x} = 0, \quad \bar{u} = 0,\ \bar{v} = 0,\ \bar{w} = 0,$ (3.38a)

$$\bar{y} = 0, \quad \bar{u} = 0,\ \bar{v} = 0,\ \bar{w} = 0, \tag{3.38b}$$

On the symmetric planes, $\bar{x} = D/2,\ \bar{u} = 0,\ \frac{\partial \bar{v}}{\partial \bar{x}} = 0,\ \frac{\partial \bar{w}}{\partial \bar{x}} = 0,$ (3.38c)

$$\bar{y} = D/2,\ \frac{\partial \bar{u}}{\partial \bar{y}} = 0,\ \bar{v} = 0,\ \frac{\partial \bar{w}}{\partial \bar{y}} = 0, \tag{3.38d}$$

At the inlet of the channel, $\bar{z} = 0, \quad \bar{u} = 0,\ \bar{v} = 0,\ \bar{w} = 1.$ (3.38e)

At the outlet of the channel, $\bar{z} = H/D,\ \frac{\partial \bar{u}}{\partial \bar{z}} = 0,\ \frac{\partial \bar{v}}{\partial \bar{z}} = 0,\ \frac{\partial \bar{w}}{\partial \bar{z}} = 0,\ \bar{p} = \frac{p - p_i}{\rho u_i^2}.$ (3.38f)

The corresponding boundary conditions for solving the energy equation of forced flow are given below in dimensionless form,

On the channel walls, $\bar{x} = 0$ and $\bar{z} \le h/D, \qquad \frac{\partial \theta}{\partial \bar{x}} = 0.$ (3.39a)

$$\bar{x} = 0 \text{ and } \bar{z} \ge h/D, \qquad \theta = 0. \tag{3.39b}$$

$$\bar{y} = 0 \text{ and } \bar{z} \le h/D, \qquad \frac{\partial \theta}{\partial \bar{y}} = 0. \tag{3.39c}$$

$$\bar{y} = 0 \text{ and } \bar{z} \ge h/D, \qquad \theta = 0. \tag{3.39d}$$

On the symmetric planes, $\bar{x} = D/2$, $\dfrac{\partial\theta}{\partial\bar{x}} = 0.$ (3.39e)

$\bar{y} = D/2$, $\dfrac{\partial\theta}{\partial\bar{y}} = 0.$ (3.39f)

At the inlet of the channel, $\bar{z} = 0$, $\theta = 1.$ (3.39g)

At the outlet of the channel, $\bar{z} = H/D$, $\dfrac{\partial\theta}{\partial\bar{z}} = 0.$ (3.39h)

Where "D" is the hydraulic diameter (which is the width of the square channel in the present study), "h" is the vertical height from top to bottom of second stage ground plate, "H" is the total vertical height of the domain.

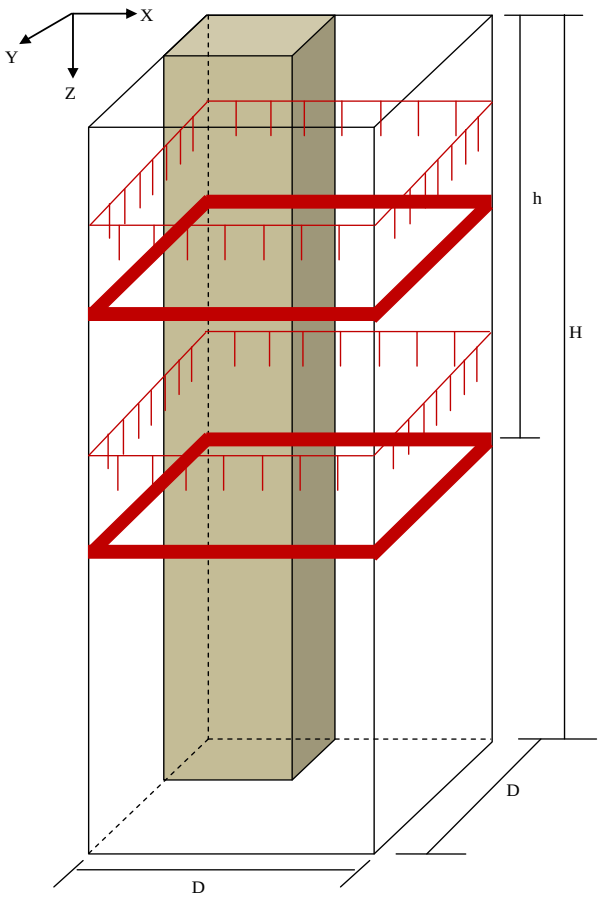

Figure 3.5 Computational Domain for a Two-Stage EHD Gas Pump in a Square. Channel.

By using the above boundary conditions the governing equations are solved. A code written in "Fortran 90" is used for solving the electric potential and the space charge density (Eqs. 3.36a-3.36h) while the commercial code "Fluent 6.3.26" is used for solving the flow and temperature fields (Eqs. 3.37a-3.37f for EHD-induced flow, Eqs. 3.38a-3.38f and Eqs. 3.39a-3.39h for forced flow). After the electric field becomes available, the electric body force is calculated and added to the fluent solver through a User-Defined Function (UDF), which is written in "C" programming language.

Three different model of the EHD gas pump is used for numerical simulations. To reduce the computational time, only a quarter of the model (due to symmetry) is considered as the computational domain.

For the electric field calculations of single stage unit, due to the fact that the electric field does not change further downstream of the grounded plate, a channel length of 10 inches long has been found sufficient. A uniform grid of 51 x 51 x 251 has been used for the electric field computational domain of 2 by 2 by 10 inches. The whole model dimension of single stage unit is 4 by 4 by 10 inches.

But for the electric field calculations of two-stage unit, a channel length of 16 inches long has been used. A uniform grid of 51 x 51 x 401 has been used for the electric field computational domain of 2 by 2 by 16 inches. A non-uniform grid is used for calculating the EHD-Induced flow fields, as shown in Fig. 3.6. Finer meshes are applied to the boundary layer region where the viscous and electric body forces dominate. Relatively coarse meshes are used in the regions far away from the boundary layer and far downstream. A total of 676,000 cells have been used in the computational

domain of 2 by 2 by 16 inches. Further refinements of the mesh do not appear to produce more accurate results, but merely increase the computational time significantly.

A uniform grid of 51 x 51 x 551 has been used for the electric field computational domain of 2 by 2 by 22 inches which is used for calculating the forced convection where both flow and temperature fields are simulated. A total of 704,000 cells have been used in the computational domain of 2 by 2 by 22 inches.

Calculations are performed on a 64-bit workstation with a 2 GHz CPU and 8 Gb of RAM. A typical run takes about seven to ten hours of CPU time for the solution of the electric field. However, the time required to solve for the flow and temperature field ranges from three hours to six hours, depending on the flow condition (i.e., the Reynolds number). In general, it takes more time for the solutions involving low Reynolds numbers than those with high Reynolds numbers.

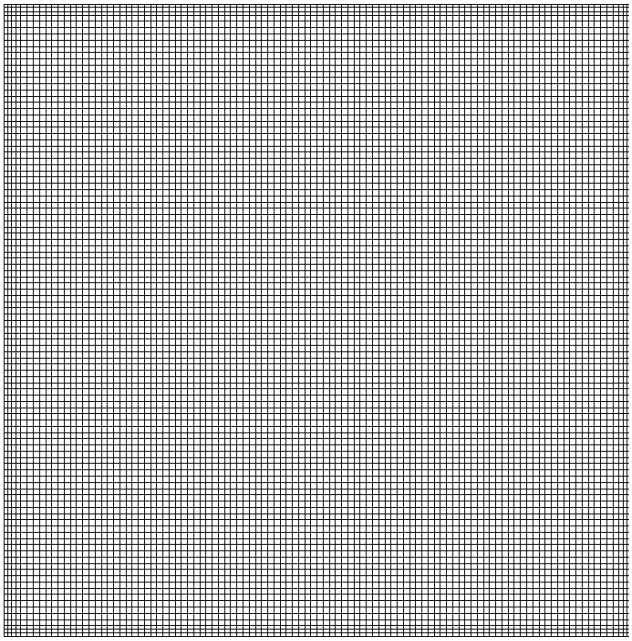

Figure 3.6 Computational Grids in the X-Y Plane.

CHAPTER FOUR

EHD-INDUCED FLOWS

Both experimental and numerical studies have been performed for the EHD gas pump with three electrode configurations in which the width of the grounded plate at the bottom stage is fixed at 0.5-inch while that of the top stage varies from 0.5-inch, 1-inch to 2-inch. For comparison, experiments have also been conducted for a single-stage electrode with the width of the grounded plate varying from 0.5 inch to 2 inches. Only positive corona discharge is considered for the present study. The results of electric field are presented first, followed by numerical results of flow field, and completed with comparison of experimental data.

4.1 Electric Field

For the present study, it is noted that room temperature and relative humidity for the experiments conducted have been varying within the range of 20-27 °C and 17-35 %, respectively. Figure 4.1 illustrates the V-I characteristics for the present experimental setup operating under positive corona discharges. It can be seen from Fig. 4.1 that no current can be detected when the applied voltage is less than 20 kV. When the applied voltage is increased beyond 20 kV, corona current increases as a function of power-law which has also been reported in previous studies. In addition, it is observed that the two-stage configuration produces more current than that of the one-stage at any applied voltage. Figure 4.2 further illustrates the V-I curve for the two-stage EHD gas pump with three different sizes of grounded electrode at the top stage: 0.5-inch, 1-inch,

and 2-inch while that of the bottom stage fixed at 0.5-inch wide. It shows that when the grounded electrode of the top and bottom stages is fixed at 0.5-inch, it produces more current than the other two at any applied voltage.

With the current data available, numerical simulation can be performed using the algorithm discussed in Chapter 3. Numerical results have thus been obtained for the electric field in a square channel with an EHD gas pump. Since the corona-induced flow is driven by the electric field, visualization of these electric fields proves very helpful for the study of flow field that will follow next. For comparison, the results for a channel with an EHD pump of single-stage corona wind generator are presented first, followed by that of a two-stage unit.

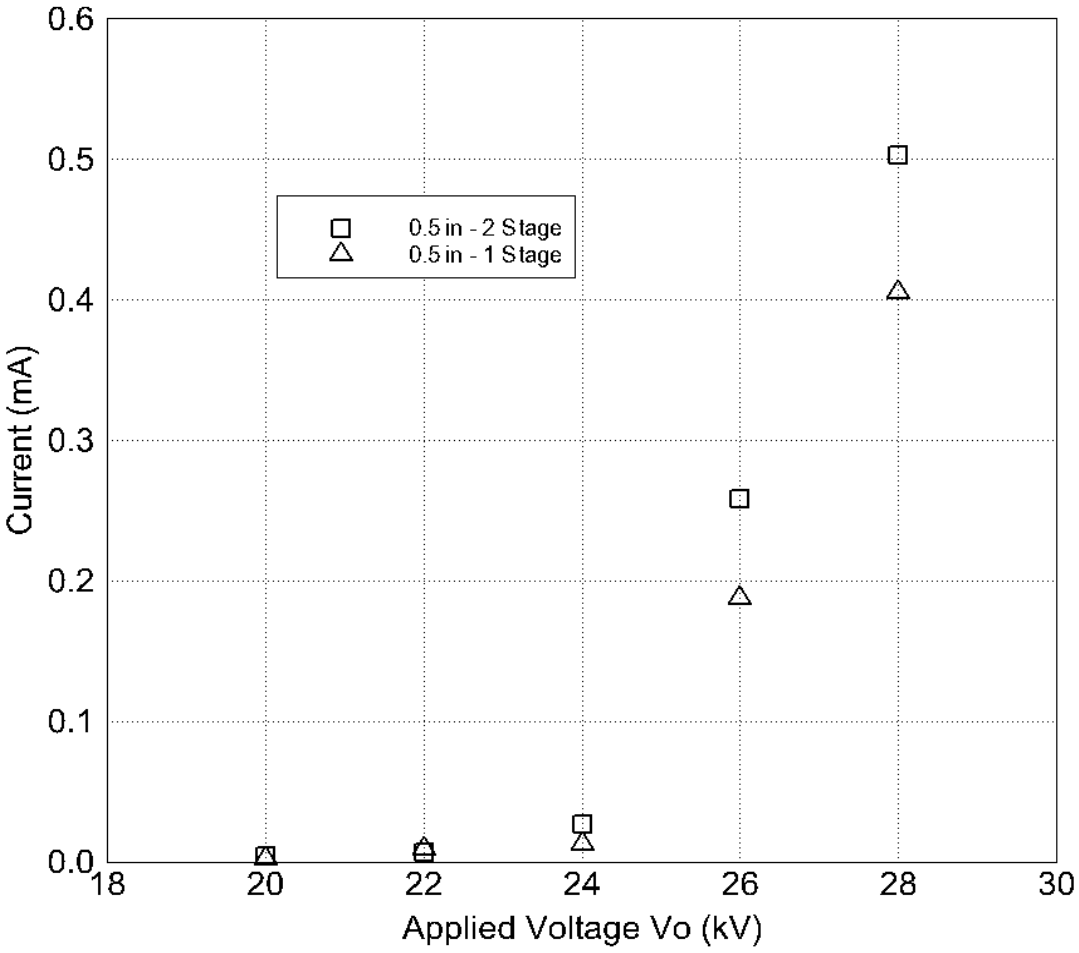

Figure 4.1 Comparison of V–I Characteristics of an EHD Gas Pump with a Single- and a Two-Stage Corona Wind Generator in a Square Channel.

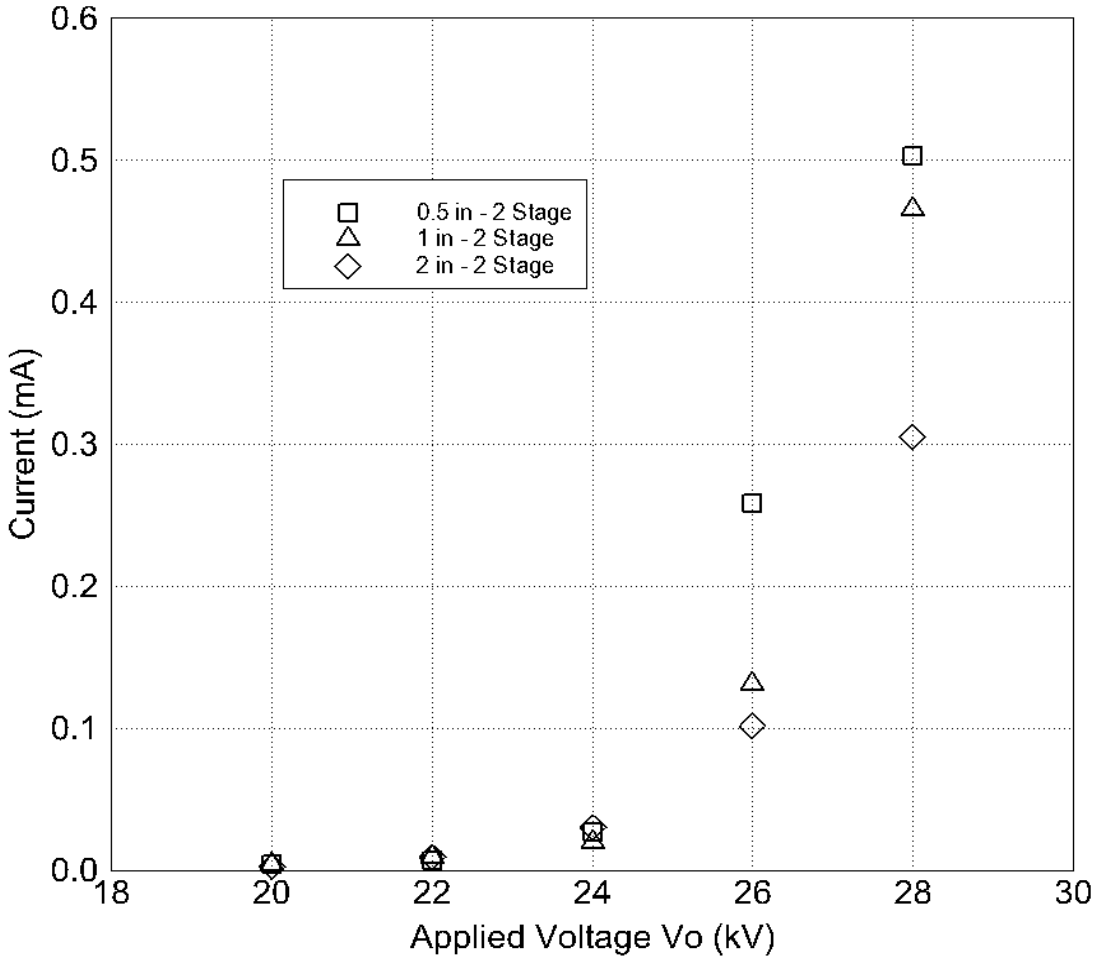

Figure 4.2 Comparison of V–I Characteristics of an EHD Gas Pump with a Two-Stage Corona Wind Generator of Various Sizes of Grounded Electrode.

4.1.1 Electric Potential Distributions

(a) EHD Gas Pump with Single-Stage Corona Wind Generator

The electric potential distributions inside the test channel are shown in Figs. 4.3 and 4.4 for a single-stage EHD gas pump with 3 different sizes of grounded electrode at an applied voltage of 20 kV and 24 kV, respectively. The electric potential displayed is normalized with its value at the emitting electrodes. One clearly observes that a large potential gradient exists between the emitting and the grounded electrodes. The electric

potential is slightly higher in the core region of the channel than that on the channel surface. Below the grounded electrode, voltage does not vary significantly. Hence, it justifies using a shorter channel length for the electric field calculations. From both figures, one can see that the electrode pins has significantly modified the electric field. This non-uniform electric field is an essential condition for the generation of corona wind.

(b) EHD Gas Pump with Two-Stage Corona Wind Generator

The distributions of electric potential inside the test channel are shown in Fig. 4.5 for a two-stage EHD gas pump with applied voltage varying from 20 kV to 28 kV at an increment of 2 kV when the grounded electrode at both stages is fixed at 0.5 inch. Same as those of single-stage EHD gas pump, a large potential gradient is present between the wire electrodes and the grounded electrode at both top and bottom stages. Below the grounded plate of the bottom stage, the potential does not vary significantly.

Figure 4.6 illustrates the electric potential contours at various cross-sections from top to bottom along the z-direction when the applied voltage is fixed at 28 kV. It can be seen from Fig. 4.6 (a) and (f), which are cross-sections at the wire-loop level of the top and bottom stages respectively (z = 1/16 & z = 7/16), the contours of electric potential are nearly concentric. This concentric pattern is perturbed by the presence of electrode pins as one move down the channel. The influence by the electrode pins can be clearly seen from Fig. 4.6 (b) and (g), the cross-section at the emitting electrode tip level of the top and bottom stages respectively (z = 2/16 & z = 8/16). The disturbance by the presence of electrode pins is still visible (Fig. 4.6 (c)) at the level midway

between the electrode tips and the grounded plate of the top stage (z = 2.75/16). However, the electric potential becomes completely uniform (Fig. 4.6 (h)) at the same level of the bottom stage (z = 8.75/16). As such, no contour line is observed. As one approaches the grounded electrode, the distributions of electric potential become concentric again as seen from the cross-sections (Fig. 4.6 (d)-(e) and (i)-(j)) at the levels aligned with the top edge (z = 3.5/16 & z = 9.5/16) and bottom edge (z = 4/16 & z = 10/16) of the grounded electrode of the top and bottom stages, respectively. The electric potential distribution is more concentric inside the channel bounded by the grounded electrode of the top stage ((Fig. 4.6 (d)-(e)) than that of the bottom stage ((Fig. 4.6 (i)-(j)).

The distributions of electric potential are shown in Figs. 4.7 and 4.8 for other two configurations of the two-stage EHD gas pump operating at the same voltage range. The contour plots show similar characteristics in the electric potential distributions as observed earlier, except that the potential gradient appears to be larger for a wider grounded electrode at the top stage.

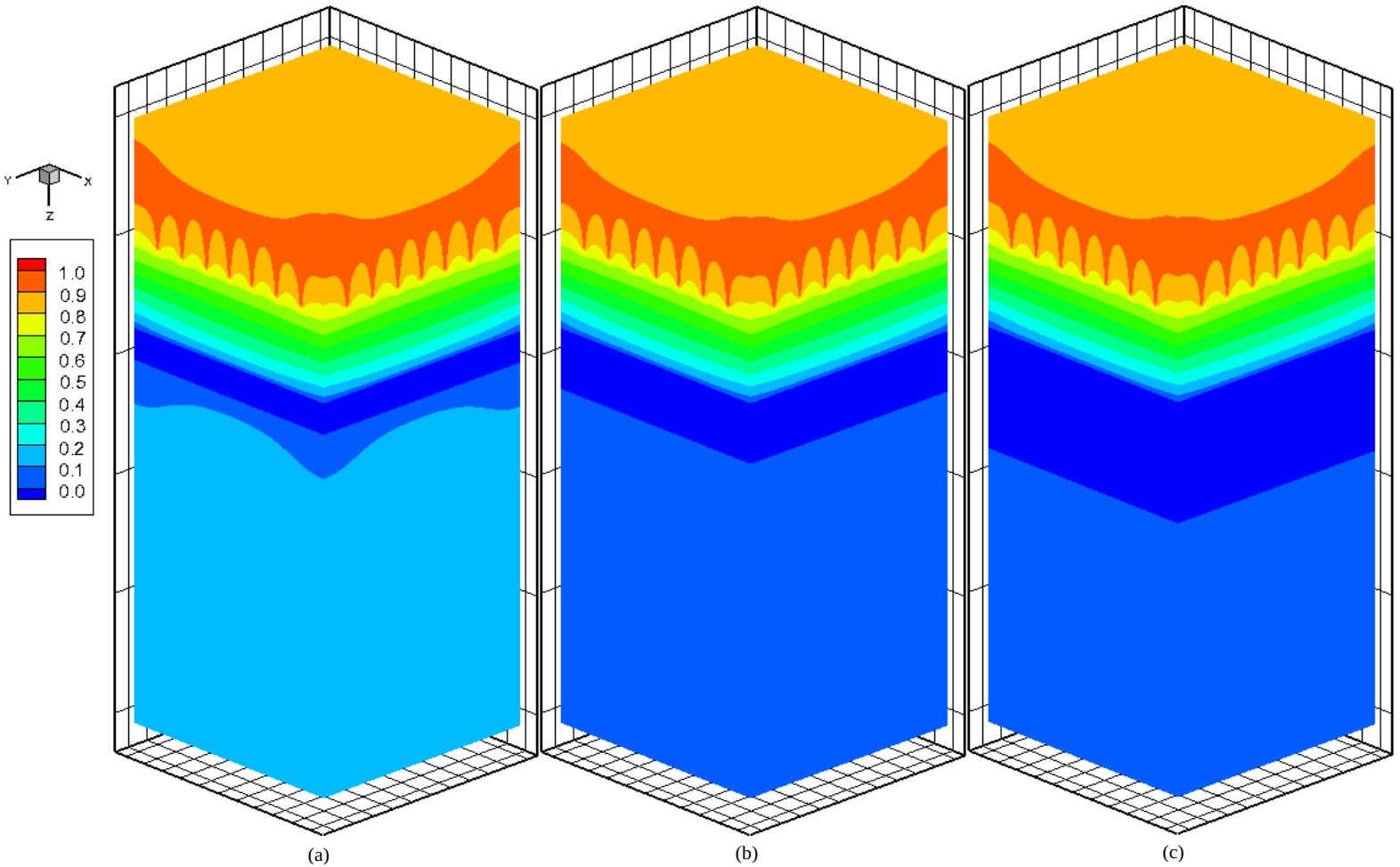

Figure 4.3 Distribution of Electric Potential in a Single-Stage EHD Gas Pump with Various Sizes of Grounded Electrode (V_o = 20 kV), (a) 0.5-inch, (b) 1-inch, (c) 2-inch.

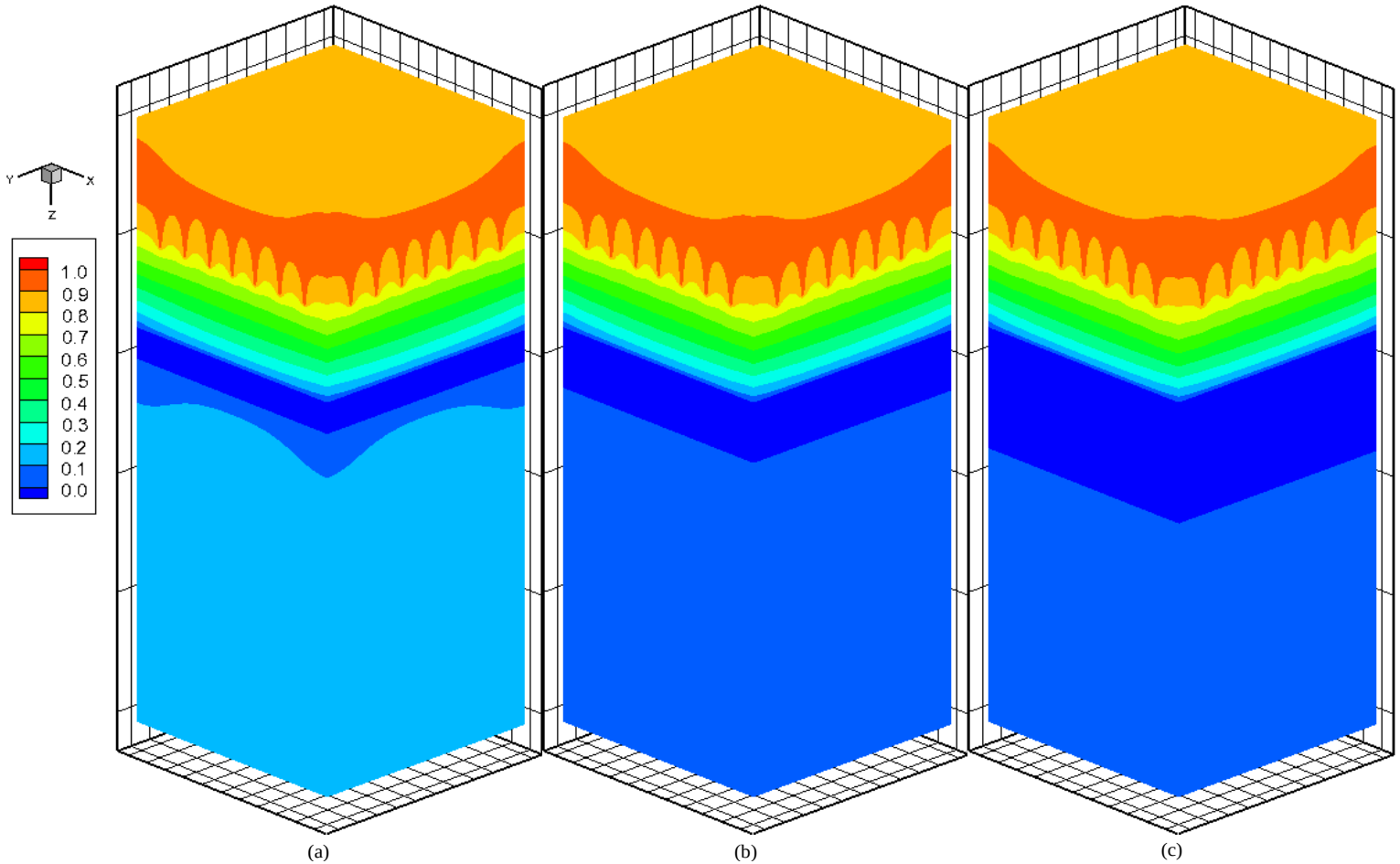

Figure 4.4 Distribution of Electric Potential in a Single-Stage EHD Gas Pump with Various Sizes of Grounded Electrode (V_o = 24 kV), (a) 0.5-inch, (b) 1-inch, (c) 2-inch.

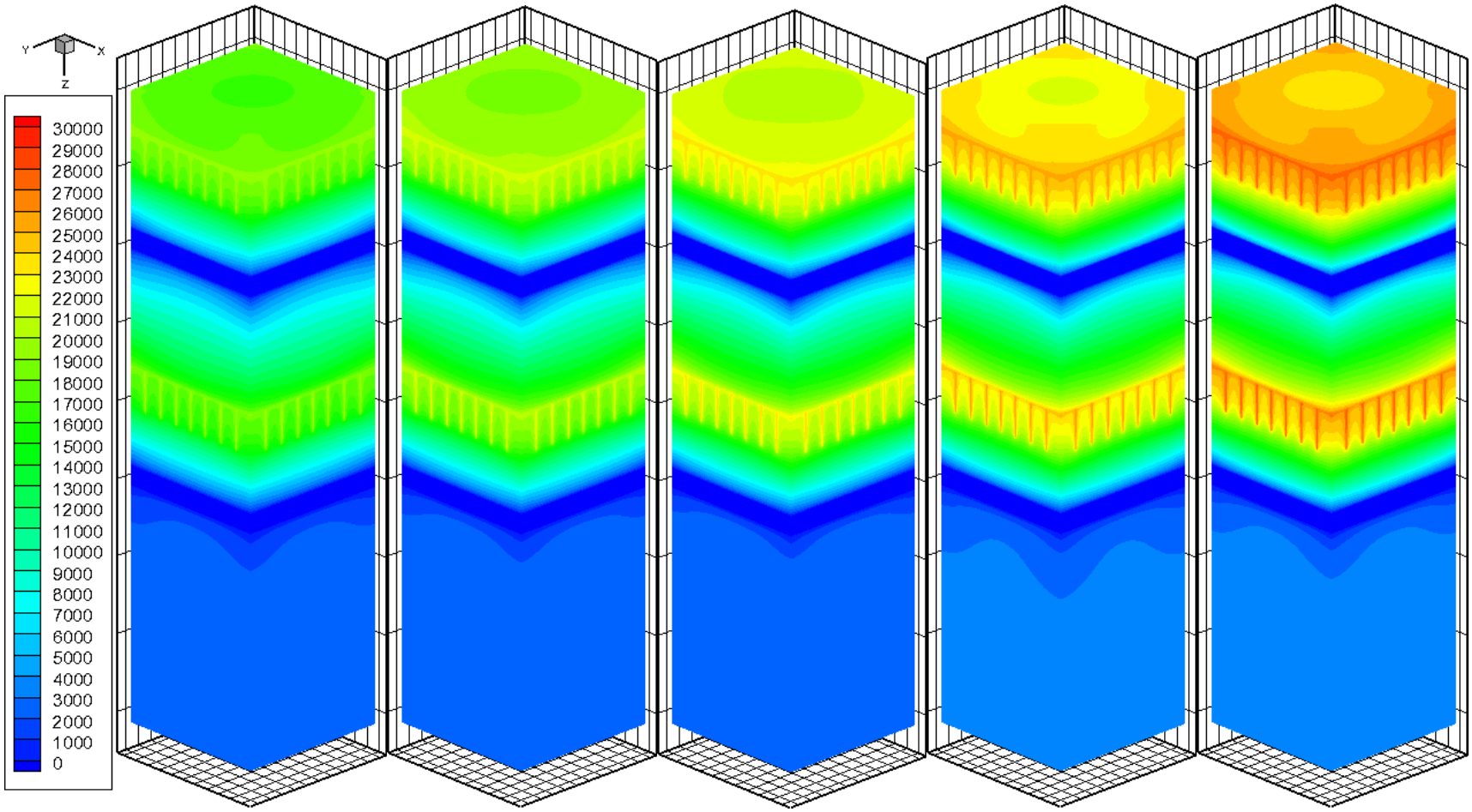

Figure 4.5 Distribution of Electric Potential in a Square Channel with a Two-Stage EHD Gas Pump (0.5-inch Wide Grounded Electrode at the Top Stage)

(a) V_o = 20 kV, (b) V_o = 22 kV, (c) V_o = 24 kV, (d) V_o = 26 kV, (e) V_o = 28 kV.

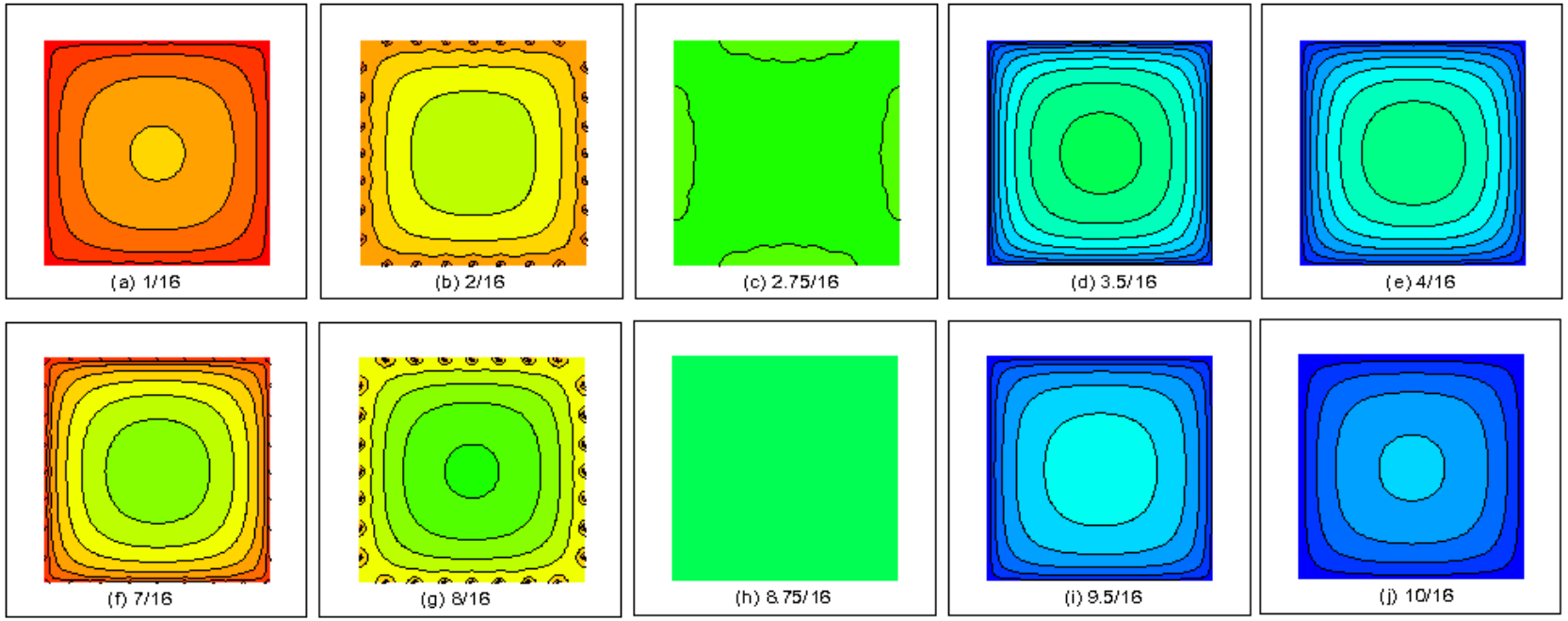

Figure 4.6 Distribution of Electric Potential at Various Cross-Sections along the Z-Direction from Top to Bottom for V_o = 28 kV (Unit of Location in Inch).

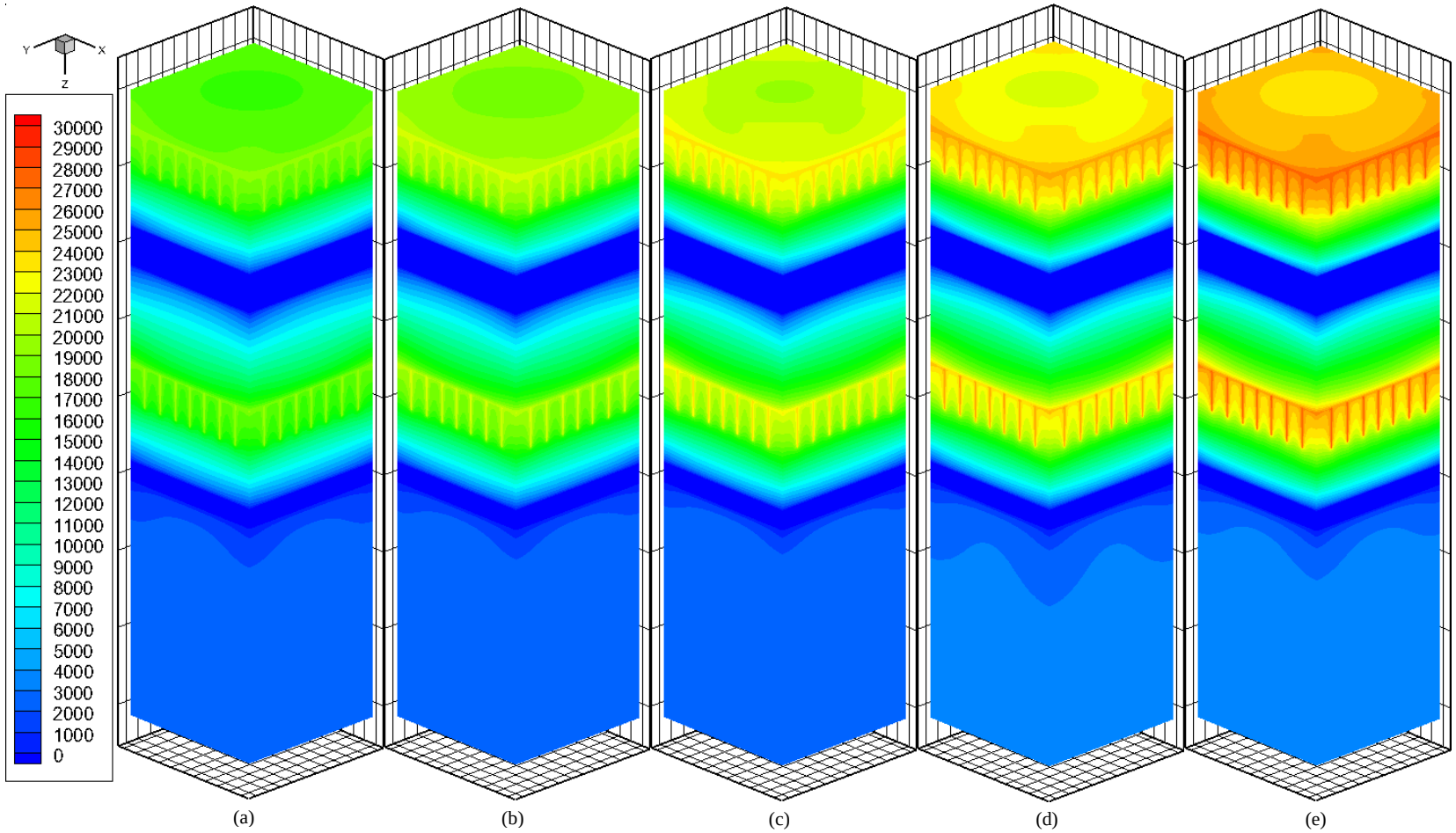

Figure 4.7 Distribution of Electric Potential in a Square Channel with a Two-Stage EHD Gas Pump (1-inch Wide Grounded Electrode at the Top Stage)

(a) V_o = 20 kV, (b) V_o = 22 kV, (c) V_o = 24 kV, (d) V_o = 26 kV, (e) V_o = 28 kV.

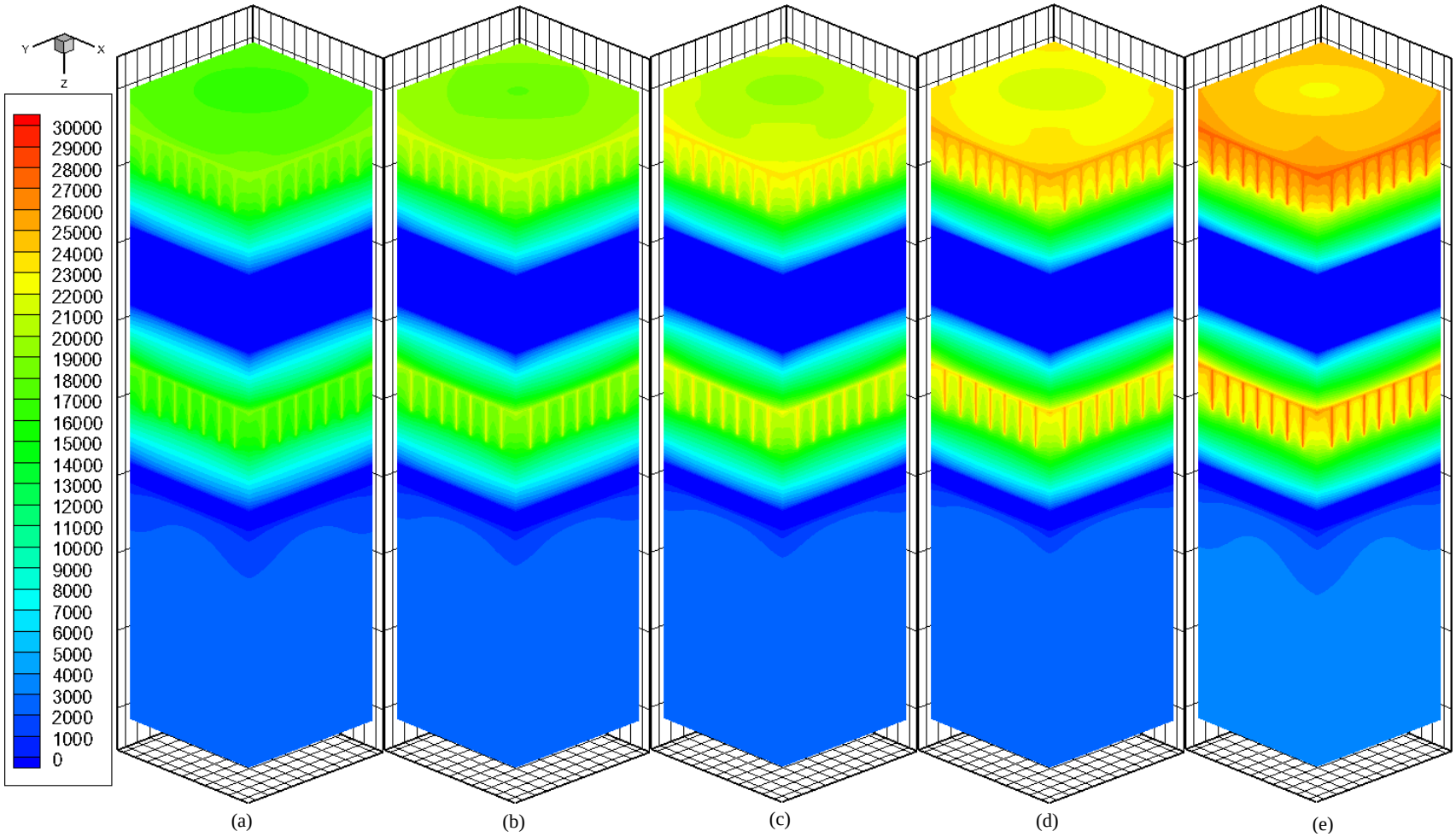

Figure 4.8 Distribution of Electric Potential in a Square Channel with a Two-Stage EHD Gas Pump

(2-inch Wide Grounded Electrode at the Top Stage)

(b) V_o = 20 kV, (b) V_o = 22 kV, (c) V_o = 24 kV, (d) V_o = 26 kV, (e) V_o = 28 kV.

4.1.2 Space Charge Density Distributions

(a) EHD Gas Pump with Single-Stage Corona Wind Generator

Space charge density distributions are shown in Figs. 4.9 and 4.10 for an EHD gas pump with various sizes of grounded electrode at an applied voltage of 20 kV and 24 kV, respectively. The charge density displayed is normalized with its value at the electrode tips. From these figures, one observes that space charges are mainly present in the region between the emitting and the grounded electrodes. Above the emitting electrodes or below the grounded electrodes, they are nearly non-existent. Furthermore, space charges are mostly centered at the electrode tips and spread downwards to the grounded electrode. Their density greatly reduces when moving away from the electrode tip. With an increase in the applied voltage, space charges are clustered in a smaller region at the tip. Also observed, as the width of the grounded electrode increases, space charges are further confined to the electrode tips and its density reduces dramatically within a short distance away from the tips.

(b) EHD Gas Pump with Two-Stage Corona Wind Generator

The space charge density distributions are shown in Fig. 4.11 for a two-stage unit with applied voltage varying from 20 kV to 28 kV at an increment of 2 kV when the grounded electrode at both stages is fixed at 0.5 inch. Same as those of a single-stage EHD gas pump that one observed earlier, space charges are centered at the electrode tips and spread downwards to the grounded electrode at both top and bottom stages. With an increase in the applied voltage, space charges are further confined to a smaller region at the tip but it fill up the entire region between the electrode tips and the

grounded electrode at a lower voltage. It can be seen from Figs. 4.11 (d) and (e), at an applied voltage of 26 kV and 28 kV, space charges are highly concentrated at the electrode tips, and their density reduces dramatically within a short distance away from the tips.

Figure 4.12 illustrates the cross-sectional space charge density contours at the same levels as those of applied voltage that were shown in Fig. 4.6. No space charge is observed on the cross-section at the wire-loop level (Fig. 4.12 (a) and (f)) at both top and bottom stages (z = 1/16 & z = 7/16). At the level of the emitting electrode tips (Fig. 4.12 (b) and (g)), space charges are confined to a small region near the tips and have a maximum value there. Since space charge propagates as a one-dimensional wave from the electrode tips towards the grounded electrode, its value decreases when moving away from the tips. This can be clearly observed at a cross-section downstream of the electrode tips (z = 2.75/16 and 8.75/16) for both stage, the space charge density decreases and spreads towards the center of the channel. Although the charge density decreases dramatically as it approaches the upper edge of the grounded electrode, its presence can still be observed at the top stage (z = 3.5/16), but not at bottom stage (z = 9.5/16). No space charges exist below the grounded electrode for both top and bottom stages (z = 4/16 & z = 10/16).

The distributions of space charge density are shown in Figs. 4.13 and 4.14 for other two configurations of the two-stage EHD gas pump operating at the same voltage range. The contour plots show similar characteristics in the space charge density distributions as observed earlier. However, one notices that the charge density has a larger value for a slimmer grounded electrode at the top stage at the same applied

voltage. This is consistent with the results shown in Fig. 4.2 that the EHD gas pump with the smallest size of grounded plate (0.5-inch) at the top stage has the maximum corona current.

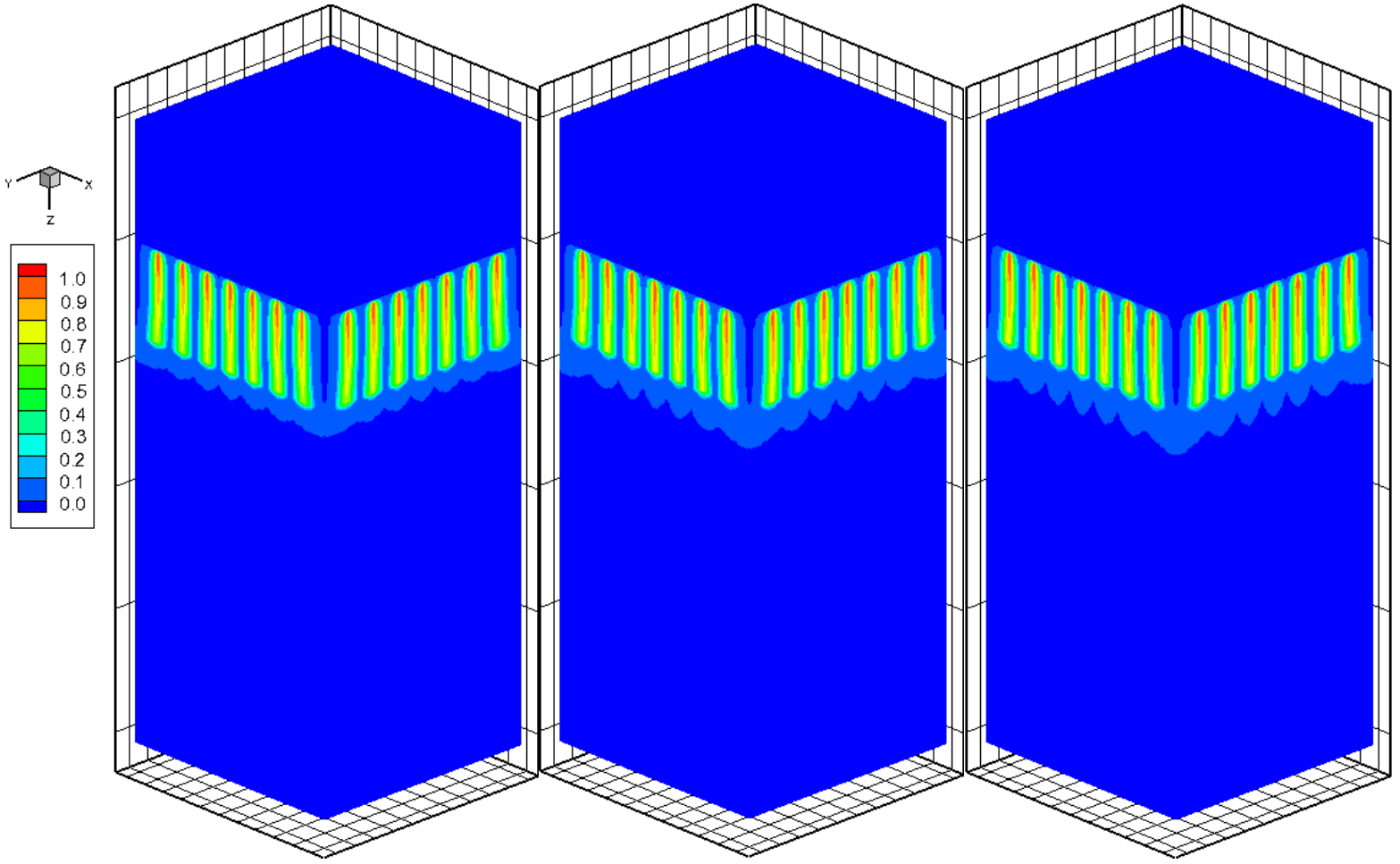

Figure 4.9 Distribution of Charge Density in a Square Channel with a Single-Stage EHD Gas Pump with Various Sizes of Grounded Electrode (V_o = 20 kV), (a) 0.5-inch, (b) 1-inch, (c) 2-inch.

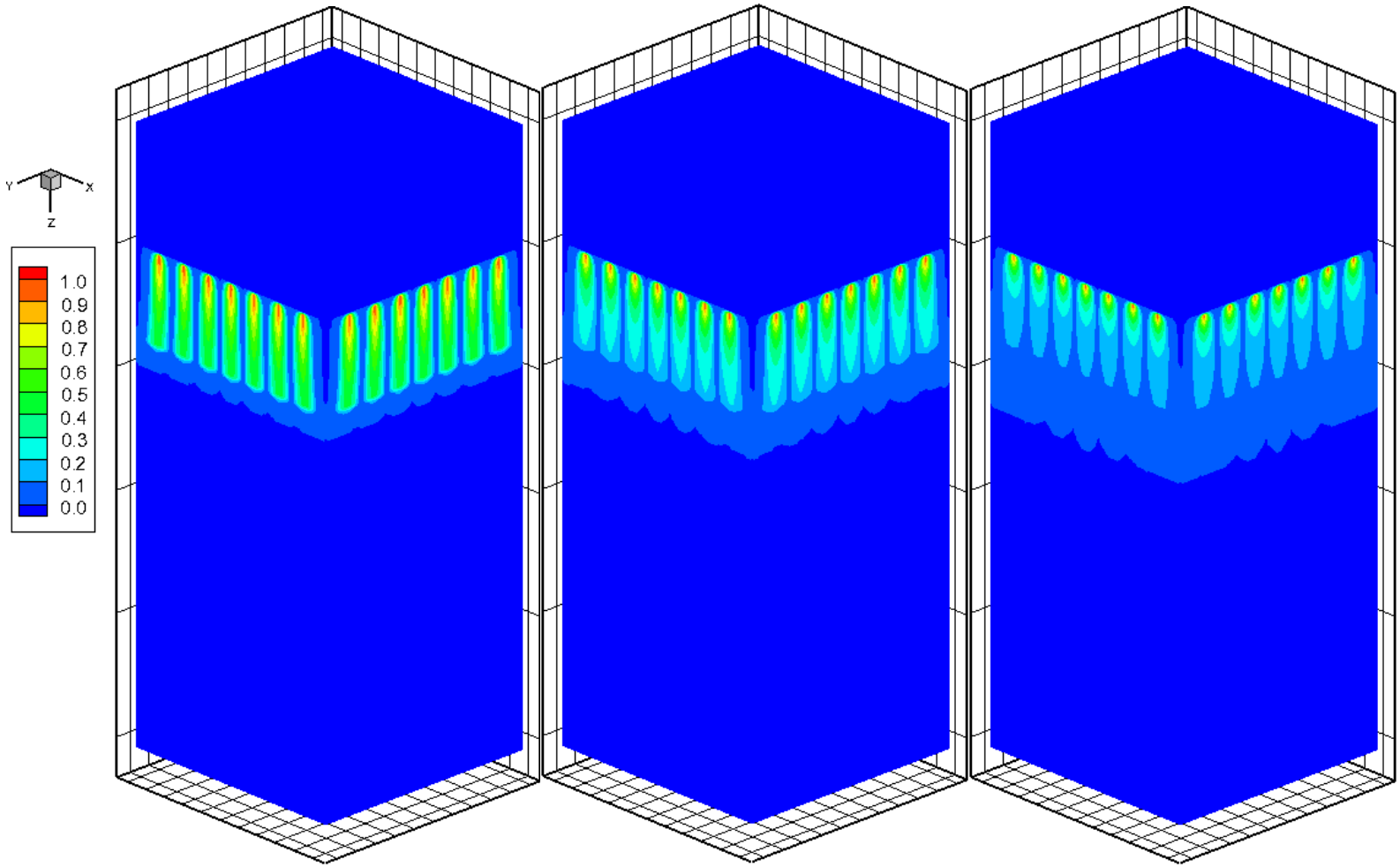

Figure 4.10 Distribution of Charge Density in a Square Channel with a Single-Stage EHD Gas Pump with Various Sizes of Grounded Electrode (V_o = 24 kV), (a) 0.5-inch, (b) 1-inch, (c) 2-inch.

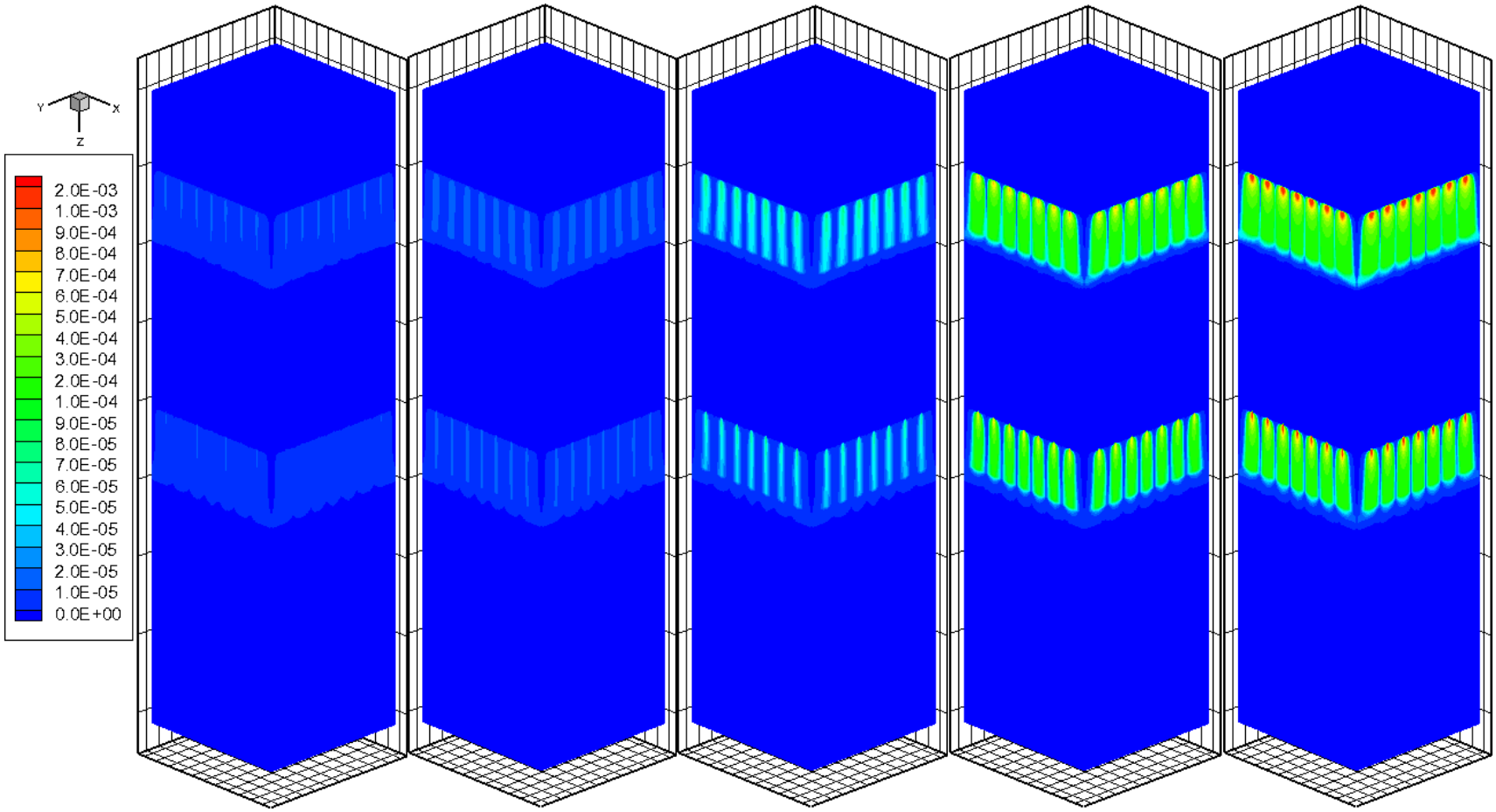

Figure 4.11 Distribution of Charge Density in a Square Channel with a Two-Stage EHD Gas Pump (0.5-inch Wide Grounded Electrode at the Top Stage)

V_o = 20 kV, (b) V_o = 22 kV, (c) V_o = 24 kV, (d) V_o = 26 kV, (e) V_o = 28 kV.

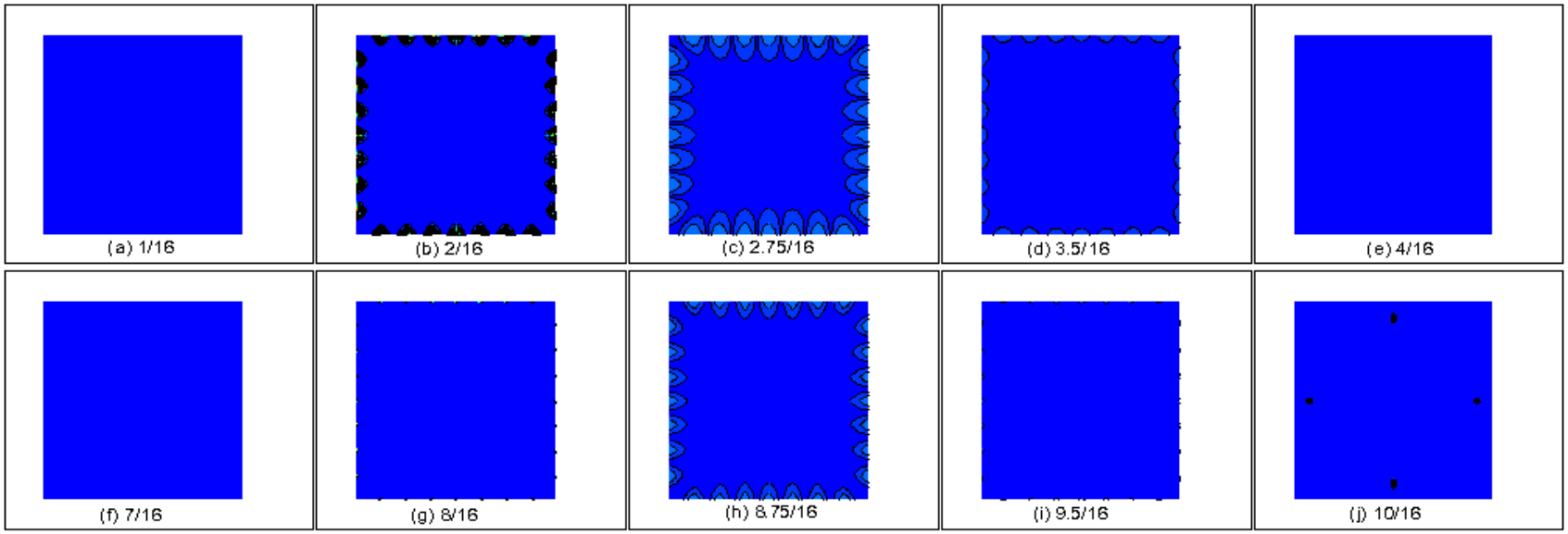

Figure 4.12 Distribution of Charge Density at Various Cross-Sections along the Z-Direction from Top to Bottom for V_o = 28 kV (Unit of Location in Inch).

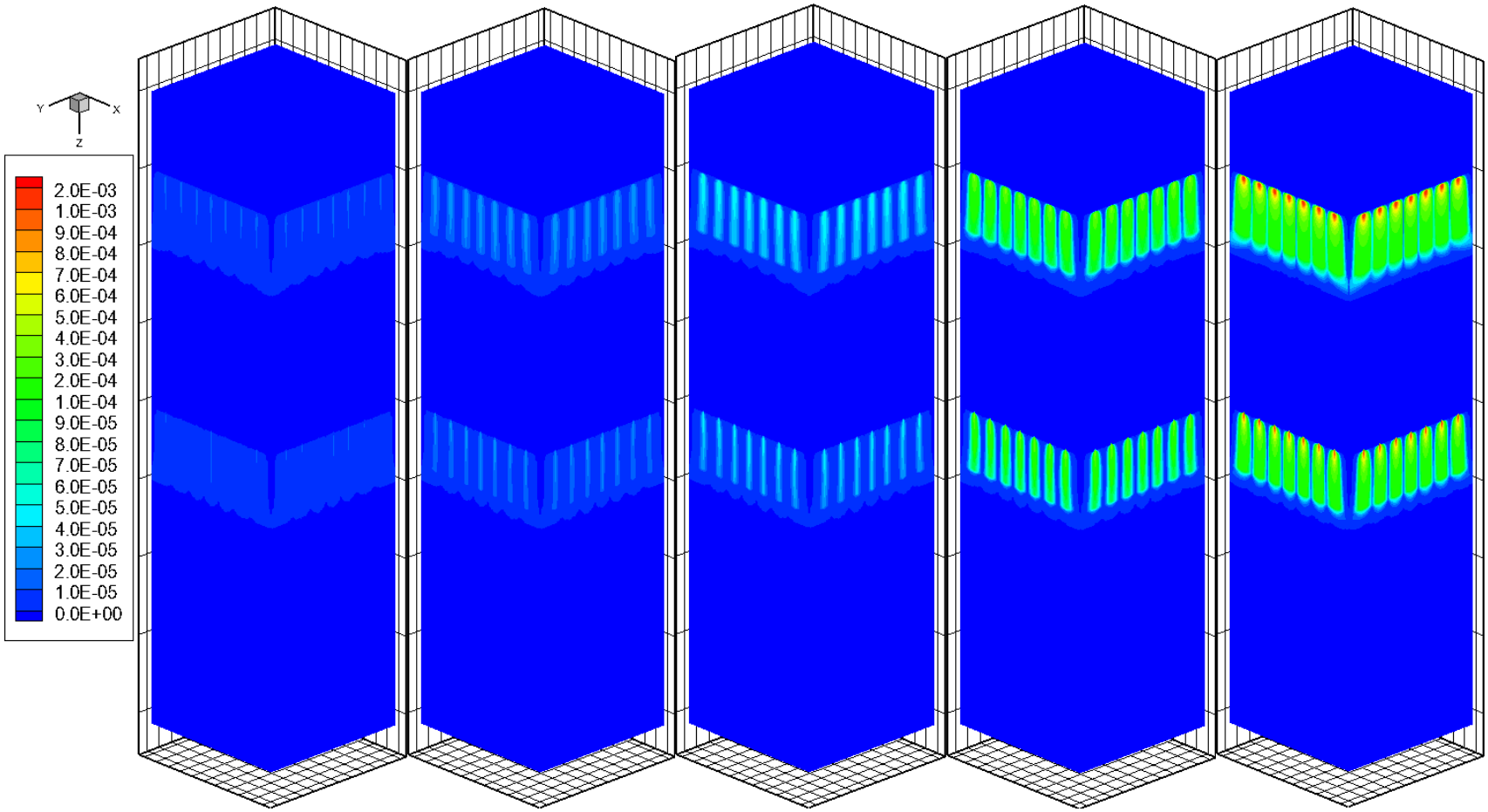

Figure 4.13 Distribution of Charge Denisyt in a Square Channel with a Two-Stage EHD Gas Pump

(1-inch Wide Grounded Electrode at the Top Stage)

(a) V_o = 20 kV, (b) V_o = 22 kV, (c) V_o = 24 kV, (d) V_o = 26 kV, (e) V_o = 28 kV.

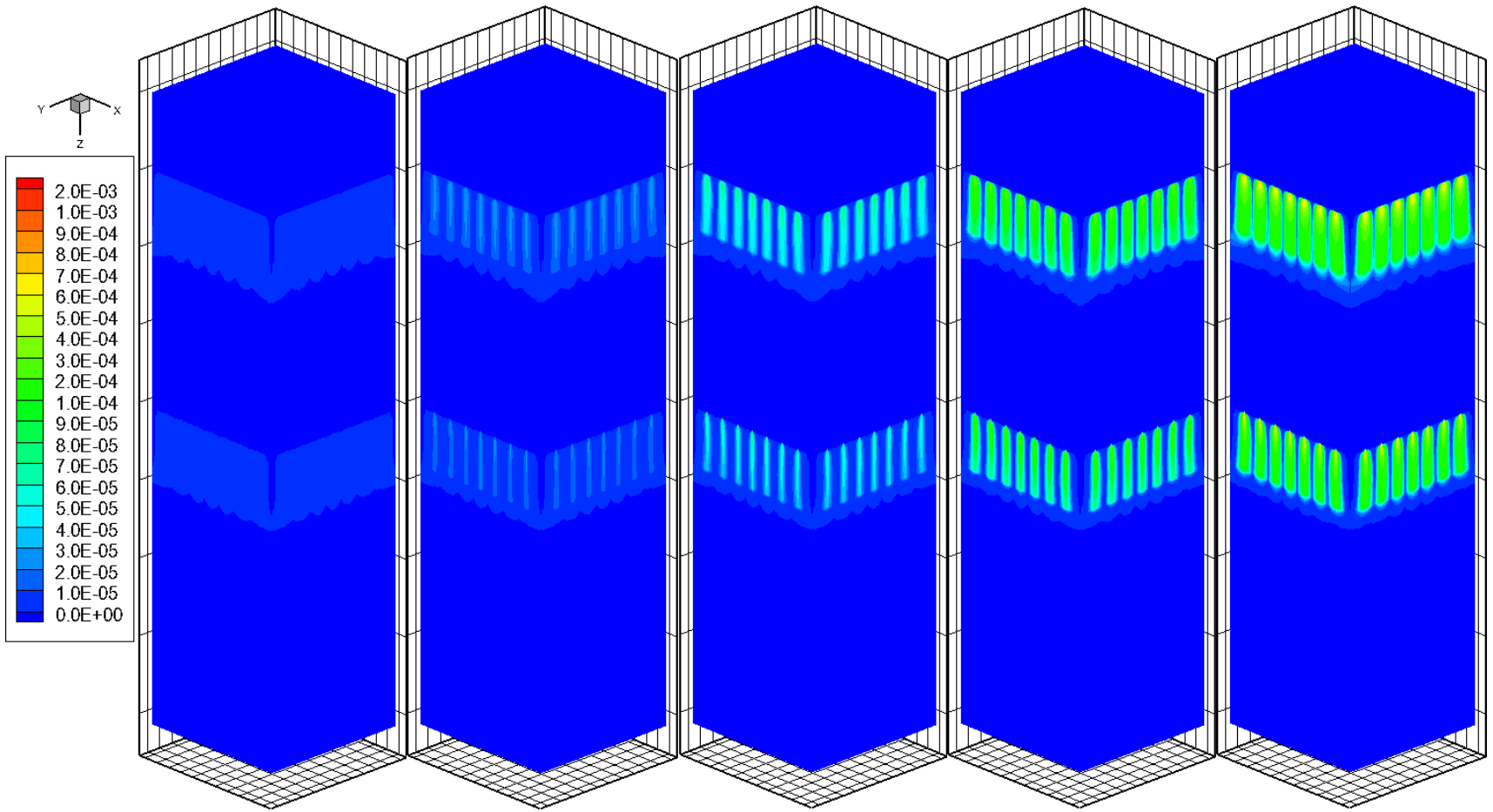

Figure 4.14 Distribution of Charge Denisyt in a Square Channel with a Two-Stage EHD Gas Pump

(2-inch Wide Grounded Electrode at the Top Stage)

(a) V_o = 20 kV, (b) V_o = 22 kV, (c) V_o = 24 kV, (d) V_o = 26 kV, (e) V_o = 28 kV.

4.2 Flow Field

With the availability of electric potential and space charge density, one can calculate the electric body force and proceed with the numerical simulation of flow field. The results thus obtained are compared with the data collected from experiments that were discussed in Chapter 2. In the following discussion, the experimental results will be presented first, then follow by the numerical results.

4.2.1 Velocity Profile

Figures 4.15 - 4.17 show the velocity profiles inside the square channel with a two-stage EHD gas pump. For the case presented, the grounded plate at both stages is fixed at 0.5 inch wide. The velocity profiles from that of a single-stage unit are also included for comparison. In these figures, the x- axis is oriented along the channel width so that the locations of x = 0 in. and x = 4 in. represent the channel walls. As observed, the induced airflow velocity increases with an increase in the applied voltage. When the applied voltage is low ($V_o \leq 24$ kV), the velocity profile is fairly uniform across the channel. However, when the applied voltage is increased beyond 24 kV, the velocity profile looks like an inverted parabola, which is opposite of that of a fully developed flow inside a channel. This is mainly due to the fact that the emitting electrodes were embedded in the channel wall. The corona wind that they produced behaves like a wall jet, leading to the maximum air velocity occurring near the wall. This feature is more pronounced when the applied voltage is greater than 24 kV. Although one would anticipate a symmetrical velocity profile, the velocity at x = 0.5 in. is actually higher than that at x = 3.5 in. This asymmetric velocity profile is caused by

the presence of the velocity measuring probe, which might have blocked and modified the flow. Despite of some distortion, one can observe that a two-stage EHD gas pump generally produces a higher air velocity than that of a single-stage inside the channel. It also appears that the air velocity increase as the flow moves downstream the channel (Figs. 4.15 and 4.17), which indicates that the corona-induced flow requires some distance from the emitting pin to reach its full strength. The highest velocity obtained from this configuration is about 1.85 m/s occurring near the wall and 4-inch downstream the grounded plate. Similar features hold for other two configurations, for which the velocity profiles are shown in the Appendix.

It is important to note that the velocity measurements for the present study is quite challenging. The experimental measurements can only provide limited information about the flow field inside the channel with an EHD gas pump. This is because a hot-wire anemometer (an intrusive measuring device) is used for velocity measurements in the experiment with understanding that its intrusion might have adversely disturbed the flow field particularly at region near the wall. Non-intrusive devices such as Laser Doppler Velocimetry (LDV) or Particle Image Velocimetry (PIV), although preferred in most cases, are not ideal in the present experiment as the seeding particles may be charged by the imposing electric field and the velocity reading can be compromised. As such, numerical simulations not only provide velocity data for verification, but also provide means for flow visualization.

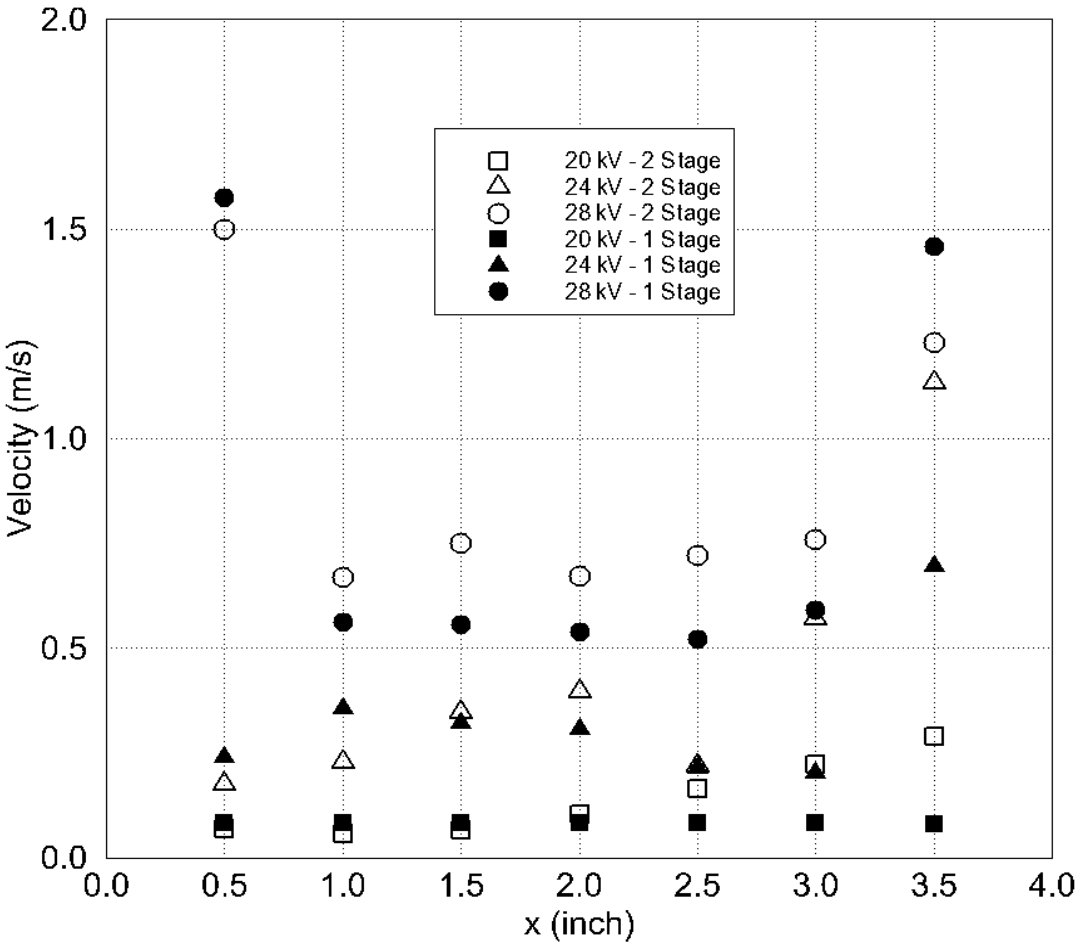

Figure 4.15 Comparison of Velocity Profiles inside the Channel at 1-inch Downstream from the Grounded Electrode of the Bottom Stage.

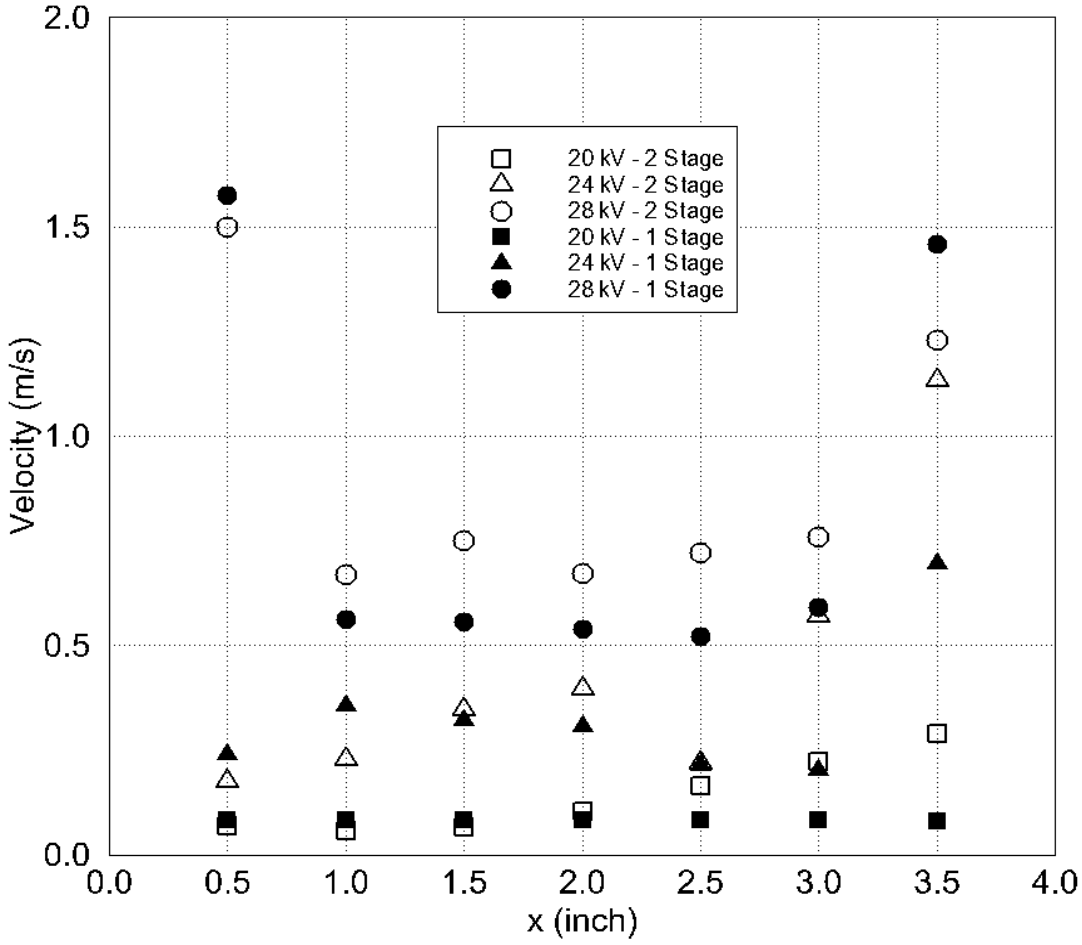

Figure 4.16 Comparison of Velocity Profiles inside the Channel at 2.5-inch Downstream from the Grounded Electrode of the Bottom Stage.

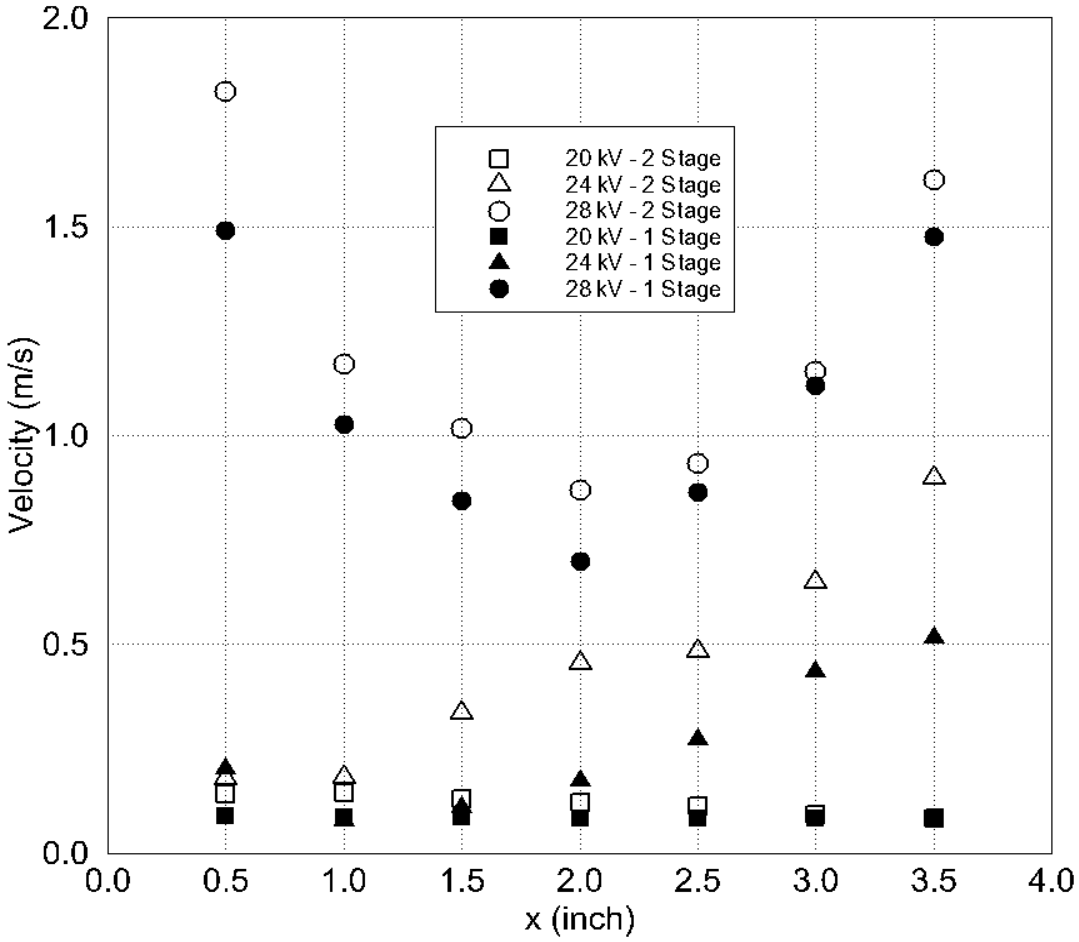

Figure 4.17 Comparison of Velocity Profiles inside the Channel at 4-inch Downstream from the Grounded Electrode of the Bottom Stage.

To better understand the flow characteristics, one can take advantage of the results obtained from numerical simulations. Through visualization of these numerical results, one may get a better insight to the flow field inside the channel. Figure 4.18 illustrates the flow field induced by a two-stage EHD gas pump with 0.5-inch wide grounded electrode at both top and bottom stages. This is presented in the form of velocity contours at the cross-section of the mid-plane of the channel (x = 2 in.). For the ease of examination, the velocity contours are presented using different increment for different applied voltage. The velocity contours for a lower applied voltage (20 and 22 kV) are plotted with an increment of 0.0001 m/s. For the applied voltage at 24 kV, they are plotted with an increment of 0.05 m/s and for a higher applied voltage (26 and 28 kV) they are 0.5 m/s. When the applied voltage is less than 24 kV, it is observed that corona-induced flow is very weak. It is only when the applied voltage is increased beyond 24 kV ($V_o \geq 24$ kV) that the flow becomes noticeable. One observes that it is initiated from the electrode tips and develops downwards (Fig. 4.18(c) - (e)). It is also observed that the high-velocity stream slightly turned away from the channel walls, which can clearly be observed from Fig. 4.18 (c). When the applied voltage is further increased ($V_o \geq 26$ kV), the induced flow not only develops further downstream but also expands towards the center of the channel. For a higher applied voltage, the velocity gradient near the electrode tips becomes much greater. In addition, Figure 4.18 (d) clearly shows an inverted parabolic velocity profile with the maximum velocity close to the channel walls, which has been observed from the experimental data (Figs. 4.15 - 4.17). This flow characteristic can be put to good use for the heat transfer enhancement.

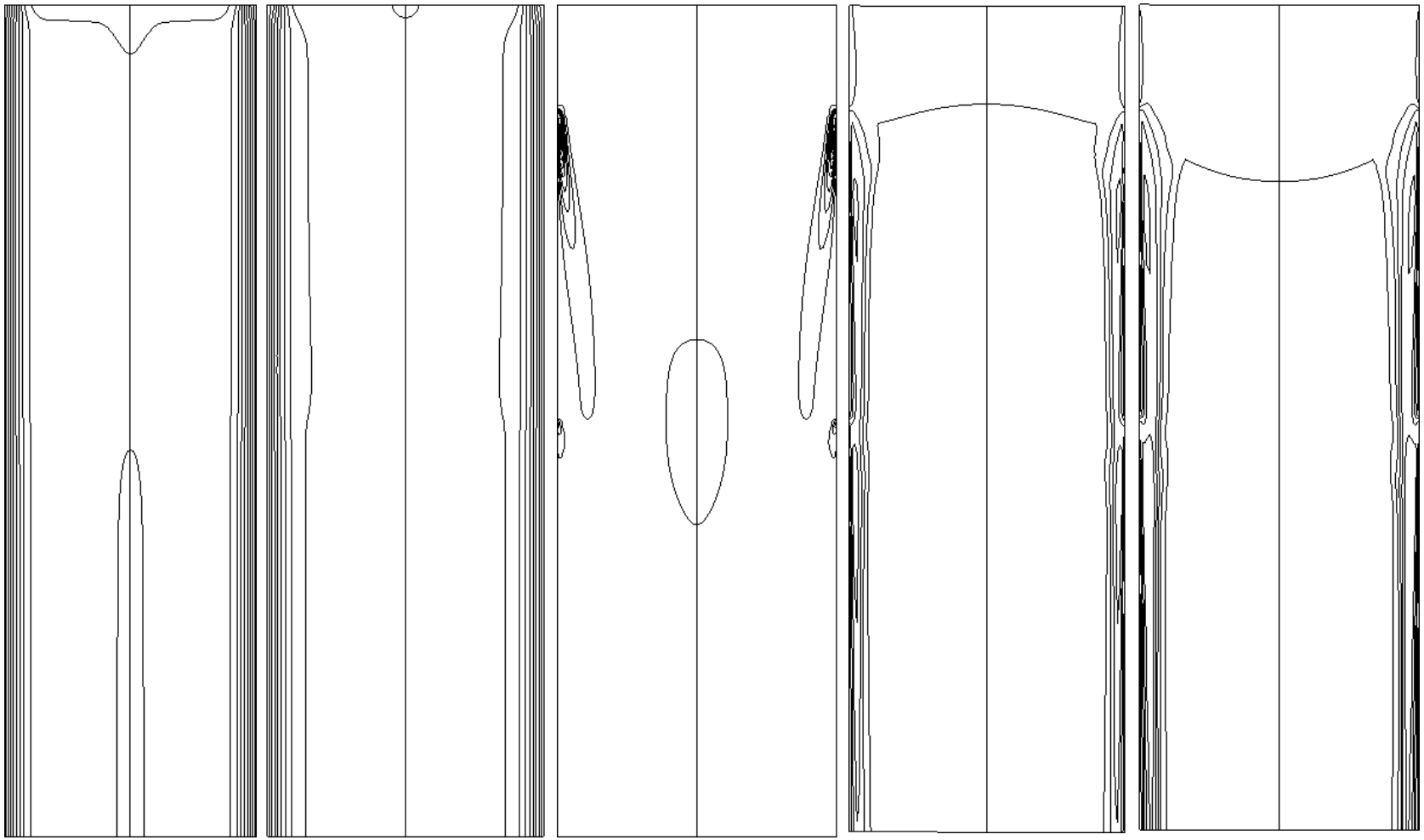

Figure 4.18 EHD-induced Flow Field (x = ½), (a) V_o=20 kV (Δw = 0.0001 m/s), (b) V_o=22 kV (Δw = 0.0001 m/s), (c) V_o=24 kV (Δw = 0.05 m/s), (d) V_o=26 kV (Δw = 0. 5 m/s), (e) V_o=28 kV (Δw = 0. 5 m/s).

Figures 4.19 - 4.22 illustrates the flow field at various cross-sections along the z-direction from top to bottom of the channel induced by a two-stage EHD gas pump with a 0.5-inch wide grounded electrode at both top and bottom stages. In these figures, cross-section (a) is located at the level of the electrode wire loop (z = 1/16) of the top stage. Cross-section (b) is leveled with the electrode tips (z=2/16) of the top stage. Cross-section (c) is located mid-way between the electrode tips and the grounded electrode (z = 2.75/16) of the top stage. Cross-section (d) aligns with the upper edge of the grounded electrode (z = 3.5/16) of the top stage. Cross-section (e) aligns with the lower edge of the grounded electrode (z = 4/16) of the top stage. The spacing between the electrode wire loop of the top and the bottom stage is six inches. That's why cross-sections (f), (g), (h), (i), and (j) are located at the same level in the bottom stage respectively with those of (a), (b), (c), (d) and (e), but six inches apart from the top stage. Two-dimensional rendering of the velocity contours are shown at each cross-sectional level. The magnitude of the velocity can be identified from the color scale shown in the legend.

For all applied voltages, the velocity is in the range between 0 and 3 m/s and the contour is thus plotted with a constant increment of 0.2 m/s. For all applied voltages, it is observed that velocity is rather uniform at the electrode wire loop level. For a lower applied voltage (20 kV), the flow is so weak that one cannot actually visualize it and distinguish the contour at different levels as they are all in same range. The flow development is much faster at a higher applied voltage (Figs. 4.21 and 4.22) than that at a lower applied voltage (Fig. 4.19). Corona wind becomes more visible downstream the channel as seen from the cross-section at the electrode wire tips (Figs. 4.21 (b) and 4.22

(b)). Although the highest charge density occurs at the wire tips, the maximum velocity occurs below the wire tips, which is consistent with the observation from experiments.

As observed, for a higher applied voltage, velocity starts to increase from the wire loop of the top stage. It has a higher value near the wall where the electrodes locate than anywhere else in the channel (Figs. 4.21 (b) and 4.22 (b)). Particularly, velocity peaks at the tip of electrode while the rest of the channel remains relatively calm. The velocity decreases slightly after it passes through the grounded plate of the top stage (Figs. 4.21 (f) - (g) and 4.22 (f) - (g)), but quickly recovers when it enters the section where the bottom stage electrode locates (Figs. 4.21 (h) - (j) and 4.22 (h) - (j)).

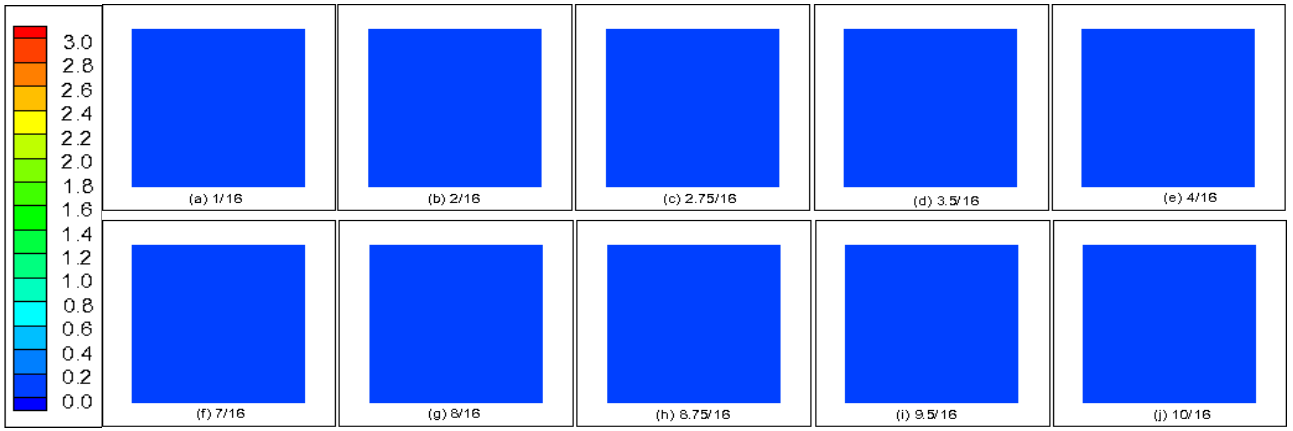

Figure 4.19 Velocity Contours at Various Cross-Sections along the Z-Direction for V_o = 20 kV (Unit of Velocity in m/s and Unit of Location in Inch).

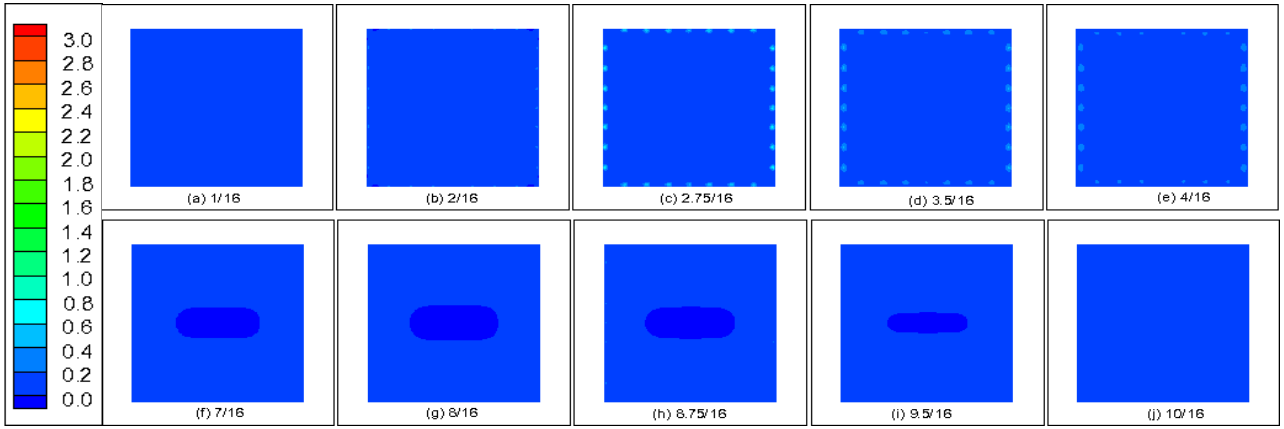

Figure 4.20 Velocity Contours at Various Cross-Sections along the Z-Direction for V_o = 24 kV (Unit of Velocity in m/s and Unit of Location in Inch).

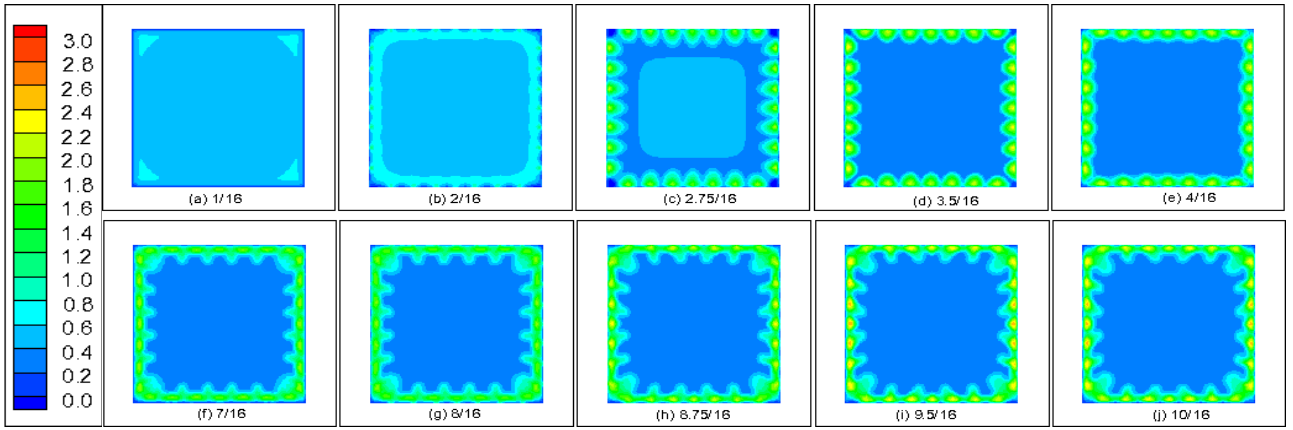

Figure 4.21 Velocity Contours at Various Cross-Sections along the Z-Direction for V_o = 26 kV (Unit of Velocity in m/s and Unit of Location in Inch).

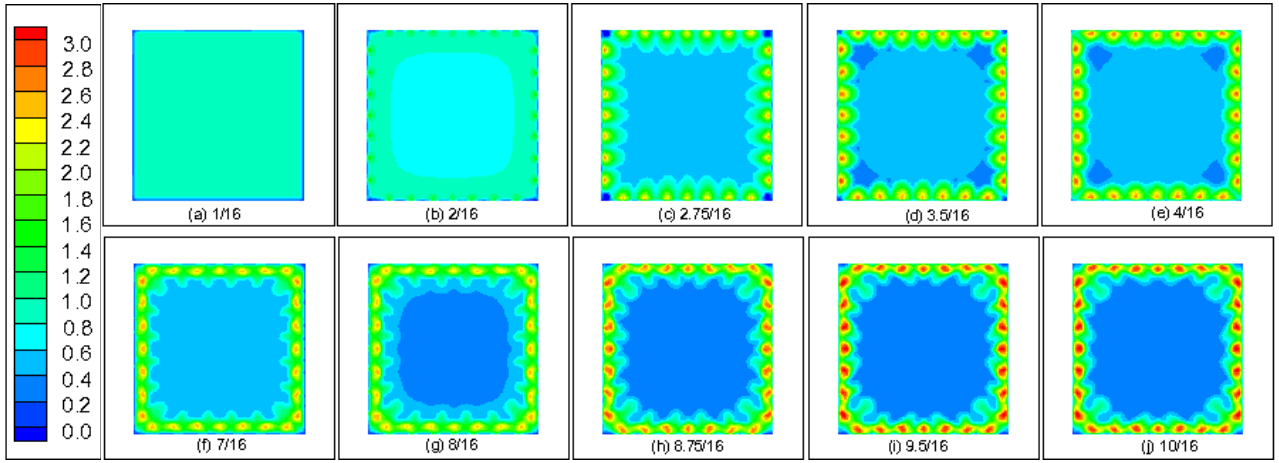

Figure 4.22 Velocity Contours at Various Cross-Sections along the Z-Direction for V_o = 28 kV (Unit of Velocity in m/s and Unit of Location in Inch).

To examine the effect of the size of grounded electrodes at the top stage on the flow field, velocity contours are shown in Fig. 4.23 for an applied voltage of 26kV at the mid-plane of the channel (x = 2 in.). The contours are plotted with a constant increment of 0.5 m/s. As observed, the flow is initiated from the electrode tips and fast approaches downstream. Although the induced flow velocity of all three configurations is in the same range, it is noticed that a slimmer grounded electrode produces a slightly higher velocity, which is also observed from experiment.

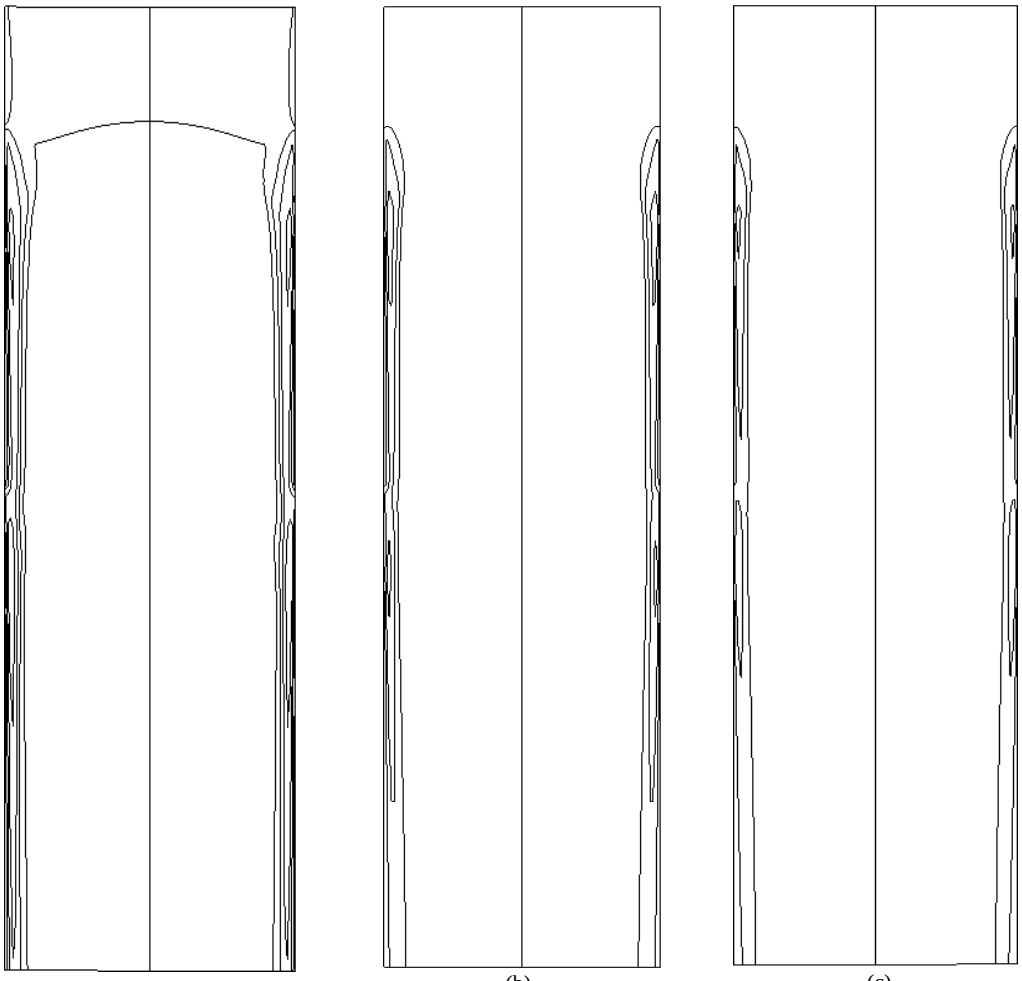

Figure 4.23 Flow Induced by a Two-Stage EHD Gas Pump with Various Sizes of Grounded Electrode at the Top Stage (V_o=26 kV, Δw = 0. 5 m/s), (a) 0.5-in, (b) 1-in, (c) 2-in.

For validation, velocity profiles inside the channel obtained from both experimental measurements and numerical simulations are compared in Figs 4.24-4.26 for a two-stage EHD gas pump with 0.5-inch wide grounded electrode at both stages. One may recall from Chapter 2 that the velocity measurements are made at twenty-one points at each cross-section on three different levels, which gives an approximate velocity profile inside the channel. Again, the x- axis in the figures marks the distance along the channel width, thus x = 0 and x = 4 referring to the channel walls.

As seen from Fig. 4.24, the velocity profile is rather uniform at a lower applied voltage (V_o = 20 and 22 kV) and there is fairy good agreement between the experimental results and numerical simulations. As the applied voltage increases to 24 kV, the velocity profiles are still uniform across the channel. The profile obtained from the numerical simulation is still in good agreement with the experimental data except for the symmetry. As discussed earlier, experimental data does not show the symmetric nature due to the intrusive measurement method used. Because of the insertion of the velocity probe, it may adversely increase the flow velocity toward the other side of the wall. When the applied voltage is further increased to 26 and 28 kV, there are discrepancies between the experimental results and numerical simulations. Although both results show a similar trend of an inverted parabolic profile, the numerical results predict a much steeper velocity profile near the walls and a more uniform velocity at the channel core region. The discrepancy in the velocity profile obtained from these two results becomes large when the applied voltage increases. However, both results reveal that corona wind issued from the electrode pins behaves like a wall jet, which can be

put to a good use in the control of boundary layer development especially in the aerospace applications to reduce the drag.

The comparison of velocity profiles obtained from experimental measurements and numerical simulations for the other two configurations are summarized and included in Appendix. Basically they show the same features as one observes for the case discussed above.

The velocity profiles obtained from the two studies at an applied voltage of 26 kV are presented in Figs. 4.27 and 4.28 for cross examination. The velocity profiles obtained from the numerical simulations only show slight variation when the flow moves downstream of the Channel, but a larger difference is observed in the velocity profiles obtained from the experimental study. Experimental results suggest that the induced flow requires some distance downstream of the grounded electrode to reach its full strength. Same as previous observation, numerical results tend to under-predict the velocities of induced flows. The comparisons of velocity profiles for the other two configurations, 1-inch and 2-inch wide grounded electrode at the top stage, show a similar trend and they are included in Appendix for reference.

Another cross examination can be made with the velocity profiles shown in Fig. 4.28 for a two-stage EHD gas pump with various size of the grounded electrode at the top stage. As observed, numerical simulations show that a slimmer grounded electrode induces flow with a higher velocity. However, the experimental data collected at this cross-section do not show a clear trend. As discussed earlier, induced flows observed in the experiment require some distance to become fully developed. Thus, the trend is better observed at the cross-section further downstream of channel (for example, at 4-

inch downstream of the grounded electrode). The comparisons of velocity profiles at the other two cross-sections are included in the Appendix for reference and completeness.

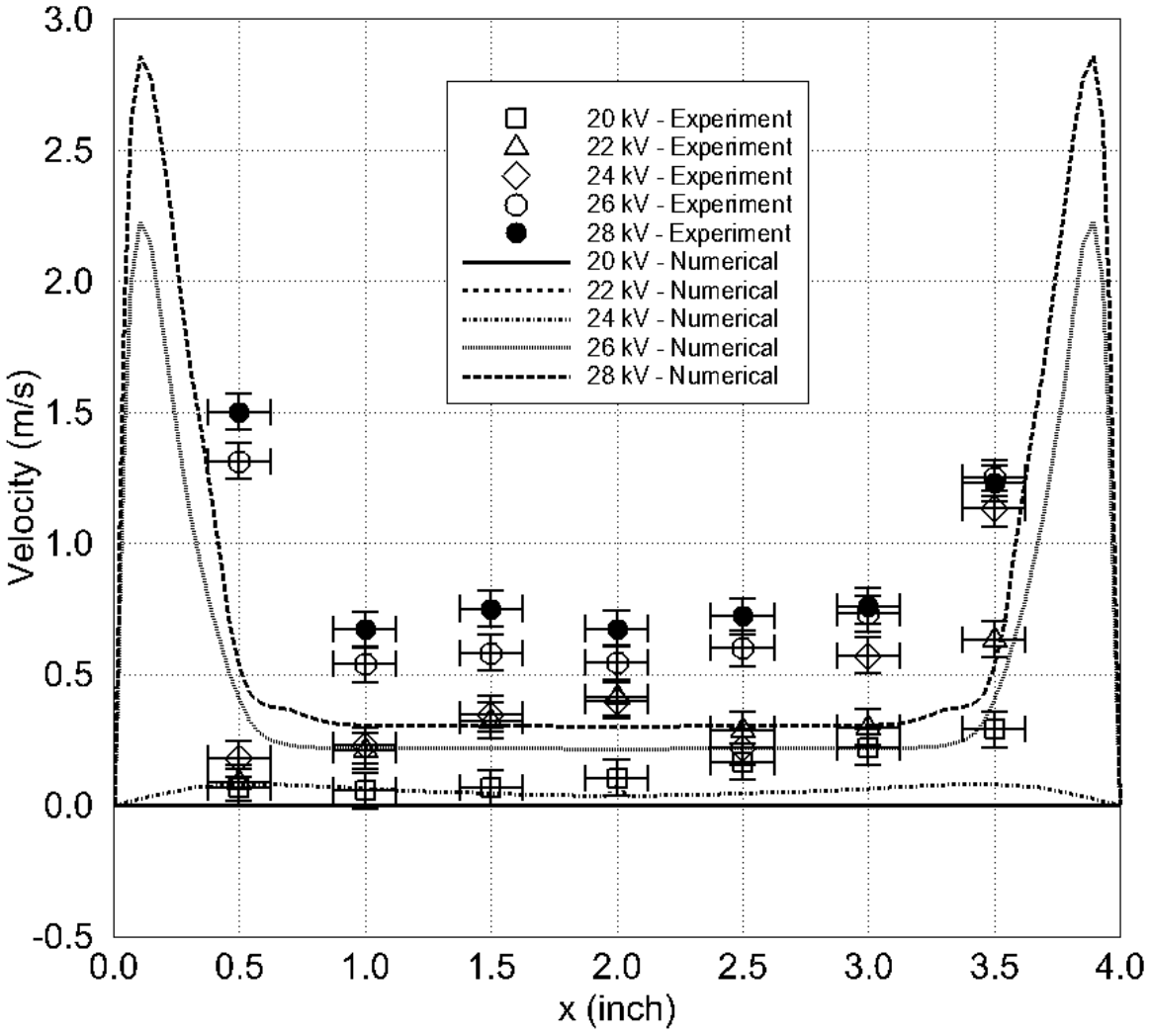

Figure 4.24 Comparison of Velocity Profiles inside the Channel at 1-inch Downstream from the Grounded Electrode of the Bottom Stage.

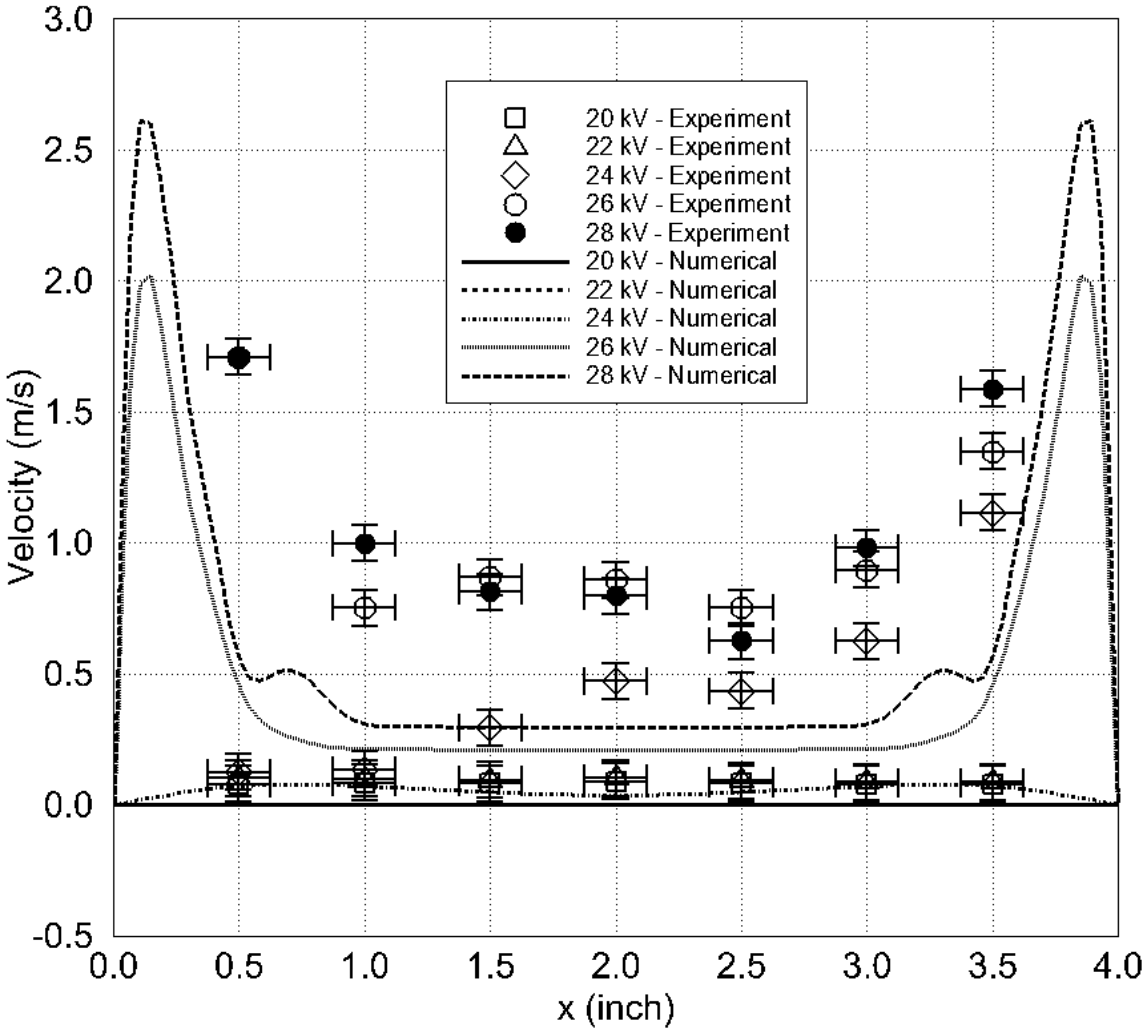

Figure 4.25Comparison of Velocity Profiles inside the Channel at 2.5-inch Downstream from the Grounded Electrode of the Bottom Stage.

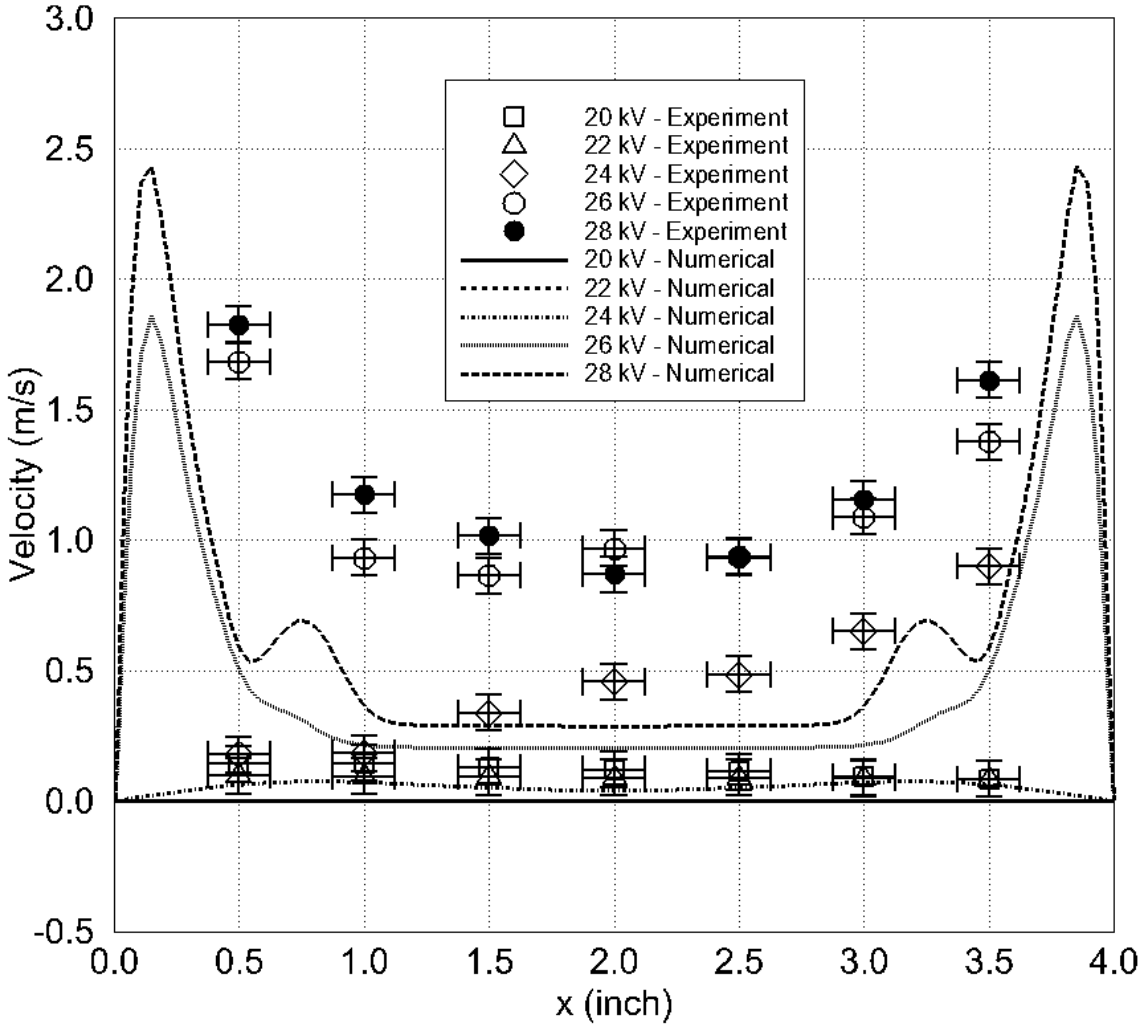

Figure 4.26 Comparison of Velocity Profiles inside the Channel at 4-inch Downstream from the Grounded Electrode of the Bottom Stage.

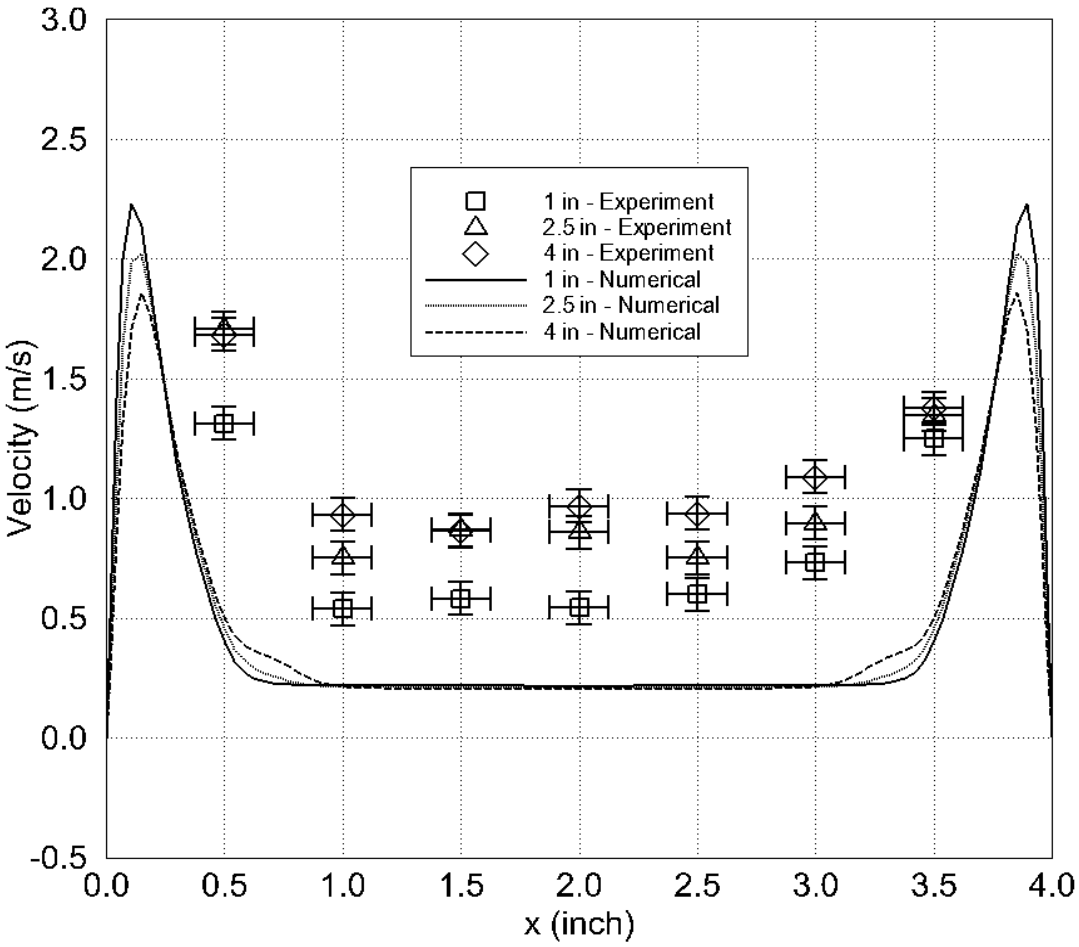

Figure 4.27 Comparison of Velocity Profiles inside the Channel, V_o = 26 kV (for an EHD Gas Pump with 0.5 inch Wide Grounded Plate at Both Stages).

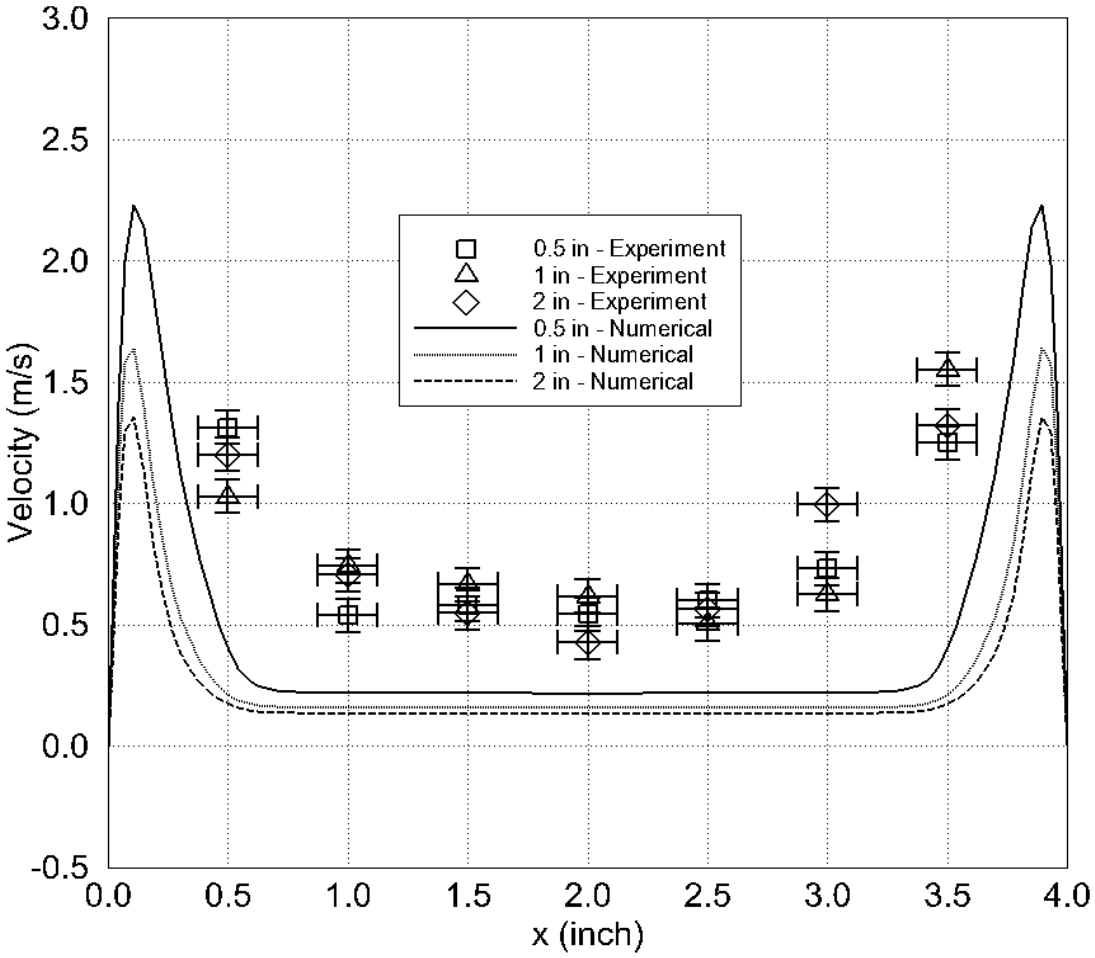

Figure 4.28 Comparison of Velocity Profiles inside the Channel at 1-inch Downstream from the Grounded Electrode of the Bottom Stage, V_o = 26 kV (for a Two-Stage EHD Gas Pump with Various Size of the Grounded Plate at the Top Stage).

4.2.2 Volume Flow Rate

With the availability of velocity data, the volume flow rate of the induced flow can be calculated using the area-weighted integration. The volume flow rates produced by a two-stage EHD gas pump are shown in Figs. 4.29-4.31 as a function of applied voltage. The volume flow rates produced by a single-stage EHD gas pump are also included for comparison. For all three configurations considered, one observes that the volume flow rate of induced air increases with an increase in the applied voltage. In general, the volume flow rate increases as the flow moves downstream from the grounded electrodes as it entrains more air from the ambient. Also observed is that a two-stage EHD gas pump delivers a larger volume flow rate than that of a single-stage one. This trend is most obvious at a higher applied voltage and at a distance further away from the grounded electrode. However, at a lower applied voltage and at a distance closer to the grounded electrode, a single-stage EHD gas pump may appear to outperform that of a two-stage. This is mainly due to the fact that the flow induced by a two-stage EHD gas pump requires a longer distance to fully establish itself as one observes from the velocity profiles shown in Figs. 4.15-4.17. It is also interesting to note that a two-stage EHD gas pump with a slimmer grounded electrode tends to produce more flow than those with a wider grounded electrode. The maximum volume flow rate observed in this study is 12.5 L/s produced by the configuration with 0.5-inch wide grounded electrode at both top and bottom stages at an applied voltage of 28 kV. Thus, it is speculated that there may exist an optimal size of grounded electrode for an EHD gas pump to produce the maximum volume flow rate of air at a given voltage.

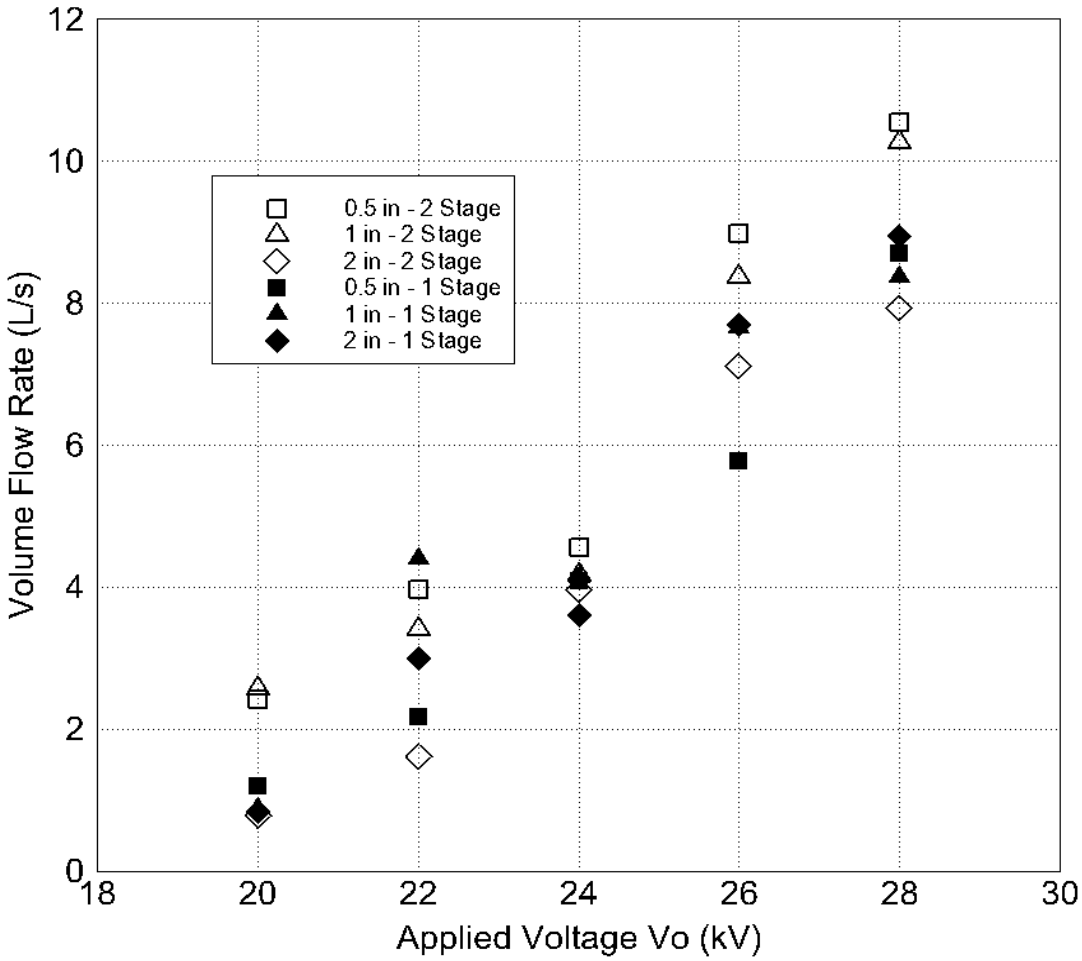

Figure 4.29 Comparison of Volume Flow Rates Produced by an EHD Gas Pump at 1-inch Downstream from the Grounded Electrode of the Bottom Stage.

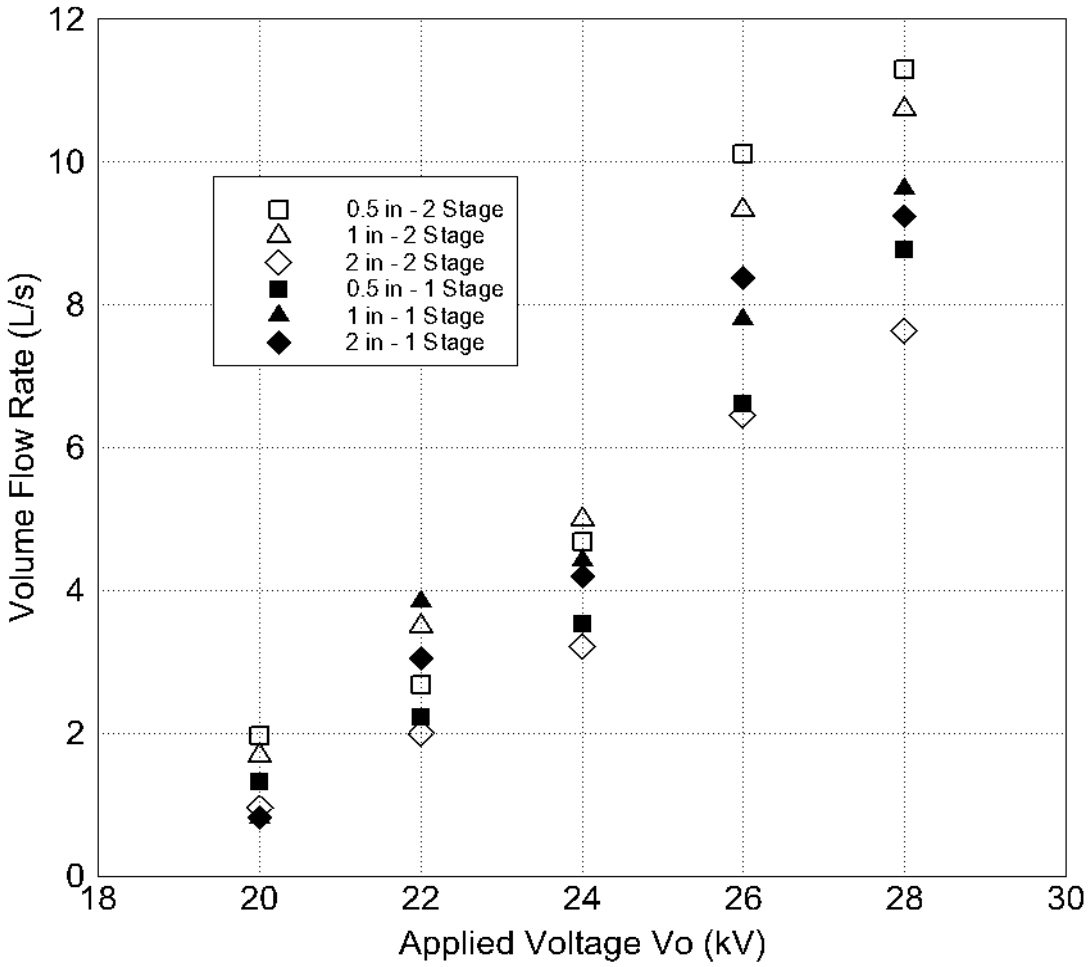

Figure 4.30 Comparison of Volume Flow Rates Produced by an EHD Gas Pump at 2.5-inch Downstream from the Grounded Electrode of the Bottom Stage.

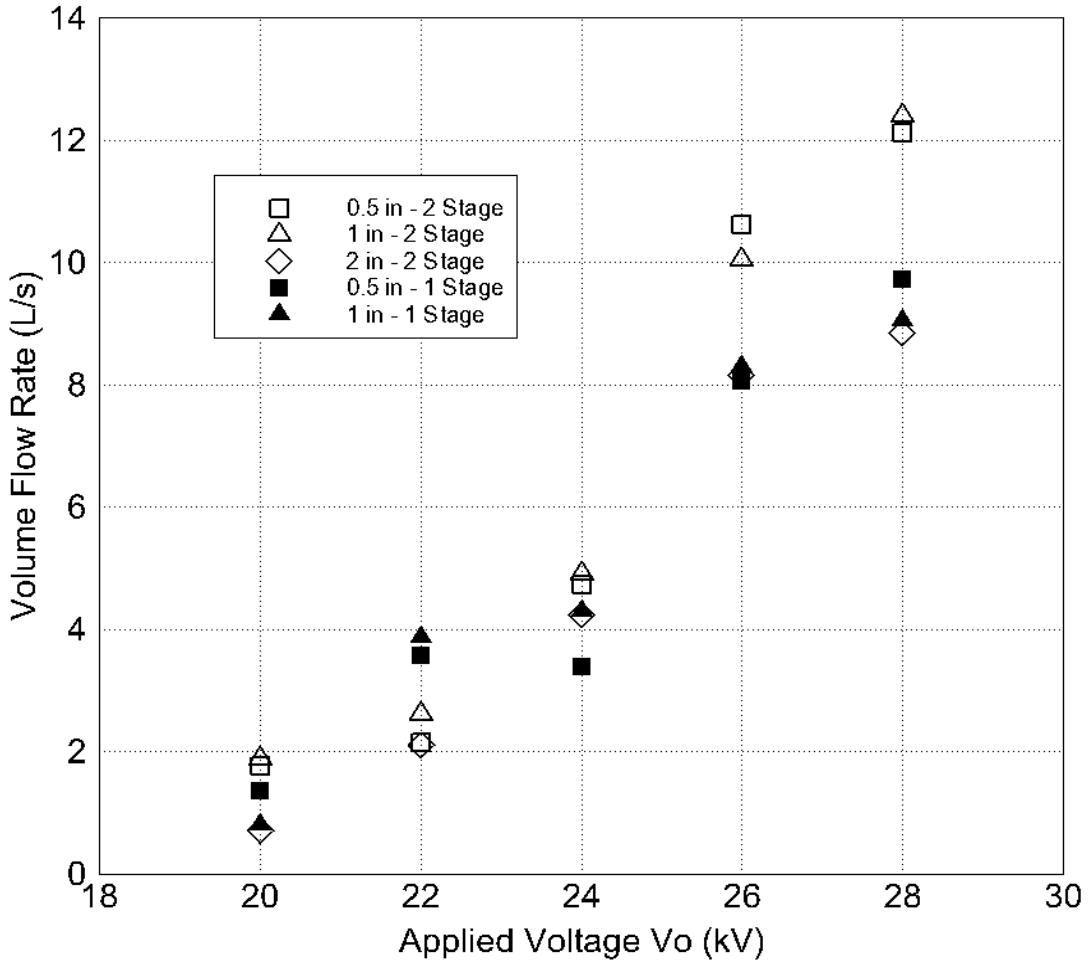

Figure 4.31 Comparison of Volume Flow Rates Produced by an EHD Gas Pump at 4-inch Downstream from the Grounded Electrode of the Bottom Stage.

Figure 4.32-4.34 shows the comparison of volume flow rates obtained from the numerical simulations and experimental results for the three configurations of the EHD gas pump considered. One may recall that in experiments, velocities are measured at twenty-one points in each cross-section on three different levels inside the channel (Fig. 2.7). A representative cross-sectional area is assigned to each velocity measurement point. The volume flow rate is calculated by summing the products of velocity and its assigned representative area for each sampling point. Thus the calculation may underestimate the actual volume flow rate because of the small number of velocity measurement points. In addition, high flow velocities near the wall are not well accounted for. This is especially true for a higher applied voltage.

Since velocities obtained from experiments are usually higher than those of numerical simulations (as seen from previous section), there is no surprise that the resulting volume flow rate calculated from the experimental data is larger than that predicted by the numerical simulations. Despite of the persistent discrepancy between the experimental and numerical results, the trend predicted by these two results is rather consistent. From Fig. 4.32, both results show that a slimmer grounded electrode at the top stage produces a larger volume flow rate, particularly at a higher applied voltage. A wider grounded electrode at the top stage does not have any advantage in producing more flow.

The same trend is preserved at a cross-section 2.5-inch downstream of the grounded plate of the bottom stage (Fig. 4.33). However, the trend becomes blurred at the cross-section further downstream (Fig. 4.34). While numerical simulations still predict a slimmer grounded electrode produces a larger volume flow rate, experimental

results suggest otherwise. The experimental results show that a grounded plate with 1-inch width produces more flow than that of 0.5-inch. However, the difference between them is rather small and is well within the experimental uncertainty. This may be worthy of further examination in the future study.

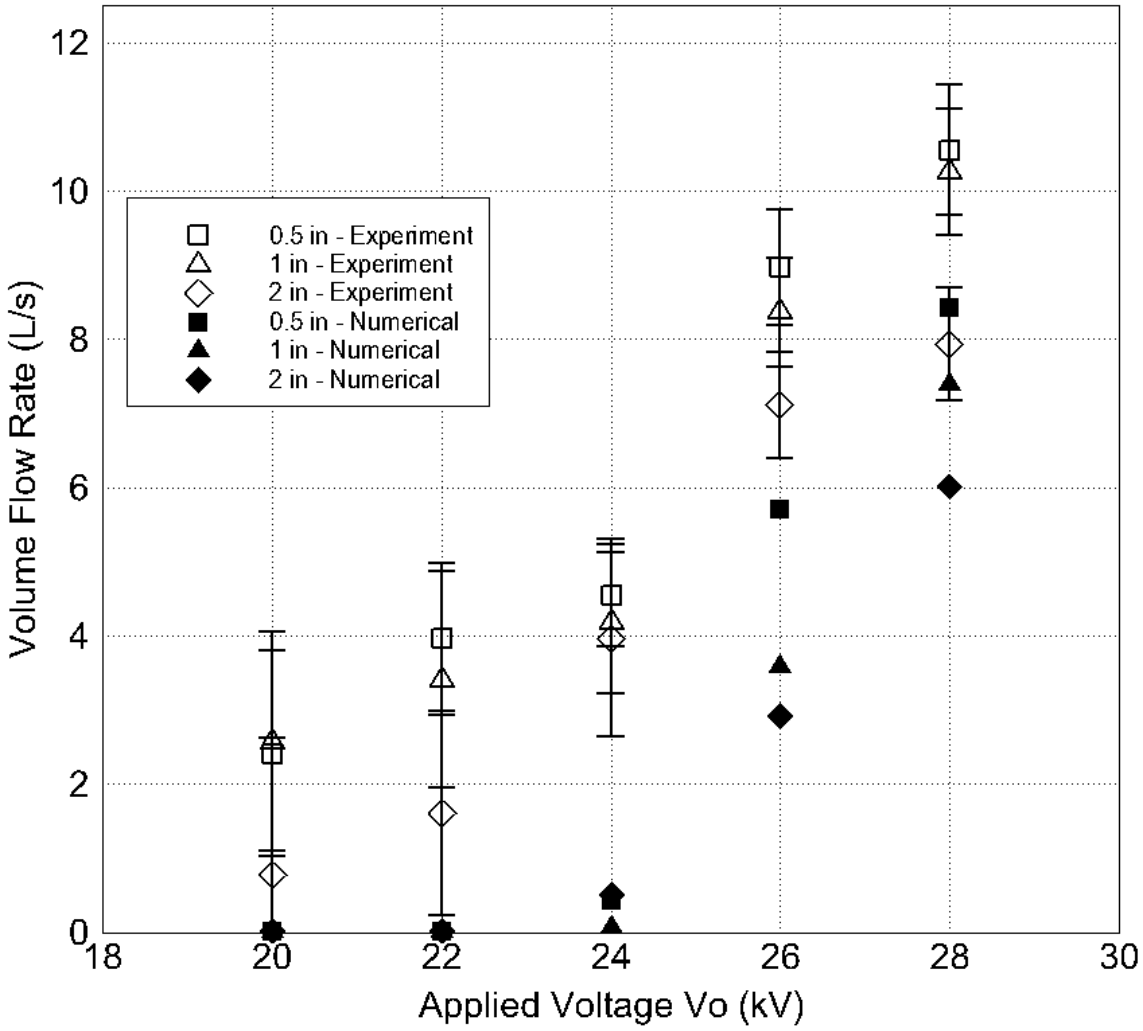

Figure 4.32 Comparison of Volume Flow Rates inside the Channel at 1-inch Downstream from the Grounded Electrode of the Bottom Stage.

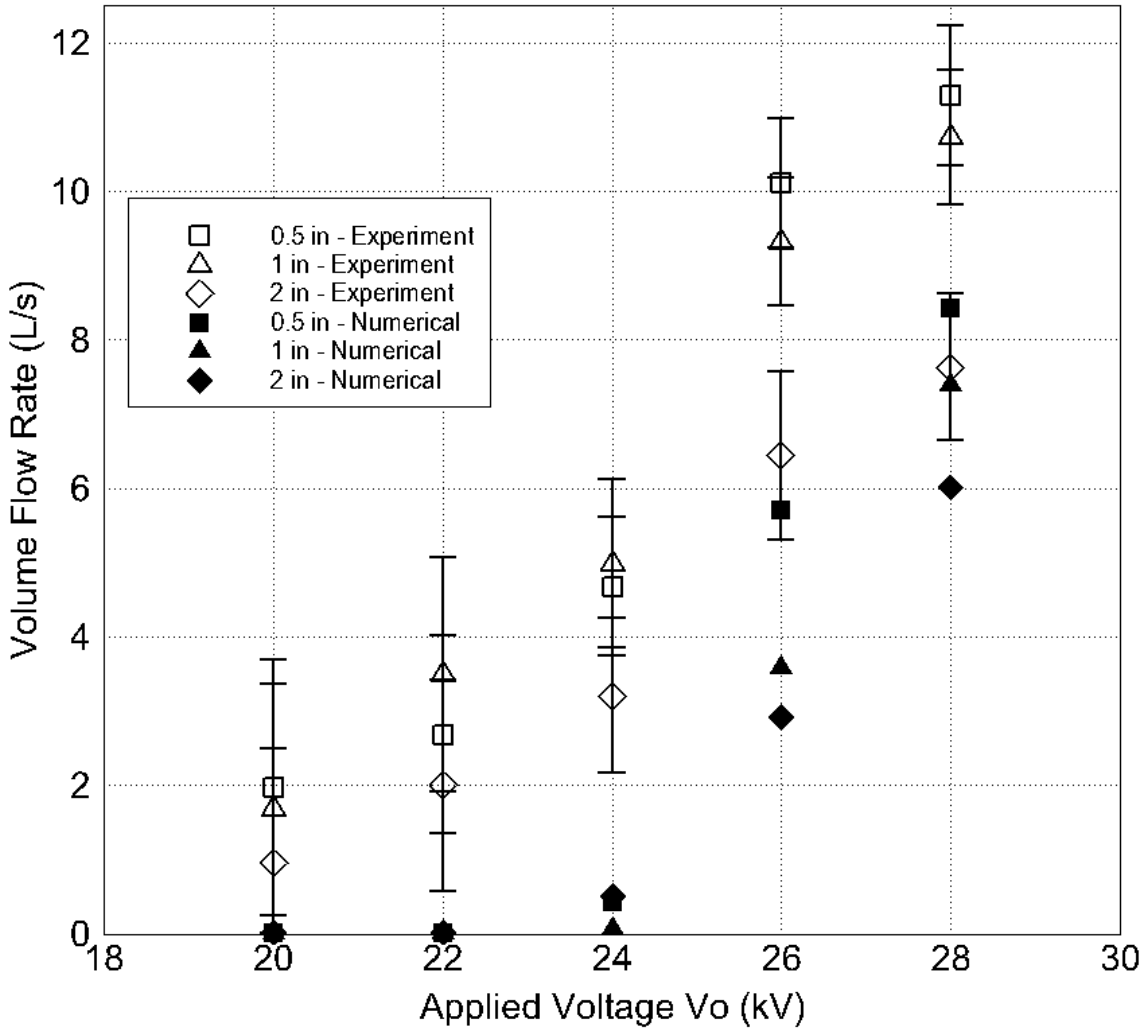

Figure 4.33 Comparison of Volume Flow Rates inside the Channel at 2.5-inch Downstream from the Grounded Electrode of the Bottom Stage.

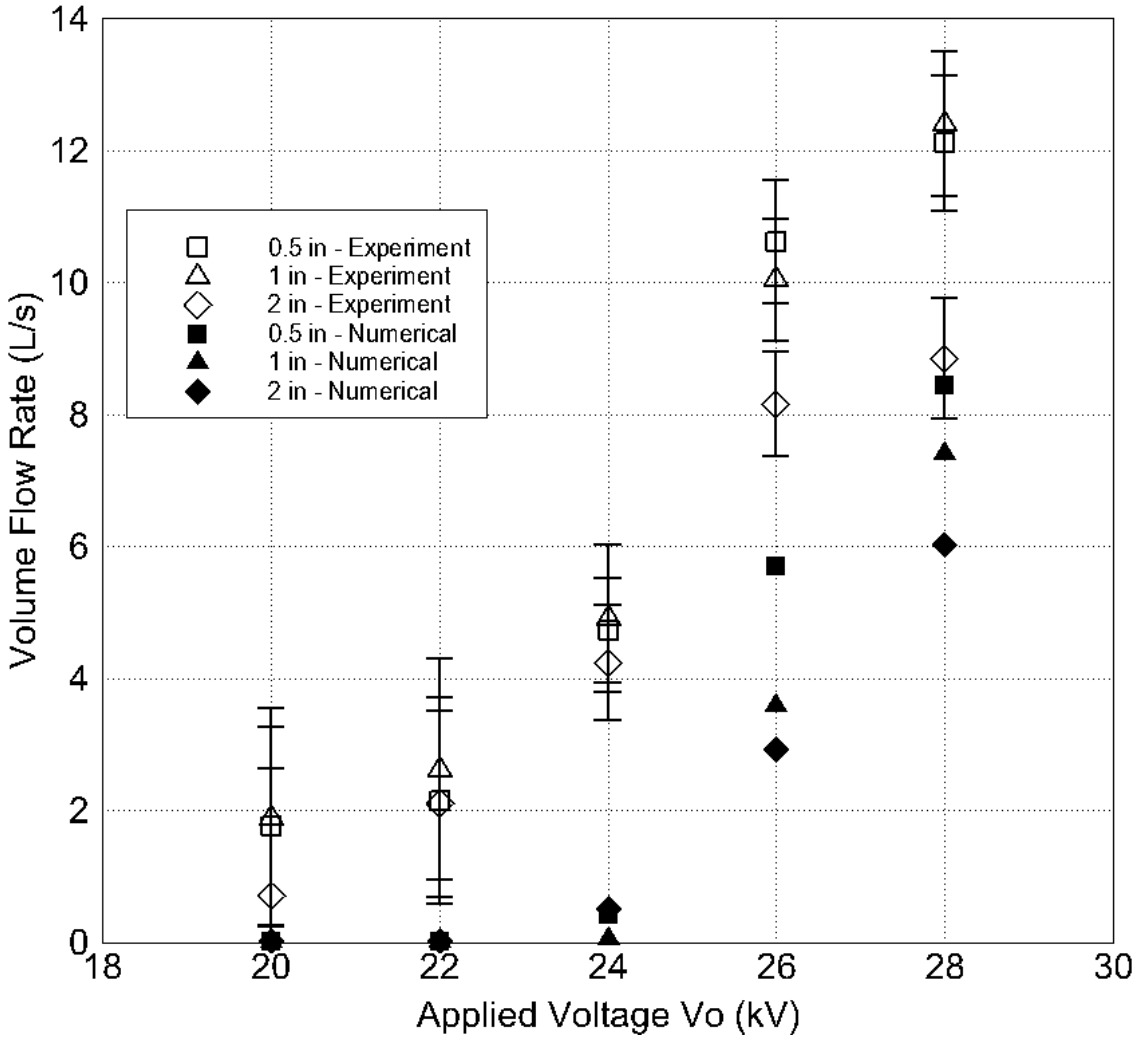

Figure 4.34 Comparison of Volume Flow Rates inside the Channel at 4-inch Downstream from the Grounded Electrode of the Bottom Stage.

4.3 Performance Evaluation

To evaluate the performance of the EHD gas pump proposed, a performance rating is employed, which is defined as the amount of air volume delivered per unit of electric power consumed. The unit for this rating is usually CFM/W (cubic feet per minute per watt) or L/s/W (liters per second per watt).

Figures 4.35-4.37 show the performance of EHD gas pumps as a function of the applied voltage for both two-stage unit and single-stage unit. As observed, the performance of EHD gas pump decreases sharply as the applied voltage increases. The reason for this decrease is mainly due to the increase of required power to deliver the flow, not because of the reduction in volume flow rate. From the figures, one notice that a single-stage EHD gas pump may be more energy-effective than a two-stage one in some operating conditions because it requires a lower electric power to run. But this should not be confused with the volume flow rate. As one has observed, a two-stage EHD gas pump does produce more flow than that of a single stage one with the same electric configurations. The results show that the two-stage EHD gas pump with 1-inch wide grounded electrode at the top stage has a maximum performance rating of 36 L/s/W when operated at an applied voltage of 20 kV.

When comparing with the performance of conventional computer cooling fans which ranges from 1 to 4 L/s/W as reported by Jewell-Larsen et al. (2006) (Table 4.1), one notices that the EHD gas pump clearly outperforms them, particularly at a lower applied voltage. The EHD gas pump examined in the current study appears to be more effective than most conventional fans in terms of its energy usage. In addition, with no

moving parts, the EHD gas pump can offer much quieter operation than the conventional fans.

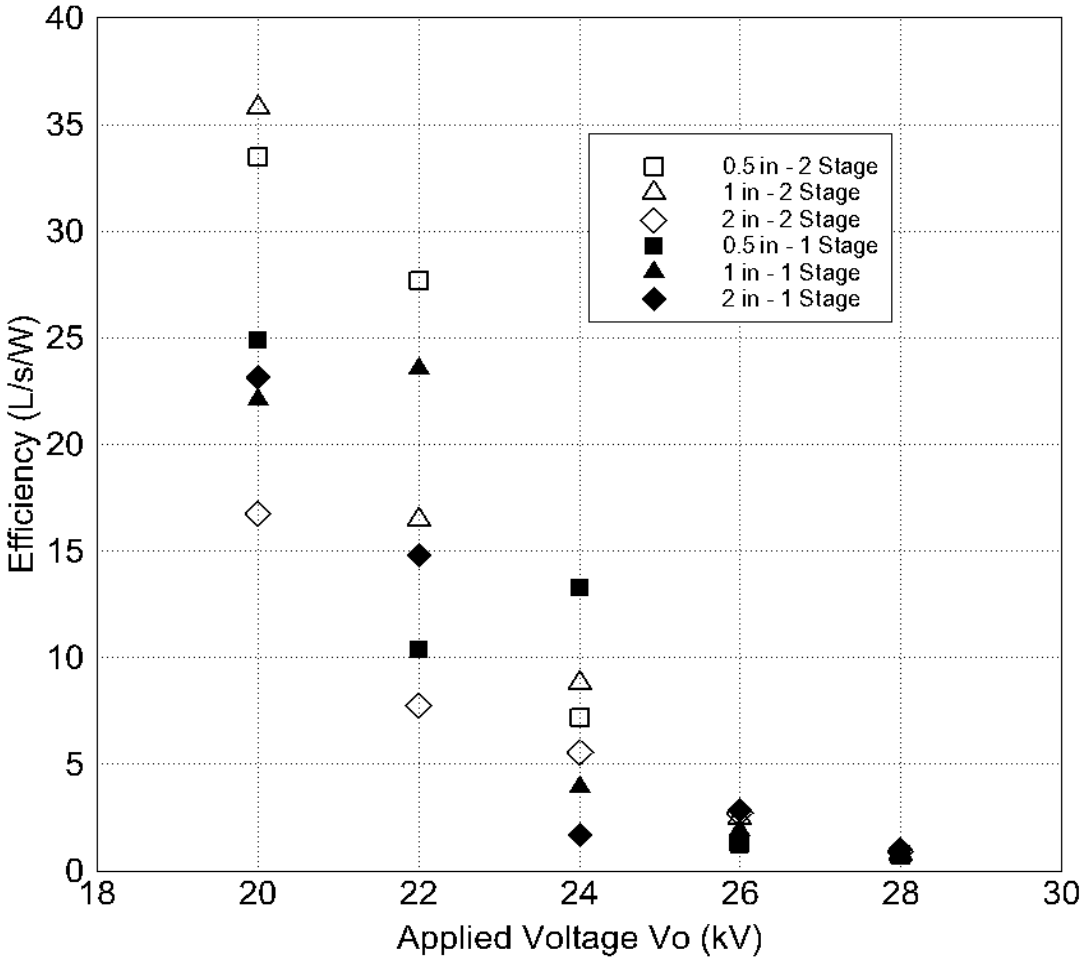

Figure 4.35 Performance of EHD Gas Pump as a Function of Applied Voltage (z = 1 inch).

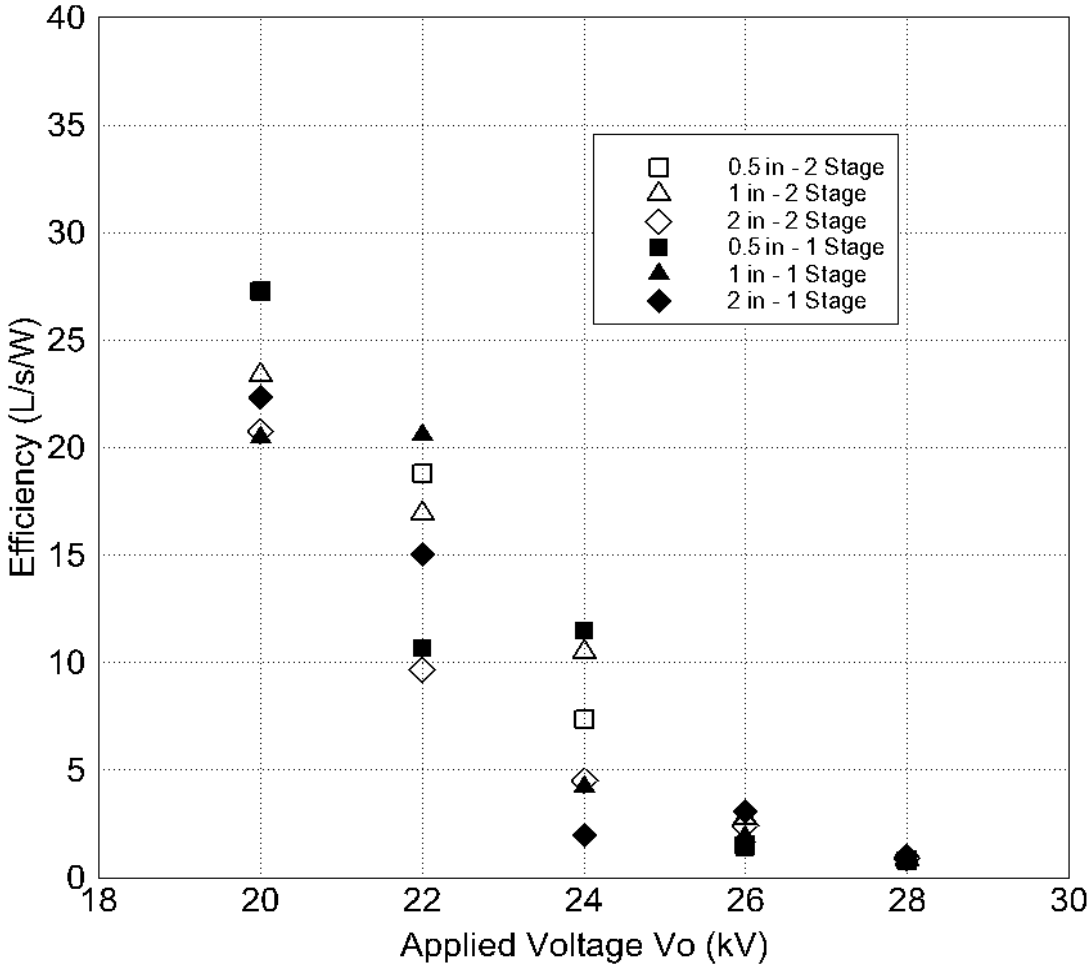

Figure 4.36 Performance of EHD Gas Pump as a Function of Applied Voltage (z = 2.5 inch).

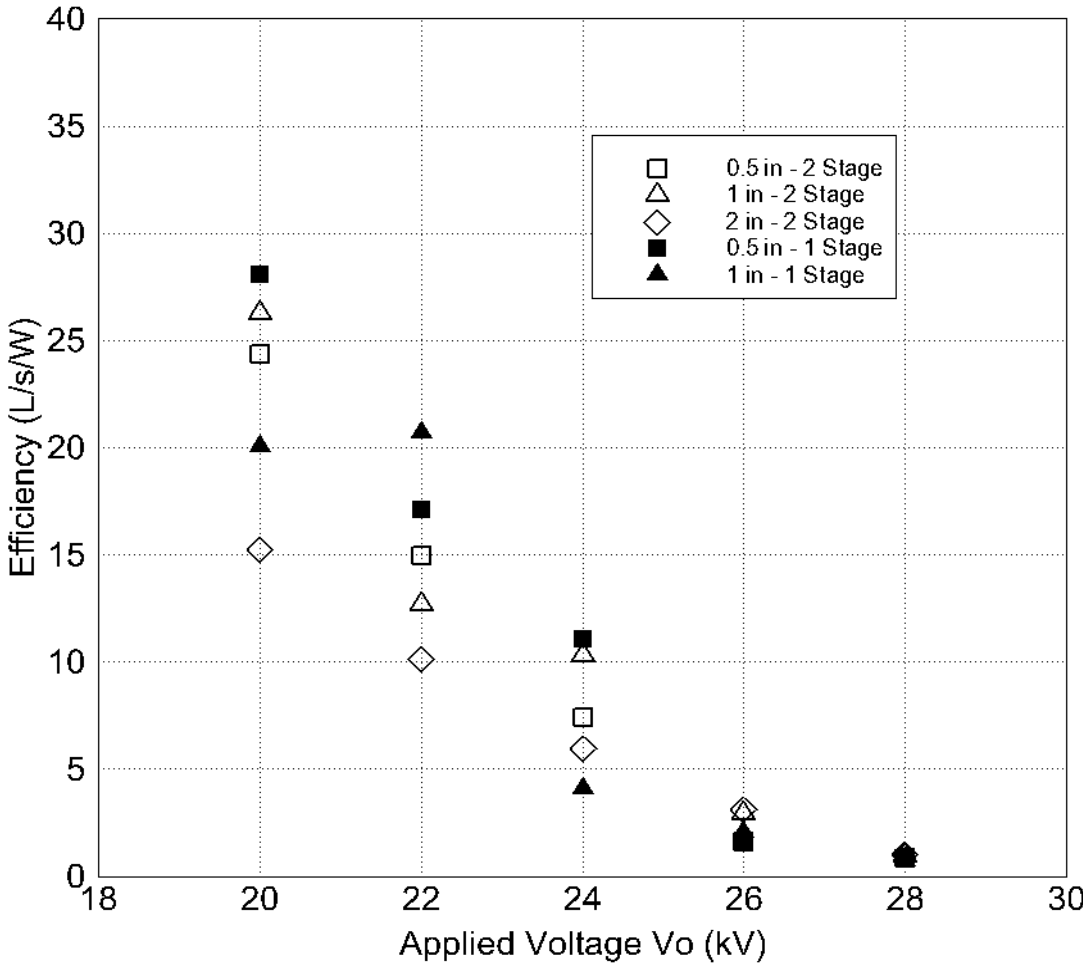

Figure 4.37 Performance of EHD Gas Pump as a Function of Applied Voltage (z = 4 inch).

Table 4.1 Performance of Conventional Cooling Fans for Personal Computer

Pentium CPU fan	Fan Diameter (mm)	Performance (L/s/W)
Pentium II in desktop chassis	40	1.79
Pentium II & III in tower chassis	50	3.15
Pentium III in 1U server chassis	50	3.67
Pentium 4 in 1U server chassis	60	2.31

CHAPTER FIVE

HEAT TRANSFER ENHANCEMENT

To study the effect of corona wind on the heat transfer enhancement, numerical simulations on forced convection are performed with and without the presence of an electric field. The nondimensionlized Navier-Stokes equations along with the energy equation are solved for a wide range of Reynolds numbers. These numerical simulations have been performed for the EHD gas pump with three configurations: 0.5-inch, 1-inch, and 2-inch wide grounded plate at the top stage while the grounded plate at the bottom stage is maintained at 0.5-inch wide. Only positive corona discharge is considered for this simulation.

5.1 EHD-Enhanced Forced Convection

It is found from the literature that the best performance of heat transfer enhancement by EHD occurs in the laminar flow regime. In this study, the range of Reynolds numbers considered varies from 100 to 2000. The Reynolds number is defined based on the hydraulic diameter, which happens to be the channel width for the present case. A dimensionless number, N_{EHD} is used to examine the interactions between the electric and flow fields, which represents the ratio of the electric body force to the flow inertia. In the present study, the EHD number being utilized was proposed by Davidson and Shaughnessy (1986) and it is defined as

$$N_{EHD} = \frac{Id}{\rho u_i^2 bA}, \tag{5.1}$$

where I is the total current, d is the distance between the electrode tip and the grounded plate, and A is the surface area of the grounded plate. When $N_{EHD} \to 0$, the flow inertia is dominant and the air flow is not affected by the corona wind. On the other hand, when $N_{EHD} \to \infty$, the electric body force is dominant and the air flow is modified by the corona wind.

To examine the heat transfer performance, the heat transfer coefficient is calculated by the following equation,

$$h = \frac{q}{T_w - T_m}, \tag{5.2}$$

where T_m is the mean fluid temperature. The temperature difference between the wall and the fluid, $T_w - T_m$, is calculated using the logarithmic mean temperature difference (LMTD), which is defined as following,

$$T_w - T_m = \Delta T_{ln} = \frac{T_i - T_o}{\ln\left[\frac{T_w - T_o}{T_w - T_i}\right]}. \tag{5.3}$$

The heat flux, q, is obtained from Fourier's law by, $q = -k\left.\frac{\partial T}{\partial y}\right|_{y=0}$.

The local Nusselt number is defined by

$$Nu_x = \frac{hD}{k} = \frac{\left(-k\left.\frac{\partial T}{\partial y}\right|_{y=0}\right)\cdot D}{\Delta T_{ln}\cdot k} = -\frac{D}{\Delta T_{ln}}\left(\left.\frac{\partial T}{\partial y}\right|_{y=0}\right), \tag{5.4}$$

where D is the hydraulic diameter. The average Nusselt number is defined in a similar fashion and is given by

$$Nu = -\frac{\ln \theta_o}{1-\theta_o} \cdot \frac{1}{A_s} \iint_{A_s} \left(\frac{\partial \theta}{\partial \bar{y}}\bigg|_{\bar{y}=0} \right) dA_s, \tag{5.5}$$

where A_s is the heat transfer surface area, θ_o is the dimensionless temperature at the outlet, and is given by $\theta_o = \frac{T_w - T_o}{T_w - T_i}$.

To maintain the flow of a forced flow, the pressure drop across the channel is directly related to the power requirement of a fan or pump. The pressure drops for all internal flows are as following,

$$\Delta p = f \frac{L}{D} \frac{\rho u_m^2}{2}, \tag{5.6}$$

where f is the friction factor. In this formula, the pressure drop Δp is defined as $\Delta p = p_i - p_o$, and L is the channel length. In the current study, the friction factor is used to evaluate the power consumption for any given flow and can be calculated by rearranging Eq. (5.6) to give

$$f = \frac{D(\Delta p / L)}{\frac{1}{2}\rho u_m^2}. \tag{5.7}$$

In order to evaluate the effect of the EHD-induced flows, two situations are considered. One is forced convection alone without any electric field applied and the other is forced convection with the presence of electric field. The first case provides the basis of comparison.

Figure 5.1 shows that the Nusselt number increases with an increase in the Reynolds number for forced convection without an electric field. It is important to note that the present channel length is shorter than the thermal entrance length for most

Reynolds numbers considered (Re > 20). For a flow with a lower Reynolds number (Re ≤ 20), both hydrodynamic and thermal entrance lengths are shorter than the channel length, resulting in an average Nusselt number closer to the value of a fully developed flow, which is 2.98 for a channel with a square cross-section (Shah and London, 1978). For flows with a higher Reynolds number, the average Nusselt number can be predicted using the correlation of simultaneously developing flows (Shah and London, 1978), which usually has a heat transfer coefficient higher than that of a fully developed one. It is seen from Fig. 5.1, there is an excellent agreement between the present numerical results and the analytical correlation.

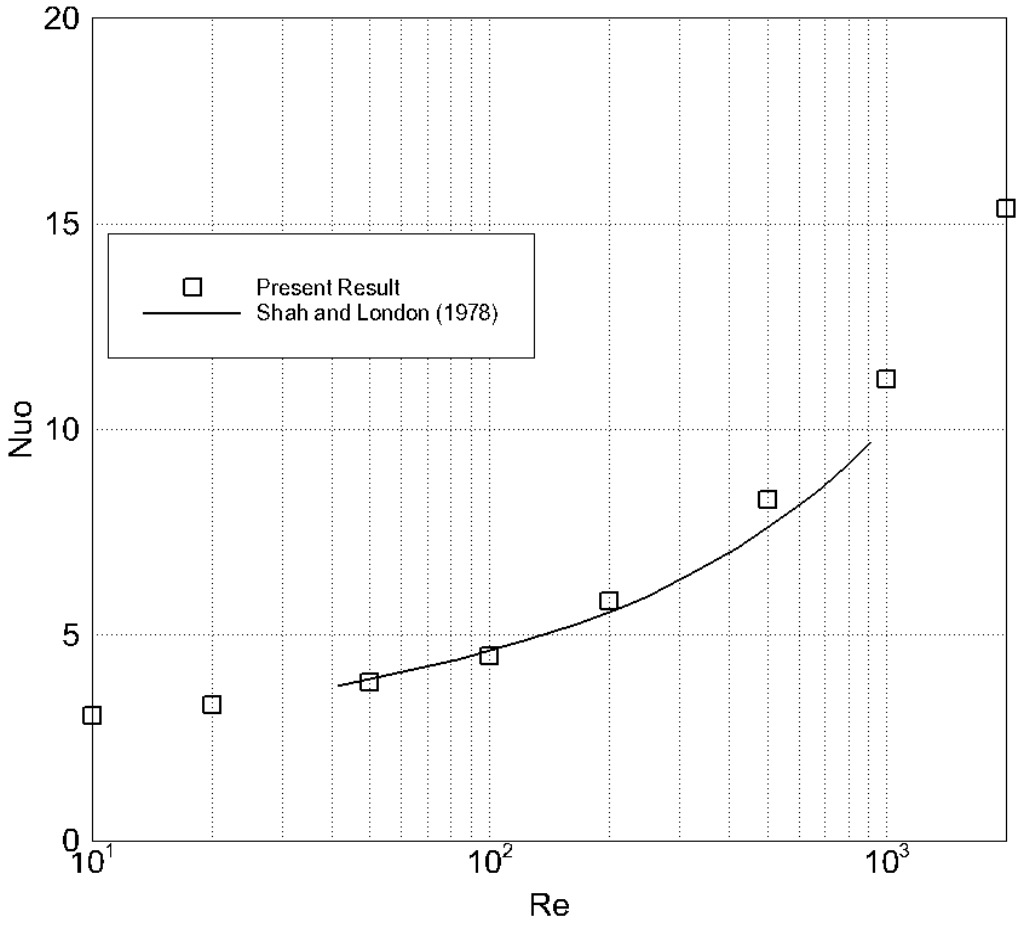

Figure 5.1 Variation of Average Nusselt Number as a Function of Reynolds Number without Electric Field (V_o = 0 kV).

5.2 Flow Field

Forced convection with the presence of an electric field is considered for three electrode configurations with various applied voltages. Figure 5.2 shows the flow field of forced convection with Re = 500 in a square channel with a two-stage EHD gas pump with 0.5-in wide grounded electrodes at both top and bottom stages. The flow field displays the normal channel flow pattern when the applied voltage is 0 kV, which refers to the case of pure forced convection. Air enters the channel with a uniform velocity. A low velocity region forms along the channel wall (which is so-called the boundary layer) due to the fluid viscosity and thus the no-slip boundary condition on the wall. To maintain the same mass flow rate throughout the channel, the fluid velocity at the midsection of the channel must increase. Hence, it leads to a parabolic velocity profile with the maximum velocity at the center. Until the flow becomes fully developed, the thickness of the boundary layer increases. The distance between the channel entrance to the point where the flow becomes fully develop is called the hydrodynamic entrance length L_h, which can be estimated by the following equation,

$$L_{h,laminar} = 0.05 \mathrm{Re} D \cdot \tag{5.8}$$

For Re = 500, the hydrodynamic entrance length is about twenty five times the hydraulic diameter. However, the length of the current channel is only five and half times the hydraulic diameter. Therefore, the flow is still developing at the exit.

When an electric field is applied to the flow field, the fluid around the electrode tips is accelerated by the electric body force. Since the electrodes in both stages are flush mounted on the channel wall, the accelerated fluid disrupts the development of the boundary layer, which can be clearly seen from Figs. 5.2 (e) and (f). At a lower applied

voltage ($V_o \leq 26$ kV), the velocity profile demonstrates the normal channel flow pattern like the case of pure forced convection. Figure 5.2 (e) shows that (at an applied voltage of $V_o = 26$ kV), the accelerated fluid due to the electrodes of first stages disrupts the development of the boundary layer which occurs at the electrode tips and starts to grow downstream until it reaches the electrodes of second stage. In a sense, this disruption delays the boundary layer development and extends the hydrodynamic entrance length. At low applied voltages ($V_o \leq 26$ kV), the velocity profile below the electrode tips displays a parabolic shape. However, when the applied voltage is very high, for instance $V_o = 28$ kV, the fluid at the electrode tips of both stages is accelerated so much that it even exceeds the flow velocity at the center of the channel, which can be seen from Fig. 5.2 (f). In addition, the high-velocity stream issued from the electrode tip thins the boundary layer, leading to an increase in the velocity gradient near the channel wall below the electrode tips of both stages. As the flow develops further downstream of the bottom stage, the disturbance by corona wind diminishes. The boundary layer grows thicker and the parabolic velocity profile begins to reappear again in the center of the channel.

The other two configurations, 1-inch and 2-inch wide grounded electrode at the top stage, show similar characteristics in the velocity profile. The velocity contours for these two configurations are shown in Appendix.

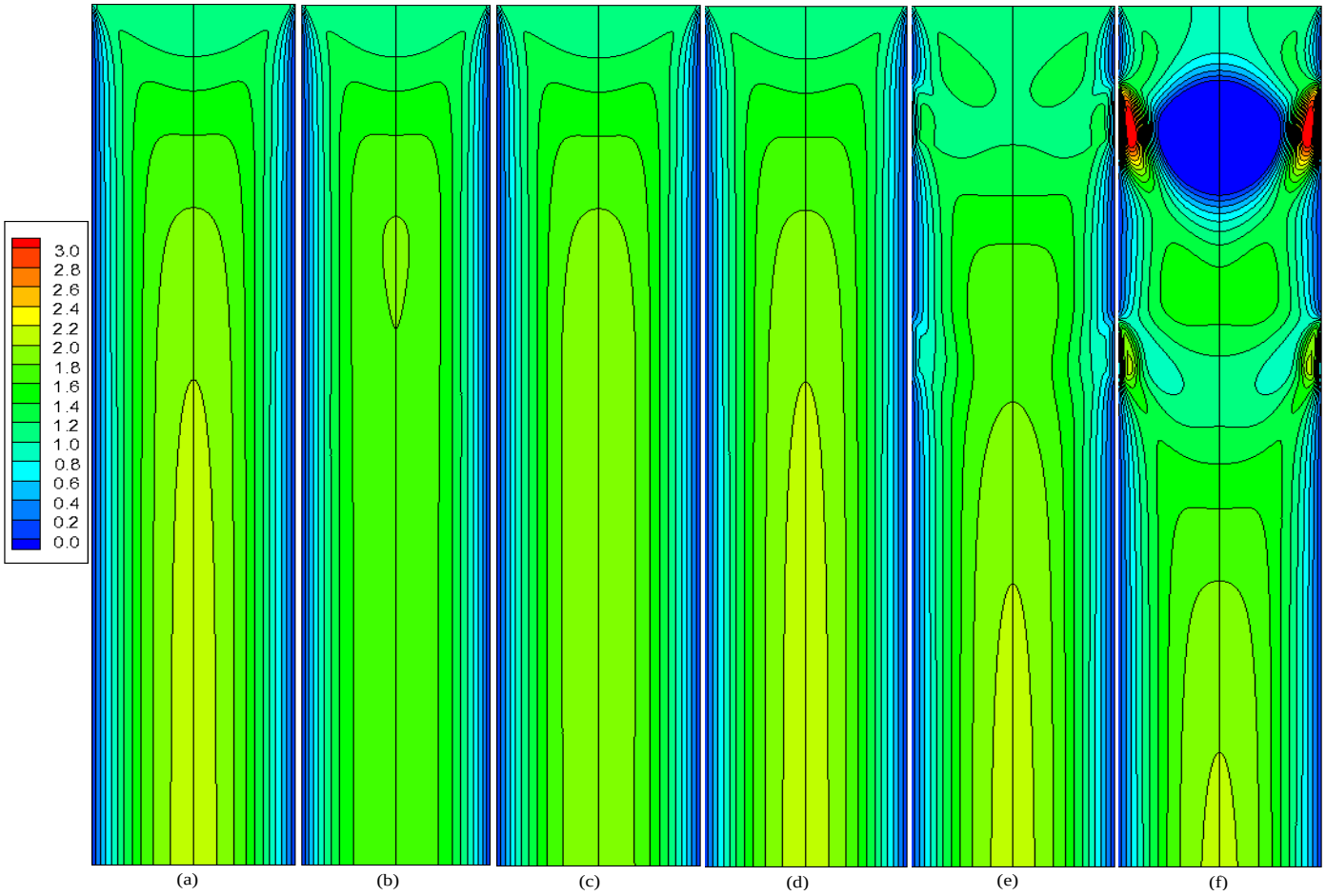

Figure 5.2 Flow Field in a Square Channel with a Two-Stage EHD Gas Pump, Re = 500

(0.5-inch Wide Grounded Electrode at Both Stages)

(a) V_o = 0 kV, (b) V_o = 20 kV, (c) V_o = 22 kV, (d) V_o = 24 kV, (e) V_o = 26 kV, (f) V_o = 28 kV.

For better understanding the flow development inside the channel, flow fields with different applied voltages at various cross-sections along the flow direction are shown in Figs. 5.3 - 5.7 for the same configuration of electrodes. In these figures, cross-section (a) is located at the level of the first stage electrode tips (z = 2/22), cross-section (b) is aligned with the bottom edge of the first stage grounded plate (z = 4/22), cross-section (c) is located at the level of the second stage electrode tips (z = 8/22) where the constant wall heat flux boundary condition applies. Cross-section (d) is aligned with the bottom edge of the second stage grounded plate (z = 10/22) where the constant wall temperature boundary condition applies. Cross-sections (e) and (f) are located further downstream (z = 14/22 and 18/22, respectively) of the channel where the constant wall temperature boundary condition still applies. With the legend of color scale, the magnitude of velocity can be easily identified. The velocity shown in these figures has been normalized by the velocity at the inlet.

Figure 5.3 shows the flow field with no electric field, which serves as a basis for evaluating the effect of electric field on the flow field. In this case, air flow develops following the regular pattern of a channel flow. High velocity gradients appear inside the boundary layer where the velocity changes from zero to the free stream velocity. The thickness of the boundary layer increases in the flow direction, as seen from Fig. 5.3 (a) - (f).

When an electric field is applied to the flow field, fluid around the electrodes is accelerated under the electric body force, as seen from Figs. 5.6 and 5.7. Since the electrodes are flush mounted on the surface of the channel wall, this acceleration disrupts the development of the boundary layer. At low applied voltages of 20 kV (Fig.

5.4) and 24 kV (Fig. 5.5), no disturbance can be seen on the velociyu contours. Air flow shows the regular pattern of a channel flow such as the one shown in Fig. 5.3 (no applied voltage, $V_o = 0$ kV).

At high applied voltages ($V_o \geq 26$ kV), disturbances can be clearly observed on the velocity contour at the tip level of both stages (z = 2/22 and 8/22). These disturbances originating from the electrode tips develop inwards and expand downstream, which can be clearly seen from Figs. 5.6 and 5.7. Further downstream (cross-sections (e) and (f) in Figs. 5.6 and 5.7), these disturbances have gradually dissipated and are no longer visible further downstream. At applied voltage $V_o = 26$ kV, the influence of electric field on the flow field is only limited to a short distance downstream from the electrode tips. However, when the applied voltage is increased to $V_o = 28$ kV, this influence can extend over a region much further downstream. The high electric intensity has produced a large acceleration of fluid flow. Hence, high velocity gradients are observed at the electrode tips (Fig. 5.7 (a)). Although the largest accelerations occur at the electrode tips, the highest velocities actually appear below the electrodes, clearly seen from Fig. 5.7 (b). To maintain the same mass flow rate at any cross-section, the high velocities close to the wall result in a low velocity region at the center of the channel.

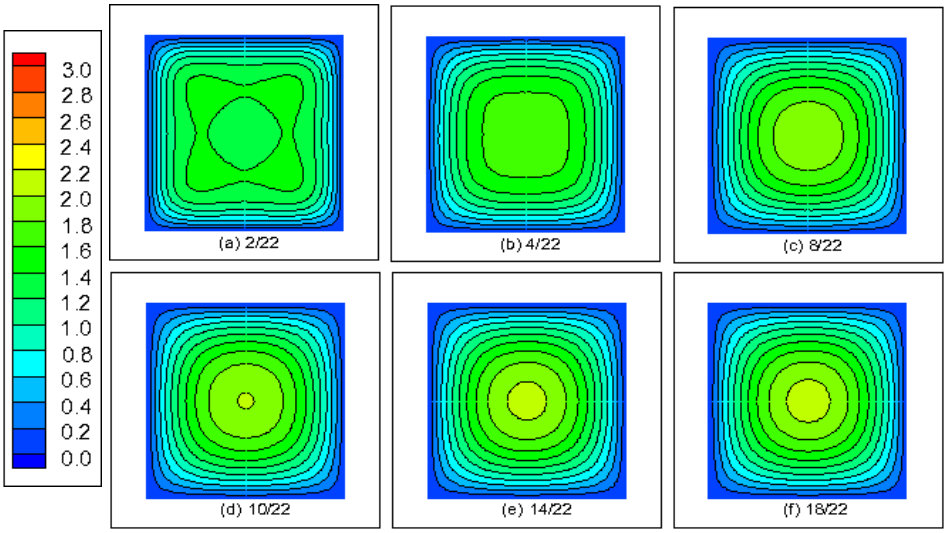

Figure 5.3 Velocity Contours at Various Cross-sections along the z-Direction for Re = 500 and V_o = 0 kV (Unit of Velocity in m/s and Cross-section Location in Inch).

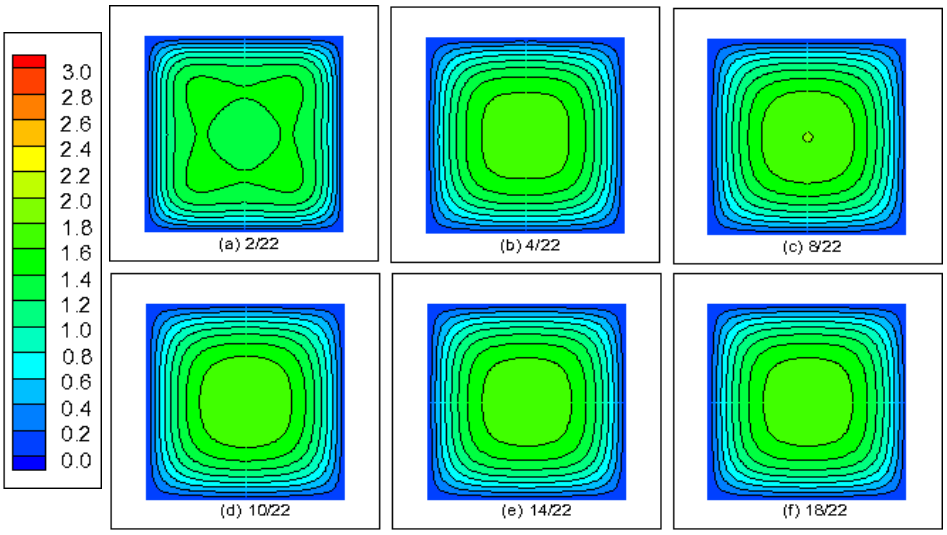

Figure 5.4 Velocity Contours at Various Cross-sections along the z-Direction for Re = 500 and V_o = 20 kV (Unit of Velocity in m/s and Cross-section Location in Inch).

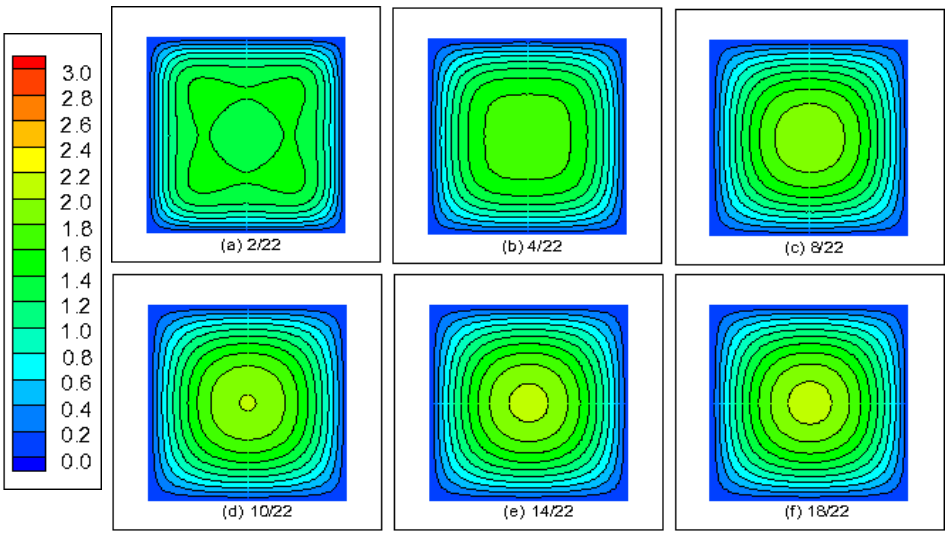

Figure 5.5 Velocity Contours at Various Cross-sections along the z-Direction for Re = 500 and V_o = 24 kV (Unit of Velocity in m/s and Cross-section Location in Inch).

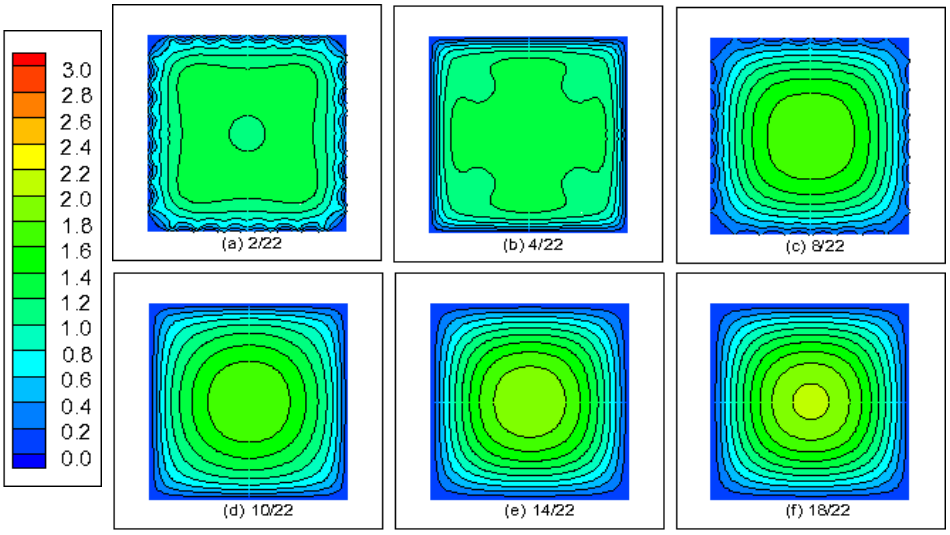

Figure 5.6 Velocity Contours at Various Cross-sections along the z-Direction for Re = 500 and V_o = 26 kV (Unit of Velocity in m/s and Cross-section Location in Inch).

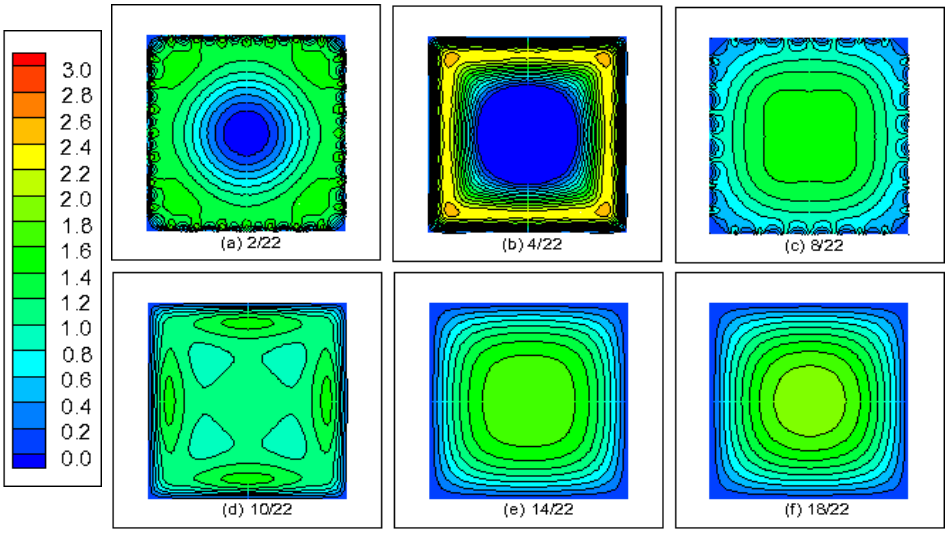

Figure 5.7 Velocity Contours at Various Cross-sections along the z-Direction for Re = 500 and V_o = 28 kV (Unit of Velocity in m/s and Cross-section Location in Inch).

To examine the effect of Reynolds number, flow fields for various Reynolds numbers at the constant applied voltage, V_o = 26 kV are shown in the mid-plane of the channel (Fig. 5.8) for the configuration with 0.5-in wide grounded electrodes at both stages. With the fixed applied voltage, flows at a low Reynolds number produce a higher electric intensity at the electrode tips of both stages as seen from Figs. 5.8 (a) and (b). In addition, the high-velocity corona wind issued from the electrode tip thins the boundary layer, leading to an increase in the velocity gradient near the channel wall below the electrode tips. As the flow develops further downstream for a higher Reynolds number (Figs. 5.8 (c) - (e)), the effect of this disturbance diminishes, the boundary layer grows thicker, and the parabolic velocity profile begins to appear again in the center of the channel.

For a better understanding of the Reynolds number effect of Fig. 5.8, it may be helpful to interpret the results in terms of the EHD number, N_{EHD}. As one recalls, EHD number is the ratio of electric body force to the flow inertia. For the configuration considered, at an applied voltage of 26 kV, the EHD numbers are calculated to be 49972, 12492, 1998, 500 and 125 for the corresponding Reynolds numbers of 100, 200, 500, 1000 and 2000, respectively. At a low Reynolds number, say 100, the electric field has a large influence on the flow field. At a higher Reynolds number, the secondary flow produced by the electric field is suppressed by the overwhelming influence of the primary flow.

The other two configurations, 1-inch and 2-inch wide grounded electrode at the top stage, have similar characteristics in the velocity profile and are shown in Appendix.

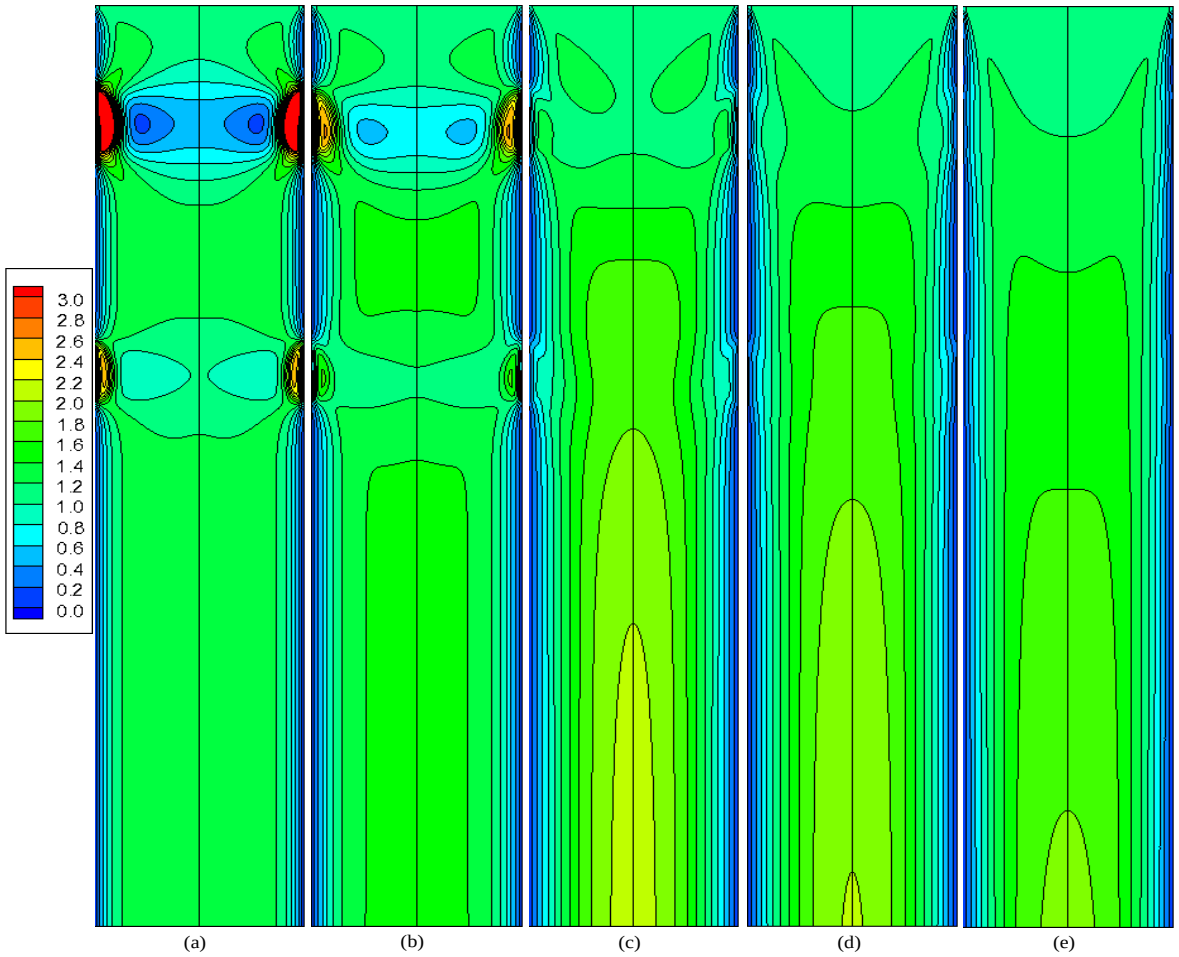

Figure 5.8 Flow Field in a Square Channel with a Two-Stage EHD Gas Pump, V_o = 26 kV

(0.5-inch Wide Grounded Electrode at Both Stages)

(a) Re = 100, (b) Re = 200, (c) Re = 500, (d) Re = 1000, (e) Re = 2000.

5.3 Temperature Field

For the present study, it is assumed that the top part of the channel (from the channel inlet down to the bottom edge of the grounded plate of the second stage) is thermally insulated (i. e., zero wall heat flux), and below the grounded plate of the second stage the channel wall is maintained at a constant temperature. Figure 5.9 shows the temperature field at the mid-plane of the channel with Re = 500 for the configuration with 0.5-in wide grounded electrode at both stages. Air enters the channel with a constant temperature. As the top part of the channel, wall is thermally insulated. The fluid temperature does not change until it reaches the lower part of the wall. When the fluid is in contact with the wall of the lower part of channel, heat transfer takes place in the form of convection and a thermal boundary layer develops along the channel wall. This thermal boundary layer starts at the location where the constant wall temperature boundary condition applies and develops downstream as seen from Fig. 5.9. The thickness of the thermal boundary layer increases until they reach the center of the channel. The distance from where the thermal boundary layer starts to the point downstream where it reaches the center of the channel is called the thermal entrance length L_t, which can be estimated by the following equation,

$$L_{t,laminar} = 0.05 \cdot Re \cdot Pr \cdot D \tag{5.9}$$

For Re = 500, the thermal entrance length for an air flow in a square channel is about seventeen times the hydraulic diameter. Therefore, the temperature field in the current case is still developing at the channel exit. Figure 5.9 shows that no significant change can be found when one compares the temperature fields between the two cases with and without the electric field. Although the electric field modifies the flow field (from Fig.

5.2), but its effect does not extend over to the thermal boundary layer as the modification of the flow field is either confined to a small region near the electrode tips, or moves away from the channel wall downstream.

The other two configurations, 1-inch and 2-inch wide grounded electrode at the top stage, show similar characteristics in the temperature field are shown in Appendix.

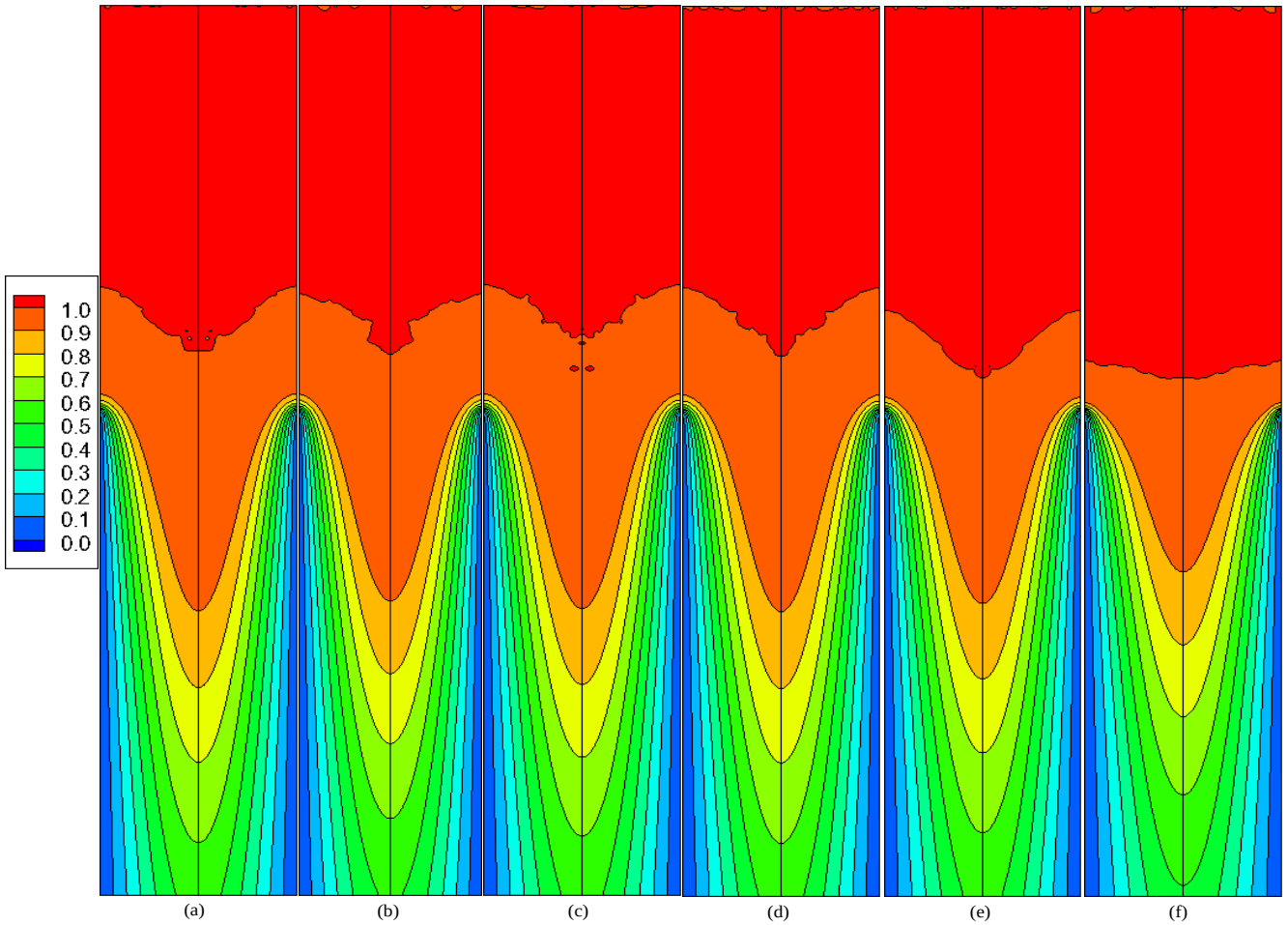

Figure 5.9 Temperature Field in a Square Channel with a Two-Stage EHD Gas Pump, Re = 500

(0.5-inch Wide Grounded Electrode at Both Stages)

(a) V_o = 0 kV, (b) V_o = 20 kV, (c) V_o = 22 kV, (d) V_o = 24 kV, (e) V_o = 26 kV, (f) V_o = 28 kV.

To examine the effect of Reynolds number, temperature fields for various Reynolds numbers with the constant applied voltage, V_o = 26 kV are shown in the mid-plane of the channel (Fig. 5.10) for the configuration with 0.5-in wide grounded electrodes at both stages. As discussed earlier, EHD number is utilized for a better understanding of the Reynolds number effect on the temperature fields. At a low Reynolds number, say 100, the electric field has a large influence on the flow field, thus greatly enhancing heat transfer. At a higher Reynolds number, the secondary flow produced by the electric field is suppressed by the overwhelming influence of the flow inertia of the primary flow, thus diminishing the heat transfer enhancement.

The results of the other two configurations (1-inch and 2-inch wide grounded electrode at the top stage) which exhibit a similar trend, are shown in Appendix.

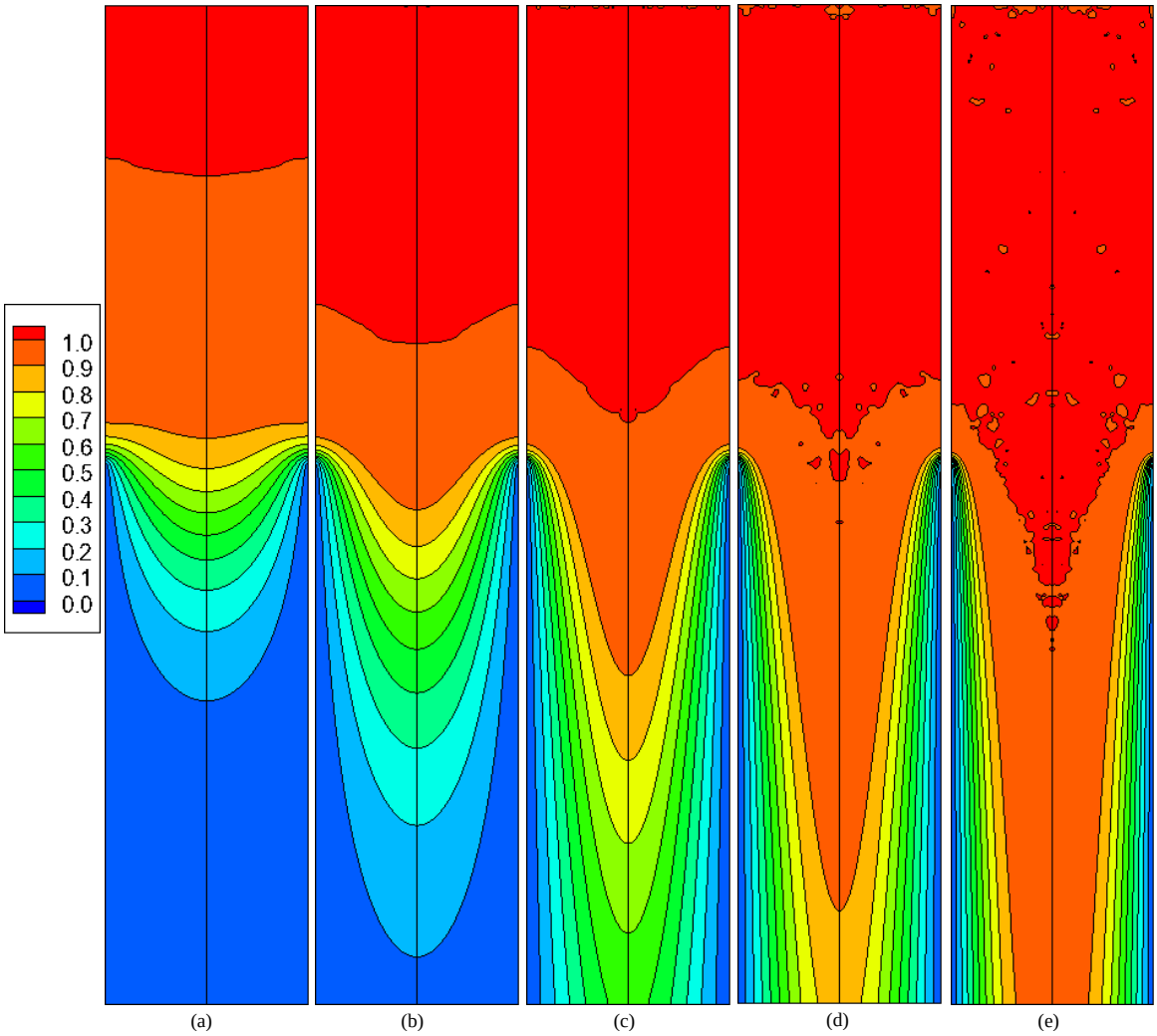

Figure 5.10 Temperature Field in a Square Channel with a Two-Stage EHD Gas Pump, V_o = 26 kV (0.5-inch Wide Grounded Electrode at Both Stages)
(a) Re = 100, (b) Re = 200, (c) Re = 500, (d) Re = 1000, (e) Re = 2000.

To examine the effect of the size of grounded electrode, flow fields for various configurations are shown in Fig. 5.11 for Re = 500 and V_o = 28 kV. The case with no grounded electrodes refers to the channel flow with no electric field, which is the same as Fig. 5.2 (a) as discussed earlier. With the fixed applied voltage, the configuration with 0.5-in wide grounded electrodes at both stages produces a higher electric intensity at the electrode tips of both stages. As seen from Fig. 5.11, the configuration with 0.5-in wide grounded electrodes at both stages produces the largest influence on the velocity profile inside the channel. The familiar parabolic velocity profile gradually recovers at the core region below the electrode tips of the second stage for the first two configurations. But for the third configuration considered (2-in wide grounded electrodes on the top stage and 0.5-in wide on the bottom stage), the familiar parabolic velocity profile recovers at the core region below the electrode tips of top stage.

As seen in Fig. 5.11 (b) and (c), the high velocity close to the wall results in a lower velocity region at the center (nearly 0 velocity at the center after the top stage electrode pins), and this high speed stream turns away from the channel wall when it develops downwards.

The corresponding temperature fields are shown in Fig. 5.12. With the application of an electric field, there is no significant change observed in the temperature field for all configurations. Although the flow field is modified by the electric field, this modification is either limited to a small region near the electrode tips or away from the channel wall, and hence has no obvious effect on the development of the thermal boundary layer downstream.

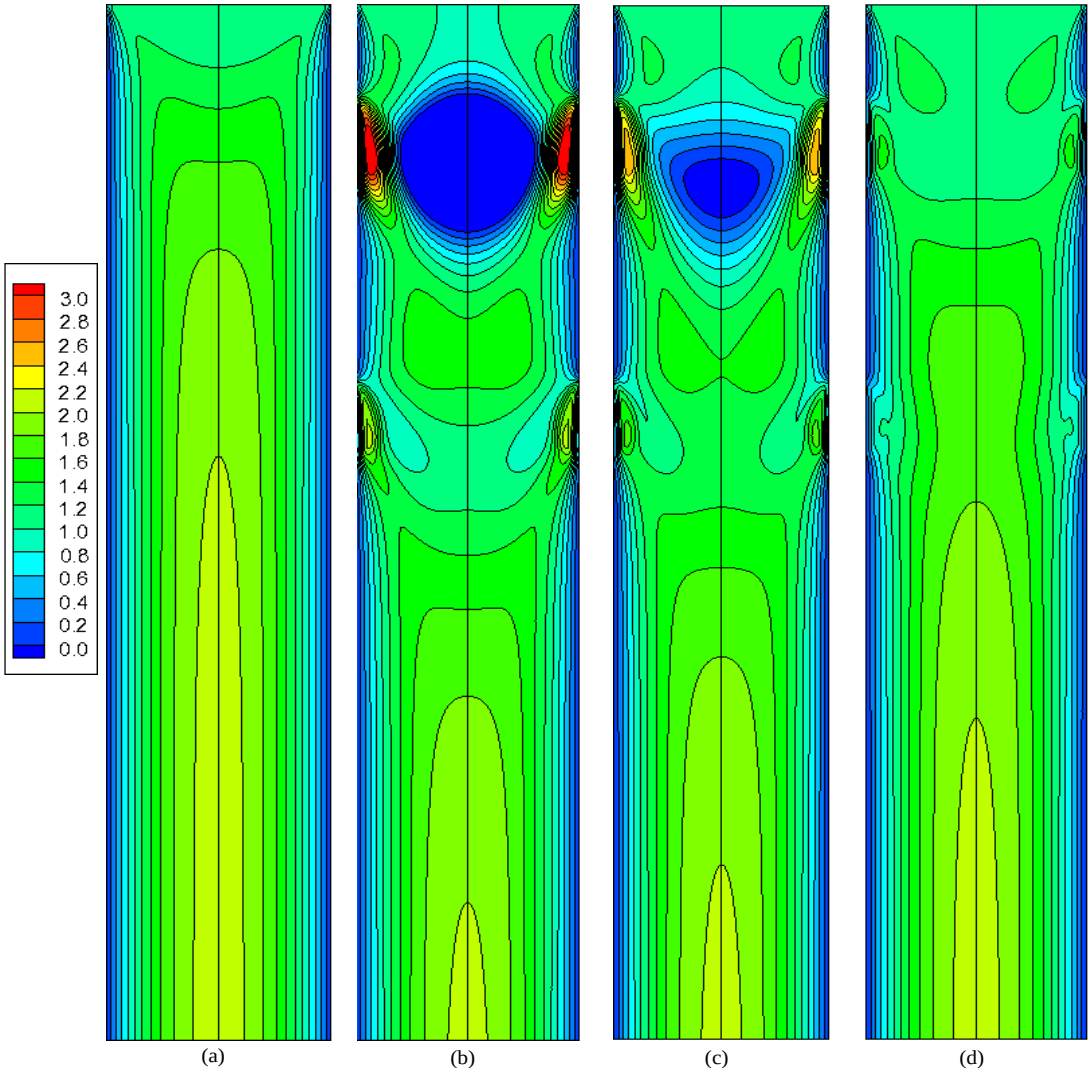

Figure 5.11 Effect of the Grounded Electrode Size at the Top Stage on the Flow Field in a Square Channel with a Two-Stage EHD Gas Pump, V_o = 28 kV, (a) no grounded electrodes, (b) 0.5-in wide, (c) 1-in wide, (d) 2 in wide.

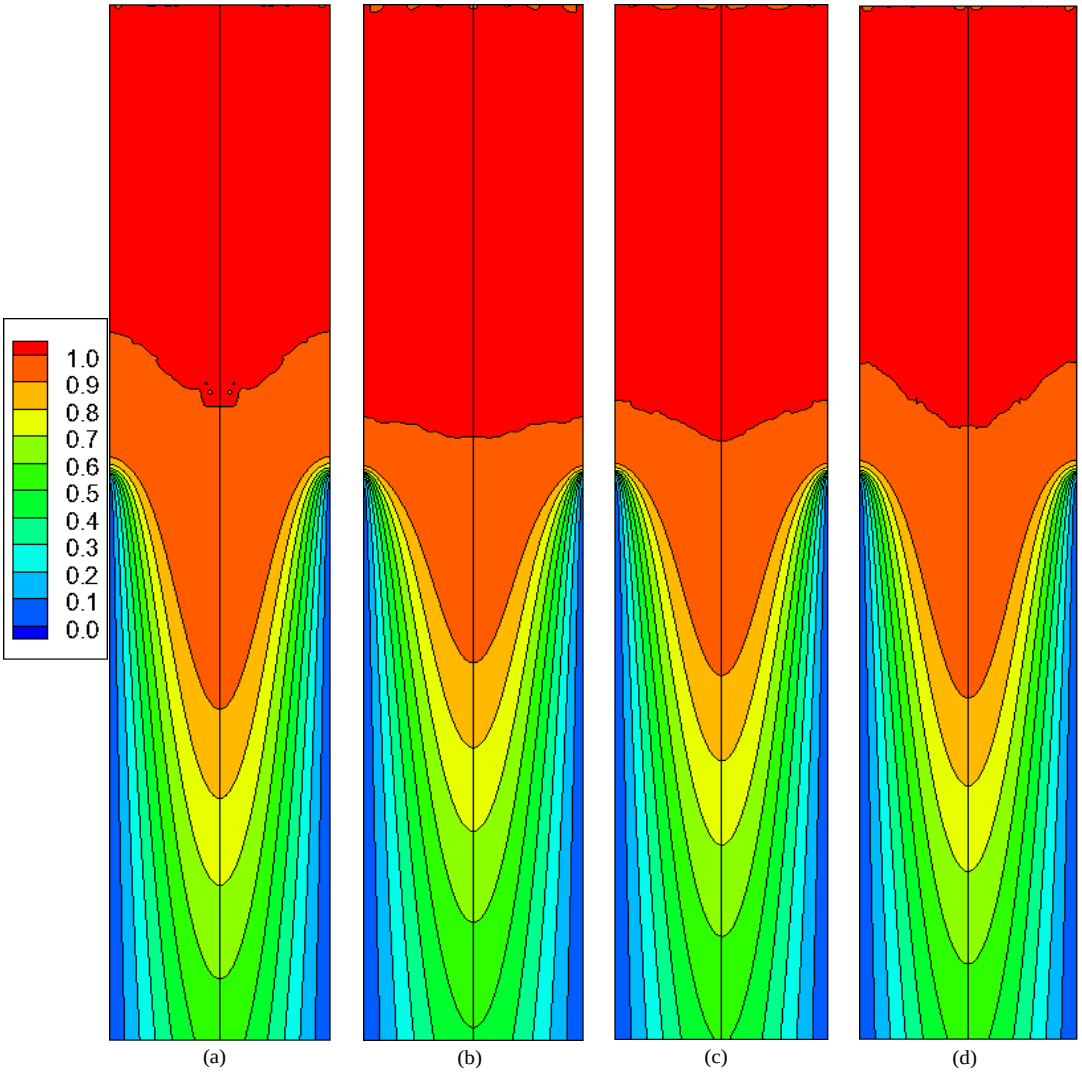

Figure 5.12 Effect of the Grounded Electrode Size at the Top Stage on the Temperature Field in a Square Channel with a Two-Stage EHD Gas Pump, V_o = 28 kV, (a) no grounded electrodes, (b) 0.5-in wide, (c) 1-in wide, (d) 2 in wide.

5.4 Heat Transfer Enhancement

For this study, it is important to evaluate the heat transfer enhancement by an electric field. Figure 5.13 shows the variation of average Nusselt number as a function of the Reynolds number at various applied voltages (20 to 28 kV) for the configuration with 0.5-in wide grounded electrodes at both stages.

The average Nusselt number is normalized by the value of forced convection alone, Nu_o. This value, Nu/Nu_o, represents the heat transfer enhancement by the application of an electric field. For Re = 500, the maximum heat transfer enhancement, which is about 8% ($Nu/Nu_o = 1.08$), can be achieved at the applied voltage of 28 kV. At a given applied voltage, the heat transfer enhancement by the electric field decreases with an increase in the Reynolds number. It is noticed that a higher applied voltage produces better heat transfer enhancement.

The other two configurations, 1-inch and 2-inch wide grounded electrode at the top stage, show a similar trend in the heat transfer enhancement and the results are shown in Appendix.

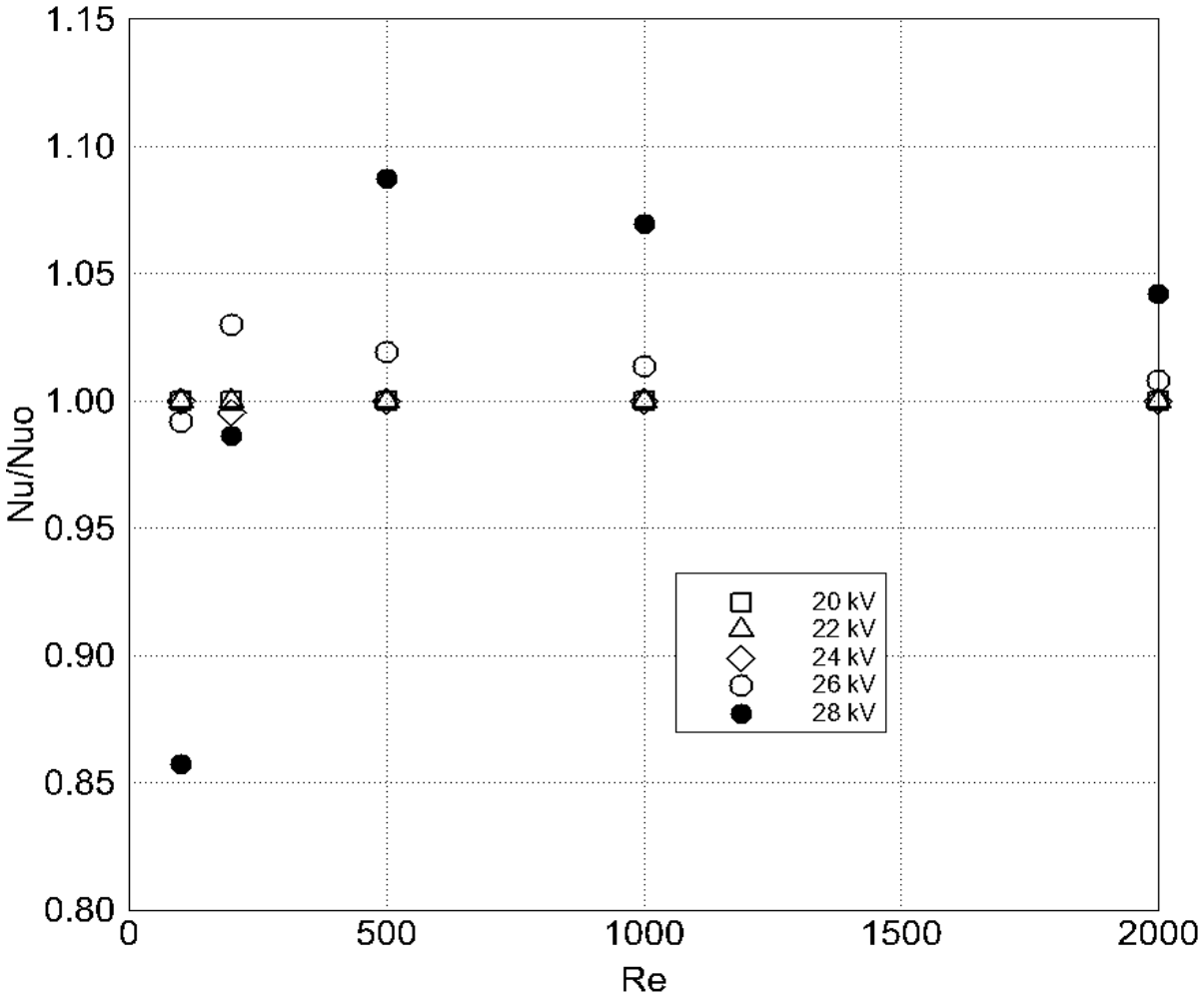

Figure 5.13 Average Nusselt Number as a Function of Reynolds Number (for a Two-Stage EHD Gas Pump with 0.5-inch Wide Grounded Electrode at Both Stages).

To examine the effect of grounded electrode sizes, the normalized Nusselt numbers for the three electrode configurations considered are shown in Fig. 5.14 as a function of Reynolds number at an applied voltage of 28 kV. The configuration of 0.5-in wide grounded electrodes at both stages produces the best heat transfer enhancement for a given Reynolds number of Re = 500.

As the Reynolds number increases, the effect of electric field on the heat transfer enhancement is suppressed by the flow inertia of the primary flow. Therefore, one can say that a smaller size of grounded electrodes produces better results in the heat transfer enhancement for a specific Reynolds number.

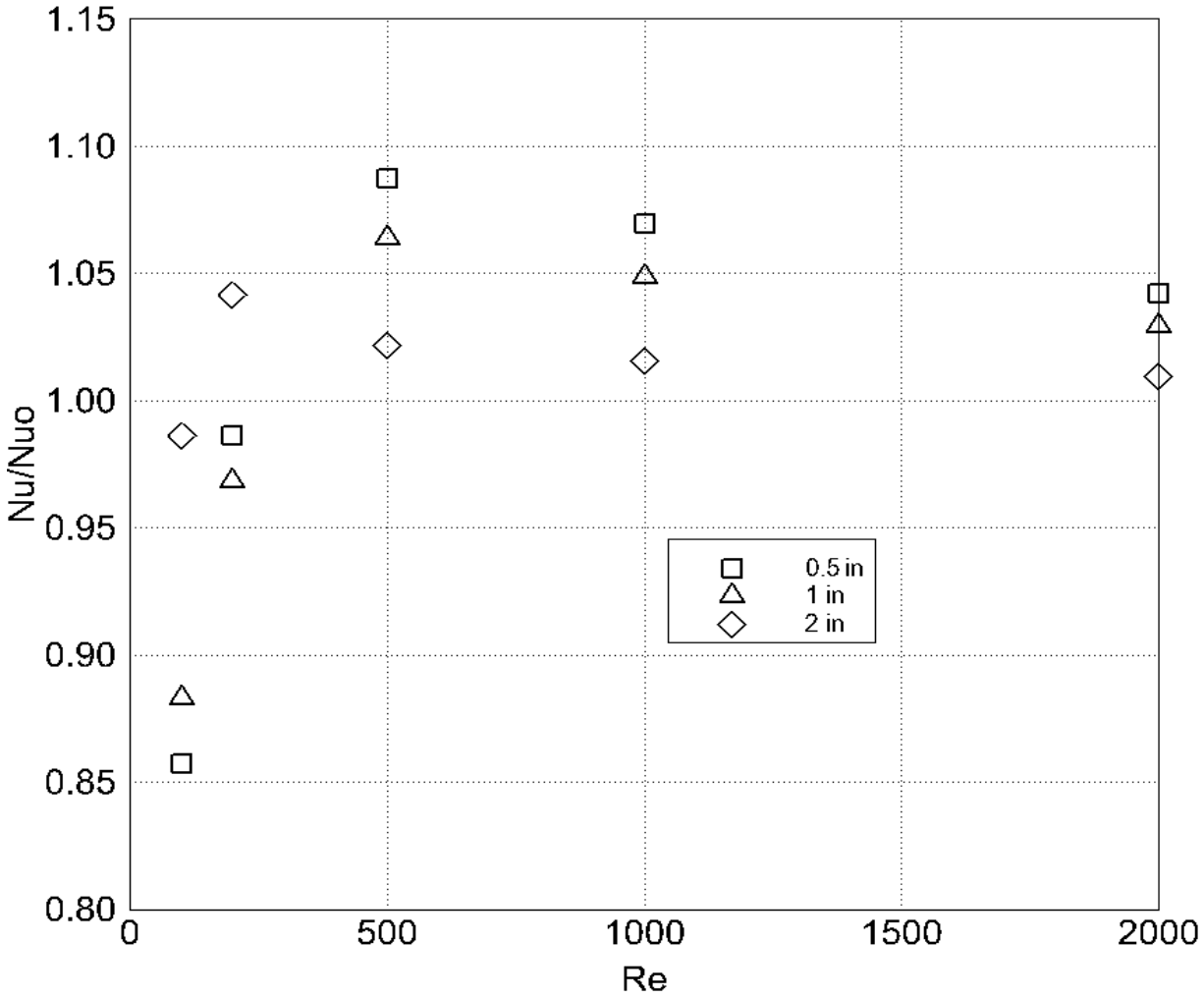

Figure 5.14 Average Nusselt Number as a Function of Reynolds number for Various Sizes of Grounded Electrodes (V_o = 28 kV).

5.5 Friction Factors

To investigate the penalty (i.e., the increased pressure drop) which is imposed by the EHD-induced flows, the friction factors as a function of Reynolds number is illustrated in Fig. 5.15 for the configuration with 0.5-in wide grounded electrodes at both stages at various applied voltages. The friction factor is normalized by the corresponding value of forced convection alone to show the effect of electric field. As seen from Fig. 5.15, the ratios of friction factors are all less than unity, which indicates that the pressure drop for a normal channel flow is actually reduced by the application of electric field. This can be attributed to the effect of entrainment brought about by the corona wind. Therefore, the amount of work required from an external fan or pump is reduced. Moreover, for a given electrode configuration, a higher applied voltage produces a stronger corona jet stream (and thus a larger amount of entrained flow), resulting in a smaller ratio of the friction factors.

At a given applied voltage (V_o = 28 kV), the configuration with 0.5-inch wide grounded electrodes at both stages (Fig. 5.16) has the lowest friction factor ratio, followed in order by the configurations of 1-inch and 2-inch wide grounded electrode at the top stage. Lastly, but not the least, friction factor ratios approach unity as the Reynolds number increases. This is due to the fact that the effect of electric field is undermined by the influence of the primary flow at higher Reynolds numbers.

The other two configurations, 1-inch and 2-inch wide grounded electrode at the top stage, show a similar trend in the heat transfer enhancement and the results are shown in Appendix.

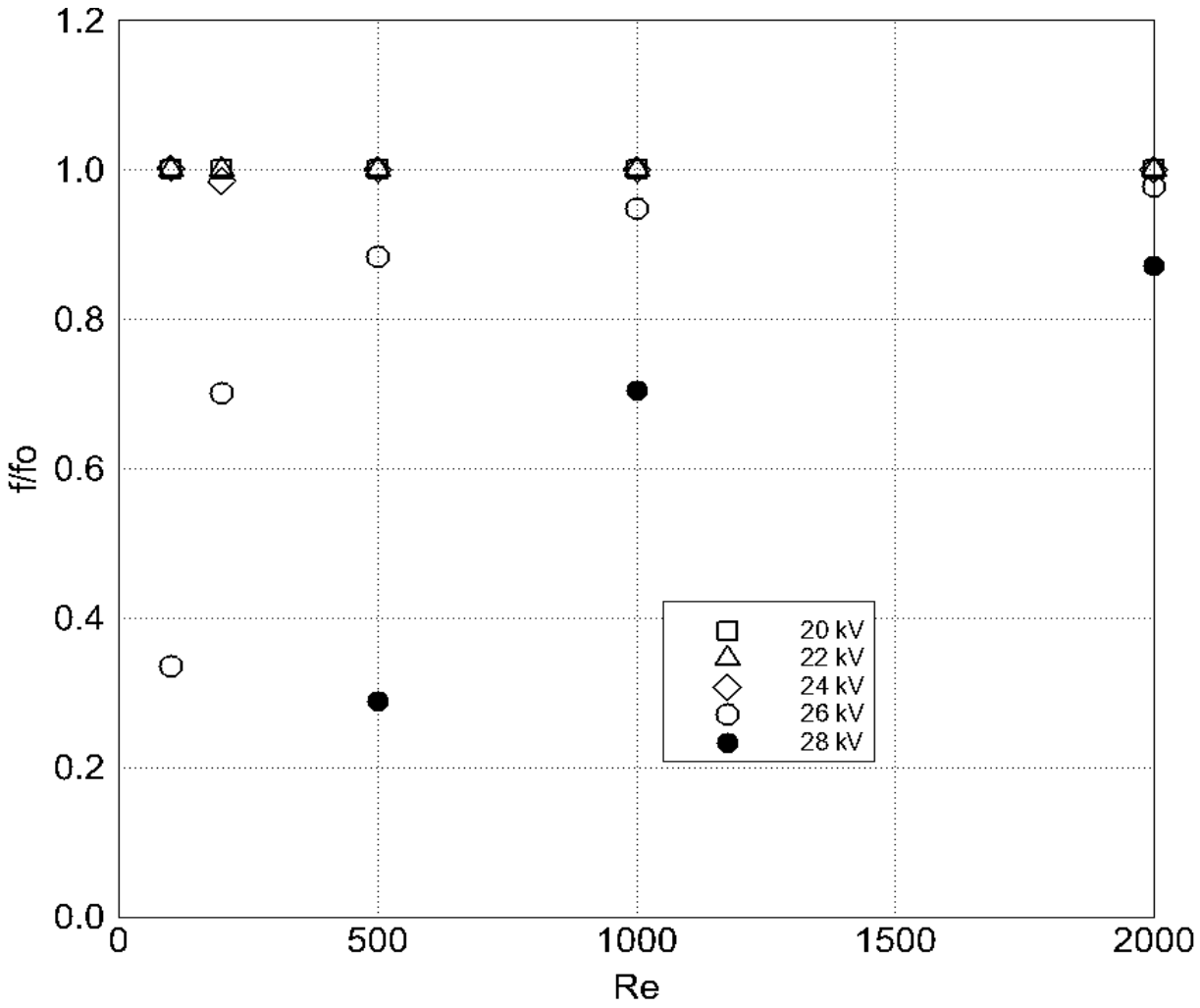

Figure 5.15 Friction Factors as a Function of Reynolds Number (for a Two-Stage EHD Gas Pump with 0.5-inch Wide Grounded Electrode at Both Stages).

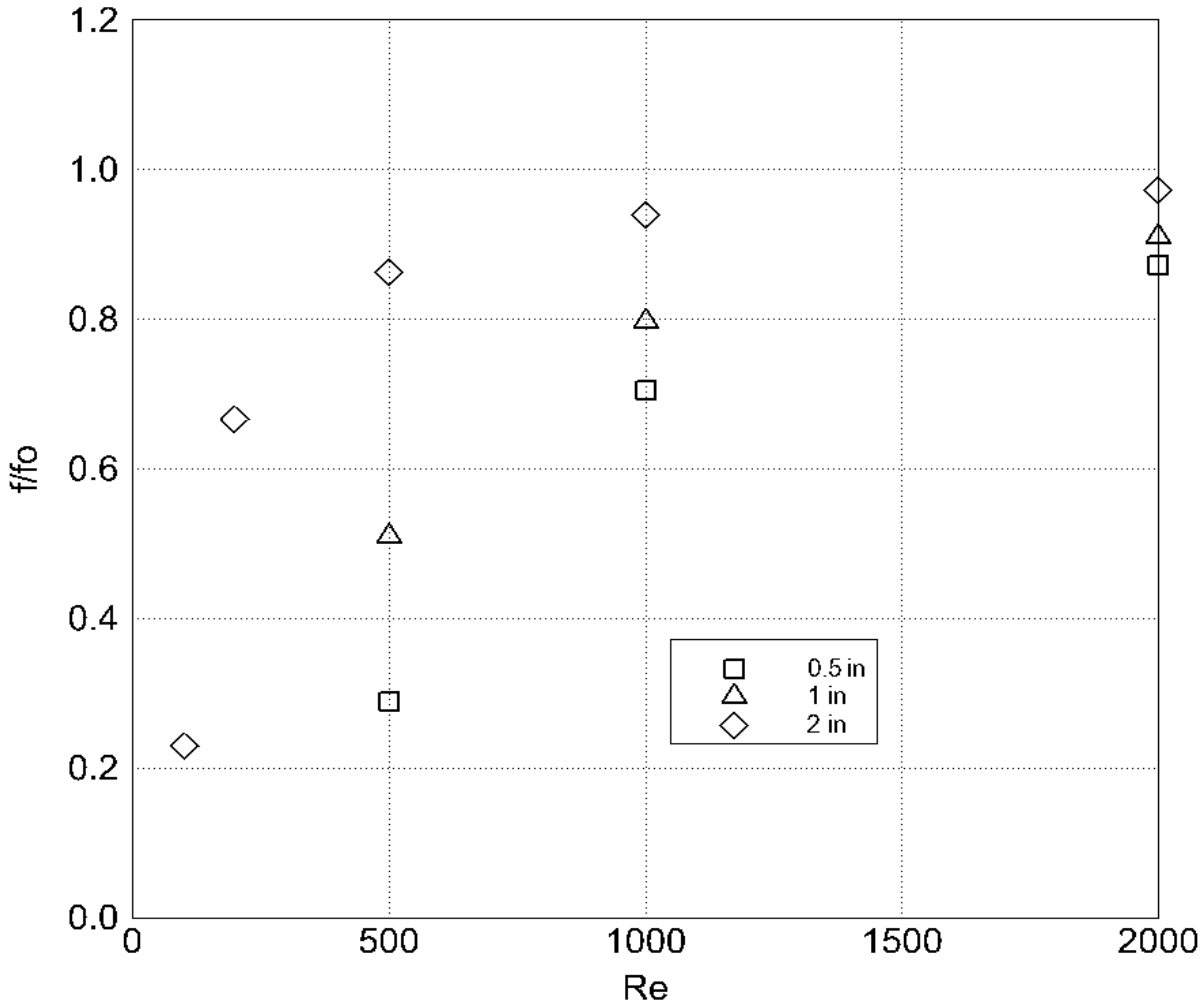

Figure 5.16 Friction Factors as a Function of Reynolds Number for Various Sizes of Grounded Electrodes (V_o = 28 kV).

5.6 Thermal Hydraulic Performance

The ratio of the average Nusselt number to the friction factor (i.e., the thermal hydraulic performance) is used to evaluate the overall effectiveness of using an EHD gas pump for heat transfer enhancement. Figure 5.17 shows the variation of this parameter at various applied voltages for the configuration with 0.5-inch wide grounded electrodes at both stages. From earlier discussion, the configuration with 0.5-inch wide grounded electrodes at both stages produces the best heat transfer enhancement and the least pressure drop at the applied voltage of 28 kV. Hence, it is no surprise that it results in the best thermal hydraulic performance (Fig. 5.17). However, the performance for this configuration at lower applied voltages (i.e., 20 kV to 24 kV) is nearly the same, which remains relatively low for all Reynolds numbers considered. At an applied voltage of 26 kV, the configuration with 0.5-inch wide grounded electrodes at both stages has a better thermal hydraulic performance than other two configurations. Also observed, the flow with low Reynolds numbers has a better performance than those at a higher Reynolds number. Most importantly, Fig. 5.17 shows that the values of $((Nu/Nu_o)/(f/f_o))$ are all greater than unity. From literature, it shows that this parameter for most heat transfer enhancement techniques has a value generally less than unity, the EHD technique is thus very promising, particularly for flows at lower Reynolds numbers.

The other two configurations, 1-inch and 2-inch wide grounded electrode at the top stage, show a similar trend in the thermal hydraulic performance and the results are shown in Appendix.

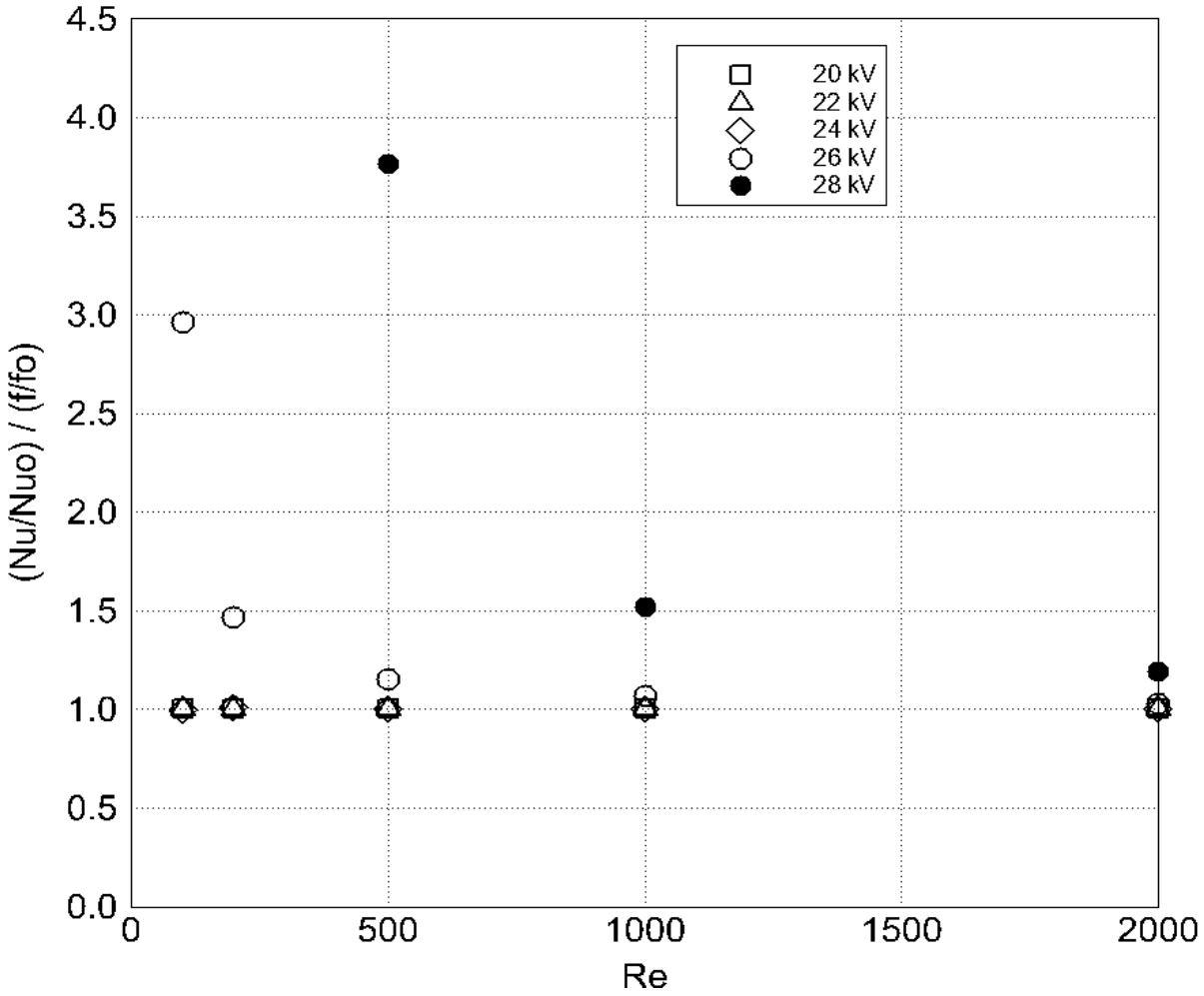

Figure 5.17 Thermal Hydraulic Performance for a Two-Stage EHD Gas Pump with 0.5-inch Wide Grounded Electrode at Both Stages.

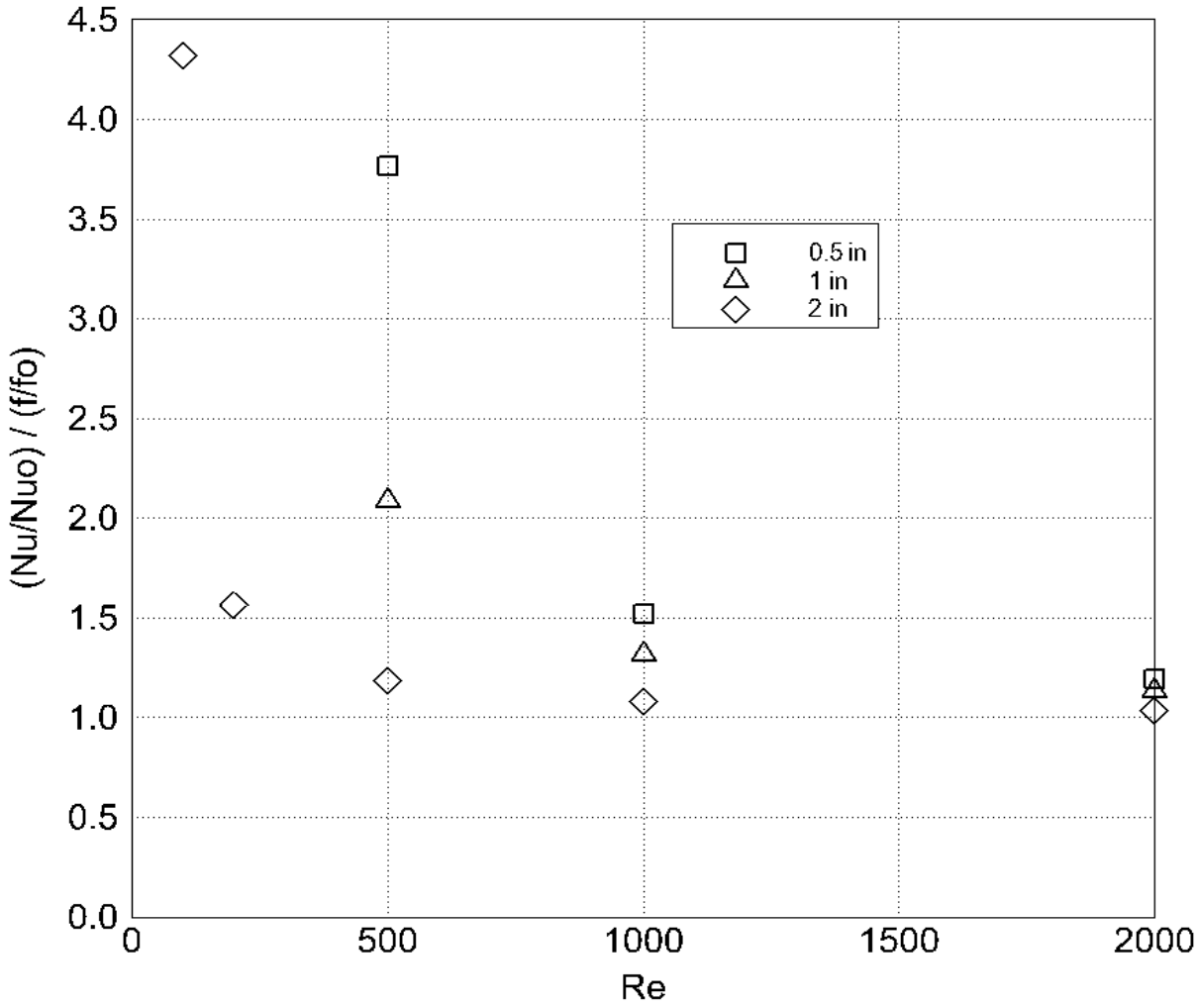

Figure 5.18 Thermal Hydraulic Performance for a Two-Stage EHD Gas Pump with Various Sizes of Grounded Electrodes (V_o = 28 kV).

CHAPTER SIX

CONCLUSIONS AND FUTURE WORK

The present study has investigated on the EHD-induced flow and heat transfer enhancement in a square channel with two-stage electrodes and various sizes of grounded electrodes. Experimental results have provided important information for the optimal design of a two-stage EHD gas pump. Numerical models have been employed in this study to investigate the distribution of electric potential and space charge density, EHD-induced flow inside the test channel as well as the influence of corona wind on forced convection and its effectiveness in the heat transfer enhancement. The conclusions from the present study are summarized in the following sections.

6.1 Experimental Study

In this study, experiments have been performed for a two-stage EHD gas pump with various sizes of grounded electrode. At each stage, there are twenty eight electrode pins, which are evenly spaced around the channel wall and are charged with positive Direct Current (DC). From the V-I characteristic curves for the present setup, it is observed that a two-stage EHD gas pump draws more current than one stage. It is interesting to note that at a higher applied voltage, a grounded electrode with a smaller width at the top stage of the pump draws more current than that with a larger width.

Corona wind issued from the emitting electrodes behaves like a set of wall jets as the electrode pins are flush mounted on the inner surface of the channel wall. As a result, one observes an inverted parabolic velocity profile at the center of the channel

with the maximum velocity close to the channel wall, which is opposite to the fully developed velocity profile of a forced flow. It is this flow characteristic that perturbs the boundary layer and improves the heat transfer coefficient. Comparing different grounded electrode configurations at the same applied voltage, one observes that the induced flow has a slightly higher velocity for an EHD gas pump with a smaller size of grounded electrode at the top stage. Since the velocity of corona wind is directly proportional to the corona current it delivers, the EHD gas pump with 0.5-inch wide grounded electrode (the smallest size considered in the present study) produces the most current, and thus the fastest corona wind.

The EHD gas pump with 1-inch wide grounded electrode appears to induce more air flow than that with 0.5-inch or 2-inch wide grounded electrode at low applied voltages. However, as the applied voltage increases, the configuration with a smaller size (0.5-inch wide) of grounded electrode at the top stage produces a higher volume flow rate. As a result, an appropriate configuration of grounded electrode and applied voltage can be tailored depending on each individual application. For example, if a large volume flow rate is desired, an EHD gas pump with a smaller size (0.5-inch wide) of grounded electrode should be used at a high applied voltage. As observed, the maximum volume flow rate of air induced by the EHD gas pump in the present study can reach as high as 11.5 L/s for a smaller size (0.5-inch wide) of grounded electrode configuration at the top stage. When comparing with the performance of conventional cooling fans for personal computers, it has been shown that EHD gas pumps clearly outperform them, particularly at a lower applied voltage.

Although the present study does not include experiments with forced air flow, the results obtained do provide important information and foundation for the subsequent numerical study in heat transfer enhancement by forced air flow, which are examined in the follow-up study.

6.2 Numerical Study

Numerical results have been obtained for the electric field as well as flow and temperature fields in a square channel with a two-stage EHD gas pump based on the experimental results obtained. The electric potential and space charge distributions have been visually examined for three grounded electrode configurations at various applied voltages. In addition, numerical results of the EHD-induced flows were compared with the experimental data. Numerical results disclose by flow visualizations that corona wind issued from the electrodes behaves like a set of wall jets, leading to high velocity gradients near the channel walls. For forced convection, it is found that electric field accelerates the fluid flow near to the wall, which reduces the boundary layer thickness and, in return, increases the heat transfer coefficient. This electric field effect is more pronounced in the low Reynolds number flow regime. At high Reynolds numbers, the secondary flow produced by the electric field is suppressed by the inertia of the primary flow. The heat transfer enhancement observed in the present study, is increased by 8% with the configuration of a smaller size (0.5-inch wide) of grounded electrode at an applied voltage of 28 kV at Re = 500. It has been also shown in the present study that the thermal hydraulic performance parameter, $((Nu/Nu_o)/(f/f_o))$, is always greater than unity. As it is found from literature that the values of this

performance parameter for most heat transfer enhancement techniques are less than unity, thus one can conclude that EHD enhancement technique has great promise for applications in thermal management.

6.3 Recommendations for Future Work

While the characteristics of a two-stage EHD-induced flow as well as their influence on heat transfer enhancement in a square channel have been successfully examined both experimentally and numerically in the present study, several improvements can be considered for the future study.

First of all, for the current experimental study, the air velocity inside the channel is measured by inserting a hot wire anemometer. The diameter of the probe is relatively large, which may have partially blocked the air flow. For the future study, a velocity measuring device with a smaller diameter is recommended to reduce the uncertainty of velocity measurements and to place the sampling point close to the wall.

Also, the current study evaluates various configurations of a two-stage EHD gas pump in terms of its grounded electrode size with a fixed number of electrode pins (a total of 28 electrode pins at each stage) charged with only positive corona. Negative corona discharge need to be considered in the future study for performance comparison. Other factors, such as the electrode diameters and the spacing between the electrodes as well as the number of electrode pins, can also be examined for the optimal design of an EHD gas pump.

Numerical simulations have discovered that an increase in the Nusselt number mostly occurs at the region close to the electrodes. Further downstream, the fluid

accelerated by the electric body force turns away from the channel wall, resulting in little influence on the boundary layer. One approach that could potentially solve this problem is to extend the grounded electrode downward to the end of the channel. It is speculated that the accelerated fluid flow will remain close to the channel wall, causing a greater disturbance to the boundary layer and thus increasing the overall heat transfer effect.

In this study for heat transfer enhancement, the top part of the channel wall (from the channel inlet down to the bottom edge of the grounded plate of second stage) is thermally insulated, and below the grounded plate of second stage the channel wall is maintained at a constant temperature. Numerical results have revealed that no significant change in the temperature fields when one compares the results obtained with and without the electric field. Although the electric field modifies the flow field upstream, it does not produce much of an effect on the thermal boundary layer. Because of the modification in flow field is confined to a small region near the electrode tips, one can insulate the top part of the channel wall (from the channel inlet down to the bottom edge of the grounded plate of first stage) and maintain the channel wall at a constant temperature below the grounded plate of first stage in the future study.

REFERENCES

Atalik, K. and Sonmezler, U., "Heat Transfer Enhancement for Boundary Layer Flow over a Wedge by the Use of Electric Fields," (in review).

Bondar, H. and Bastien, F., 1986, "Effect of Neutral Fluid Velocity on Direct Conversion from Electrical to Fluid Kinetic Energy in an Electro-Fluid-Dynamics (EFD) Device," Journal of Physics D: Applied Physics, Vol. 19, pp. 1657-1663.

Chang, J. S., Brocilo, D., Urashima, K., Dekowski, J., Podlinski, J., Mizeraczyk, J. and Touchard, G., 2006, "On-set of EHD Turbulence for Cylinder in Cross Flow under Corona Discharges," Journal of Electrostatics, Vol. 64, pp. 569-573.

Choi, K. H., Rahman, A., Ko, J. B., Rehmani, A., Ali, A., Doh, Y. H. and Kim, D. S., 2010, "Development and Ejection Behavior of Different Material-based Electrostatic ink-jet Heads," Int. Journal Adv. Manuf Technology, Vol. 48, pp. 165-173.

Chang, J. S.,Tsubone, H., Chun, Y. N., Berezin, A. A. and Urashima, K., 2009, "Mechanism of Electro-Hydrodynamically Induced Flow in a Wire-non-parallel Plate Electrode Type Gas Pump," Journal of Electrostatics, Vol. 67, pp. 335-339.

Davidson, J. H., and Shaughnessy, E. J., 1986, "Turbulence Generation by Electric Body Forces," Experiments in Fluids, Vol. 4, pp. 17-26.

FLUENT 6.3 User's Guide, 2006, Fluent Inc., Lebanon, NH.

Forte, M., Leger, L., Pons, J., Moreau, E. and Touchard, G., 2005, "Plasma Actuators for Airflow Control: Measurement of the Non-stationary Induced Flow Velocity," Journal of Electrostatics, Vol. 63, pp. 929-936.

Foroughi, P., Shooshtari, A., Dessiatoun, S. and Ohadi, M. M., 2010, "Experimental Characterization of an Electrohydrodynamic Micropump for Cryogenic Spot Cooling Applications," Heat Transfer Engineering, Vol. 31, No. 2, pp. 119-126.

Goodenough, T. I. J., Goodenough, P. W. and Goodenough, S. M., 2007, "The Efficiency of Corona Wind Drying and its Application to the Food Industry," Journal of Food Engineering, Vol. 80, pp. 1233-1238.

Goldman, M., Goldman, A. and Sigmond, R. S., 1985, "The Corona Discharge, its Properties and Specific Uses," Pure and Applied Chemistry, Vol. 57, No. 9, pp. 1353-1362.

Huang, M. and Lai, F. C., 2003, "Numerical Study of EHD-Enhanced Forced Convection Using Two-Way Coupling," Journal of Heat Transfer, Vol. 125, pp. 760-764.

Huang, M. and Lai, F. C., 2006, “Effects of Joule Heating on EHD-Enhanced Natural Convection in an Enclosure,” Journal of Thermophysics and Heat Transfer, Vol. 20, pp. 939-945.

Hsu, C. P., Larsen, N. E. J., Krichtafovitch, I. A., Montgomery, S. W., Dibene, J. T. II and Mamishev, A. V., 2007, "Miniaturization of Electrostatic Fluid Accelerators," Journal of Microelectromechanical Systems, Vol. 16, No. 4, pp. 809-815.

Hyun, K. T. and Chun, C. H., 2003, "The Wake Flow Control behind a Circular Cylinder Using Ion Wind," Experiments in Fluids, Vol. 35, pp. 541-552.

Jewell-Larsen, N. E., Tran E., Krichtafovitch I. A. and Mamishev, A. V., 2006, "Design and Optimization of Electrostatic Fluid Accelerators," IEEE Transactions on Dielectrics and Electrical Insulation, Vol. 13, No. 1, pp. 191-203.

Kawamoto, H. and Umezu, S., 2005, "Electro-hydrodynamic Deformation of Water Surface in a Metal Pin to Water Plate Corona Discharge System," Journal of Physics D: Applied Physics, Vol. 38, pp. 887-894.

Kalman, H. and Sher, E., 2001, "Enhancement of Heat Transfer by Means of a Corona Wind Created by a Wire Electrode and Confined Wings Assembly," Applied Thermal Engineering, Vol. 21, pp. 265-282.

Kamkari, B. and Alemrajabi, A. A., 2010, "Investigation of Electrohydrodynamically-Enhanced Convective Heat and Mass Transfer from Water Surface," Heat Transfer Engineering, Vol. 31, No. 2, pp. 138-146.

Kasayapanand, N., 2010, "Electrohydrodynamic Induced Flow and Heat Transfer in Vertical Channel with Fin Array Attached," Heat Transfer Engineering, Vol. 31, No. 2, pp. 127-137.

Kim, Y., Son, S., Choi, J., Byun, D., and Lee S., 2008, "Design and Fabrication of Electrostatic Inkjet Head using Silicon Micromachining Technology," Journal of Semiconductor Technology and Science, Vol. 8, No. 2, pp. 121-127.

Komeili, B., Chang, J. S., Harvel, G. D., Ching, C. Y. and Brocilo, D., 2008, "Flow Characteristics of Wire-rod Type Electro-hydrodynamic Gas Pump under Negative Corona Operations," Journal of Electrostatics, Vol. 66, pp. 342-353.

Komeili, B., Chang, J. S. andHarvel, G., 2006, "Polarity Effect and Flow Characteristics of Wire-RodType Electro-hydrodynamic Gas Pump," Annual Report Conference on Electrical Insulation and Dielectric Phenomena, pp. 182-185.

Lai, F. C., McKinney, P. J. and Davidson, J. H., 1995, “Oscillatory Electrohydrodynamic Gas Flows,” Journal of Fluids Engineering, Vol. 117, pp. 491-497.

Lai, F. C., 1998, “Effects of Buoyancy on EHD-Enhanced Forced Convection in a Horizontal Channel,” Journal of Thermophysics and Heat Transfer, Vol. 12, pp. 431-436.

Lai, F. C. and Mathew, J., 2006, “Heat Transfer Enhancement by EHD-Induced Oscillatory Flows,” Journal of Heat Transfer, Vol. 128, pp. 861-869.

Lai, F. C. and Kulkarni, S. S., 2007, “Effects of Buoyancy on EHD-Enhanced Forced Convection in a Vertical Channel,” Journal of Thermophysics and Heat Transfer, Vol. 21, pp. 730-735.

Lai, F. C. and Tay, K. K., 2010, “Electrohydrodynamically-Enhanced Forced Convection in a Horizontal Channel with Oscillatory Flows,” Heat Transfer Engineering, Vol. 31, pp. 147-156.

Lee, S., Byun, D., Jung, D., Choi, J., Kim, Y., Yang, J. H., Son, S. U., Tran, S. B. Q. and Ko, H. S., 2008, “Pole-type Ground Electrode in Nozzle for Electrostatic Field Induced Drop-on-demand Inkjet Head,” Journal of Sensors and Actuators A, Vol. 141, pp. 506-514.

Li, J. L., 2006, “On the Meniscus Deformation When the Pulsed Voltage is Applied,” Journal of Electrostatics, Vol. 64, pp. 44-52.

Magnier, P., Hong, D., Chesneau, A. L., Pouvesle, J. M. and Hureau, J., 2007, "A DC Corona Discharge on a Flat Plate to Induce Air Movement," Journal of Electrostatics, Vol. 65, pp. 655-659.

Mendes, R. V., and Dente, J. A., 1998, "Technical Briefs of Boundary-Layer Control by Electric Fields," Journal of Fluids Engineering, Vol. 120, pp. 626-629.

Meng, X., Zhang, H. and Zhu, J., 2008, "The Characteristics of Particle Charging and Deposition during Powder Coating Processes with Coarse Powder," Journal of Physics D: Applied Physics, Vol. 41, pp. 195207-195218.

Meng, X., Zhu, J. andZhang, H., 2008, "The Characteristics of Current Density Distribution during Corona Charging Processes of Different Particulates," Journal of Physics D: Applied Physics, Vol. 41, pp. 172007-172011.

Meng, X., Zhang, H. and Zhu, J., 2008, "A General Empirical Formula of Current-Voltage Characteristics for Point-to-plane Geometry Corona Discharges," Journal of Physics D: Applied Physics, Vol. 41, pp. 065209-065218.

Molki, M., Ohadi, M. M., Baumgarten, B., Hasegawa, M. and Yabe, A., 2000, "Heat Transfer Enhancement of Airflow in a Channel Using Corona Discharge," Enhanced Heat Transfer, Vol. 7, pp. 411-425.

Molki, M. and Bhamidipati,K. L., 2004, "Enhancement of Convective Heat Transfer in the Developing Region of Circular Tubes Using Corona Wind," International Journal of Heat and Mass Transfer, Vol. 47, pp. 4301-4314.

Molki, M., Ohadi, M. M., Baumgarten, B., Hasegawa, M. and Yabe, A., , 2000, "Heat Transfer Enhancement of Air Flow in a Channel Using Corona Discharge," Journal of Enhanced Heat Transfer, Vol. 7, pp. 411-425.

Moreau, E., Leger, L. and Touchard, G., 2006, "Effect of a DC Surface-Corona Discharge on a Flat Plate Boundary Layer for Air Flow Velocity up to 25 m/s," Journal of Electrostatics, Vol. 64, pp. 215-225.

Moreau, E. and Touchard, G., 2008, "Enhancing the Mechanical Efficiency of Electric Wind in Corona Discharges," Journal of Electrostatics, Vol. 66, pp. 39-44.

Moss, R. and Grey, J., 1966, "Heat Transfer Augmentation by Steady and Alternating Electric Fields," Proc. 1966 Heat Transfer and Fluid Mechanics Institute, Stanford University press, Stanford, California, pp. 210-235.

Patankar, S., 1980, Numerical Heat Transfer and Fluid Flow, Hemisphere Publishing Corporation, New York.

Pekker, L. and Young, M., 2010, "A Model of an Ideal Electrohydrodynamic Thruster," Journal of Propulsion and Power (in review).

Rashkovan, A., Sher, E. and Kalman, H., 2002, "Experimental Optimization of an Electric Blower by Corona Wind," Applied Thermal Engineering, Vol. 22, pp. 1587-1599.

Rickard, M., Dunn-Rankin, D., Weinberg, F. and Carleton, F., 2005, "Characterization of Ionic Wind Velocity," Journal of Electrostatics, Vol. 63, pp. 711-716.

Roth, J. R., 2003, "Aerodynamic Flow Acceleration Using Paraelectric and Peristalticelectro-hydrodynamic Effects of a One Atmosphere Uniform Glow Discharge Plasma," Physics of Plasmas, Vol. 10, No. 5, pp. 2117-2126.

Shah, R. K. and London, A. L., 1978, "Laminar Flow Forced Convection in Ducts," Advances in Heat Transfer, Supplement 1, Academic Press, New York.

Takeuchi, N., Yasuoka, K. and Chang, J. S., 2009, "Effect of Discharge Electrode Parameters on the Flow Velocity Profile of the Wire-rod Type Electrohydrodynamic Gas Pump Exit," IEEE Transactions on Dielectrics and Electrical Insulation, Vol. 16, No. 3, pp. 615-621.

Tsubone, H., Ueno, J., Komeili, B., Minami, S., Harvel, G. D., Urashima, K., Ching, C. Y. and Chang, J. S., 2008, "Flow Characteristics of a DC Wire-non-parallel Plate Electro-hydrodynamic Gas Pumps," Journal of Electrostatics, Vol. 66, pp. 115-121.

T. Yamamoto and H. R. Velkoff, 1981, "Electrohydrodynamics in an Electrostatic Precipitator," Journal of Fluid Mechanics, Vol. 108, pp. 1-18.

Yamada, K., 2004, "An Empirical Formula for Negative Corona Discharge Current in Point-grid Electrode Geometry," Journal of Electrostatics, Vol. 96, No. 5, pp. 2472-2475.

Zhang, J., 2010, "EHD-Induced Flow and Heat Transfer in a Square Channel," PhD Dissertation, School of Aerospace and Mechanical Engineering, University of Oklahoma, Norman, Oklahoma.

Zeng, J., 2009, "Electrohydrodynamic Modeling for Micro-fluidic Devices," Proceedings of the ASME 2009 International Mechanical Engineering Congress & Exposition, November 13-19, Lake Vista, Florida, USA, pp. 589-597.

APPENDIX A

EHD-INDUCED FLOWS RESULTS

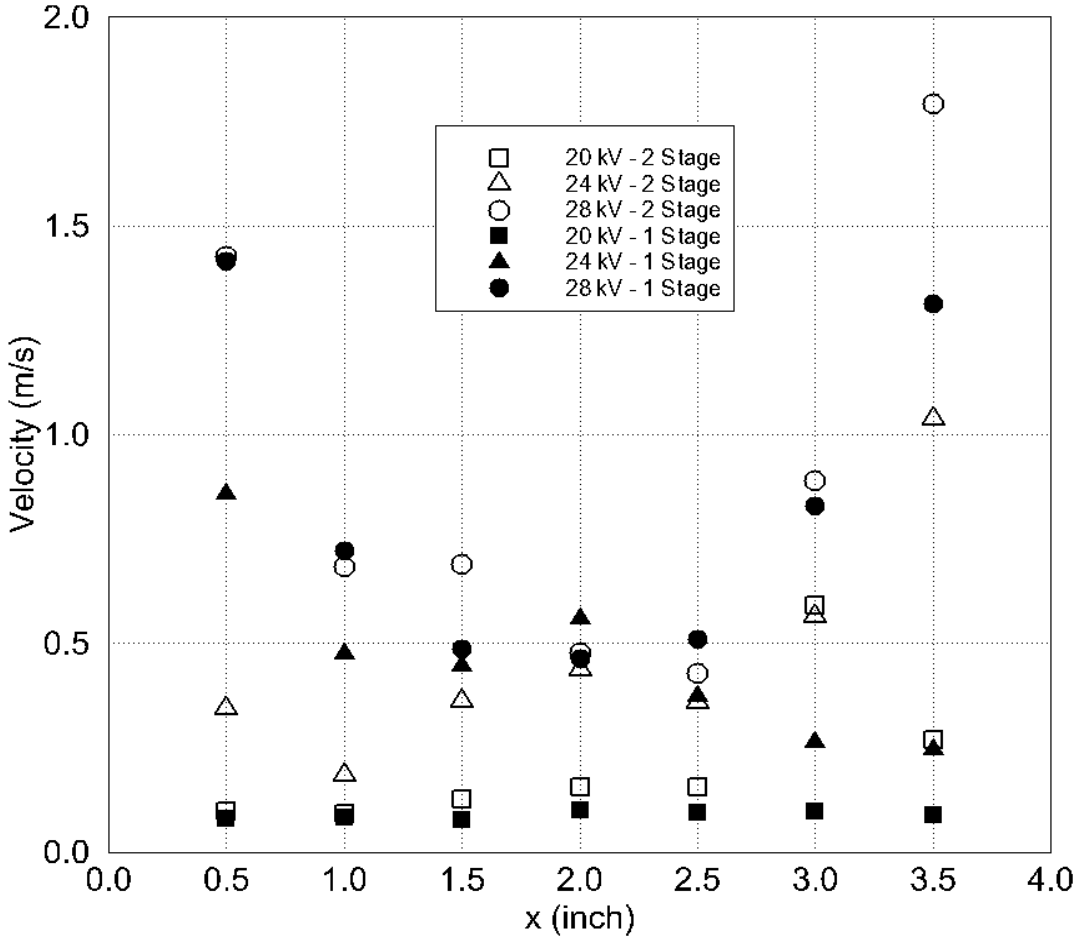

Figure A.1 Comparison of Velocity Profiles inside the Channel at 1-inch Downstream from the Grounded Electrode of the Bottom Stage (for an EHD Gas Pump with 1 inch Wide Grounded Plate at the Top Stage).

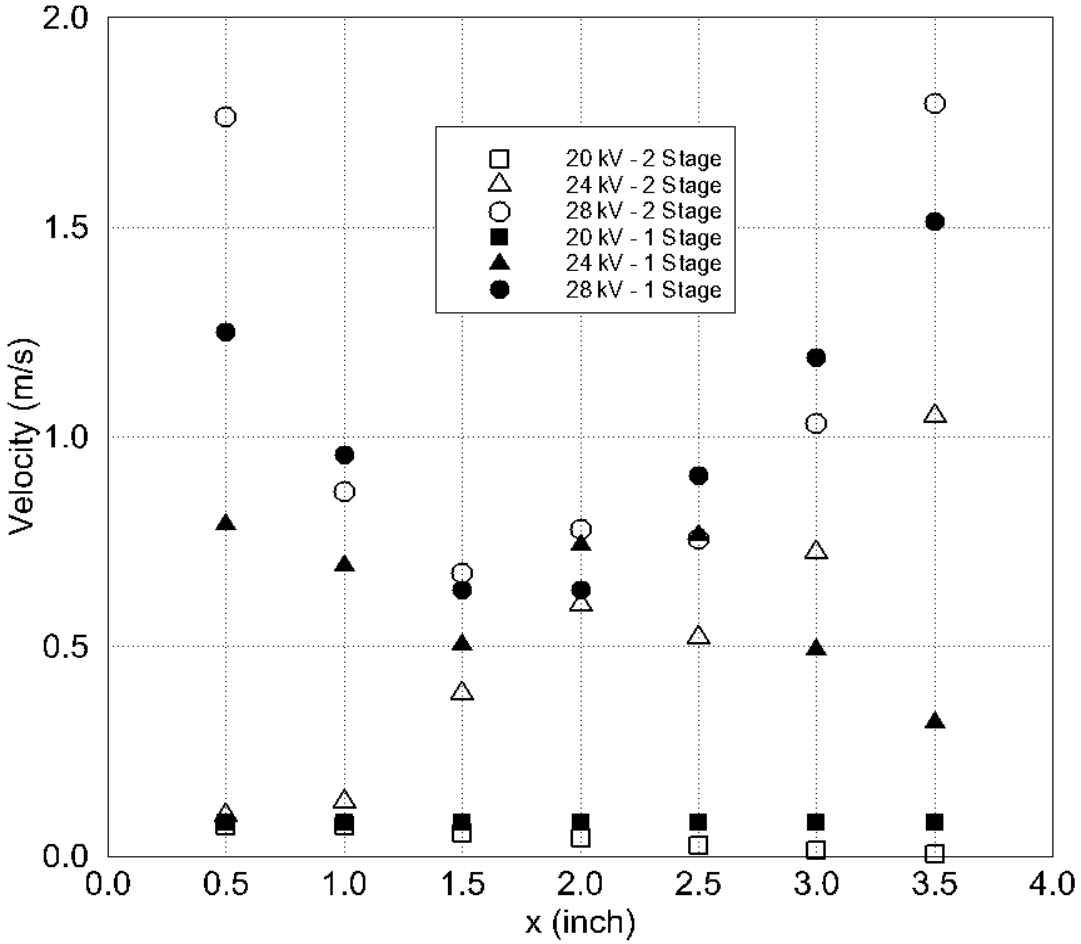

Figure A.2 Comparison of Velocity Profiles inside the Channel at 2.5-inch Downstream from the Grounded Electrode of the Bottom Stage (for an EHD Gas Pump with 1 inch Wide Grounded Plate at the Top Stage).

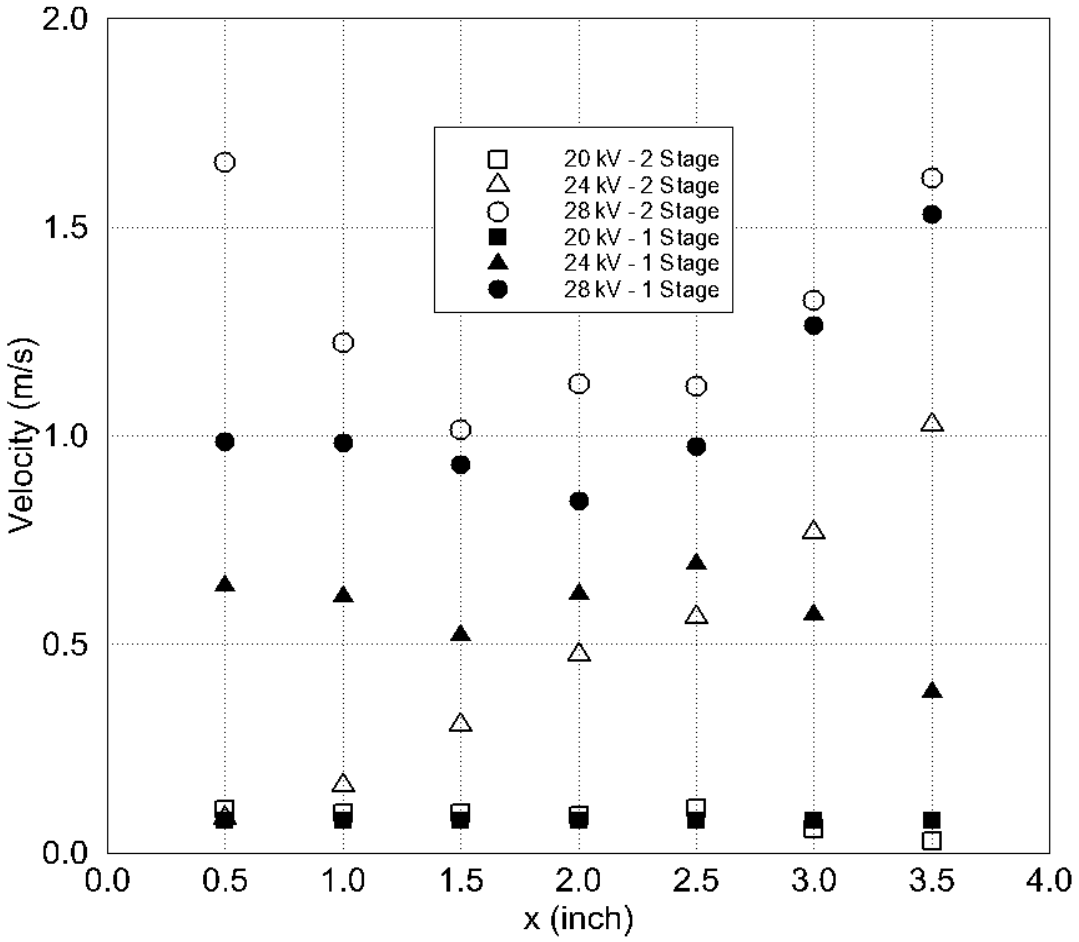

Figure A.3 Comparison of Velocity Profiles inside the Channel at 4-inch Downstream from the Grounded Electrode of the Bottom Stage (for an EHD Gas Pump with 1 inch Wide Grounded Plate at the Top Stage).

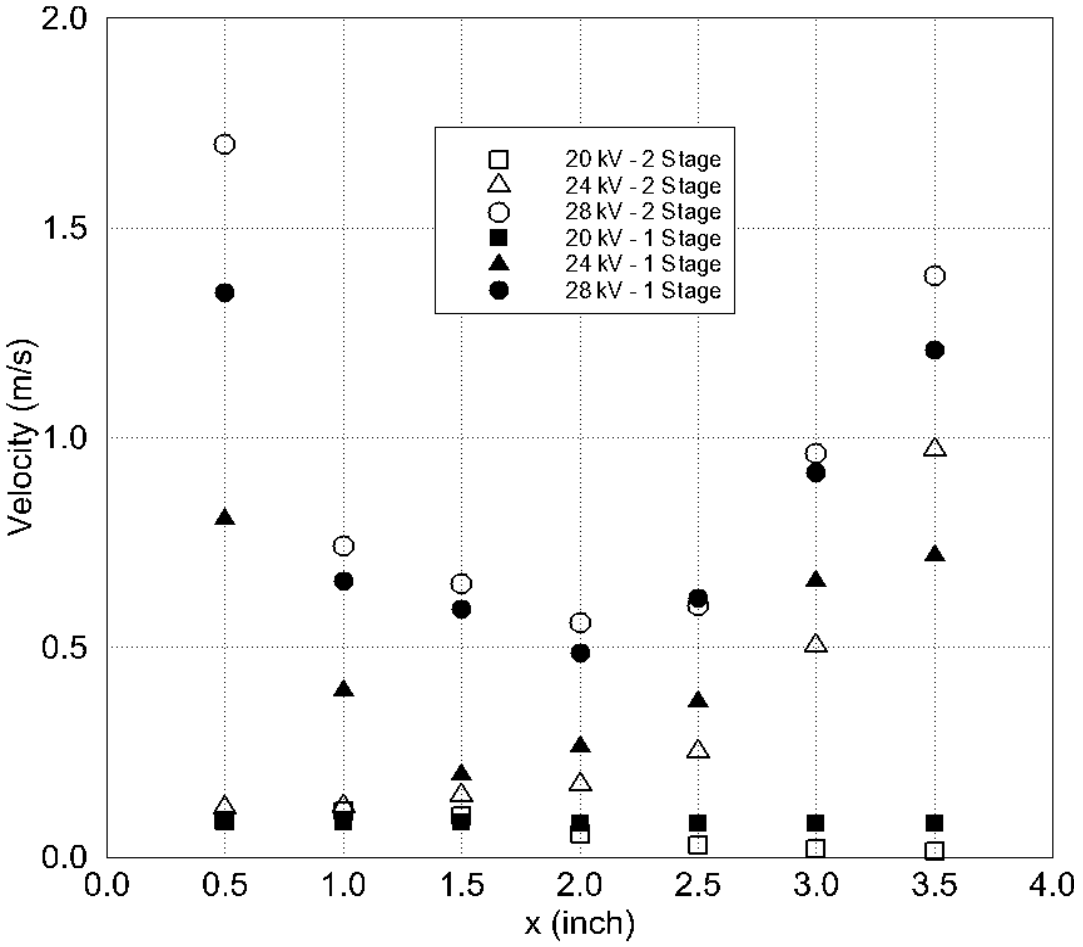

Figure A.4 Comparison of Velocity Profiles inside the Channel at 1-inch Downstream from the Grounded Electrode of the Bottom Stage (for an EHD Gas Pump with 2 inch Wide Grounded Plate at the Top Stage).

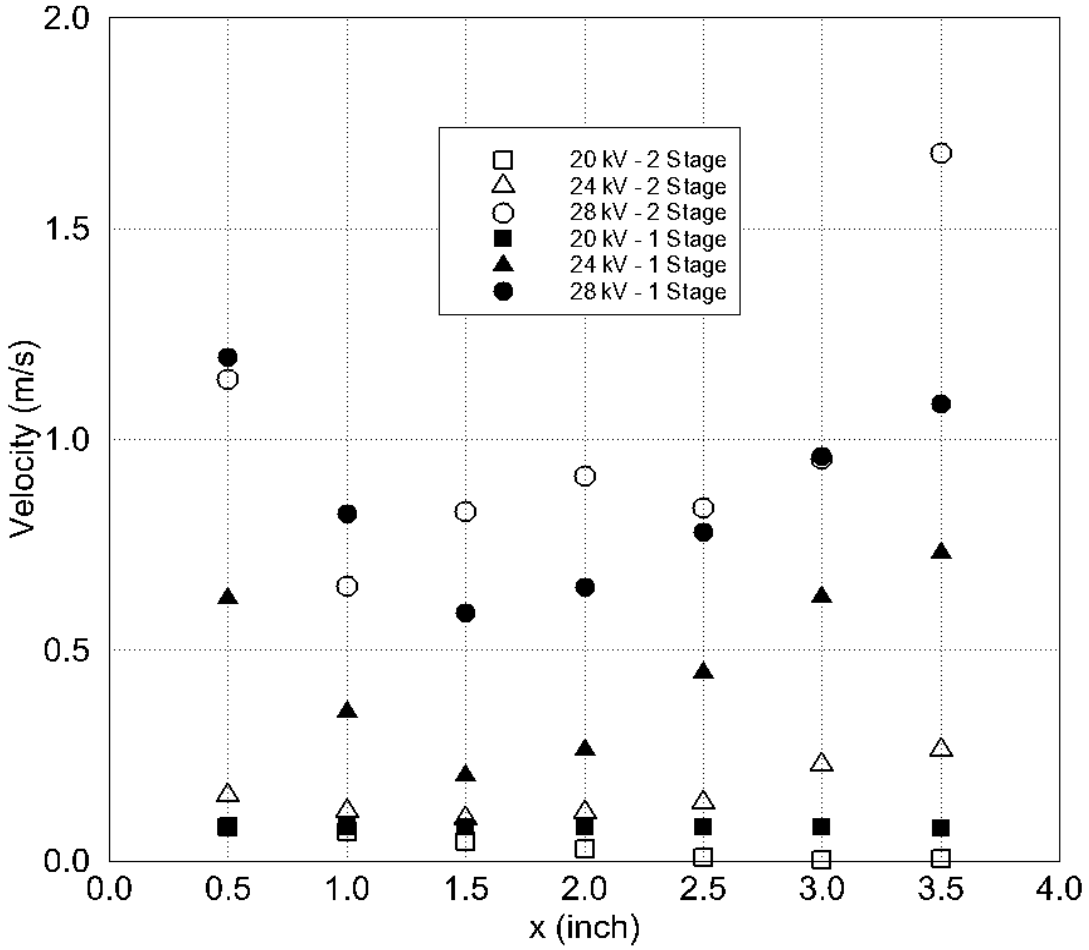

Figure A.5 Comparison of Velocity Profiles inside the Channel at 2.5-inch Downstream from the Grounded Electrode of the Bottom Stage (for an EHD Gas Pump with 2 inch Wide Grounded Plate at the Top Stage).

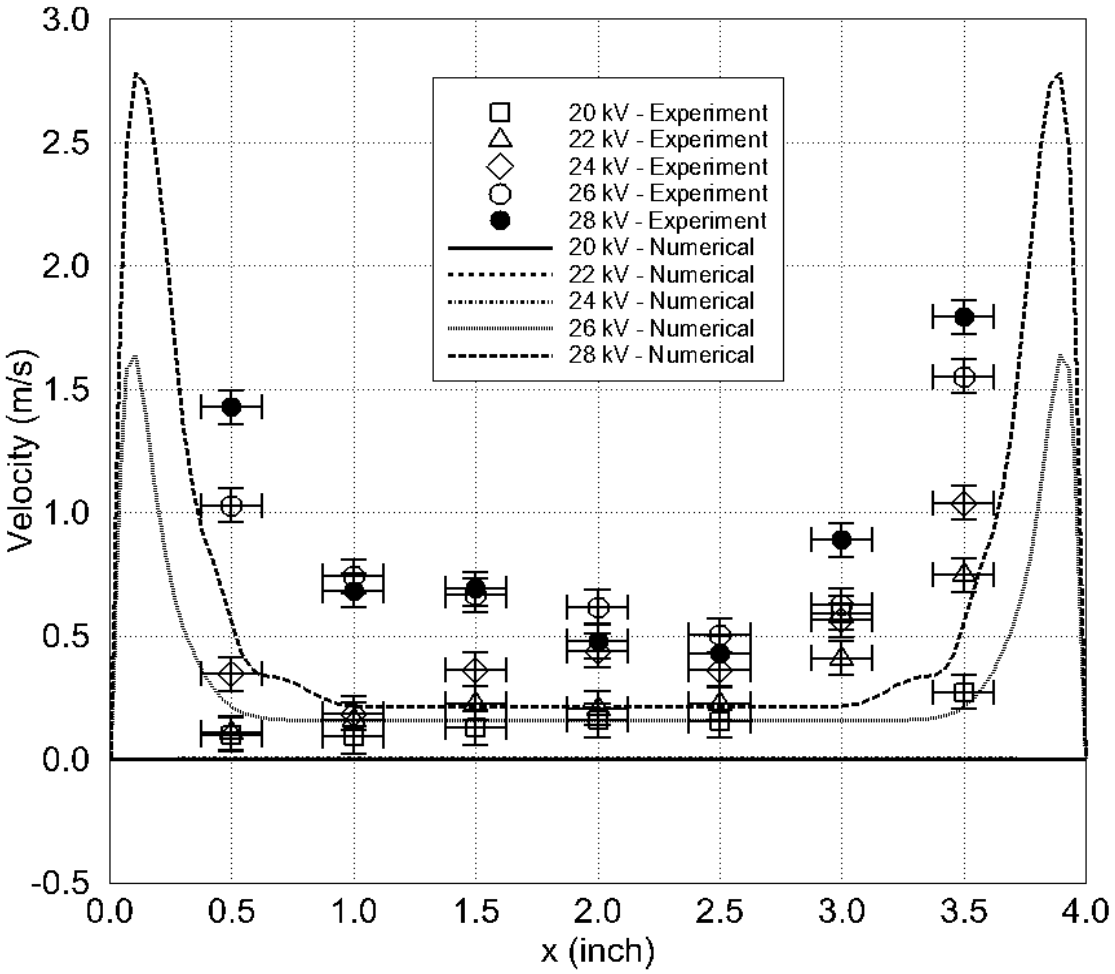

Figure A.6 Comparison of Velocity Profiles inside the Channel at 1-inch Downstream from the Grounded Electrode of the Bottom Stage (for an EHD Gas Pump with 1 inch Wide Grounded Plate at the Top Stage).

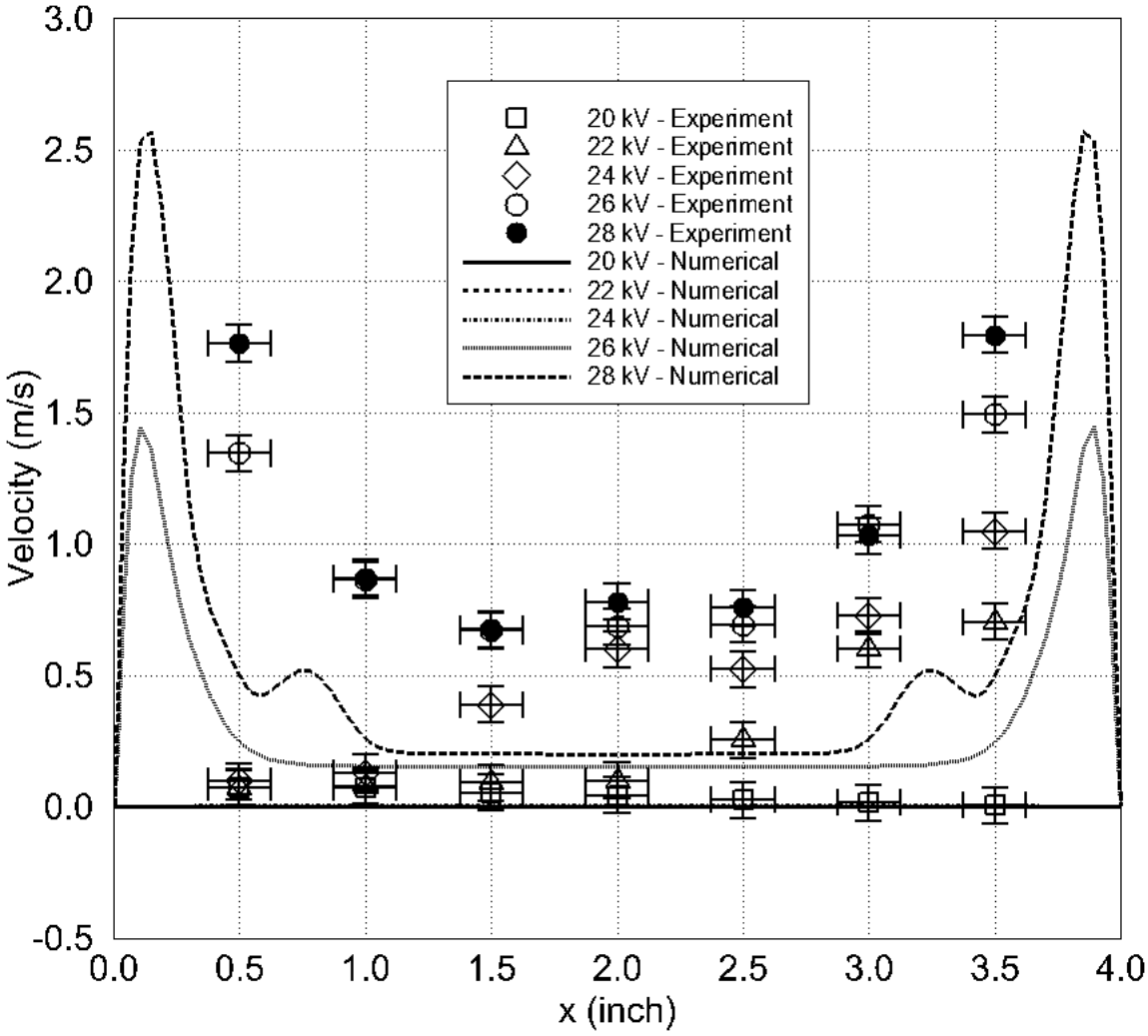

Figure A.7 Comparison of Velocity Profiles inside the Channel at 2.5-inch Downstream from the Grounded Electrode of the Bottom Stage (for an EHD Gas Pump with 1 inch Wide Grounded Plate at the Top Stage).

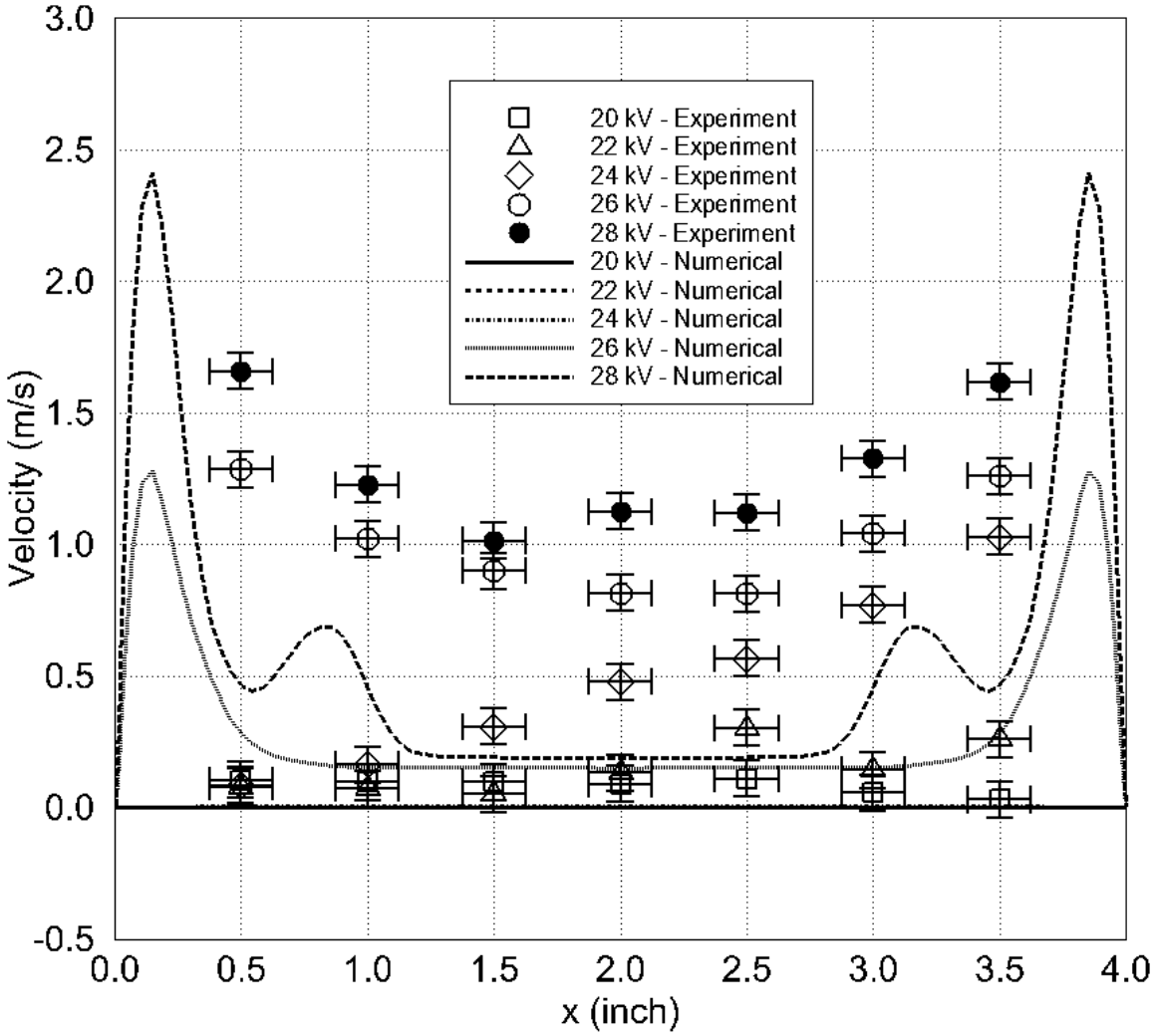

Figure A.8 Comparison of Velocity Profiles inside the Channel at 4-inch Downstream from the Grounded Electrode of the Bottom Stage (for an EHD Gas Pump with 1 inch Wide Grounded Plate at the Top Stage).

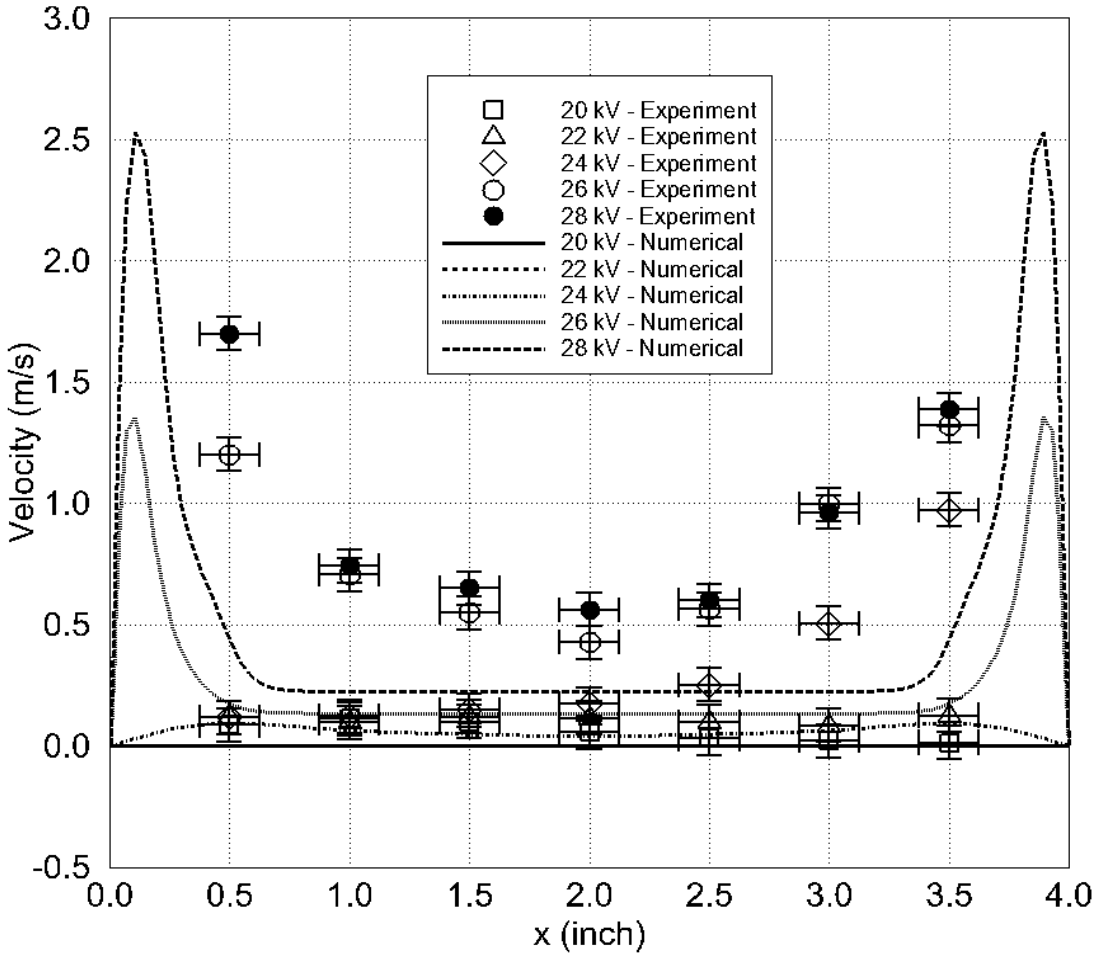

Figure A.9 Comparison of Velocity Profiles inside the Channel at 1-inch Downstream from the Grounded Electrode of the Bottom Stage (for an EHD Gas Pump with 2 inch Wide Grounded Plate at the Top Stage).

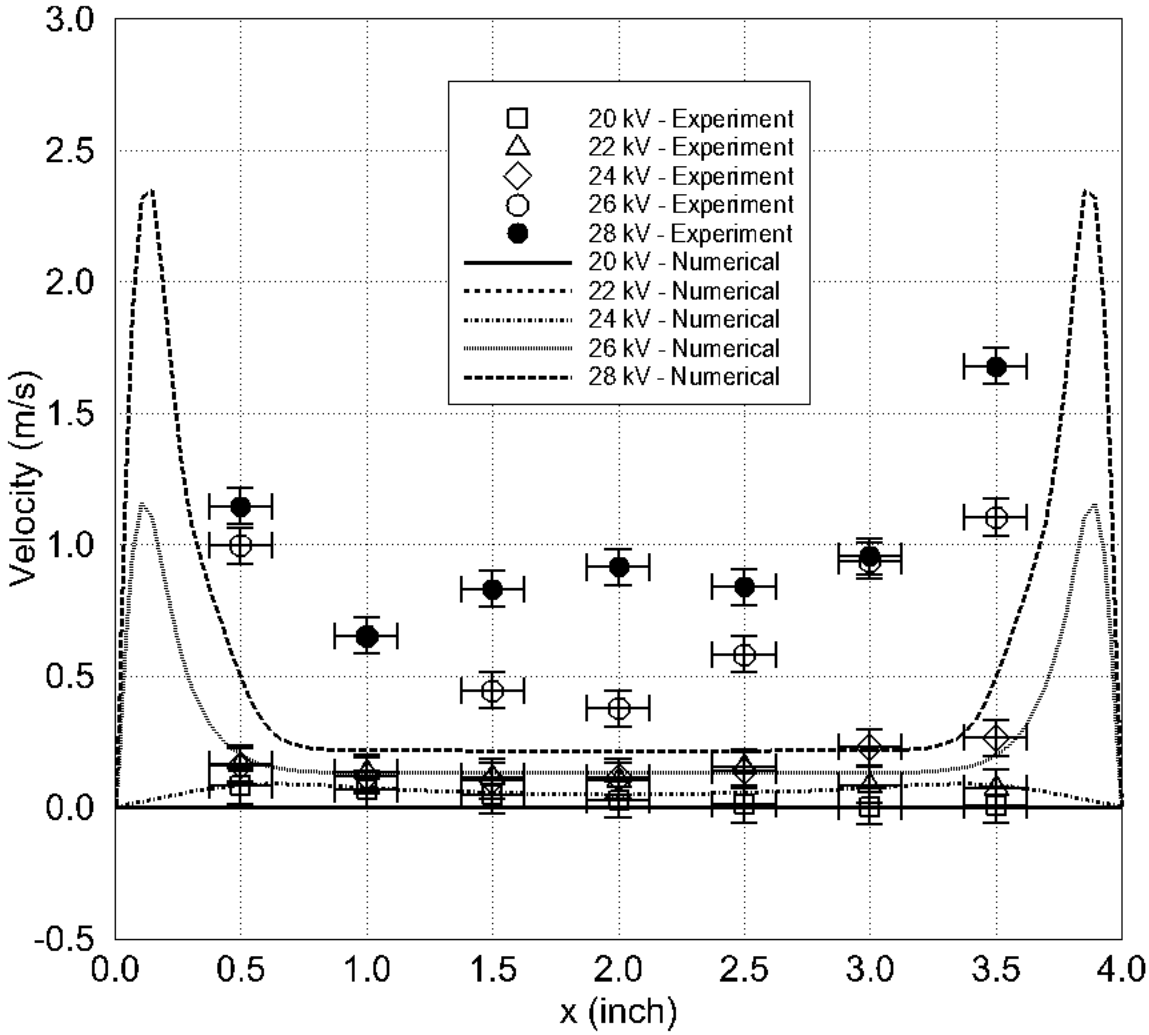

Figure A.10 Comparison of Velocity Profiles inside the Channel at 2.5-inch Downstream from the Grounded Electrode of the Bottom Stage (for an EHD Gas Pump with 2 inch Wide Grounded Plate at the Top Stage).

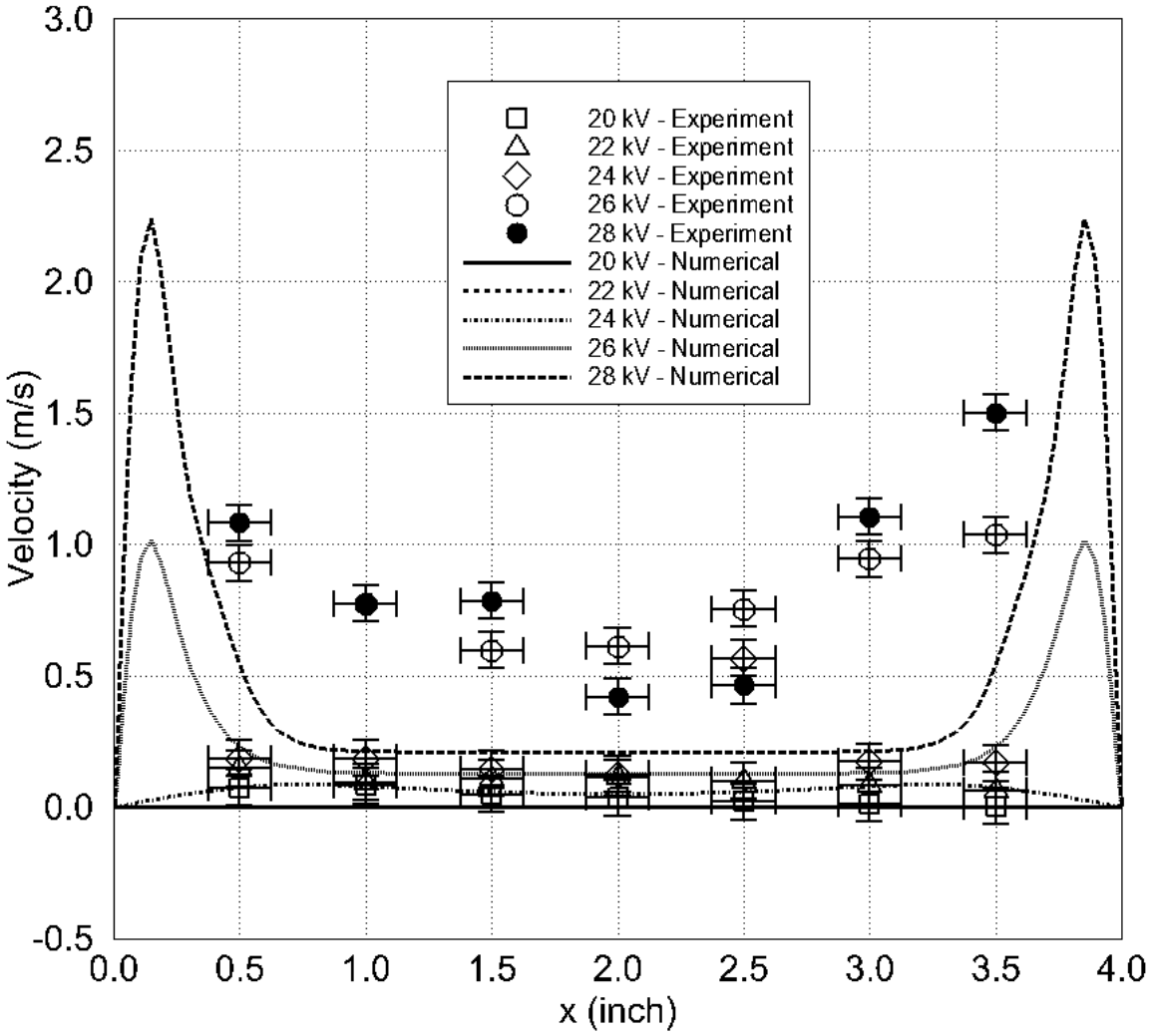

Figure A.11 Comparison of Velocity Profiles inside the Channel at 4-inch Downstream from the Grounded Electrode of the Bottom Stage (for an EHD Gas Pump with 2 inch Wide Grounded Plate at the Top Stage).

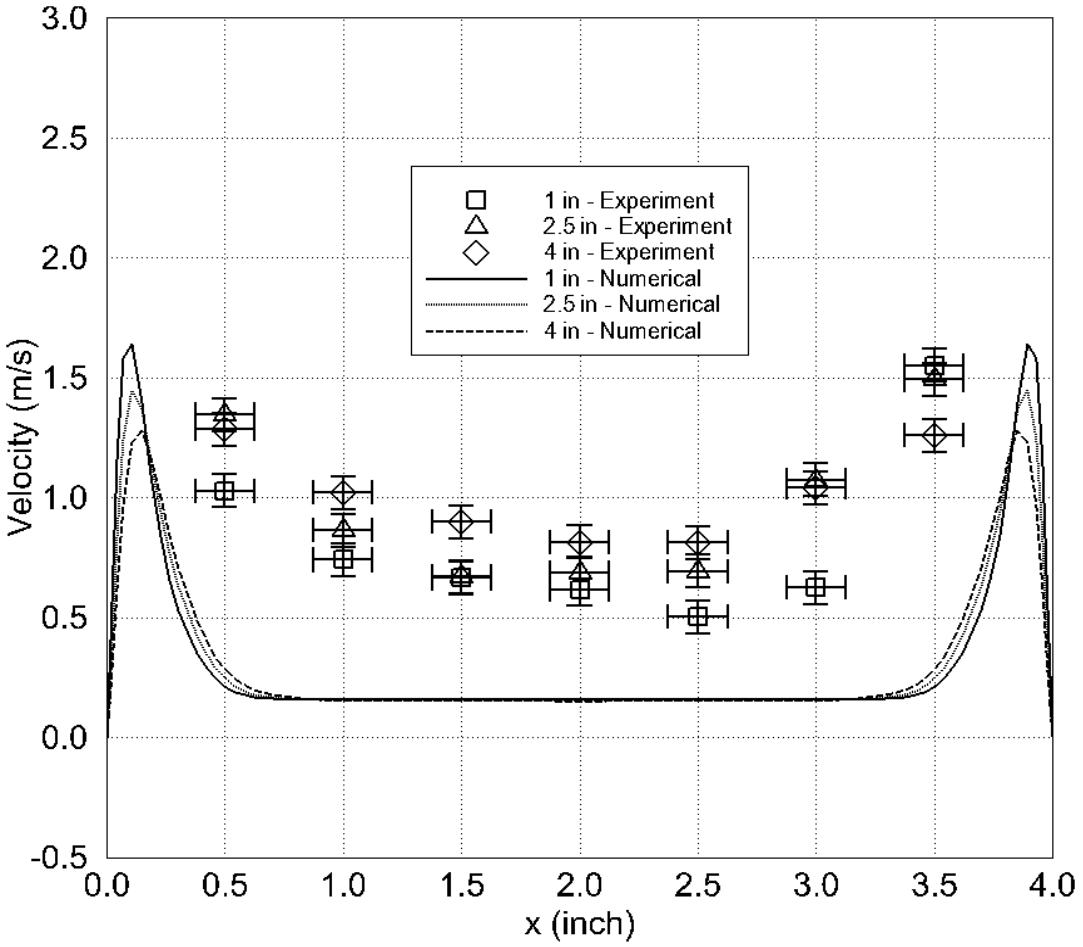

Figure A.12 Comparison of Velocity Profiles inside the Channel, V_o = 26 kV (for an EHD Gas Pump with 1 inch Wide Grounded Plate at the Top Stage).

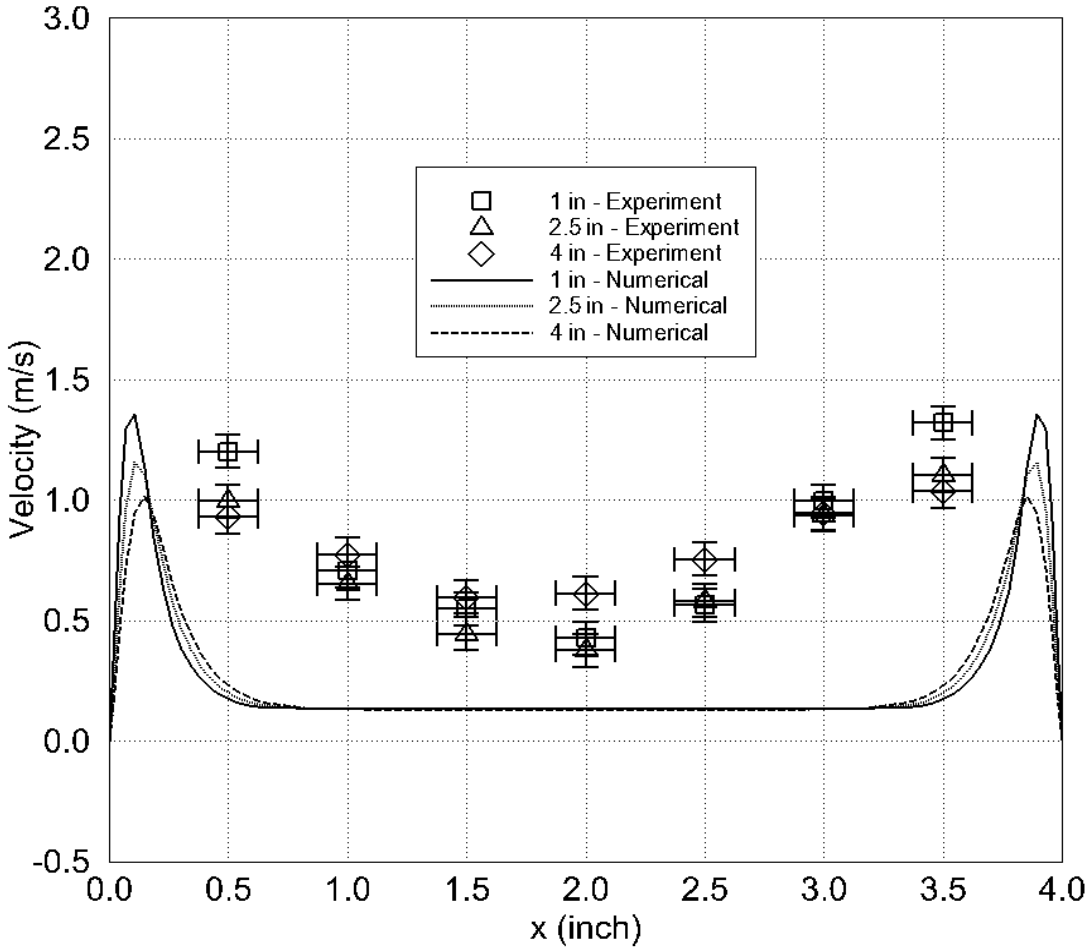

Figure A.13 Comparison of Velocity Profiles inside the Channel, V_o = 26 kV (for an EHD Gas Pump with 2 inch Wide Grounded Plate at the Top Stage).

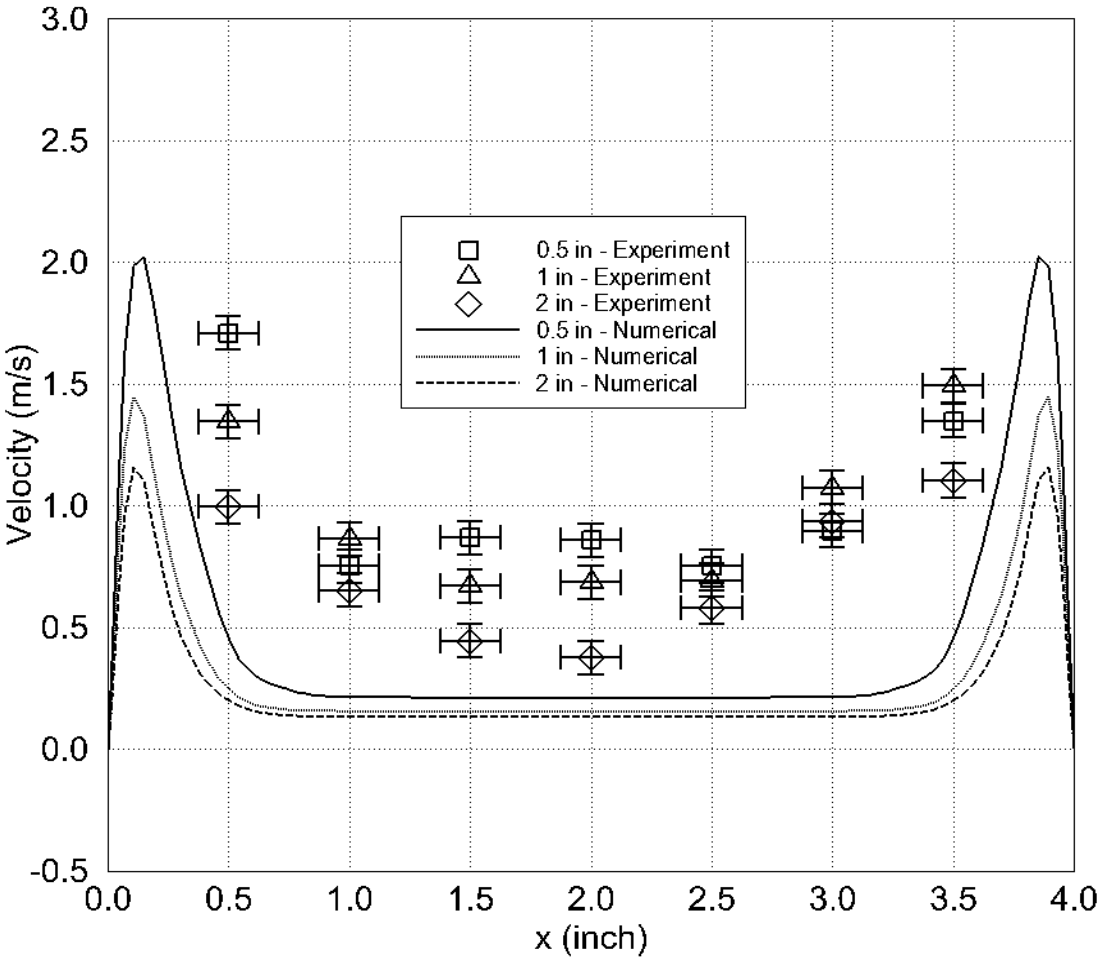

Figure A.14 Comparison of Velocity Profiles inside the Channel at 2.5-inch Downstream from the Grounded Electrode of the Bottom Stage, V_o = 26 kV (for a Two-Stage EHD Gas Pump with Various Size of the Grounded Plate at the Top Stage).

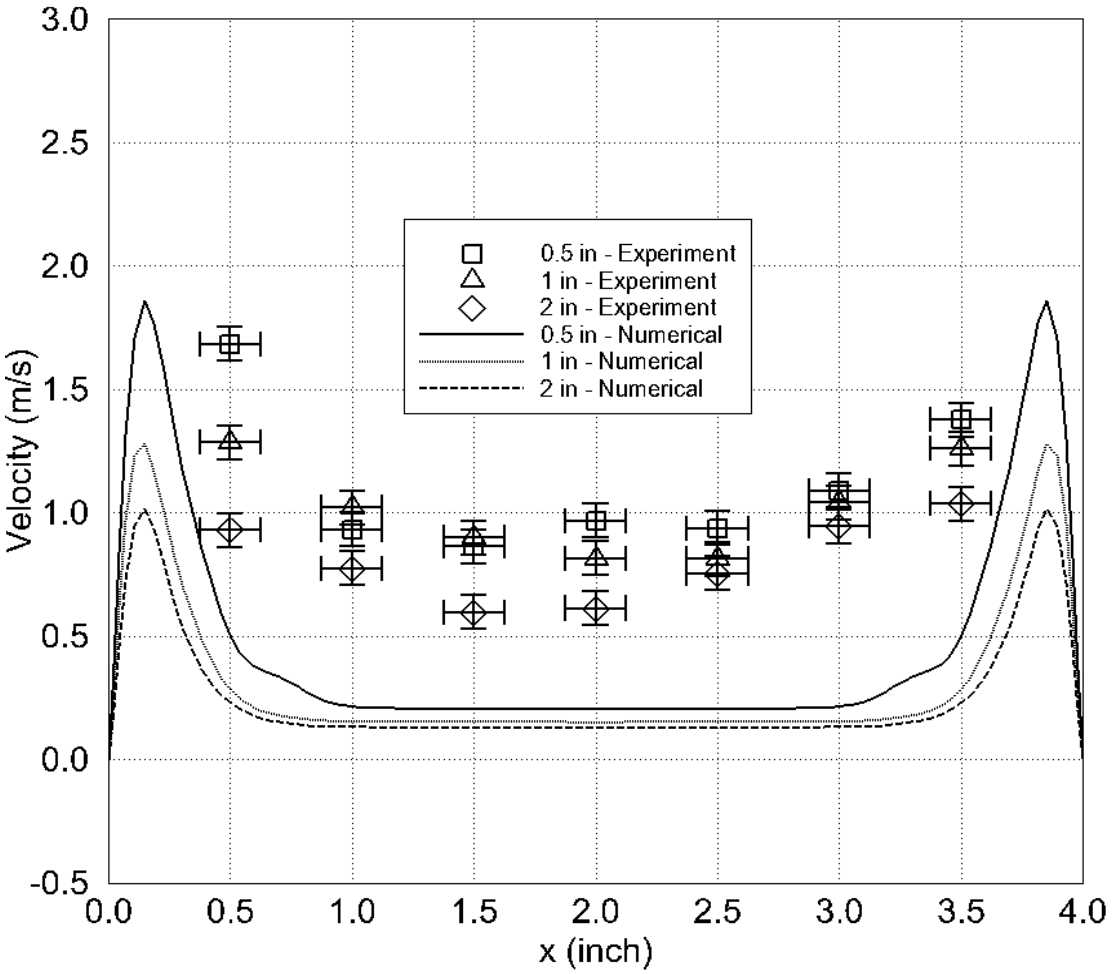

Figure A.15 Comparison of Velocity Profiles inside the Channel at 4-inch Downstream from the Grounded Electrode of the Bottom Stage, V_o = 26 kV (for a Two-Stage EHD Gas Pump with Various Size of the Grounded Plate at the Top Stage).

APPENDIX B

FORCED CONVECTION RESULTS

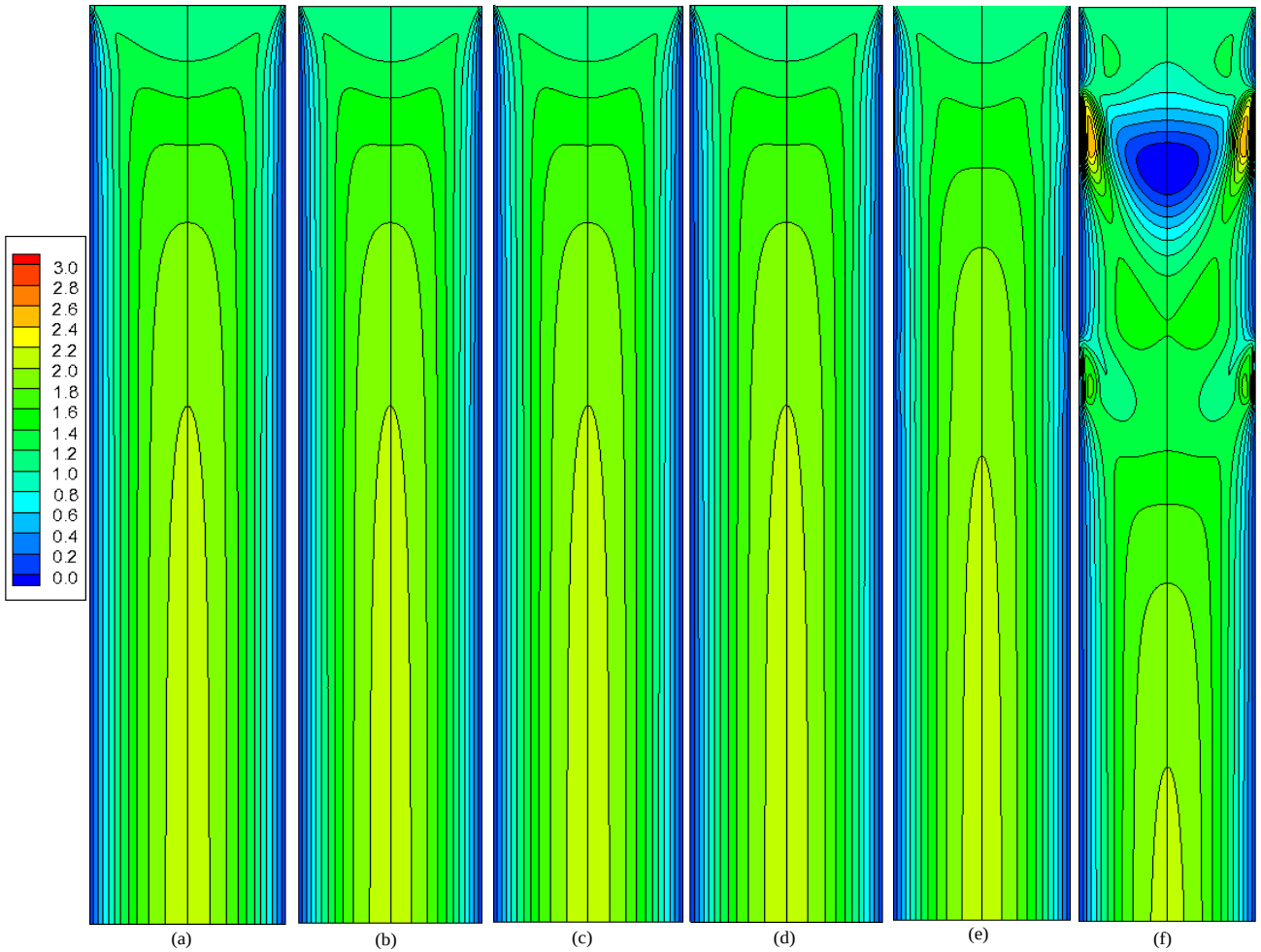

Figure B.1 Flow Field in a Square Channel with a Two-Stage EHD Gas Pump, Re = 500

(1-inch Wide Grounded Electrode at the Top Stage)

(a) Vo =0 kV, (b) Vo =20 kV, (c) Vo =22 kV, (d) Vo =24 kV, (e) Vo =26 kV, (f) Vo =28 kV.

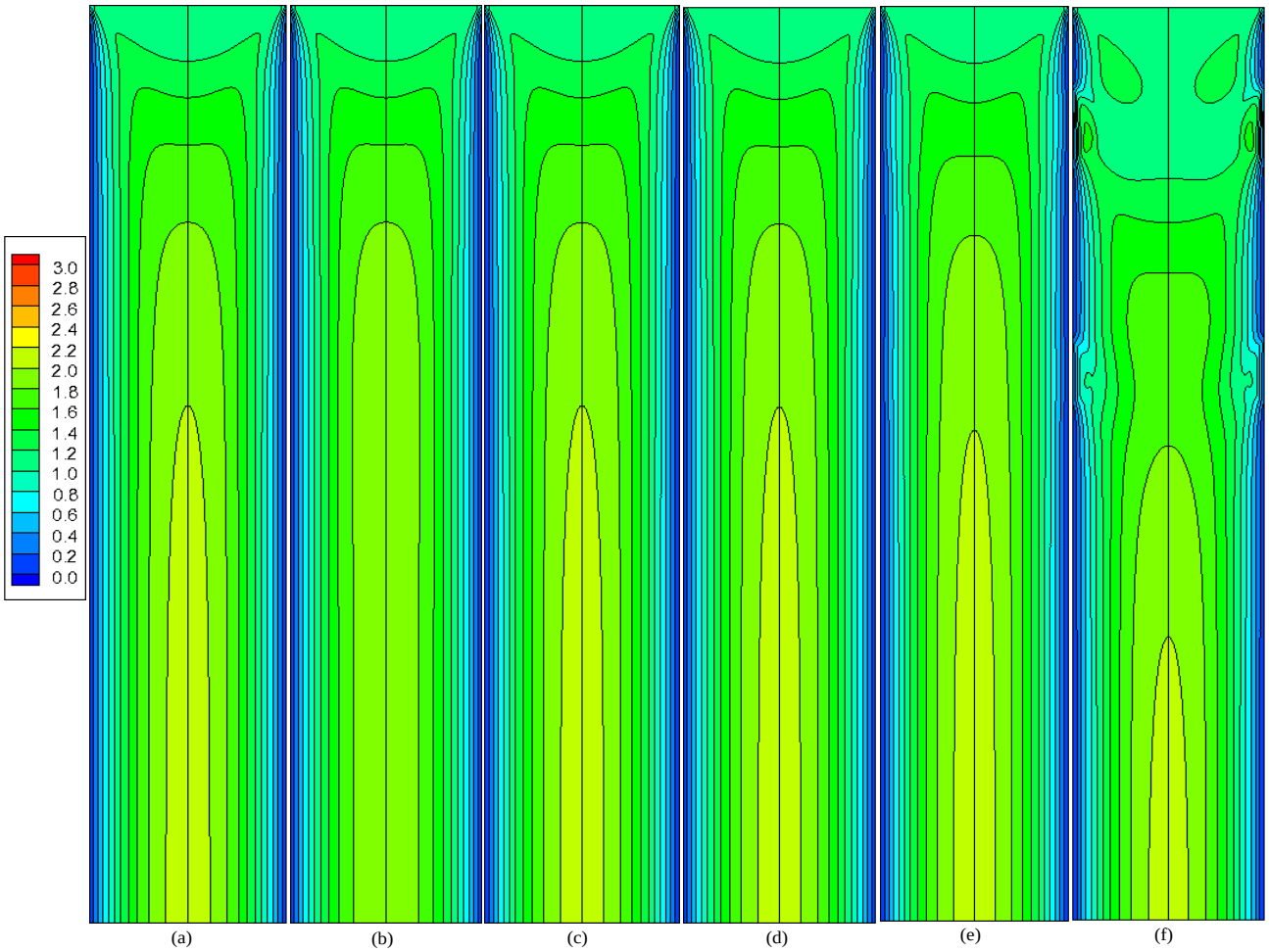

Figure B.2 Flow Field in a Square Channel with a Two-Stage EHD Gas Pump, Re = 500

(2-inch Wide Grounded Electrode at the Top Stage)

(a) Vo =0 kV, (b) Vo =20 kV, (c) Vo =22 kV, (d) Vo =24 kV, (e) Vo =26 kV, (f) Vo =28 kV.

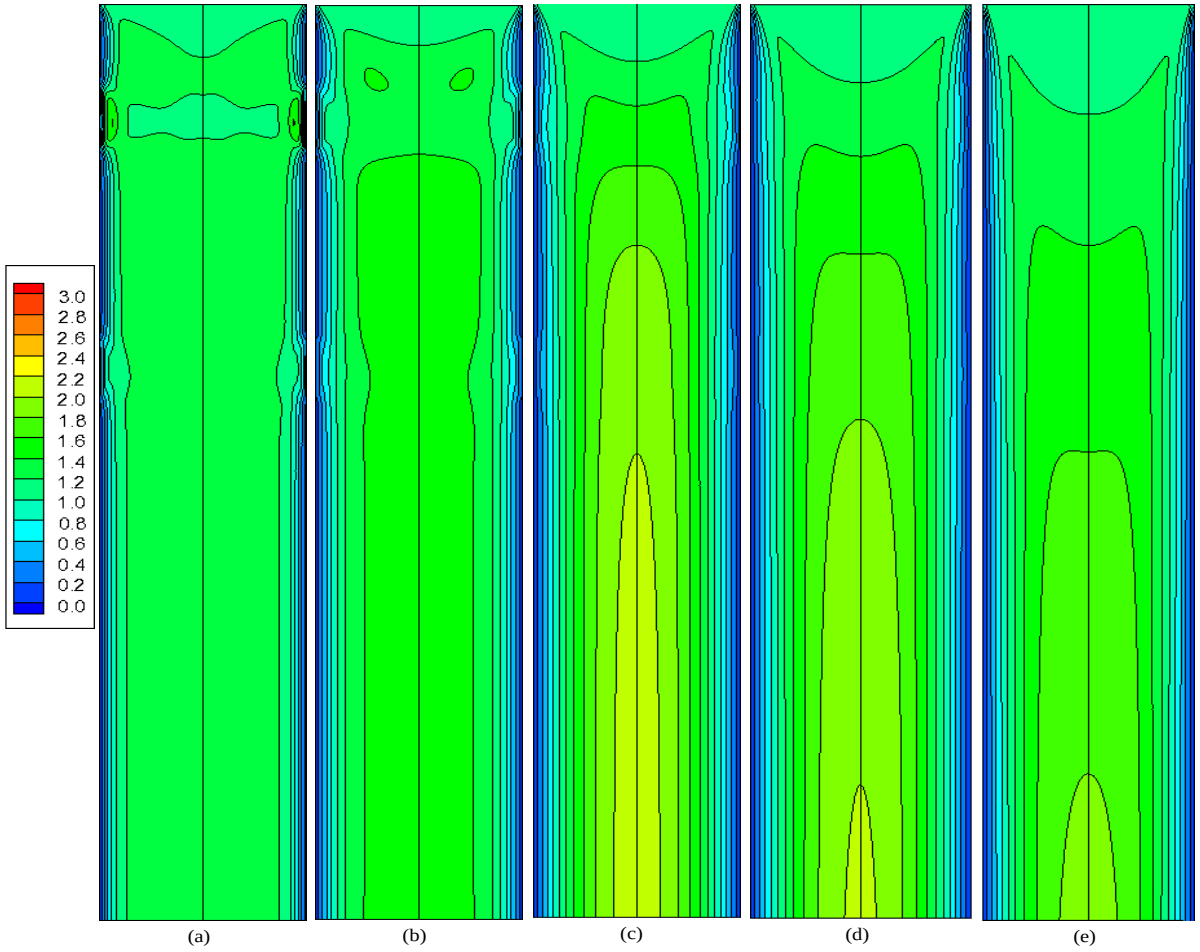

Figure B.3 Flow Field in a Square Channel with a Two-Stage EHD Gas Pump, Vo =26 kV

(1-inch Wide Grounded Electrode at the Top Stage)

(a) Re =100, (b) Re =200, (c) Re =500, (d) Re =1000, (e) Re =2000.

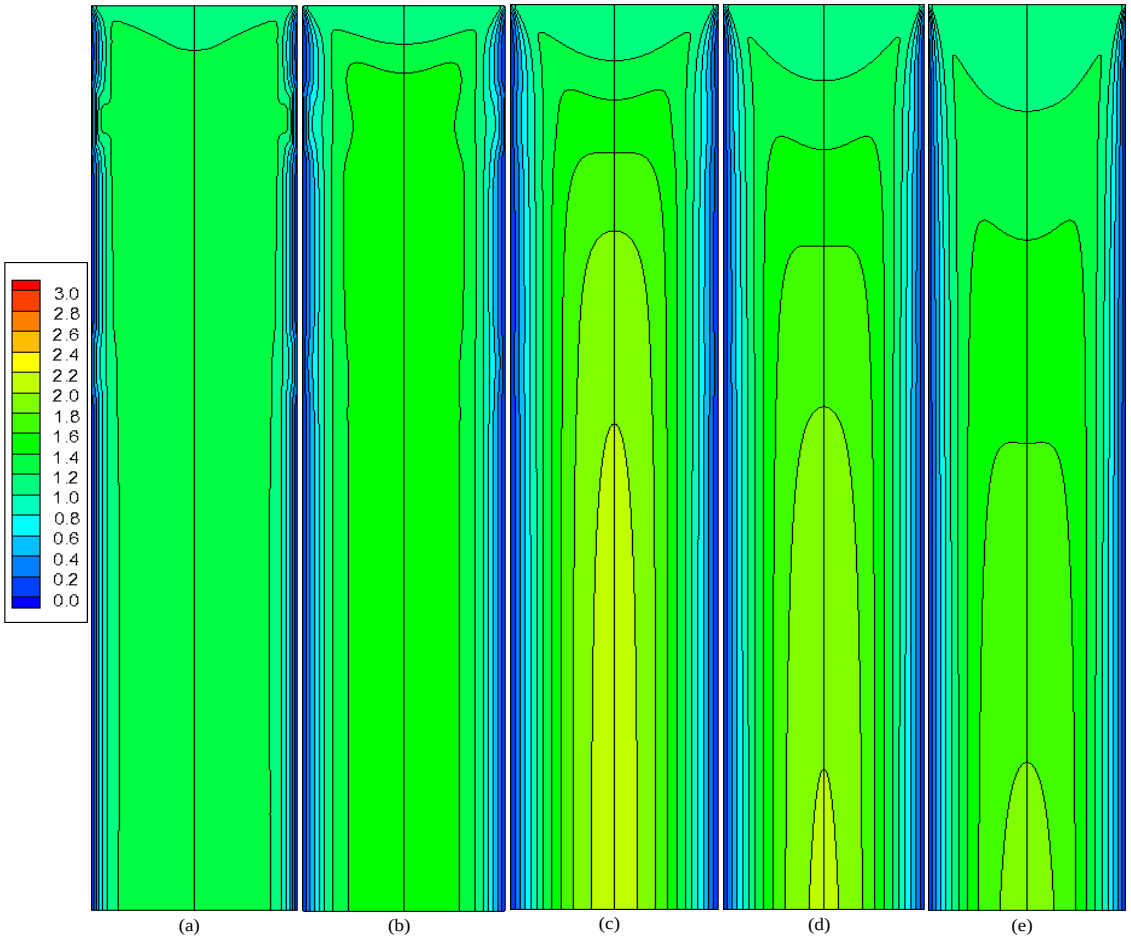

Figure B.4 Flow Field in a Square Channel with a Two-Stage EHD Gas Pump, Vo =26 kV

(2-inch Wide Grounded Electrode at the Top Stage)

(a) Re =100, (b) Re =200, (c) Re =500, (d) Re =1000, (e) Re =2000.

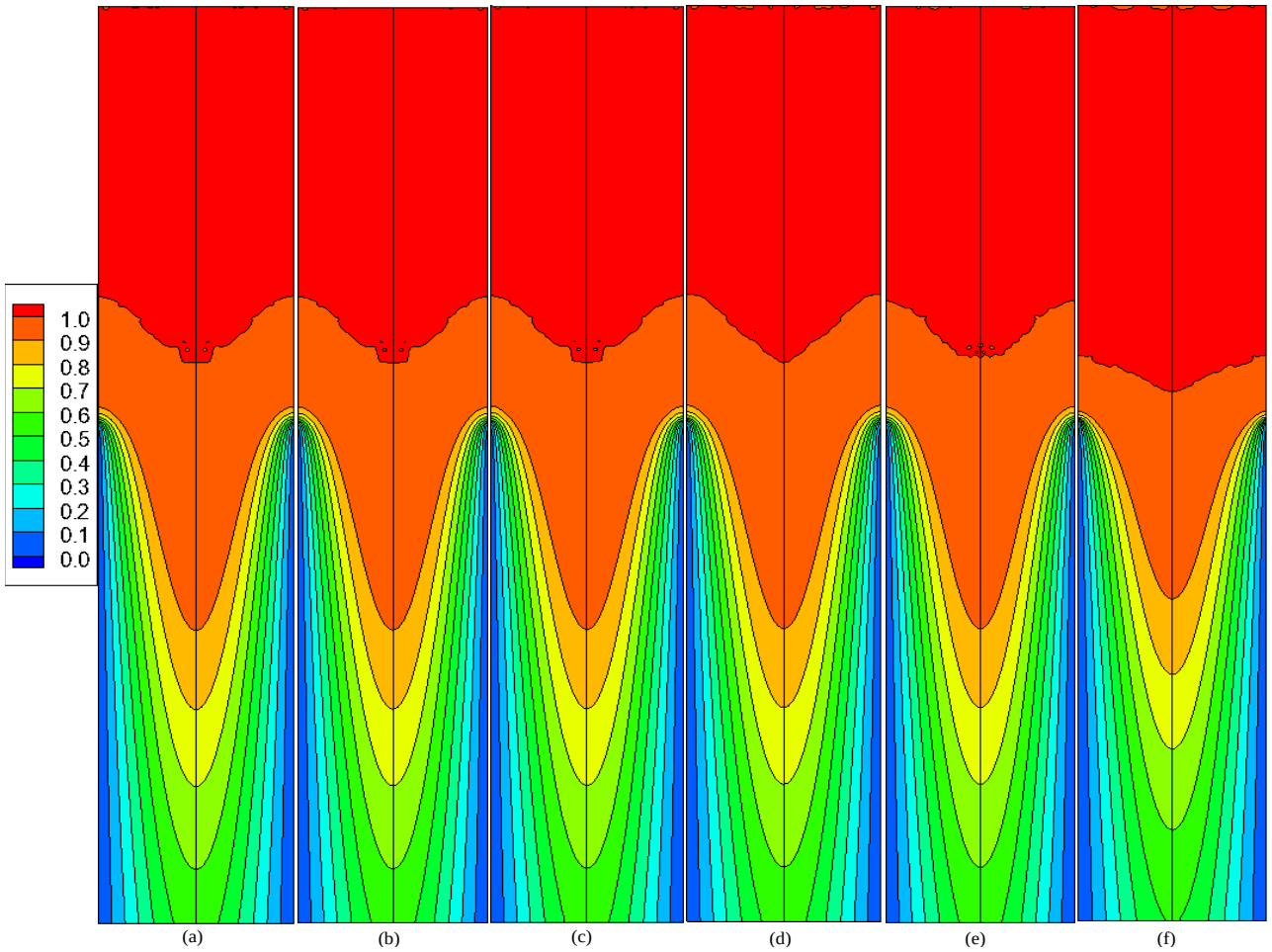

Figure B.5 Temperature Field in a Square Channel with a Two-Stage EHD Gas Pump, Re = 500

(1-inch Wide Grounded Electrode at the Top Stage)

(a) Vo =0 kV, (b) Vo =20 kV, (c) Vo =22 kV, (d) Vo =24 kV, (e) Vo =26 kV, (f) Vo =28 kV.

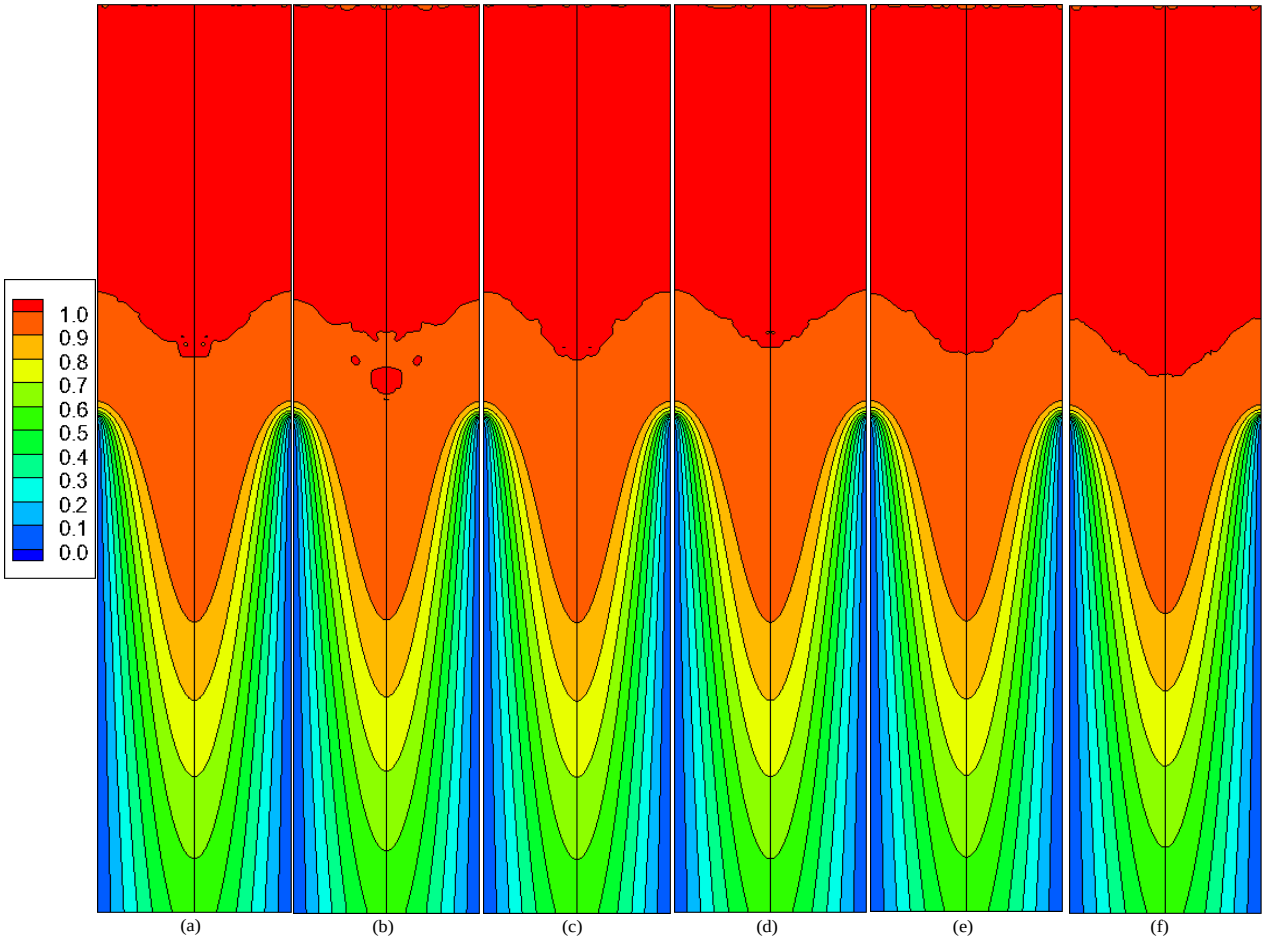

Figure B.6 Temperature Field in a Square Channel with a Two-Stage EHD Gas Pump, Re = 500

(2-inch Wide Grounded Electrode at the Top Stage)

(a) Vo =0 kV, (b) Vo =20 kV, (c) Vo =22 kV, (d) Vo =24 kV, (e) Vo =26 kV, (f) Vo =28 kV.

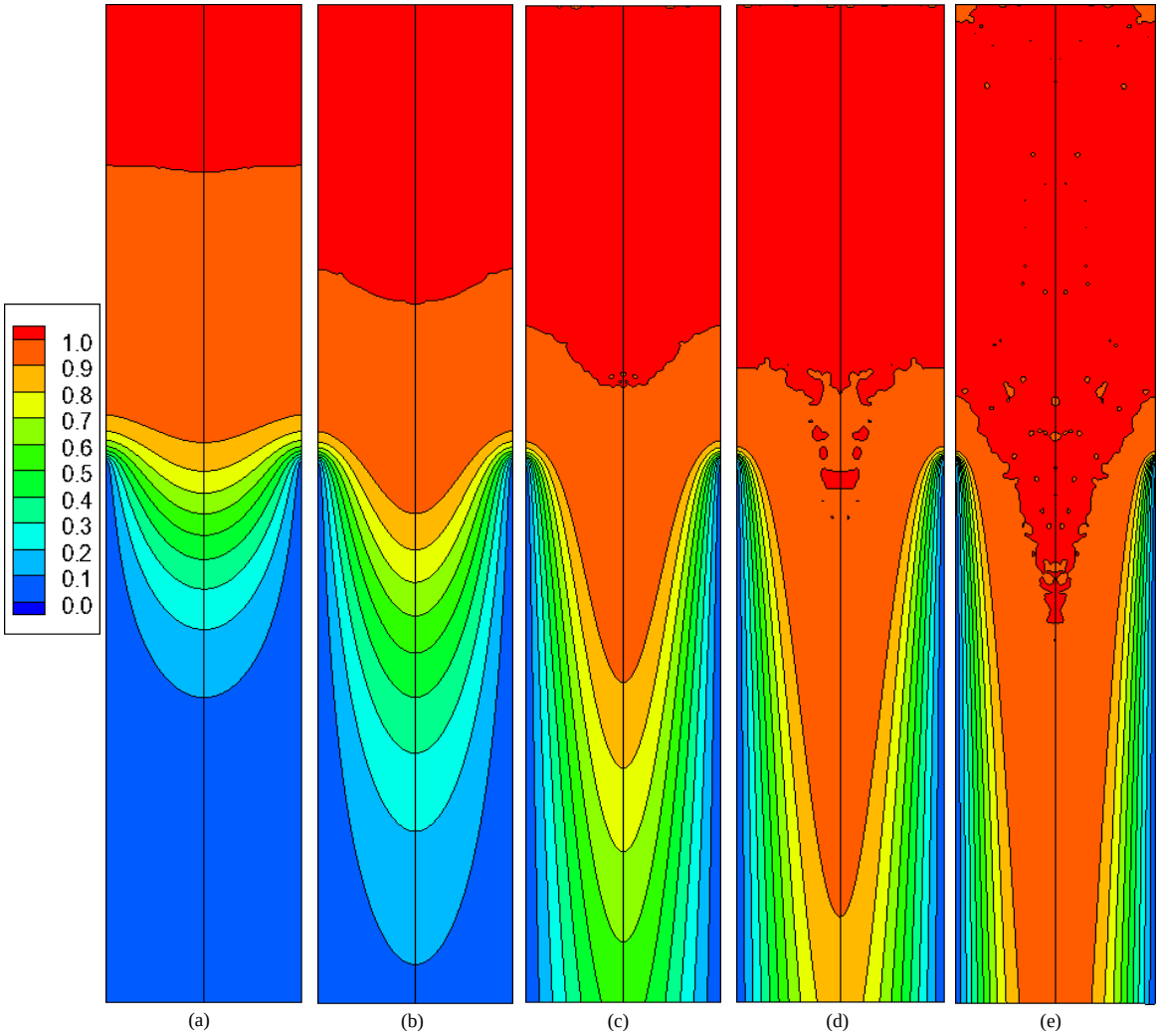

Figure B.7 Temperature Field in a Square Channel with a Two-Stage EHD Gas Pump, Vo =26 kV (1-inch Wide Grounded Electrode at the Top Stage)

(a) Re =100, (b) Re =200, (c) Re =500, (d) Re =1000, (e) Re =2000.

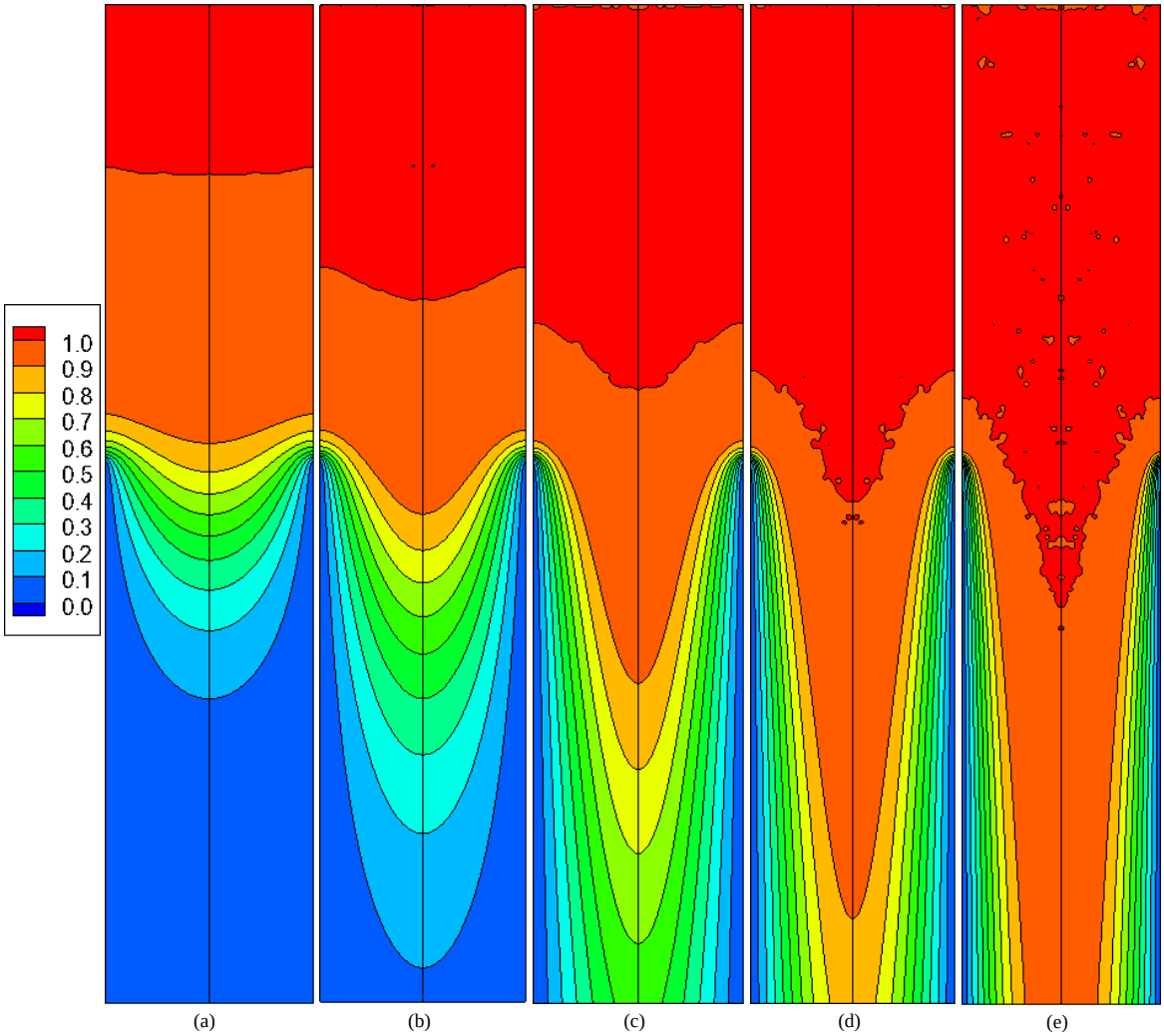

Figure B.8 Temperature Field in a Square Channel with a Two-Stage EHD Gas Pump, Vo =26 kV (2-inch Wide Grounded Electrode at the Top Stage)

(a) Re =100, (b) Re =200, (c) Re =500, (d) Re =1000, (e) Re =2000.

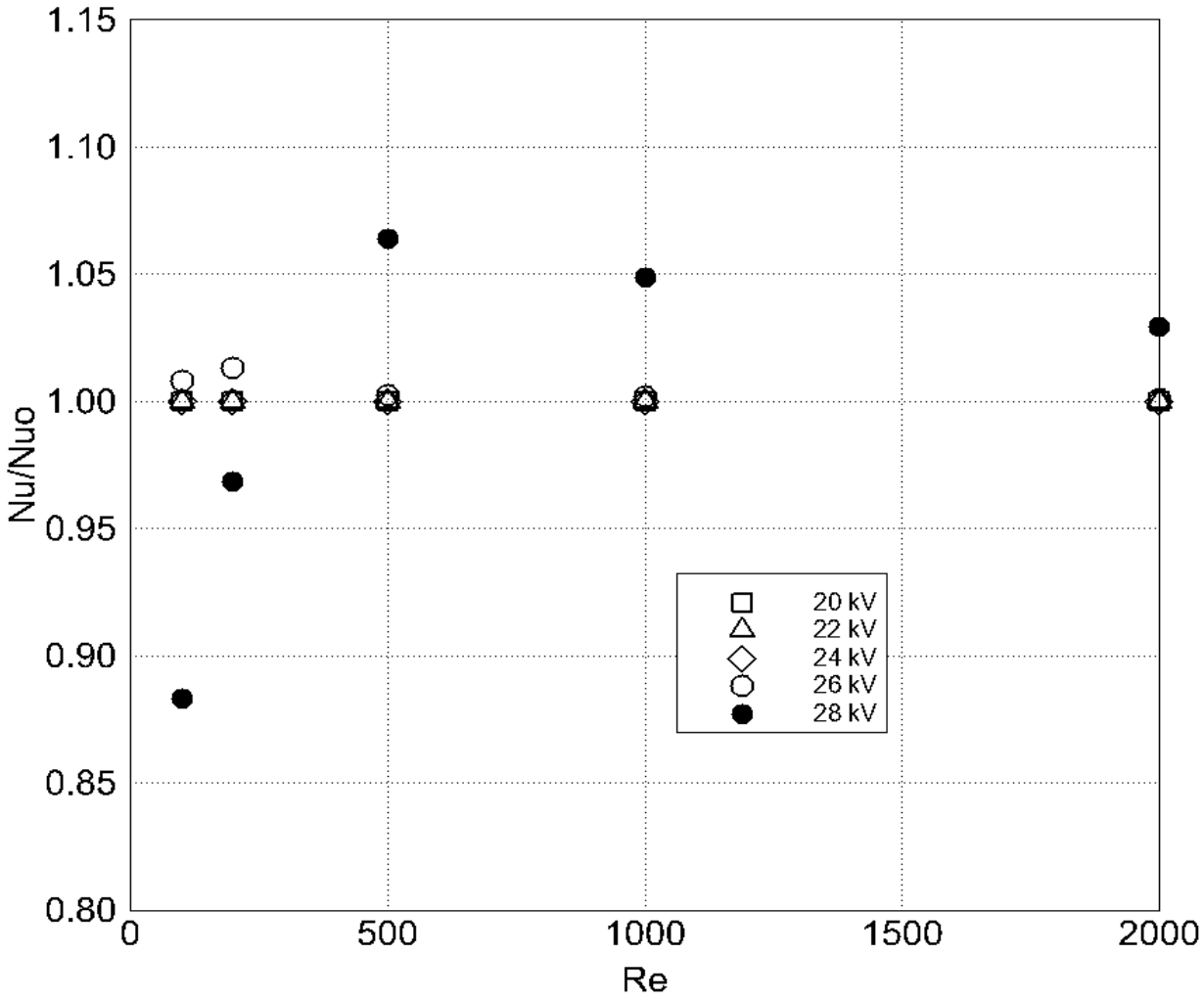

Figure B.9 Average Nusselt Number as a Function of Reynolds Number (for a Two-Stage EHD Gas Pump with 1-inch Wide Grounded Electrode at the Top Stage).

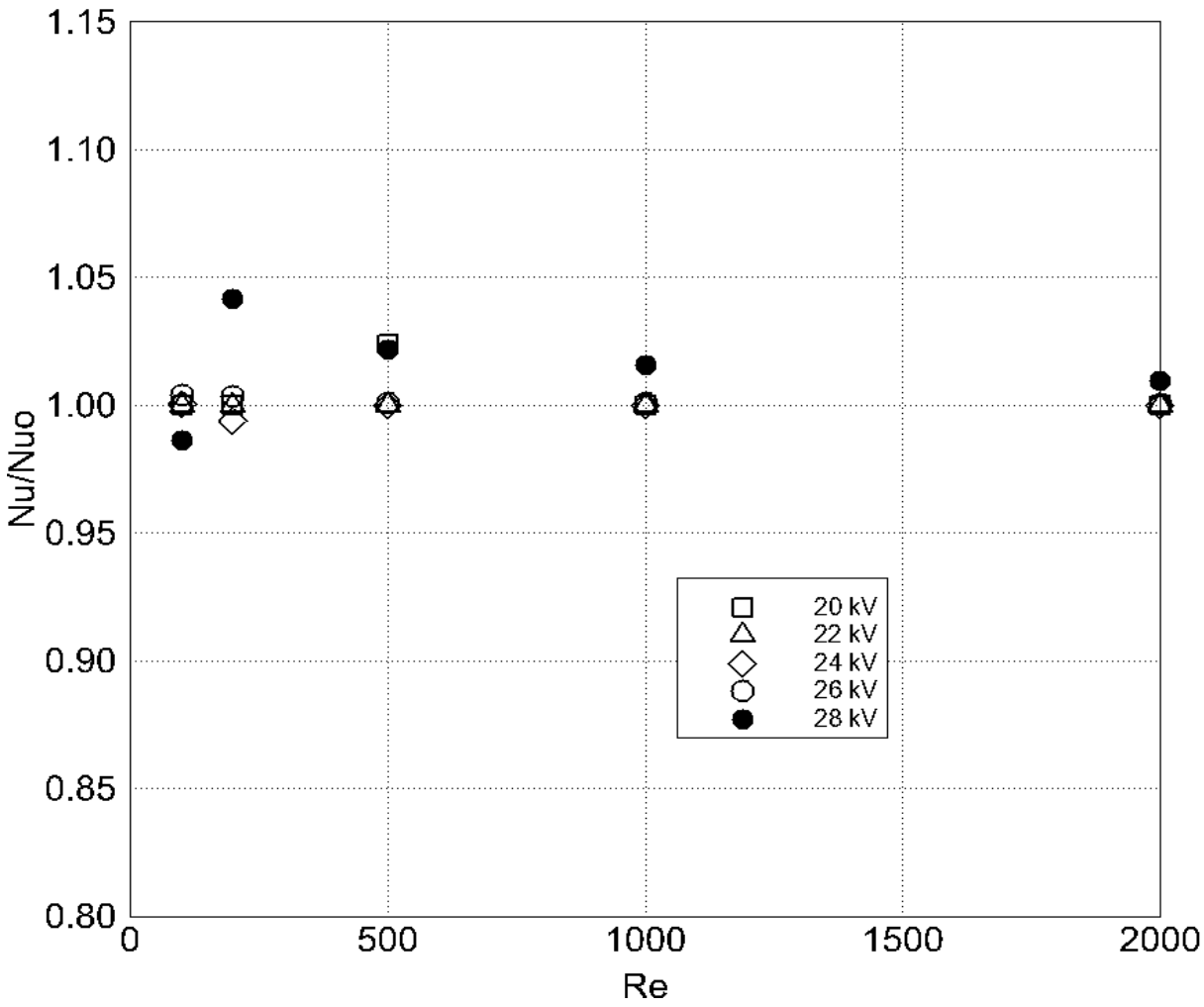

Figure B.10 Average Nusselt Number as a Function of Reynolds Number (for a Two-Stage EHD Gas Pump with 2-inch Wide Grounded Electrode at the Top Stage).

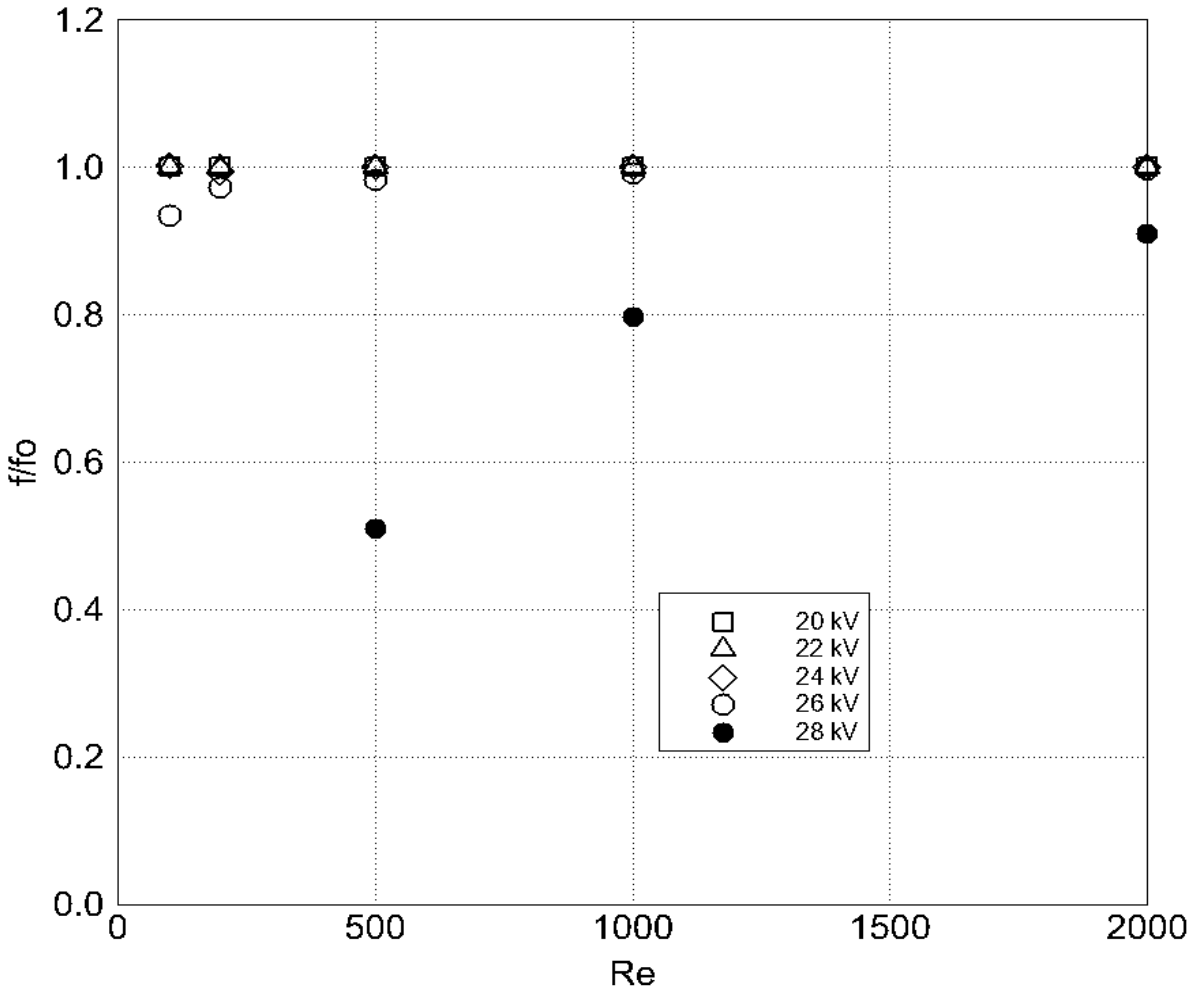

Figure B.11 Friction Factors as a Function of Reynolds Number (for a Two-Stage EHD Gas Pump with 1-inch Wide Grounded Electrode at the Top Stage).

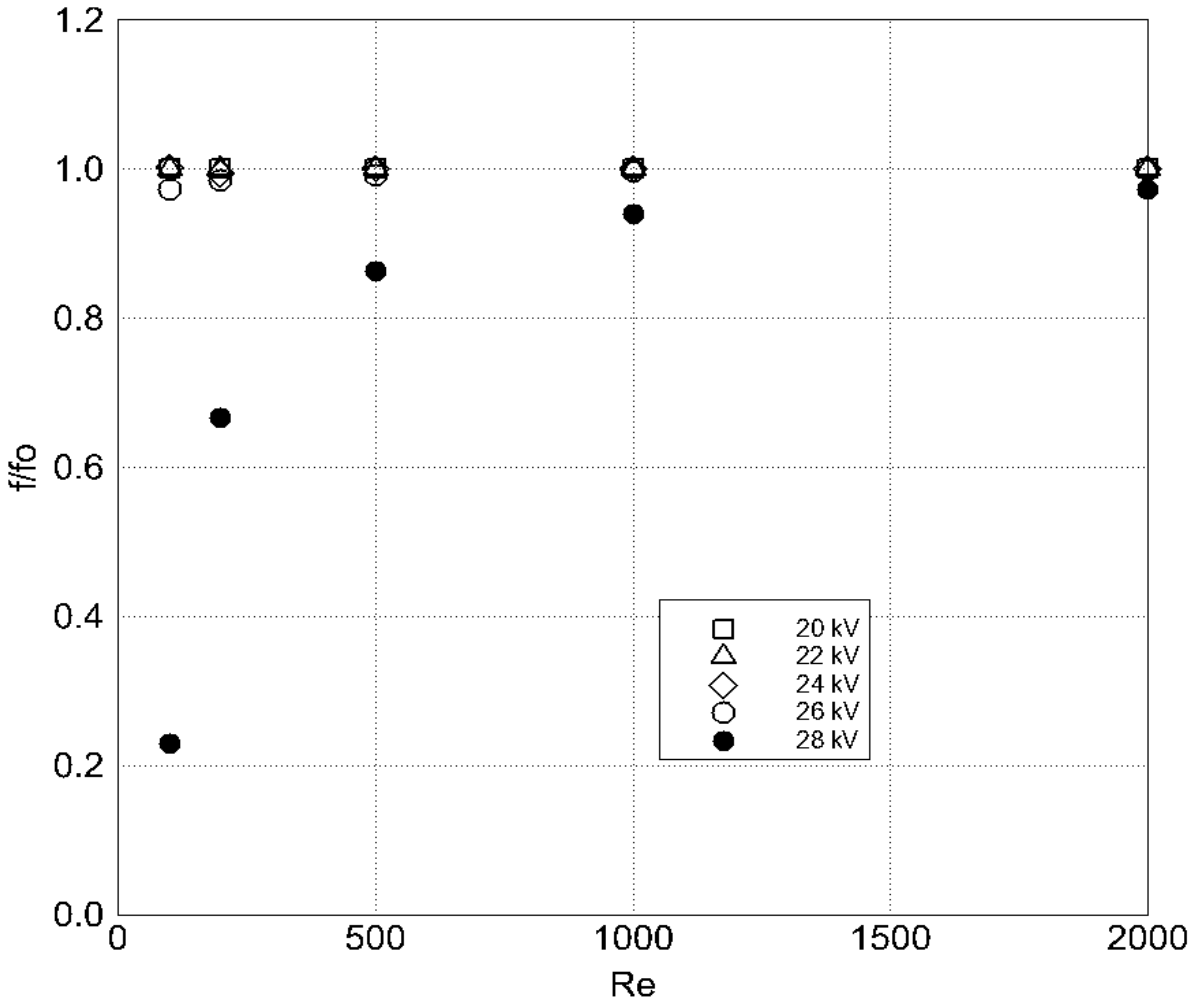

Figure B.12 Friction Factors as a Function of Reynolds Number (for a Two-Stage EHD Gas Pump with 2-inch Wide Grounded Electrode at the Top Stage).

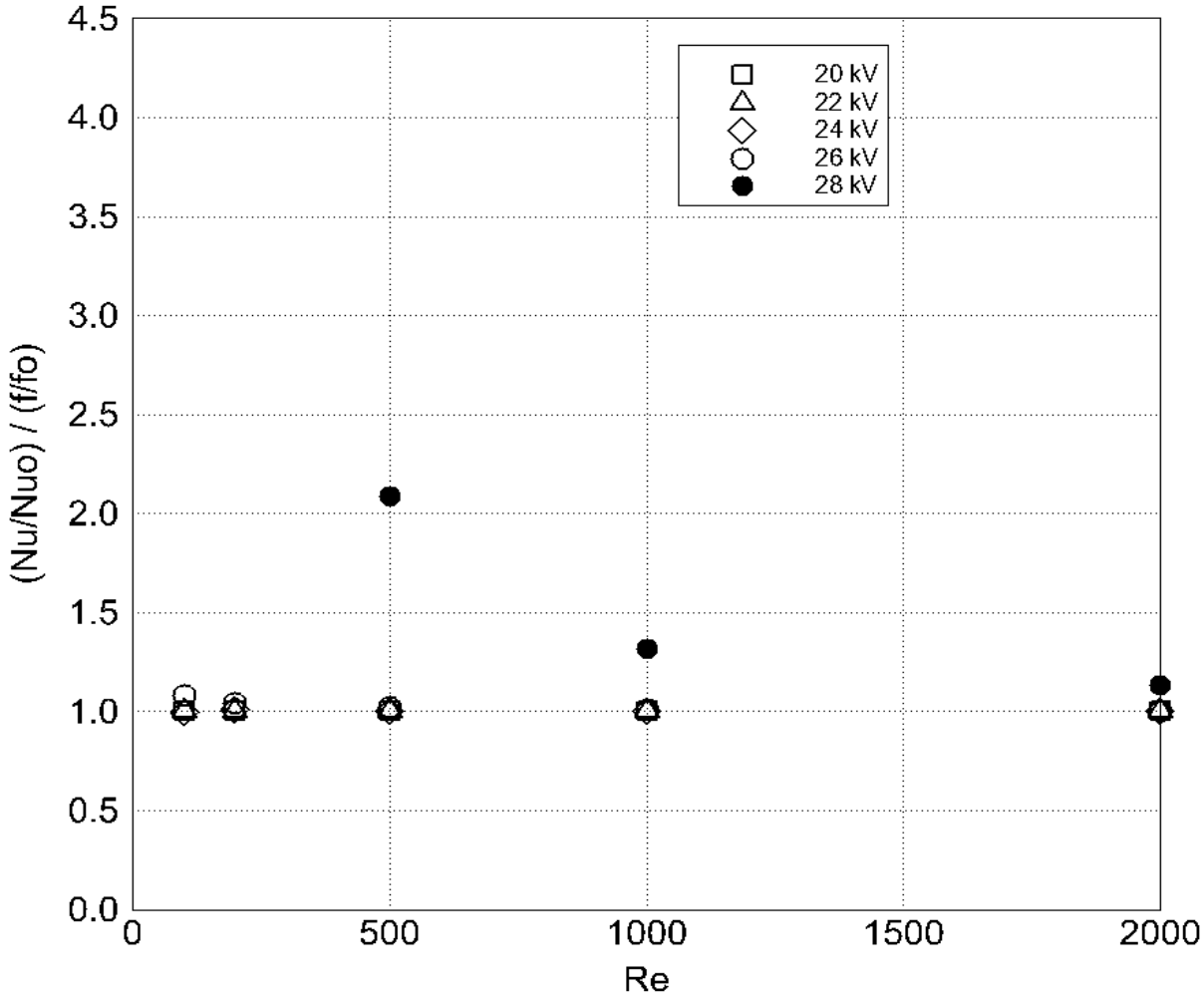

Figure B.13 Thermal Hydraulic Performance for a Two-Stage EHD Gas Pump with 1-inch Wide Grounded Electrode at the Top Stage.

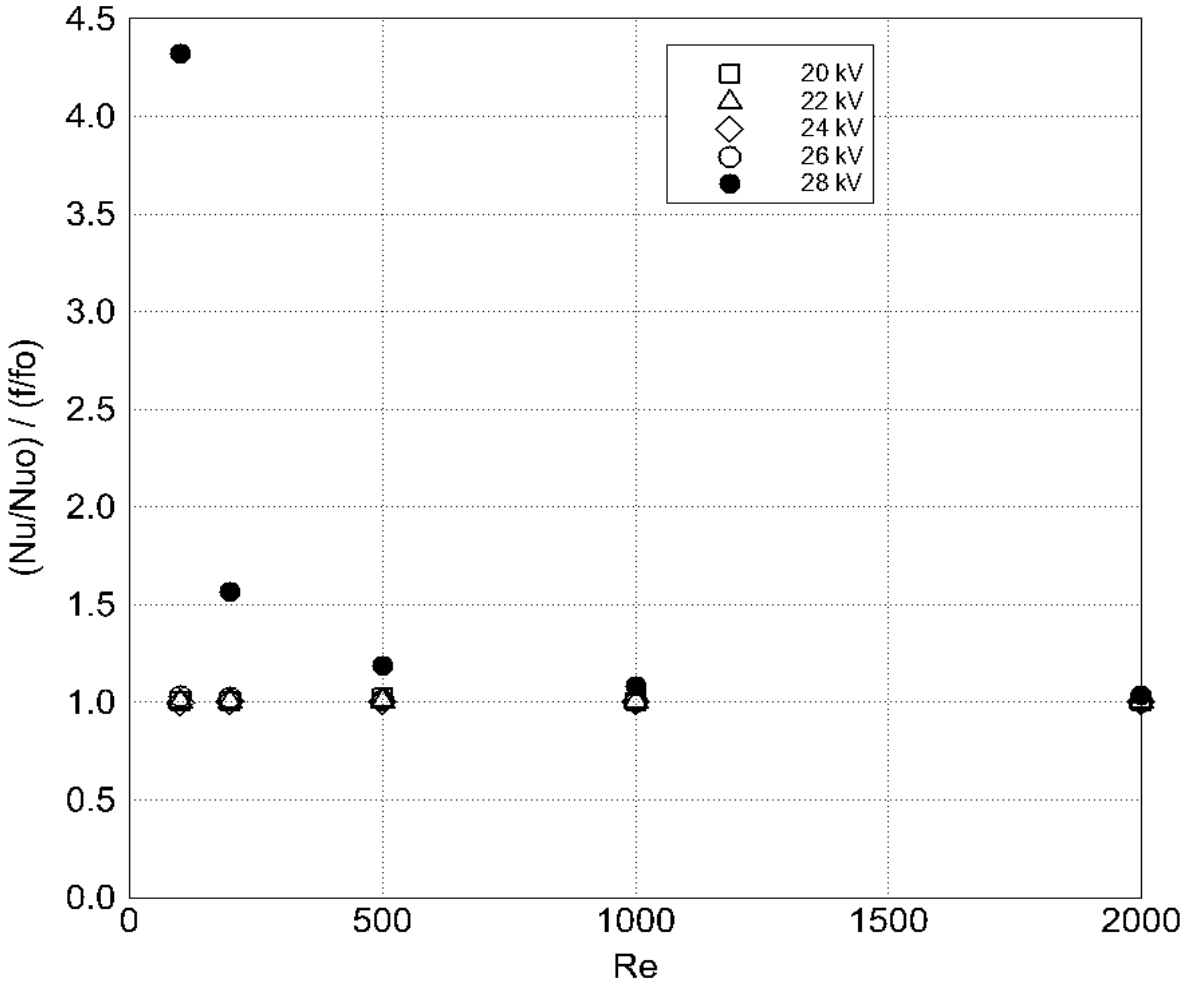

Figure B.14 Thermal Hydraulic Performance for a Two-Stage EHD Gas Pump with 2-inch Wide Grounded Electrode at the Top Stage.

NOMENCLATURE

A	Surface area of the grounded plate, [m^2]
A_s	heat transfer surface area, [m^2]
b	ion mobility, [$m^2/V \cdot s$]
d	distance between electrode tip and grounded plate, [m]
D	hydraulic diameter, [m]
$\mathbf{E}$	electric field strength, [V/m]
E_x	x-component electric field strength, [V/m]
E_y	y-component electric field strength, [V/m]
E_z	z-component electric field strength, [V/m]
f	friction factor
$\mathbf{f}_e$	electric body force, [N]
g	gravitational acceleration, [m^2/s]
h	convective heat transfer coefficient, [$W/m^2 \cdot K$]
I	total corona current, [A]
$\mathbf{J}$	current density, [A/m^2]
k	thermal conductivity, [$W/m \cdot K$]
L	channel length, [m]
L_h	hydrodynamic entry length, [m]
L_t	thermal entry length, [m]
N_{EHD}	EHD number
Nu	average Nusselt number, hD/k

Nu_0 average Nusselt number without electric field, hD/k

p pressure, [Pa]

p_i pressure at the inlet, [Pa]

p_o pressure at the outlet, [Pa]

Pr Prandtl number, ν/α

$\bar{p}$ dimensionless pressure, $(p - p_i)/\rho u_i^2$

q heat flux, [W/m^2]

Re Reynolds number, $u_i D/\nu$

t time, [s]

T temperature, [K]

T_i incoming fluid temperature, [K]

T_m mean fluid temperature, [K]

T_o temperature at the outlet, [K]

T_w wall temperature, [K]

$\mathbf{u}$ fluid velocity, [m/s]

u x-component of velocity, [m/s]

u_e characteristic velocity of corona wind, $\sqrt{\rho_{c0} V_0/\rho}$

u_i inlet fluid velocity, [m/s]

u_m mean fluid velocity, [m/s]

$\bar{u}$ dimensionless velocity in x direction, u/u_i

v y-component of velocity, [m/s]

V electric potential, [V]

V_0 electric potential at the wire, [V]

$\bar{v}$ dimensionless velocity in y direction, v/u_i

$\bar{V}$ dimensionless electric potential, V/V_0

w z-component of velocity, [m/s]

$\bar{w}$ dimensionless velocity in z direction, w/u_i

x, y, z Cartesian coordinates, [m]

$\bar{x}, \bar{y}, \bar{z}$ dimensionless Cartesian coordinates

Greek Symbols

α thermal diffusivity, [m^2/s]

ε electric permittivity, [F/m]

ν kinematic viscosity, [m^2/s]

θ dimensionless temperature, $(T - T_w)/(T_i - T_w)$

θ_0 dimensionless temperature at the outlet, $(T_0 - T_w)/(T_i - T_w)$

ρ fluid density, [kg/m^3]

ρ_c space charge density, [C/m^3]

ρ_{c0} space charge density at the wire tip, [C/m^3]

$\bar{\rho}_c$ dimensionless space charge density, ρ_c/ρ_{c0}